Natural, numerical and structure-induced mixing in dense gravity currents: idealised and realistic model studies

---

Dissertation zur Erlangung des akademischen Grades
doctor rerum naturalium (Dr. rer. nat.)
der Mathematisch-Naturwissenschaftlichen Fakultät
der Universität Rostock

vorgelegt von
Hannes Rennau, geb. am 28.4.1980 in Rostock
Rostock, 30. März 2011

urn:nbn:de:gbv:28-diss2011-0093-2

Liste der Gutachter:

Prof. Dr. Hans Burchard (Leibniz Institute for Baltic Sea Reseach Warnemünde)
Seestraße 15
D-18119 Rostock

PD Dr. Thomas Pohlmann (Institut für Meereskunde, Universität Hamburg)
Bundesstraße 53
D-20146 Hamburg

Datum der Verteidigung: 27. Mai 2011

Kurzzusammenfassung

Diese Arbeit befasst sich mit der quantitativen Untersuchung von natürlicher, numerischer und durch vertikale Strukturen verursachter Vermischung dichter Bodenströmungen mit Hilfe idealisierter sowie realistischer Modellsimulationen der westlichen Ostsee. Zusätzlich wurde das Ausbreitungsverhalten dichter Bodenströmungen in der westlichen Ostsee mit passiven Tracern im Modell analysiert. Obwohl die in der Arbeit modellierten dichten Bodenströmungen in der westlichen Ostsee ein hohes Maß an Übereinstimmung mit den Messungen zeigen, konnte ebenfalls gezeigt werden, dass die durch Diskretisierungfehler der Advektionsschemen hervorgerufene numerische Vermischung ähnliche Größenordnungen wie die rein natürliche Vermischung aufweist. Die Arbeit schließt mit der Analyse der zusätzlichen Vermischung in geschichteten Strömungen der westlichen Ostsee durch vertikale Zylinder (Offshore-Windparks) ab.

Contents

Chapter 1

General introduction

1.1 Context

1.1.1 Abstract

The advection and mixing of gravity currents, sometimes called buoyancy or density currents, is a phenomena occurring in both man-made and natural situations. Manifestations of gravity currents and its academic research range from large scale oceanic processes as the thermohaline circulation, sea-breeze fronts, oil spillage from a ship to airborne- and snow-avalanches.

Understanding the thermohaline circulation (see e.g.. figure 1.1) of the transport and dilution of dense bottom gravity currents for example is very important in order to obtain their contribution to global climate or their response to climate change which again may change global ocean circulation. It is found with the help of tracer experiments that in mixing large scale dense bottom currents is astonishingly low over long travel distances down to the abyss and connects the world oceans via transporting energy (temperature gradients and momentum) and matter such as dissolved gases and solid substances which are all more or less subject to entrainment. Consequently it is a challenge for numerical models of any kind to realistically reproduce turbulent mixing of gravity currents on their pathway over long distances (see section 1.1.3).

Various scientific publications pointed out that numerical models are fairly reliable tools to reproduce complex non-linear physical processes and dynamics but they always need to be calibrated and validated against observational data. In this work the natural mixing, the spreading behavior and the spreading times of such dense currents in the Western Baltic Sea is reproduced by a numerical model, whereas a number of observations have been used for validation of the model results. To obtain the measure of the reliability of numerical model simulations concerning dilution and hence mixing of the gravity currents (chapter 2), a numerical mixing analysis is additionally conducted. This has shown a surprisingly strong overall contribution of spurious mixing but is connected to a different spatial and temporal distribution than the pure physical mixing (chapter 3).

Finally the impact of additional mixing due to vertically aligned structures (offshore wind farms to be

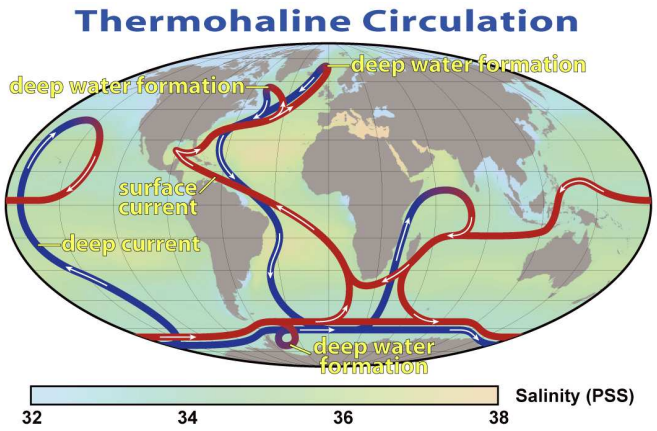

Figure 1.1: This sketch shows thermohaline circulation in the world oceans as a climate relevant large scale phenomenon of gravity currents (picture taken from `wikipedia.org`).

build in the Arkona Sea region) is investigated with the help of the model. Here a parameterisation of the structure-induced mixing is developed, based on the quadratic friction law and calibrated concerning turbulence generation and mixing with a high resolution local model. The final results quantify the amount of water mass transformation and dilution of the dense bottom currents due to Offshore Wind-parks. After some qualitative investigations with idealised scenarios, an existing realistic Western Baltic Sea hindcast model is applied in two different scenarios covering (i) *weak mixing* and (ii) *strong mixing* for enhanced mixing due to vertical cylindrical structures. The scenarios are completed by two cases with unrealistically extensive wind farms simulating a theoretical future worst case scenario. By means of analysing annual model simulations, it is found that the impact of additional, cylinder-induced mixing due to realistic wind farm distributions is comparably low with a typical decrease of bottom salinity in the range of $0.1 - 0.3$ psu. The annual mean bottom salinity at the outflow from the Arkona Sea through the Bornholm Channel into the direction of the Baltic Proper shows a decrease due to mixing from realistic wind farm distribution of only 0.02 psu which is more than one order of magnitude smaller than the standard deviation of the bottom salinity change. As the main reason for this weak impact the decelerating effect of the structures due to friction and entrainment (locally reduced velocities and hence decreased turbulent mixing) is suggested. More significant impact is found on dilution of short-duration, high-density plumes. Investigations using a passive tracer, released at the Bornholm Channel, reveal that the inflows interleave from the bottom into their reference density up to 3 m higher only for the case of unrealistically extensive offshore wind farm distributions. It is concluded that the impact of offshore wind farms as they are currently planned for the Western Baltic Sea on inflows into the Baltic Sea basins is negligibly low.

This PhD thesis consists of three published papers (Burchard et al. (2009), Rennau and Burchard (2009), Burchard and Rennau (2008)) as well as one paper which currently is under review (Rennau et al. (2010)) and a further one which is in preparation (Mohrholz and Rennau (2010)). A detailed description of my contributions to the journal publications is given in section 1.3.

The work for this study was carried out within the framework of the international QuantAS Consortium (Quantification of water-mass transformation processes in the Arkona Sea), which is partially funded by the QuantAS-Off project (QuantAS-Impact of Offshore Wind Farms) by the German Federal Ministry of Environment, Nature Conservation and Nuclear Safety (BMU).

1.1.2 Motivation

The inflow of dense bottom water from the Kattegat into the stratified Baltic Sea is known as the only process to ventilate intermediate or deeper layers with oxygen. This is a very important process for the whole ecosystem. In order to understand the main pathways and to quantify the associated amount of natural mixing in these bottom currents, idealised and realistic model simulations have been carried out. After a careful model validation with the help of ship-based measurements and permanent station observations the amount of natural mixing of dense bottom currents in the Western Baltic Sea could be quantified. As the individual spreading behavior, spreading time and interleaving process of the Darss Sill and Drogden Sill water masses in the Western Baltic Sea is rather unknown, this work results in an analysis which gives first answers with the help of two passive tracers marking the two water masses separately.

As the next step the amount of spurious - model-induced - mixing has been quantified and qualified in both highly idealised and realistic model simulations. This is a useful contribution to the natural mixing analysis as this gives additional information on the performance and reliability of the physical mixing scheme used. This research in numerical mixing is suggesting a generic method in calculating the numerical mixing due to the tracer advection schemes and it is the first contribution of this kind to the ocean modelling community which gives insight into both the amount and spatial distribution of numerically induced mixing in coastal ocean models directly being compared to natural mixing in the model. For any linear or non-linear advection scheme and for all z-level or layer models (such as σ-layer or general vertical coordinate models) with equidistant or non-equidistant grid spacing the numerical tracer variance decay is simply calculated as the rate of change between the advected square of the tracer and the square of the advected tracer. The advantage of the generic method introduced and applied in this work is, that until now all diagnostic tools for quantifying the numerical mixing have certain restrictions like for example (i) they are restricted to a certain advection scheme only (ii) or the method applied is invasive and hence influencing the model result.

As reduction of green house gas emissions is a major goal of the German Federal government, renewable energies are planned to make at least 20% of the power generated until 2020. Hence the establishment of offshore wind farms in the German EEZ areas and the North Sea and the Baltic Sea is planned. While additional vertical mixing due to offshore wind farms in the well-mixed coastal waters of the German Bight (South-Eastern North Sea) have an negligible impact on the marine ecosystem, there may be significant effects for the stratified, almost tide-less Western Baltic Sea. To quantify this additional mixing it is the final goal of the present thesis to estimate this impact. Recent measurements of turbulence, stratification and velocities downstream and upstream of the

Great Belt Bridge revealed a significant effect of the vertical structures on both flow dynamics and mixing (Lass et al. (2008)). The research presented in this thesis attempts to quantify the additional mixing and dilution of dense bottom gravity currents due to foundations of wind turbines in offshore wind farms projected in the region of Western Baltic Sea. To some extent these offshore wind farms are planned to be build directly into the main pathways of dense bottom currents propagating into the Baltic Sea. These inflows are important for the Baltic Sea ecosystem because they are carrying high amounts of oxygen, necessary to ventilate the deeper basins of the Baltic Sea. Thus, dilution of these dense bottom currents by less dense ambient waters will decrease their potential to ventilate deep basins. Earlier work on the flow resistance of the Øresund bridge estimated a flow resistance of 0.6 % (Stigebrandt (1992)) which has almost no effect on the water exchange between the Baltic Sea and the North Sea. However, Stigebrandt (1992) did not further quantify the amount of additional dilution of the dense bottom currents, a gap which is partially filled with the quantitative model study on additional mixing due to Offshore Wind Farms as conducted in chapter 4. The effect of the generation of internal waves due to the vertical structures which might export momentum and mixing far from the structures was not considered in this study. This mixing process needs further research as Lass et al. (2008) found Karman straight downstream of the Great Belt bridge. Lass and Mohrholz (2003) provide a discussion on internal waves and corresponding mixing of naturally forced internal waves. However, the knowledge about the contribution of internal wave mixing in the Baltic Sea is not yet fully understood and quantified (Reissmann et al. (2009)).

In the present study, cylindric structures are assumed for the underwater construction of the individual wind turbines, which are assembled in wind farms with typically 50-100 structures. A parameterisation of the additional mixing and friction due to structure was developed as an extension of the k-ε two-equation turbulence closure model to carry out realistic simulations in the regional scale using the hydrostatic numerical ocean model GETM. Results of a high resolution Reynolds-Averaged Navier-Stokes (RANS) model of the local scale are used to calibrate this parameterisation for hydrostatic coastal ocean models. A range of different RANS simulations of dense bottom currents with varying internal Froude numbers were analysed to obtain a measure of the additional mixing due to vertically aligned cylindrical structures. The structure mixing parameterisation within the hydrostatic ocean circulation model GETM is then used to estimate the additional impact of Offshore-Wind-Parks on stratified flow in the Western Baltic Sea with several different model scenarios.

1.1.3 Gravity currents

Environmental flows driven by density differences tend to form layers of fluid which are separated by density interfaces. As briefly addressed in the section 1.1.1, gravity currents with sharp density gradients at the leading edge and the lateral boundaries are one example and the main focus of this work. These gravity currents tend to form a bottom layer of dense water which properties are influenced on several parameters such as Coriolis force, bottom friction, internal pressure gradient, velocity shear in the interface region, bottom slope which consequently influences transport and dilution (see e.g. figure 1.4).

Apart from numerical issues in modelling oceanic currents which are extensively addressed in chapter 3, several natural mixing processes are still not fully understood, whereas the interaction of the dense bottom flow with the sloping sea bed involves complex flow dynamics such as eddies, bottom boundary mixing and entrainment. An example is the Denmark Strait overflow where transport and dilution is highly variable within the first $100 - 200$km from the sill (Girton and Sanford (2003)).

The entrainment process (e.g. Turner (1973)) is the turbulent mixing process of the ambient fluid into the the gravity current. Production of turbulent kinetic energy influenced by bottom friction, buoyancy and shear strain induces a flux of mass, which will lift the plume interface level and lead to higher values in potential energy (e.g.. Oguz et al. (1990)). Generally the entrainment is a bulk characterisation of the turbulent mixing against the stabilizing effects of stratification and can be explained as a function of the Froude number. The concept of entrainment:

$$E = \frac{w_E}{U}, \tag{1.1}$$

with the entrainment rate E defined as the ratio between the entrainment velocity w_E and the current speed, has been applied by Ellison and Turner (1959) for a dense bottom current on a slope. During laboratory experiments they showed that E is a function of the bulk Richardson number:

$$Ri = \frac{g'h}{\Delta U^2} = \frac{1}{Fr^2}, \tag{1.2}$$

which is always positive and gives the ratio of potential to kinetic energy. Here g' is the reduced gravity $g' = g\Delta\varrho/\varrho_0$ with the reference density ϱ_0 which is the density of the ambient fluid and the density difference $\Delta\varrho$ which is the difference between the density of the plume and the ambient fluid, h the thickness of the gravity current, ΔU^2 the velocity difference between plume and ambient fluid and Fr the Froude number. The Richardson number is the reciprocal of the square root of the Froude number Fr which is more common for numerical modellers than Ri in describing whether flow conditions are subcritical ($Fr < 1$), critical ($Fr = 1$) or supercritical ($Fr > 1$). Low numbers of Ri indicate weak vertical density gradients compared to stronger velocity gradients which potentially decreases the density difference between plume and ambient water due to the increasing importance of kinetic energy leading to vertical turbulent mixing. For oceanographers the Richardson number is a measure of how much vertical stratification suppresses vertical turbulent mixing and is hence an appropriate measure to be coupled to linear or non-linear mathematical constructions to predict entrainment rates. The same holds for entrainment concepts using the Froude number. It must further be mentioned that for oceanic, coastal or estuarine flows the turbulent exchange is approximated to act in vertical direction only which is justified as vertical velocities are significantly lower than horizontal velocities and as such horizontal diffusivities can generally be neglected in numerical models. Strong vertical stratification will furthermore dampen processes such as the development of Kelvin-Helmholtz instabilities which could significantly contribute to vertical mixing processes as they are able to shear dense water above lighter water leading to vertical overturning.

A well-known example of an application of this entrainment concept is the investigation of ascending gases in the layered atmosphere by Turner (1986) based on the data of Ellison and Turner (1959):

$$E = \frac{0.08 - 0.1Ri}{1 + 5Ri}. \tag{1.3}$$

This entrainment concept gives reasonable entrainment rates for $Ri < 0.8$, prescribes no entrainment for $Ri = 0.8$ and is not valid for all $Ri > 0.8$. However this implies that this entrainment concept is only valid for oceanic flows with high Froude numbers. Only recently Arneborg et al. (2007) obtained even high entrainment rates of $E = 1.6\text{x}10^{-4}$ in an observed gravity current in the Western Baltic Sea characterised by low Froude numbers of $Fr = 0.5...0.6$ where the above entrainment concept predicts $E = 0$. This entrainment rate is comparable to what has been observed in the ocean (Red Sea overflow: $E = 2\text{x}10^{-4}$, see Peters and Johns (2005b)).

The entrainment parameter has further been found to depend on very simple concepts such as the bathymetry slope angle α as suggested by Bo Pedersen (1980b):

$$E = c_p \sin\alpha \tag{1.4}$$

with c_p being experimentally determined ($c_p = 0.072$, see Bo Pedersen (1980b); Buch (1982)) and $sin\alpha < 0.01$ (which is a realistic value for a steep continental slope). This relation has later been generalised by additionally taking bottom friction and Froude number into account and been proved to be a satisfying approximation at that time also by Coriolis driven currents (Bo Pedersen (1980a)). Britter and Linden (1980) provided a study of laboratory experiments where they demonstrated that the propagation speed is fairly insensitive to the slope angle. They obtained that the increase in current velocities due to gravitational forces at greater slope angles is compensated by buoyancy due to entrainment which is approximately linearly related to the slope angle.

In the literature several different more or less complex assumptions for the entrainment parameter E exist depending on (i) Froude or Richardson number only (Turner (1986), Wahlin and Cenedese (2006)), (ii) a combination of both Froude number and Ekman number (Arneborg et al. (2007)), (iii) depending on the bottom slope or slope angle (Bo Pedersen (1980b), Buch (1982)). However, most of the assumptions in the literature are successful for the individual conditions only which mainly depend on plume velocity, thickness, density and stability of the stratification, strength of rotational forces, magnitude of Fr and consequently no unifying entrainment theory exists predicting entrainment rates in the open ocean and coastal areas in different latitudes of estuarine, coastal or oceanic regimes. The well-known entrainment concept by Ellison and Turner (1959) adapted by Turner (1986) for example is still used in global ocean circulation models as a parameterisation of entrainment (Papadakis et al. (2003), Legg et al. (2006)) with reasonable performance. These rather simple parameterisations in large-scale ocean models are necessary as physical mixing processes are subgrid-scale due to the restricted horizontal resolution applied. However, these simple parameterisations have been found to show unrealistically high entrainment rates when the Ellison-Turner entrainment model is applied

to the Pacific Equatorial Undercurrent in global models (Legg et al. (2009)). Furthermore the Ellison-Turner entrainment concept neglects the influence of the bottom boundary layer on vertical homogenisation of the overflow at the bottom due to velocity shear related to bottom friction (which has been found to influence transport and dilution for example in the Red Sea overflow, see Peters and Johns (2005b)) and furthermore potentially leads to differential advection at sloping boundary (e.g. van Aken (1986) or in lakes Wüest and Lorke (2003)). This missing turbulent regime when using the Ellison-Turner entrainment model alone can be included via using a certain amount of the energy of bottom friction (e.g. 20%, Legg et al. (2009)) to mix and homogenize near bottom densities. Entrainment rates significantly vary with values from for example $2\text{x}10^{-4}$ for the Red Sea overflow (Peters and Johns (2005b)) to $1\text{x}10^{-3}$ when considering the Denmark Strait overflow (Girton and Sanford (2003)) where Froude numbers greater than unity are not uncommon. Due to low Froude numbers, entrainment rates in the Baltic Sea are comparably low with values in the order of $E \sim 10^{-6}$ estimated by simple salt budget estimates (Sellschopp et al. (2006)) up to values even one order of magnitude higher with $E = 6.6\text{x}10^{-5}$ as observed with the help of a 19h time-series of a water column during an observed inflow into the Western Baltic Sea (Arneborg et al. (2007)). Arneborg et al. (2007) observed entrainment rates varying about one order of magnitude when comparing the entrainment rates of two different 5h time frames during the observed 19h time-series which shows the complexity in obtaining a unifying entrainment equation even for the individual observed flow field in the Baltic Sea, not to mention an entrainment equation which is valid globally. Sellschopp et al. (2006) found that the entrainment rates are significantly overestimated when using the entrainment rates derived with the help of the findings of Wahlin and Cenedese (2006) which are based on flows with $Fr \sim 1$. As the concept of relating the physical mixing to Froude numbers is still promising (see e.g. Hallberg (2000), Xu et al. (2006)), Wells et al. (2010) predicts constant entrainment rates for high Froude numbers, $E \sim Fr^2$ for intermediate bulk Froude numbers and for small Froude numbers a power law significantly greater than 2 (e.g. $Fr = 0.5...0.6$ as common during an observed overflow into the Western Baltic Sea, see Sellschopp et al. (2006), Arneborg et al. (2007)). However, Arneborg et al. (2007) and Umlauf and Arneborg (2009a) provide entrainment rates in a shallow gravity current in a channel which is characterised by Froude numbers below unity. As the earth rotation plays a major role for oceanographic flows (Coriolis force), Arneborg et al. (2007) presented a study where the entrainment rate depends on both Froude and Ekman number:

$$E \quad = 0.084 C_D Fr^{2.65} K^{0.6}, \tag{1.5}$$

where they based their work on a 19h time-series of gravity current dynamics and turbulence in the Western Baltic Sea combined with one-dimensional high resolution turbulence modelling using the GOTM (see section 1.2.1). The observed inflow event was during the medium-intensity inflow in January and February 2004 (see also section 2.4.3). Via comparing simulated and observed vertical profiles of stratification, velocity and dissipation they obtained the above empirical equation defining the dependency of the strength of vertical mixing on both Froude and Ekman number which basically describes the balance between gravitational forces in flow- and cross-flow direction by bottom friction and Coriolis force.

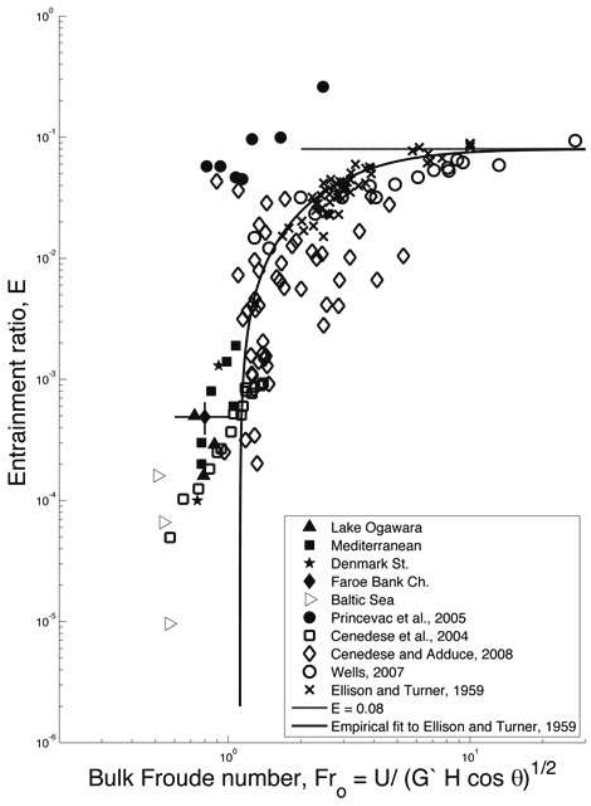

Figure 1.2: This sketch shows the dependency of the bulk Froude number to density current entrainment. The data is based on different sites on the globe together with observations in the Western Baltic Sea (picture taken from Wells et al. (2010)). The data from the Baltic Sea is taken from Arneborg et al. (2007).

Other studies address the entrainment parameter to be more complex than earlier simple linear assumptions or the entrainment model depending only in Froude number. Some studies derived entrainment rates depending on ambient stratification (Baines (2001)) or wave breaking (Cenedese et al. (2004)). Relations between hydraulic control points and entrainment have been carried out by Hornung et al. (1995). Another parameterisation is the so called K-profile parameterisation (KPP, Large et al. (1994),Large and Gent (1999)) where eddy viscosity and eddy diffusivity are prescribed as a dimensional constant which is multiplied by an analytical function of the gradient Richardson number (Pacanowsky and Philander (1981)). Of course this is a rough estimation and not universally valid. A better parameterisation than simply prescribing eddy coefficients was introduced by Hallberg (2000) by adapting the work of Turner (1986). Hallberg (2000) translated their entrainment velocity definition using the bulk Richardson number into a parameterisation using the gradient Richardson number which calculates the entrainment velocity as the velocity difference across the interface times an analytical function of the gradient Richardson number. This parameterisation has been build into isopycnic coordinate models (MICOM, Papadakis et al. (2003)).

The entrainment (mixing of ambient waters into the gravity current) is an important process

in estuarine, coastal and large-scale global ocean circulation. Only recently the Legg et al. (2009) presented a discussion of the need of a correct numerical representation of entrainment and the contribution of eddies on the mean flow in large-scale overflows (Kida et al. (2008)) in order to improve global hind- and forecast models as overflows may change the properties of surface water masses which exchange heat and water with the atmosphere. Furthermore Legg et al. (2009) discussed the need of properly representing the outflow source and the outflow product water properties in global models with restricted horizontal resolution. The horizontal and vertical resolution in global climate models have a significantly lower spatial resolution than the model setup used in this thesis and may hence not resolve important mixing or transformation processes such as due to hydraulic processes Girton et al. (2006), internal waves originating from geostrophic adaptation in the ocean (Gill (1982)) or vertical homogenisation of water masses close to the bottom and in the interface in overflow plumes (Peters and Johns (2005b)). Furthermore bottom friction or baroclinic instabilities (Cenedese et al. (2004)) may also influence the geostrophic balance of the flow field. The parameterisation of gravity current entrainment has proven to be challenging in ocean general circulation models (OGCMs) for two main reasons: (i) the horizontal and vertical model resolution (Riemenscheider and Legg (2007), Burchard and Rennau (2008)) and (ii) the type of vertical coordinates used which are known to respond different even when the same forcing is applied (Willebrand et al. (2001)), not to name the problems in applying a proper model bathymetry for coarse resolution models. Especially resolving the source region of large-scale dense overflows is a critical issue as the corresponding vertical and horizontal dimensions drive the properties of the dense bottom currents and hence the amount of entrainment which might be highly variable downstream of the source region (Girton and Sanford (2003)). The remaining issue that needs to be addressed is the surprisingly strong dependence of the performance of the entrainment parameterisation on the horizontal grid spacing (Riemenscheider and Legg (2007), Burchard and Rennau (2008)). Especially geopotential vertical coordinate models have problems in obtaining a realistic amounts of dilution and transport in gravity currents due to the difficulty in the representation of continuous slopes which effects the bottom boundary layer (Beckmann and Döscher (1997), Winton et al. (1998a), Killworth and Edwards (1999), Nakano and Suginohara (2002)). However, recent simulations of the Mediterranean overflow using both isopycnic (Papadakis et al. (2003)) as well as bottom following coordinates (Jungclaus and Mellor (2000)) are promising. Concerning the use of mixing parameterisations, isopycnic models have the advantage that the vertical resolution migrates to the density front and predifined pycnoclines of the gravity current (for isopycnic model see e.g. Papadakis et al. (2003)). Hence any parameterisation of diapycnal mixing can be prescribed which means no spurious - numerically induced - mixing occurs as in bottom following coordinate models (Burchard and Rennau (2008) and Rennau and Burchard (2009)) or geopotential coordinate models (Griffies et al. (2000)). Due to the rather high contribution of numerically induced mixing to the total mixing (natural + numerical) it is a challenge for numerical models to reproduce currents which even show significantly low mixing (e.g.. Rooth and Östlund (1972); Veronis (1977); Ledwell et al. (1993); Toole et al. (1994); Kunze and Sandford (1996)). As numerical issues in properly reproducing the adiabatic process of advection (no mixing) and dilution (mixing) of oceanic gravity currents is a broad field of research, a more detailed analysis of state-of-the-art modelling of gravity currents related to the problem of spurious, numerically induced mixing will be given in chapter 3.

The advantage of the model applied in this thesis is the high horizontal resolution which resolves the Rossby radius of deformation (Fennel et al. (1991), Osiski et al. (2010)). The Rossby radius of deformation is related to the mesoscale dynamics Gill (1982) and as such a precondition for numerical models to resolve the mesoscale dynamics such as the development of eddies and their advection which are important for the characteristics of the mean flow and mixing (Robinson (1983)). Furthermore the numerical model used in this work (section 1.2.2) comes with a state of the art turbulence model (section 1.2.1). An example of successfully reproducing vertical turbulent mixing in a gravity current of the Western Baltic Sea with a state of the art turbulence model and a high resolution model setup is the work of Arneborg et al. (2007) applying a one-dimensional scenario and already mentioned earlier in this section.

1.1.4 Gravity currents in the Baltic Sea

The Baltic Sea (figure 1.3) is a semi-enclosed estuarine system on the European shelf with only shallow and narrow connections to the North Sea. Due to dominant river runoff and precipitation the water exchange between North Sea and Baltic Sea is composed of a net outflow of brackish surface water of about 8 psu (Knudsen (1900), Matthäus (2006)) and frequently occurring so-called medium-intensity inflow events (Lass and Mohrholz (2003), Burchard et al. (2005), Lass et al. (2005), Mohrholz et al. (2006), Sellschopp et al. (2006), Burchard et al. (2009)) as well as major Baltic barotropic and baroclinic inflows, occurring at the inter-annual time scale (Wyrtki (1954), Matthäus and Frank (1992), Kõuts and Omstedt (1993); Fischer and Mattäus (1996), Lass and Matthäus (1996), Feistel et al. (2003a), Piechura and Beszczyińska-Möller (2003), Lehmann et al. (2004), Feistel et al. (2006), Reissmann et al. (2009)) of dense vertically well mixed Kattegat water into the Baltic Sea. The inflow events typically have salinities of more than 20 psu at Darss Sill and Drogden Sill. Three-dimensional circulation models have also been applied in modelling the major Baltic inflows of 1993 and 2003 (Lehmann (1995), Meier et al. (2003), Lehmann et al. (2004), Stips et al. (2005), Hofmeister et al. (2010a)).

Due to the location of the Baltic Sea in the humid climate zone, rather low salinities are found in the central Baltic Sea. Salinities higher than 25 psu are only found in the Great Belt and the Øresund. Mean bottom salinities at the Arkona station in the Central Baltic Sea are already only about 15 psu and about 5 psu in the Gulf of Bothnia which is located in the northernmost part of the Baltic Sea. The annual river run-off amounts to 436 km^3, precipitation to 224 km^3, 184 km^3 evaporation and 947 km^3 of surface water outflow which is partly compensated by nearly 500 km^3 of inflowing dense bottom water from the Kattegat entering the Baltic Sea (Reissmann et al. (2009)) via the shallow Darss Sill and Drogden Sill with 18 m and 7 m respectively.
Figure 1.5 presents the governing mixing processes leading to vertical turbulent mixing in the Baltic Sea. A number of different mixing processed can be found in the Baltic Sea similar to those in the open ocean (figure 1.4). There are for example shear-induced entrainment, boundary mixing (open ocean: Ledwell et al. (2000) and in lakes: Wüest and Lorke (2003), Umlauf and Lemmin

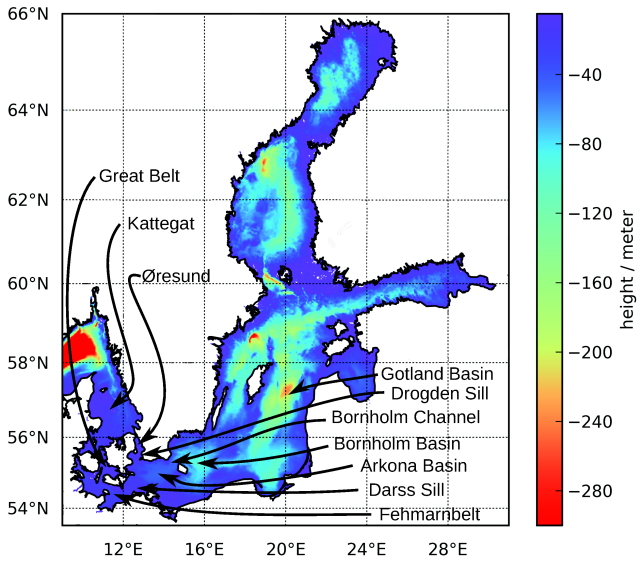

Figure 1.3: Bathymetric map of the Baltic Sea.

(2005)), differential advection (dense water is sheared above lighter water, see e.g. van Aken (1986) or in lakes Wüest and Lorke (2003)), coastal upwelling (ocean: Sverdrup (1937); Baltic Sea: Walin (1972), Fennel and Seifert (1995), Lehmann and Myrberg (2008), Fennel et al. (2010)), internal wave generation (see Garrett and Munk (1975), Polzin et al. (1995) for models of internal wave field; see Lass and Mohrholz (2003) for a discussion of observed internal waves and mixing in the Baltic Sea) and their dissipation into turbulent mixing. Not shown in figure 1.5 is the potential influence of mesoscale Baltic eddies (so-called 'Beddies'; see e.g. Zhurbas and Paka (1999), Lass and Mohrholz (2003) Reissmann et al. (2009)) on transport and mixing which has been generally discussed by Robinson (1983). Observed Beddies have a characteristic diameter of 10-20 km, a propagation velocity of 1 cm/s and are found to be in geostrophic balance. Anyway, Reissmann et al. (2009) summarised that the lifetime of the Beddies in the Baltic Sea is still unknown. They mentioned that the lifetime is rather restricted as the horizontal dimensions of the Baltic Sea potentially lead to an early collapse due to a collision. There are also a number of different dependencies between the above mentioned mixing processes. Upwelling for example, which will very likely occur at every possible wind direction in the Baltic Sea due to the complex distribution of coast lines, potentially leads to differential advection at the sloping boundary due to the influence of bottom friction which again leads to convection processes carrying nutrients from the intermediate layers of the Baltic Sea to the surface (Janssen et al. (2004)). Also the balance between Ekman offshore transport of surface layers and the Ekman onshore transport in intermediate layers shears denser water above lighter water which again leads to convection and hence mixing. Based on a seven-year hydrodynamic model simulation Kowalewski and Ostrowski (2005) identified 12 upwelling zones in the southern Baltic Sea which were in good agreement with observations of sea surface temperatures (SST).

The Baltic Sea can be viewed as a laboratory where most of the oceanic processes such as geostrophically balanced currents or internal waves together with highly turbulent conditions are

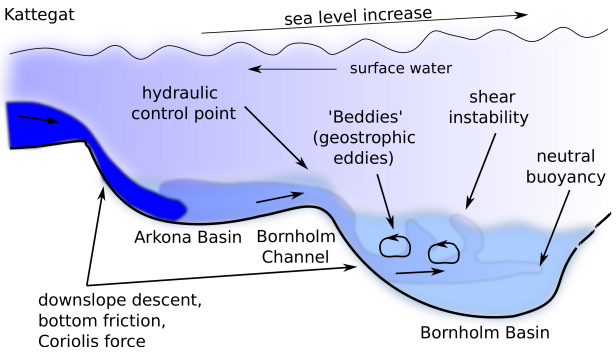

Figure 1.4: Sketch showing some physical processes during a Baltic Sea inflow event which are valid also for oceanic overflows (figure adapted from Legg et al. (2009), their figure 2). Visible is the low horizontal gradient in surface salinities and the significantly stronger horizontal salinity gradient at the bottom. Furthermore a new and denser inflow event is shown, which shears below old water in the Arkona Basin. Another plume ventilates intermediate layers in the Bornholm Basin at the depth of neutral buoyancy (see also model result in figure 4.12). Additionally the mean sea level increase from the North Sea to the Baltic Sea is shown, driving surface currents directed out of the Baltic Sea.

present. However, for example the internal wave model by Garrett and Munk (1975) based on the assumption of an open ocean, cannot easily being applied to the Baltic Sea as internal waves in the Baltic Sea are rather radiated due to the complex bathymetry and the strong influence of the coasts than due to geostrophic adaptation which leads to internal waves in the open ocean Gill (1982). Furthermore, due to the complex bathymetry with a number of different channels and shallow sills, the existence of gravity currents which are geostrophically balanced over long distances of a few hundred kilometers, which is a common feature in the open ocean, cannot been found in the Baltic Sea where significant variations in both depth and horizontal dimensions of the bathymetry are in the order of only about 50-100 km. Lass and Mohrholz (2003) also found that the internal wave spectrum of the model by Garrett and Munk (1975) is different from that of the Baltic Sea.

The individual character of the Baltic Sea is the permanent stratification due to a halocline at about 50-60 m depth (Fennel et al. (1991), (Reissmann et al. (2009))) in the deeper basins which is effectively separating surface and bottom water masses. The only process leading to deeper layer ventilation is the inflow of vertically well-mixed, oxygenated dense bottom water originating from the Kattegat which travels all the way from the Western Baltic Sea to the far-off Gotland Basin within a few months passing several sills and channels (see e.g. figure 1.4). During summer a seasonal thermocline is characteristic which protects the halocline from erosion due to turbulent motion in the surface mixed layer (Reissmann et al. (2009)). The halocline develops at a depth between 10 and 30 m (Matthäus (1984)). However, the existence of the thermocline alone does not prevent the erosion of the halocline from processes such as for example internal wave breaking or coastal upwelling leading to differential advection and finally convective entrainment (Reissmann et al. (2009)). In winter the thermocline disappears because of the influence of winds and cooling of the surface leading to convection. Winter cooling does not lead to an erosion of the halocline as the density of cold surface water in winter does not reach the densities of the saline bottom water (Reissmann et al. (2009)). Hence, as summarised by Stigebrandt et al. (2002), the properties of water masses below the halocline

are mainly governed by advection. During winter stratification, Lass et al. (2003) have shown that the turbulence generated below the surface mixed layer is rather independent on the strength and fluctuations of the wind fields.

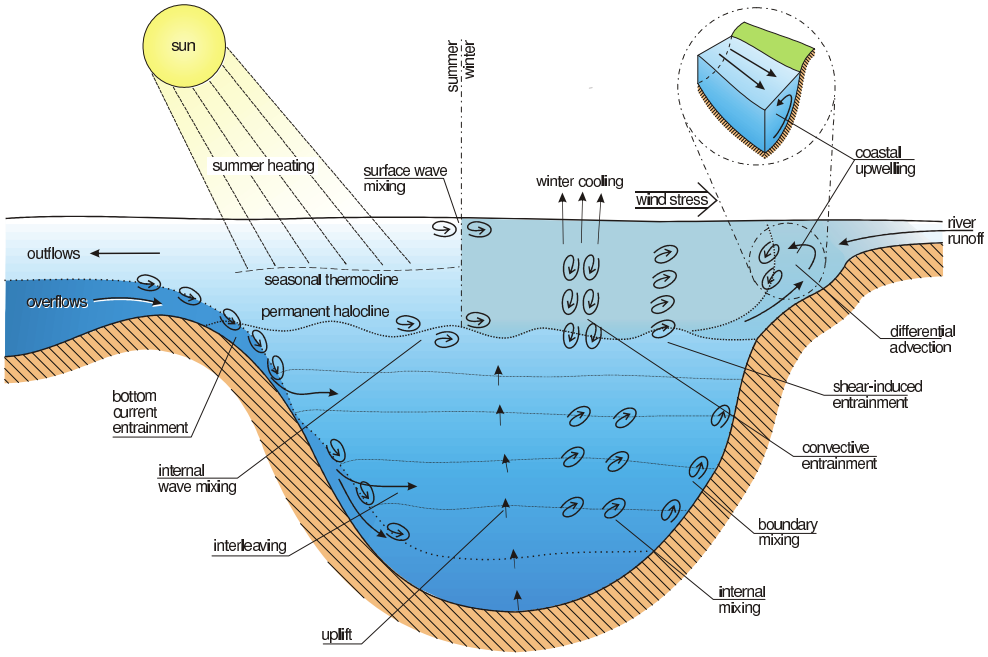

Figure 1.5: Schematic view of mixing processes in the Baltic Sea (adapted from Stigebrandt (2003)). Picture taken from Reissmann et al. (2009).

A further individual attribute of the Baltic Sea is the rather negligible influence of tidal currents and low Froude numbers of $Fr = 0.5...0.6$ in the area of the Arkona Sea (Arneborg et al. (2007)) and further east. The work of Wells et al. (2010) provides a plot where the entrainment rate E is plotted over the bulk Froude number for several different areas of the earth (figure 1.2). Compared to most of the examples given in figure 1.2 the Baltic Sea is characterised by low Froude numbers combined with low entrainment rates. The tidal currents are successfully damped due to the shallow and horizontally restricted transition area in the Danish Belts, the Fehmarnbelt and the Øresund with a complex bathymetry consisting of a number of narrow sills and underwater channels. However, Lass et al. (2008) observed internal Froude numbers greater than unity in the Great Belt due to the influence of tides.

The occurrence of Major Baltic Sea inflow events (MBI) - driven by exceptionally strong sea level differences between the Baltic Sea and the Kattegat (see location in figure 1.3) due to persistent wind fields is known as the only process to potentially ventilate the Baltic Sea deep waters below the permanent halocline via horizontal advection of the dense water masses from the Kattegat along the Baltic basins. The vertical salt transport into the entire surface mixed layer of the Baltic Sea is estimated to about 30 kg/(m^2a) (Reissmann et al. (2009)) which is derived knowing

that the Baltic Sea exports and imports a value of about 4 Gt salt per year (Feistel and Feistel (2006)) together with the assumption that, due to the conservative property of salt, this is balanced by the vertical salt transport of 30 kg/(m^2a) across the pycnocline at 60 m depth with 130,000 km^2 (Reissmann et al. (2009)). Consequently the process of dense overflows across Drogden Sill and Darss Sill significantly affects the marine environment due to the property that such bottom currents transport high amount of saline and oxygenated water and interleave at the level of neutral buoyancy. As a consequence of sinking organic material, the mineralization of the organic material reduces the oxygen content in the deeper layers leading to the typical anoxic conditions (hydrogen sulfide may occur and phosphate is released from the sediments) during the so-called 'stagnation period'. This happens between two major Baltic inflows below the halocline in the permanently stratified Gotland Basin with a depth of about 240m where only MBI's can potentially influence the deeper layer ventilation. After the MBI in early 2003 has reached the Gotland Basin in mid 2003, a significant reduction of observed phosphate concentrations and improved oxygen conditions were detected (Nausch et al. (2003)). On the other hand, medium intensity inflow events, occurring on the monthly time scale with almost different intensities and spreading behavior between the different inflow events (see chapter 2), are able to fully ventilate the deeper layers in the Arkona Basin but are not strong enough to be traced in the Gotland Basin due to their rather low transport capacity.

The last three major Baltic inflows occurred in 1983, 1993 and 2003 where high amounts of vertically well mixed Kattegat water masses were entering the stratified Baltic Sea which consists of a permanent halocline in the southern and central Baltic separating the deeper water from fresh surface water. During the last decades the frequency of major inflows has decreased whereas during the last century they occurred at intervals of about one to several years. Increasing stagnation periods then lead to oxygen depletion (Mohrholz et al. (2006)) in the deeper basins and an increase in hydrogen sulphide may occur which locally affects the ecosystem. However, numerical models have been found to be satisfactory in reproducing dense bottom current spreading through most of the Baltic Sea as shown in figure 1.6 comparing observations at the Arkona Deep (50 m depth), Bornholm Deep (90 m depth) and Gotland Deep (250 m depth) with model simulations using the Rossby Centre Ocean model (RCO). Furthermore figure 1.6 is nicely demonstrating how the major Baltic inflows do significantly affect the stratification in the Bornholm Deep and the Gotland Deep. Additionally this demonstrates the physically very active regime of the Arkona Sea governed by medium-intensity inflow events which can not be traced in the Gotland Basin. Moreover the permanent existence of the halocline in all three basins is visible leading to strongly stratified conditions, where deeper layer ventilation is governed by horizontal advection of dense and oxygenated water from the Kattegat only. A sketch of the horizontal and vertical exchange of water masses is drawn in figure 1.7. This so-called 'Baltic Conveyor Belt' shows the 'Baltic Deep Convection' with residence times of about 20 years for the Baltic deep water, indicating time-scales of decades (Meier and Kauker (2003), Meier et al. (2006), Feistel et al. (2006)) considering the influence of deep water renewal due to advection, diffusion and turbulent exchange. Furthermore Meier et al. (2006) found that the Neva river water masses travel in about 30 years across the Baltic Sea on a distance of 1500 km. On the other side, dense bottom currents propagate significantly faster. For the inflow in 1997-1998 Hagen and Feistel

(2001) found a propagation time of about 3-4 months for the 800 km from the Danish Belt to the Gotland Basin. Hagen and Feistel (2004) estimated permanent current velocities of about 3 cm/s at the bottom which nicely agrees with mean current velocities of 3-4.5 cm/s obtained in the Central Arkona Basin with the help of the realistic numerical model setup used in this thesis (see section 2.4.2).

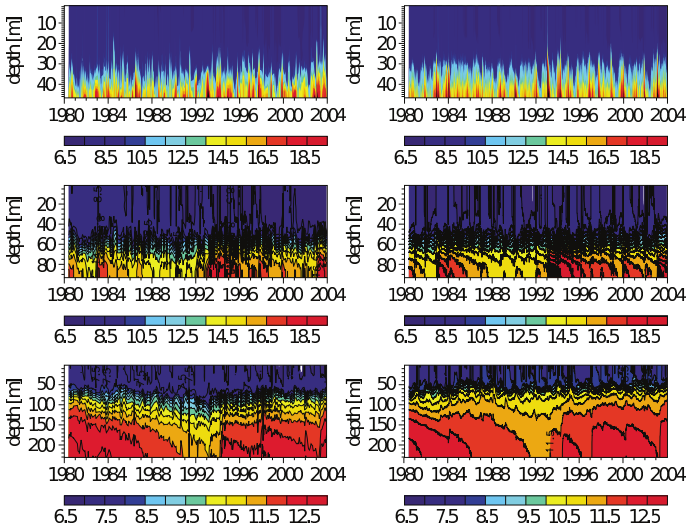

Figure 1.6: Observed (left) and modelled (right) salinities between 1980 and 2003 in the Arkona Deep upper panels), the Bornholm Deep (middle panels) and the Gotland Deep (lower panels). The model simulations are based on results of the Rossby Centre Ocean model, RCO (from H.E.M. Meier, R. Döscher, B. Broman, J. Piechura, presentation at the BSSC 2005)

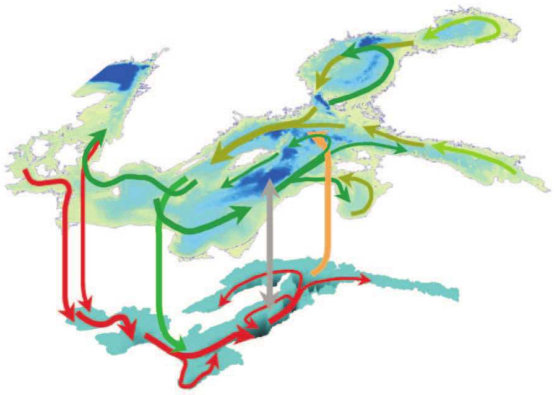

Figure 1.7: Schematic view of the 'Baltic Conveyor Belt' (picture taken from Elken and Matthäus (2008) showing the 'Baltic Deep Convection'. Green and red arrows denote the surface and bottom layer circulation, respectively. The light green and beige arrows show entrainment. The gray arrow denotes diffusion.

So called baroclinic inflows - driven by the horizontal density gradient between the Kattegat and the Baltic Sea during meteorological calm summer conditions of about 20 days or longer - have been observed in 2002 and 2003 (Feistel et al. (2003b), Feistel et al. (2004), Feistel et al. (2006)) and are also changing the hydrography of the deeper layers as demonstrated by Mohrholz et al. (2006) for the Bornholm Basin although they transport less oxygen than barotropically driven dense bottom currents

due to their lower transport capacity and lower density. As the Drogden Sill with a depth of only 7 m is very shallow, baroclinic inflows do only pass though the Great Belt and Darss Sill passage (figure 1.3). However, despite of relatively low oxygen content of the baroclinic inflow events in summer 2002 and 2003, they could still be traced in the halocline of the Bornholm Basin and even in the Gotland deep improving the oxygen conditions (Mohrholz et al. (2006)). This emphasizes the investigations conducted in chapter 4 on the potential additional dilution of these dense bottom currents due to the erection of Offshore Wind Farms in the Western Baltic Sea which is characterised as a hot spot for water mass transformation in the Baltic Sea (Kõuts and Omstedt (1993), Lass and Mohrholz (2003), Burchard et al. (2009)).

As summarised by (Reissmann et al. (2009)) the observed temperature in October 2004 was the highest ever observed in the halocline layer (here defined by 8.95-14.3 psu) of the Bornholm Basin (Mohrholz et al. (2006)) and considerable changes in deeper layer ventilation of the Gotland Basin has been found by Feistel et al. (2006). They showed that the high temperatures of several warm inflows in the last two decades (barotropically forced warm inflows: September 1997, October 2001, see Hagen and Feistel (2001), and baroclinically driven warm inflows August 2002 and August 2003) raised the temperature at 200m depth in the Gotland Basin significantly. Even though the warm summer inflow in August 2003 carried less saline water than the MBI in early 2003, a temperature increase by about 1.5C at 200m depth in the Gotland Basin could still be traced (Feistel et al. (2006)). This consequently leads to the assumption that the amount of naturally induced mixing (see chapter 2) together with an estimation of man-made additional structure induced mixing in the Arkona Sea (see chapter 4) is of high interest to give estimations on potential ecological consequences. However all governing processes leading to turbulent mixing of the dense bottom current are not fully understood and quantified where Matthäus (2006) and Reissmann et al. (2009) present a review on research of saline water intrusion into the Baltic Sea and a discussion of corresponding mixing processes (figure 1.5.

The aim of this study is the investigation of natural mixing and spreading of medium intensity inflow events which enter the Baltic Sea several times per year. These inflows have the potential in ventilating intermediate layers of the Baltic Sea, especially in the Arkona- and the Bornholm-Basin which are subject to oxygen depletion (Lass and Mohrholz (2003), Mohrholz et al. (2006)). These dense bottom currents enter the Baltic Sea via the Sound (about 20 m depth) and the Drogden Sill (about 8 m depth) and are subject to strong turbulent mixing especially at the shallower areas of sills and downstream (Burchard et al. (2009)). Model simulations supported that higher amounts of dense bottom waters are entering the Baltic Sea across the Darss Sill than through the Sound due to the broader transition area. However, plume salinities are higher for dense bottom currents originating from the Sound as those travelled less distance than Darss Sill bottom currents. Water masses crossing the Great Belt are consequently subject to stronger entrainment of overlaying brackish waters which reducing their density. An example on the importance of the Western Baltic Sea as a hot spot of water mass transformation is the work of Kõuts and Omstedt (1993) which estimated the volume flux to be increased by 53% in the Arkona Sea. Lass and Mohrholz (2003) estimated an increase in volume flow of 30% from Drogden Sill to Bornholm Channel due to physical processes such as wind

entrainment, upwelling, diapycnal mixing and differential advection of the dense bottom water in the Arkona Sea which has a thickness of a few meters only. Consequently, the area of the Drogden Sill, Darss Sill and the Arkona Sea is known as a hot spot of water mass transformation (Burchard et al. (2009)) where it is essential to correctly quantify the mixing, spreading behavior and spreading times in order to estimate the sensitivity to human impact (as shown in the final chapter of this thesis) and climate change (see e.g. the recent discussion by Legg et al. (2009) on the correct representation of entrainment and mixing in overflows by numerical models in relation to estuarine, coastal and global modelling). As this thesis of a realistic numerical model study investigating the natural mixing only (chapter 2), attention is necessary in quantifying also the amount of spurious mixing (see e.g. Lee et al. (2002)) in the model (discretisation errors of the numerical advection schemes, Burchard and Rennau (2008)), which is analysed and directly compared to the model derived natural mixing in order to demonstrate and discuss the influence of model numerics when analysing mixing rates (chapter 3).

The focus of this work is the area of the Arkona Sea, where the salt water plumes are spilling over the Darss Sill and the Drogden Sill and are both spreading through the Central Arkona Basin and the Bornholm Channel into the Bornholm Basin (see figure 1.3 for geographical locations). The plume crossing Drogden Sill is separated north-east of Kriegers Flak into two separate branches one traveling north and one south of Kriegers Shoal with higher velocities and higher salinities (Lass et al. (2005), Burchard et al. (2005), Burchard et al. (2009)) for the northern trench. In the classical view both Coriolis force and pressure gradient tend to establish a geostrophically balanced dense bottom current which is in contradiction to the finding that the current north of Kriegers Flak is stronger. South-east of Kriegers Shoal the Drogden Sill plume joins the Darss Sill plume which might induce increased mixing and eddy shedding Lass et al. (2005) which is not supported by the work presented in chapter 2 and analysing Darss Sill and Drogden Sill water masses separately via two independent passive model tracers. Here no increased mixing but a strong tendency of interleaving of both water masses consisting of a three layer stratification with dense Drogden Sill water at the bottom, rather thick dense Darss Sill water in the middle and fresh surface water of about 7 psu on top. Lass and Mohrholz (2003) suggested that the spreading into the Arkona Basin is governed by a geostrophically driven bottom current aligned at the rims of the Arkona Basin and spiralling cyclonically. Furthermore the influence of bottom friction forces the dense bottom flow to propagate into the core of the Arkona Basin. With the help of the model derived mean bottom velocity, the tendency of a cyclonic mean current at the rim of the Arkona Basin is not found (see section 2.4.2). The plume thickness in the area of the Arkona Sea is roughly about 5-10 m. In contrast, large-scale oceanic overflows can be either about 100 m in case of the Red Sea overflow (Peters and Johns (2005b)) up to about 250 m for the Faroe Bank Channel overflow (Peters and Johns (2005a)) which indicates that the impact of mixing and entrainment due to bottom friction and interfacial dynamics in the rather thin Baltic Sea gravity currents (Umlauf and Arneborg (2009b)) may differ from large-scale overflows. This might explain why Fer et al. (2010) were not able to see a wedge-shaped interface in their observations of the Faroe Bank Channel overflow such as observed in the Baltic Sea (Umlauf and Arneborg (2009b)).

1.2 Turbulence model and coastal ocean model

1.2.1 General Ocean Turbulence Model (GOTM)

GOTM (General Ocean Turbulence Model, see `www.gotm.net`, Burchard et al. (1999) and Umlauf et al. (2005)) is a one-dimensional hydrodynamic model for marine and limnological applications which resolves time- and depth-varying (vertical) turbulent fluxes of tracers such as temperature and salinity or nutrients over the water column. The model core solves the one-dimensional transport equations of momentum, salinity and temperature. The model additionally reproduces processes such as the logarithmic law of the wall, turbulence suppression by stratification, wind mixing or entrainment. The GOTM includes various different turbulence models ranging from simple prescribed expressions of turbulent quantities to complex Reynolds-stress models (Umlauf and Burchard (2003),Umlauf and Burchard (2005)).

The GOTM is integrated in the 3D hydrostatic circulation model GETM (`www.getm.eu`) which is used for idealised and realistic applications in this work. The turbulence model of all 2D and 3D model setups in this work is the k-ϵ model with transport equations for the turbulent kinetic energy (TKE), k, and the turbulence dissipation rate, ϵ. As second-moment closure, the model suggested by Cheng et al. (2002) is used.

1.2.2 General Estuarine Transport Model (GETM)

The applied numerical model GETM is an abbreviation for General Estuarine Transport Model (see `www.getm.eu`, Burchard and Bolding (2002), Burchard et al. (2004)) which is a primitive-equation, fully baroclinic, hydrostatic, free-surface ocean model using general vertical coordinates. This type of vertical coordinates has advantages compared to z-level models in representing dense bottom currents, as gravity currents are near bottom processes following the depth contours (Ezer and Mellor (2004)). Geopotential coordinate models intrinsically have stronger discretisation errors due to the step-like bottom approximation which introduces comparably stronger discretisation errors as the bottom flows need to be advected through vertical coordinates when travelling down the incline. An additional advantage of the model used in this thesis is that a non-linear bottom zooming of the vertical coordinates can be applied which allows for higher near-bed resolution. For the Western Baltic Sea model applied in this thesis this guarantees a constant bed layer thickness of 0.2 m in regions with more than 10 m depth as shown by Burchard and Bolding (2002).

The model is implemented using the Arakawa C-grid (Arakawa and Lamb (1977)) for horizontal discretisation. For horizontal discretisation the characteristic numerical features of GETM are the mode splitting between the fast barotropic and the much slower baroclinic mode, the high-order advection schemes for tracer and momentum-advection (Pietrzak (1998)) and the possibility in applying various different turbulence closure models due to the implementation of the well-tested state-of-the-art turbulence model GOTM. For calculating the internal pressure gradient a parabolic splines density Jacobian scheme suggested by Shchepetkin and McWilliams (2003) is applied. However,

the pressure gradient error (Haney (1991), Kliem and Pietrzak (1999)) is of minor importance, as the Western Baltic Sea is a very dynamic and energetic regime and the dense bottom currents are mainly aligned to the vertical coordinates which keeps this error small. In the transport equations horizontal eddy diffusivity and viscosity coefficients are set to zero.

The advection of momentum and tracers is implemented using a directional-split scheme meaning that advection is calculated with subsequent full (or half) steps in x- and y -direction and a full step in z-direction. This allows to apply well-tested monotone (TVD, Total Variation Diminishing) one-dimensional methods. The advection scheme used for salinity, temperature and velocities in this thesis is a third-order monotone ULTIMATE QUICKTEST method (Leonard (1991) and Pietrzak (1998)). Another feature of the GETM to avoid the CFL criterion for explicit advection schemes being violated is that whenever the Courant number is larger than unity, the vertical advection time step is divided by the the next integer larger than the Courant number to calculate the vertical advection iteratively with a reduced time step.

The turbulence model used is the $k - \epsilon$ which is used via implementation of the GOTM (see section 1.2.1) into GETM, solving the vertical mixing for every water column.

Additionally it is noteworthy that the GETM successfully modelled Arkona Basin dynamics, see Burchard et al. (2005) and Burchard et al. (2009) as well as transports and mixing in different other idealised and realistic model applications for coastal and shelf sea regions and for lakes (Stanev et al. (2003), Stips et al. (2004), Umlauf and Lemmin (2005), Banas and Hickey (2005), Hofmeister et al. (2007)). For high resolution model setups, the GETM is able to run on parallel computers which has been the case for the realistic high resolution model setup in this thesis. Furthermore the load-balancing (similar amount of computations on each node per timestep) in the parallel setup is achieved by calculating similar number of wet points (no land) on each computer in the cluster where scripts are available to obtain the best choice of subdomain distribution. Additionally it must be pointed out, that not the full model domain needs to be put into the memory, because the GETM includes a system where most of the land area in the domain is excluded and communication between the subdomains is still guaranteed.

1.3 Outline of the thesis

Chapter 2 covers the description, validation and application of a realistic model setup of the Western Baltic Sea - which is also primarily used for investigations in Chapter 3 and Chapter 4 - and quantitatively investigates physically induced mixing as well as the spreading behavior, and pathways of dense bottom currents in the Western Baltic Sea. The combination of a state of the art turbulence model (solving vertical mixing) together with a 3D hydrostatic coastal ocean model (basically calculating horizontal advection of passive tracers and momentum) successfully reproduces sea surface elevations as well as transport and dilution of gravity currents as published by Burchard et al. (2009) where I contributed to the paper via running and calibrating the model runs and further by analysing the

model simulations and creating the corresponding plots. The content of the work of Burchard et al. (2009) is combined in the first chapter with the modelling part of Mohrholz and Rennau (2010) (in preparation). The modelling part of Mohrholz and Rennau (2010) is the application of the realistic model setup in order to obtain spreading behavior, spreading times and the main pathways of dense bottom currents in the Western Baltic Sea. The observational part of Mohrholz and Rennau (2010) (done by Volker Mohrholz, Leibniz Institute for Baltic Sea Research Warnemünde) is not included in this PhD thesis. The derivation of the equations of the physical tracer variance decay in section 2.4.7 is directly taken from Burchard et al. (2009). Furthermore section 2.4.7 has been extended by findings of Mohrholz and Rennau (2010) on quantification of mixing of Arkona Sea passive tracers which shows only my contributions.

Chapter 3 quantifies the spurious mixing in numerical ocean models due to truncation errors of the numerical advection schemes as suggested by Burchard and Rennau (2008). In this publication I contributed in implementing the numerical mixing analysis into the ocean circulation model applied, setting up and running the 2D and 3D idealised model simulations and analysing the results. Section 3.3 in Chapter 3 dealing with the investigation of idealised simulations has directly been copied from Burchard and Rennau (2008) and does only show the model simulations which I have created and analysed. The second part of chapter 3 uses the realistic model simulation introduced in Chapter 2 concerning the research on the location, behavior and amount of numerical and physical mixing in Western Baltic Sea dense overflows as published by Rennau and Burchard (2009) where I am fully responsible of the whole journal publication. As already found in previous publications, the numerical mixing shows orders of magnitude similar to those of pure physically induced mixing. In this chapter the contribution to previous work is that (i) numerical mixing is directly compared to physical mixing where, surprisingly, both show same orders of magnitude in both idealised and realistic scenarios and (ii) it is shown that physical and numerical mixing show different spatial and temporal behavior which furthermore corresponds to the individual characteristics of the applied numerical model grid and the strength and dynamics of the tracer fields.

Chapter 4 develops a parameterisation of structure-induced mixing (vertical cylindrical structures) for 3D hydrostatic models which is then applied to investigate potential additional mixing due to offshore wind farms (Rennau et al. (2010)). With the help of idealised 1D and 3D hydrostatic model simulations of stratified flow, this parameterisation is found to be fairly independent on horizontal model resolution. As additional structure-induced mixing of dense bottom currents in the Western Baltic Sea may be critical for the whole ecosystem, this research estimates additional mixing with the help of four different scenarios with the realistic model setup described, calibrated and investigated in Chapter 2. In this journal publication I was responsible for running, analysing and discussing the 2D and 3D idealised model runs as well as the realistic model scenarios.

Summarizing, this study presents a quantitative model study of the physical mixing of gravity driven dense bottom currents in the Western Baltic Sea. As numerical models do represent reality only to a certain - but for most applications almost satisfying - degree, in a second step this work

additionally quantifies numerical mixing due to the numerical advection schemes and discusses the result together with the obtained natural mixing. Finally, a parameterisation of structure induced mixing is developed and applied to a realistic model setup in simulating the effects of offshore wind farms on transport and dilution in stratified flow.

Chapter 2

Turbulent mixing and spreading behavior of dense bottom currents in the Western Baltic Sea

2.1 Introduction

The importance of mixing and spreading of dense bottom currents across shallow sills into the Arkona Sea and their role in the ecosystem of the Baltic Sea has already been extensively discussed in section 1.1.4 together with a brief introduction on the entrainment process in section 1.1.3. The complete domain of interest and the domain for the numerical model are shown in figure 2.1 with the northern (west-east) boundary in the Kattegat and a eastern (north-south) open boundary in the Bornholm Basin. The first sections of this chapter deal with the basic model setup, including model calibration with the help of a number of observations and the discussion of necessary changes to the open boundary forcing and the model bathymetry. The later sections focus on the quantification of the naturally induced mixing, main pathways, spreading behavior and spreading times of dense bottom currents in the Western Baltic Sea.

2.2 Model setup

2.2.1 Model description

The coastal ocean circulation model GETM which is used for the present thesis has been introduced in section 1.2.2 with all corresponding specifications and individual settings for the applied realistic model setup of the Western Baltic Sea. The turbulence model GOTM (coupled one-dimensionally to the GETM), represents processes such as the logarithmic law of the wall, entrainment of wind-induced mixing and has been introduced in section 1.2.1, including a short description of the specific turbulence model and second moment closure applied here.

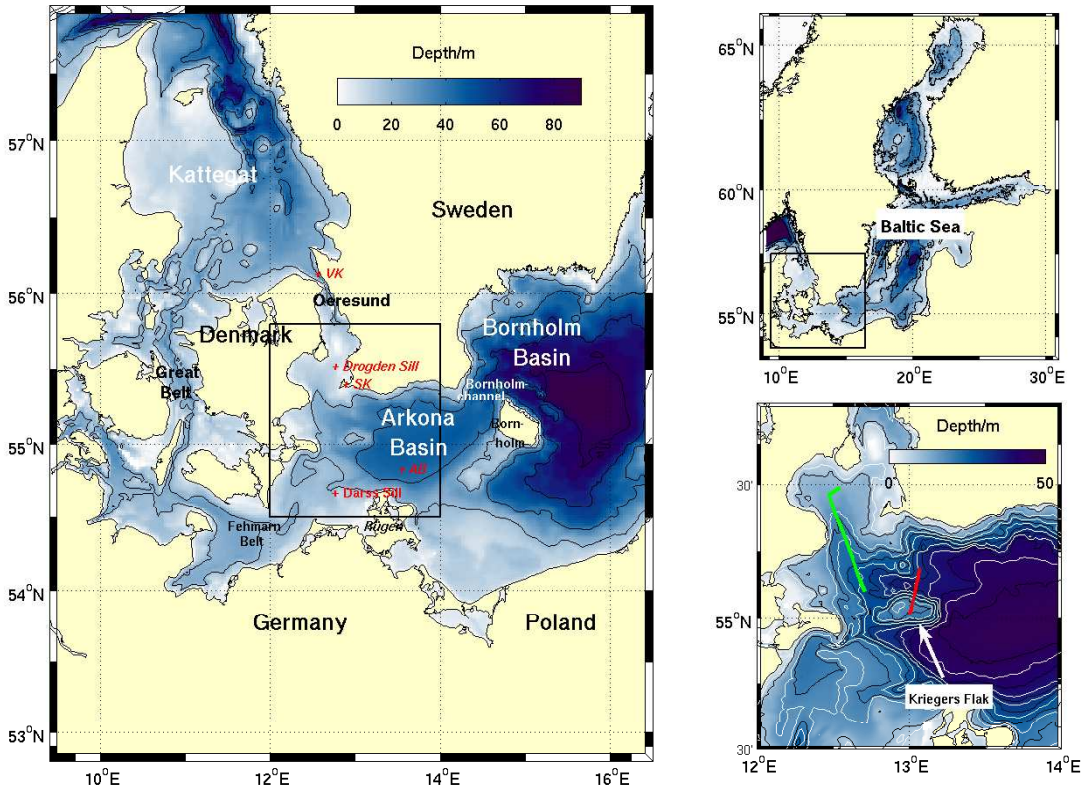

Figure 2.1: Map of the Baltic Sea showing the domain of the Baltic Sea model (upper right panel), the domain of the Western Baltic Sea model (left panel) and the area of the Drogden Sill and Kriegers Flak area (lower right panel). The latter map shows the cross-sections which have been observed during a field campaign on February 1 (green) and February 5 (red). The positions of the Drogden Sill, Darss Sill (DS) and Arkona Buoy (AB) stations are shown in the left map as well as the locations of the coastal gauges in Viken (VK) and Skanör (SK). The Baltic Sea model has an open boundary in the Skagerak at 9°E, and the Western Baltic Sea model has open boundaries between Kattegat and Skagerak at 57°30'N and east of the Bornholm Sea at 16°30'E.

2.2.2 Realistic model setup

For the case of coarse resolution models there is a close connection between the numerical schemes and the mixing formulations (see detailed discussions in chapter 3). Hence it must be mentioned that the model resolution has to respect the admitted scales of motion (e.g. importance of eddies on the mean flow, see Robinson (1983)) in which models with a horizontal resolution smaller than the internal Rossby Radius are required. For the coastal model application presented here using the GETM (see section 1.2.2) a horizontal resolution of $\sim$ 1 km is used which is below the known values for the baroclinic Rossby Radius of O($\sim$ 3 km) in the Western Baltic Sea (Fennel et al. (1991)), but may not fully resolve it. Furthermore, high model resolution in the area of the Western Baltic Sea provides higher accuracy in resolving deep trenches and narrow straights as found in the Danish Belt Sea which cannot be fully resolved with the model bathymetry used in this thesis with a resolution of half a nautical mile in both longitudal and latitudal direction (Δlon=0.017°E, Δlat=0.0084°N).

As a high resolution model setup with $\sim$ 1 km horizontal resolution of the whole Baltic Sea was not

feasible, a nested model setup with two open boundaries was created, a west-east directed in the Kattegat and a north-south directed in the eastern Bornholm Basin. This area fully resolves the water mass transformation of high saline Kattegat water masses with salinities above 30 psu along the pathway of narrow straits in the Danish Belt Sea (see e.g. Great Belt in figure 2.1), shallow sills as Darss Sill and Drogden Sill until it finally reaches the Bornholm Channel with salinities less than 20 psu to spread into the Bornholm Basin. As observations with high vertical and horizontal resolution at the two open boundaries were not available, the boundary conditions were extracted from model simulations of a Baltic Sea model with 3 nm horizontal resolution and 77 vertical geopotential grid layers (Neumann et al. (2002) and Janssen et al. (2004))). The near surface resolution of this model is 2 m, increasing with depth. The Baltic Sea model uses the Modular Ocean Model (MOM-3.1, Griffies et al. (2001)) and was initialised on May 1, 2002 with salinities and temperatures analyzed from observations (Meier et al. (1999)). As surface meteorology data from European Centre for Medium-Range Weather Forecasts Reanalysis Project ERA40 (ECMWF re-analysis project) with a horizontal resolution of 100 km and 6 hours (until August 2002) and the German Weather Service Global Model with a resolution of 60 km and 6 hours (from September 2002) was used. The open boundary conditions in the Skagerak were analyzed from sea level data observed at the tide gauge in Kungsvik (Sweden), temperature and salinity boundary conditions are interpolated from the monthly climatology by Janssen et al. (1999). From the large scale Baltic Sea simulation, surface elevations at the open boundaries of the Western Baltic Sea model (between Kattegat and Skagerak at 57°30'N and east of the Bornholm Basin at 16°30'E) are stored every 15 min. for the surface elevation and every hour for temperature and salinity.
The high resolution nested model setup of the Western Baltic Sea using 50 vertical layers with a non-linear zooming to the sea bed, was initialised on September 1, 2003, with open boundary conditions and initial temperatures and salinities interpolated from the larger scale Baltic Sea model. For the barotropic mode the time step used was 10 s and a factor of 30 higher for the internal (baroclinic) mode (see 'mode splitting' in section 1.2.2 and corresponding references). Surface boundary data (meteorological forcing) was delivered from DWD (German Weather Service) maintaining the German Weather Service local model (LM) with a horizontal resolution of 7 km and 3 hours. The influence of riverine freshwater input was neglected in the investigations within the model period between September 2003 and May 2004 (Burchard et al. (2009)) because they have only a minor influence on transport and dilution of dense bottom currents which are the main focus of this work. Later the model simulations have been extended until January 1, 2006. In the updated simulation the riverine freshwater input was included where the riverine freshwater input has been found to have only neglectable impact on net flow, plume salinities as well as surface salinities in the Arkona Sea. The model period between September 2003 and May 2004 was chosen to include a field campaign in January/February 2004 (Burchard et al. (2005), Sellschopp et al. (2006)) where an inflow event has directly being observed. From the extended model period until January 1, 2006 the year 2005 has been applied to investigate spreading behavior and spreading times of Darss Sill and Drogden Sill water masses separately using passive tracers. In 2005 observations at all three stations (Darss Sill, Drogden Sill and Arkona station) have been nearly fully available, which is in contrast to the simulation period used in the work of Burchard et al. (2009) where only a few months were covered by observations at Drogden Sill. An analysis of spreading behavior and spreading times of Darss Sill and Drogden Sill water masses separately requires

a reasonably well agreement of the model with observations at all three stations (see section 2.3).
As the high resolution model setup needs comparably large amounts of memory, it cannot be set up on a single machine. Hence the model simulation has been carried out on a 4 node quad-core machine, see figure 2.2 for an explanation of the distribution of subdomains to nodes.

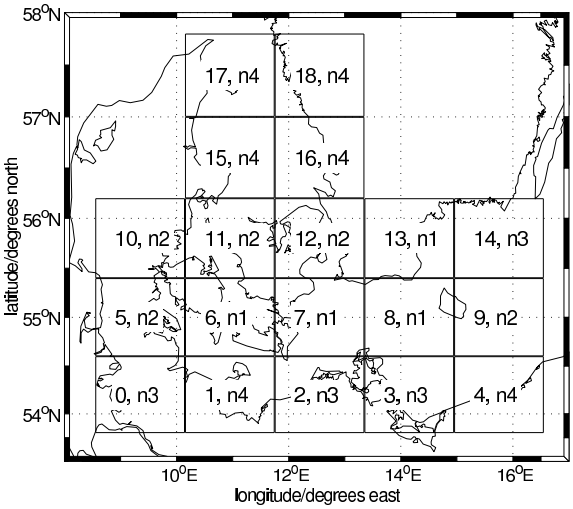

Figure 2.2: Domain decomposition map for the GETM simulation. The 19 subdomains (numbered 0 - 18) are allocated to the four available nodes of the LINUX-Cluster (with four processors each) in a way that the loads and communication times are balanced in an optimal way.

2.2.3 Bathymetry, barotropic flow and bottom roughness corrections

The Western Baltic Sea has a complex bathymetry with narrow underwater channels (see figure 2.3a) which requires a model setup with at least a few hundred meter horizontal resolution to properly resolve most of the smaller topographic features. As the model setup used does not fully resolve the deep and narrow channels of partly not more than 200 m width in the Danish Belts with its 0.5×0.5 nm horizontal resolution, the model bathymetry was modified by hand to include the deep channels in the Great Belt and the southern Kattegat. The original bathymetry (Seifert and Kayser (1995)) is shown in figure 2.3b with the final model bathymetry shown in figure 2.3c. This modification has additionally become necessary, as the model validation has shown unrealistically low salinities at Darss Sill and Drogden Sill stations. Hence the Great Belt has been deepened by up to 35 % and 15 % in the Øresund followed by increasing the depth and the width of the deep channel in the Great Belt. A number of model simulations with stepwise introduction of the mentioned modifications to the model bathymetry have shown that these changes improved the overall salt transport through the Great Belt with a better representation of timing and especially of higher salinities of dense bottom currents at Darss Sill station and Arkona buoy station as proved by figures 2.4-2.9.
In order to obtain correct net transports through the model domain of about 15000 m^3s^{-1} out of the Baltic Sea (Reissmann et al. (2009)), which is contributed of a mean inflow of dense, high saline bottom waters and a stronger outflow of fresh surface waters due to rivers and precipitation, the flow within the model had to be adjusted. While using the originally prescribed open boundary sea surface elevations

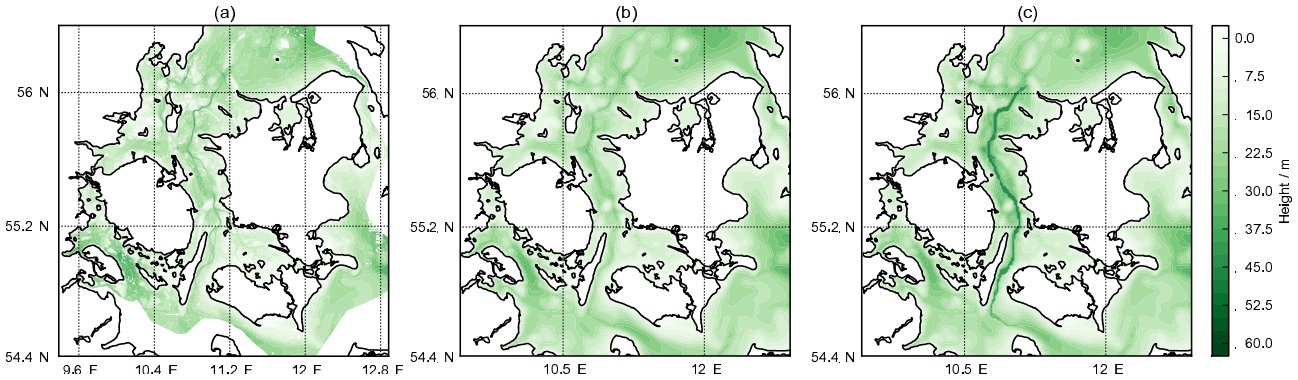

Figure 2.3: Panel (a) showing a high resolution bathymetry kindly provided by DHI (Denmark) and (b) showing the model original model bathymetry by Seifert and Kayser (1995) and (c) the modified model bathymetry with a deepened Great Belt and Øresund as well as increasing depth in the 40 m deep and thin channel in the Great Belt which is represented by about 2-3 grid cells in the 0.5×0.5 nm model setup.

which are obtained from a full Baltic Sea model (see section 2.2.2), the GETM nested Arkona Sea setup gives an unrealistic net volume flow into the Baltic Sea, probably due to balances between mean surface and bottom stresses which are different between the high resolution model setup used (0.5×0.5 nm horizontal resolution) and the low resolution Baltic Sea model with 3 nm horizontal resolution. Hence the barotropic pressure difference between northern and eastern open boundary has been increased stepwise. It has been found that adding 0.05 m at the eastern model boundary leads to realistic net transports through the nested model.

It has additionally become necessary to use a bottom roughness length of $z_0 = 10^{-3}$ m instead of $z_0 = 10^{-2}$ m in order to obtain more realistic and more homogeneous vertical velocity profiles as well as to improve the timing of dense bottom currents between Drogden Sill and Kriegers Flak (see figure 2.1) similar as observed (not shown here). The timing between Drogden Sill and Kriegers Flak north has been delayed by about one day when using $z_0 = 10^{-2}$ m, whereas the mean model derived spreading time of dense bottom currents from Drogden Sill to Kriegers Flak north based on 2005 model simulations is about 5.46 days as calculated later in this work (see section 2.4.6).

2.3 Model validation

2.3.1 Salinities

Within the model domain three main stations with long-term observational data can be found which are Darss Sill station (operated by the Leibniz Baltic Sea Research Institute Warnemünde, IOW, for the German Federal Maritime and Hydrographic Agency, BSH), Drogden Sill station (operated by the Royal Danish Administration of Navigation and Hydrography, FRV) and the Arkona Basin buoy (operated by IOW for BSH). A proper reproduction of dense bottom currents in this area by numerical models requires a realistic reproduction of both dense bottom currents from Darss Sill and from Drogden Sill which then influences the properties in the central Arkona Basin, represented by the Arkona buoy observations located at about 48 m depth. As such the modelled salinities at Drogden Sill and Darss Sill agree well with the observations (see figure 2.4 for Darss Sill and figure 2.5 for Drogden

Sill). A correct reproduction at these two stations is a precondition in obtaining correct salinities at Arkona buoy station which is shown if figure 2.6. It must be mentioned that even in the area of the halocline the variation is being captured by the model at all three stations. This can especially been seen at 25 m depth at Arkona buoy where the time-series partly contains salinities from dense bottom waters and partly from fresh surface water. The water masses with high salinities mainly originate from Drogden Sill which is later shown in section 2.4.5. Problematic is the surface salinity at Arkona buoy station which shows a positive bias of about 0.5 psu in 2004. Burchard et al. (2009) mentioned that this may be due to numerical diffusion which has a significant impact on the overall mixing in this model application as shown with a quantitative analysis of numerical versus physical mixing in section 3.4 and published by Rennau and Burchard (2009). Burchard et al. (2009) further mentioned that this may be due to the lack of riverine freshwater inflow. For the 2005 model runs later used in this thesis the rivers Oder, Peene, Trave, Schwentine and Warnow have been added where the impact on surface salinities in the Arkona Sea due to additional riverine freshwater input has been found to be neglectable and improvements in surface salinities are not found as the surface salinity bias in the simulations without rivers (figure 2.6) shows a similar offset of about 0.5 psu in 2005 (figure 2.9). It is more likely that the salinity and temperature boundary conditions from the coarser Baltic Sea model do not prescribe the correct surface salinities at the open boundary in the eastern Bornholm Basin which are responsible for realistic surface salinities in the Arkona Basin and further west as the mean flow of fresh surface water is directed out of the Baltic Sea. However, the modelled bottom salinity at 40 m depth and at intermediate depth of 25 m shows a reasonable degree of agreement with the observations, indicating that the model physics and numerics reproduce the relevant processes in the Arkona Sea.

However, occasionally the model shows overestimations and underestimations of inflow events (see e.g. Darss Sill salinity in March and April 2004, figure 2.4 or October 2005 in figure 2.7). This can be explained by inaccuracies of frontal positions or by inaccurate representation of the exact interface position by the model where a few meter difference in the interface height may result in the significant bias at 12m depth at Darss Sill station in March and April 2004. Still, this does not mean that the overall advective fluxes are inaccurate. The good agreement of salinities at Arkona buoy even at intermediate depth of 25 m allows to trust the model in addressing further investigations using this model application.

As the inflow in late January and early February 2004 (see peak value of 21 psu in early February in figure 2.5) is part of further investigations in this thesis, it must be pointed out that the event is not covered by the sensors at Drogden Sill station. However the salinities are captured for all depths at Drogden Sill from March until end of May 2004 although the depth is only 10 m. In order to further validate the flow across Drogden Sill, an empirical equation of barotropic flow through the Øresund is successfully applied and discussed in section 2.3.2.

Since measurements at Drogden Sill station were not fully available in 2003/2004 the model has been extended until January 1, 2006 where salinity and temperature measurements in 2005 are nearly fully available for all three stations. The model validation of the 2005 model run is shown by figures 2.7-2.9. The 2005 model run has explicitly been used to give estimations of main pathways of dense bottom currents in this area and further to quantify the individual spreading times of Darss Sill and Drogden

Sill water masses separately.

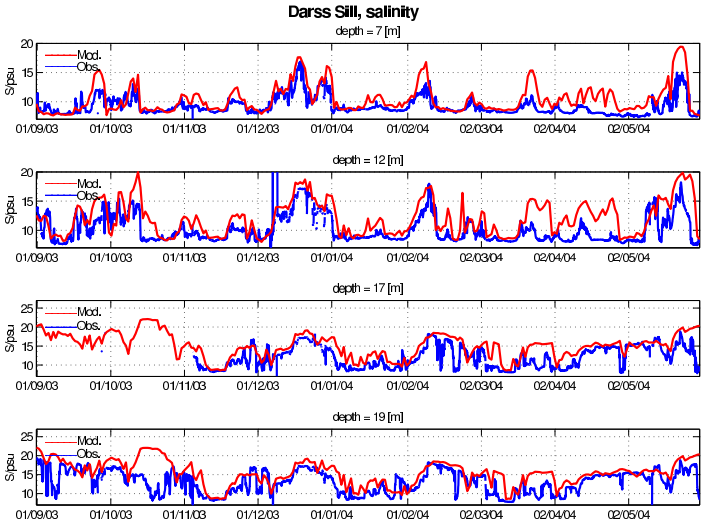

Figure 2.4: Time series of salinity at the Darss Sill mast. Blue: observations, red: model results. Shown are data at 7 m, 12 m, 17 m and 19 m below the mean sea level. The mean water depth at this station is 20 m.

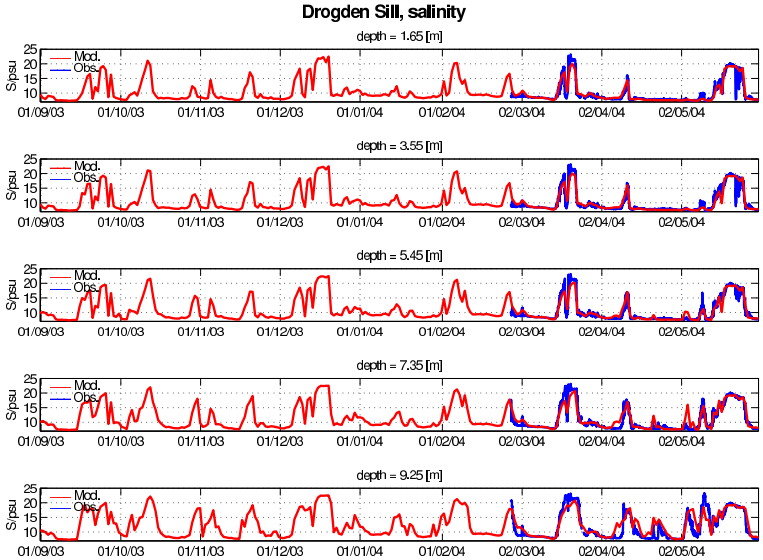

Figure 2.5: Time series of salinity at the Drogden Sill buoy. Blue: observations, red: model results. Shown are data at 1.65 m, 3.55 m, 5.45 m, 7.35 m and 9.25 m below the mean sea level. The mean water depth at this station is 9.5 m. Data before March 2004 have not been recorded.

2.3.2 Transports

In order to validate if the model properly successfully reproduces volume fluxes depending on sea surface level differences - which is a necessary precondition for simulating barotropically driven medium-intensity inflow events into Western Baltic Sea - the barotropic flow through the Øresund has been calculated based on sea levels at Viken and Skanör (north and south of the Øresund at the Swedish

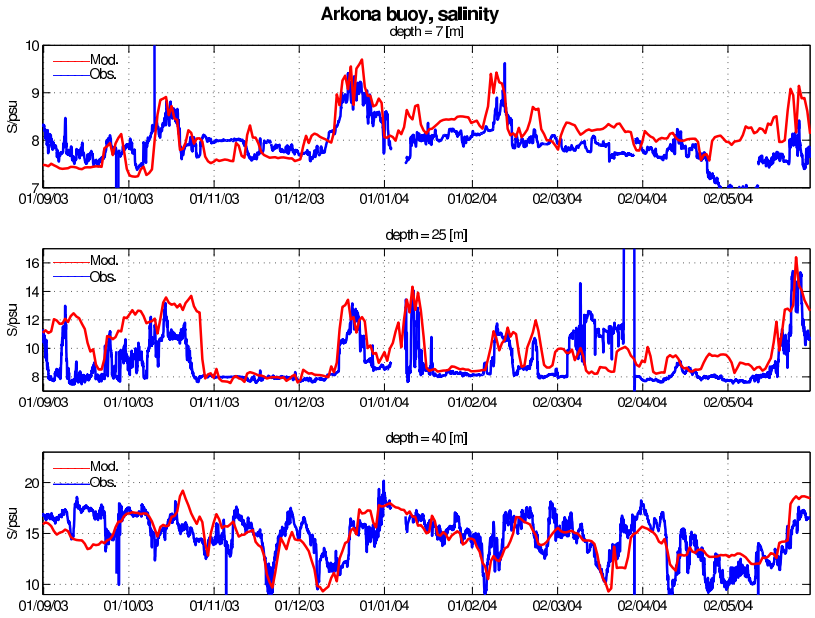

Figure 2.6: Time series of salinity at the Arkona buoy. Blue: observations, red: model results. Shown are data at 7 m, 25 m and 40 m below the mean sea level. The mean water depth at this station is 43 m.

coast, see figure 2.1) and compared to the the empirical law (see e.g. Jakobsen et al. (1997)) which is as follows:

$$\eta_N - \eta_S = KQ|Q| \tag{2.1}$$

where η_N is the sea level at Viken and η_S the sea level at Skanör, Q is the southward volume flux over Drogden Sill and K is the specific resistance for which has been estimated to be $K = 226 \cdot 10^{-12}$ s^2m^{-5} (Jakobsen et al. (1997)). As there are several inflows reproduced in the simulation period of the current model simulations, the conditions leading to an inflow in early 2004 have been chosen to apply the above equation, because this inflow has already been observed and discussed in previous studies (Burchard et al. (2005) and Sellschopp et al. (2006)), also regarding the individual meteorological conditions.

The first step in applying the empirical formulation is to compare modelled sea levels at Viken and Skanör with observations. Here a reasonably good agreement has been found as shown by figure 2.10 which is the precondition to successfully reproduce barotropic flows with the resulting inflow event across the shallow Drogden Sill.

Figure 2.11 shows calculations of the empirical model derived transport and the empirical transport based on observations. This is additionally compared to the directly calculated model transports through a west-east transect at Drogden Sill whereas all three different transport calculations show a strong correlation leading to the assumption that both the empirical equation agrees with the model transport (via comparing directly calculated model transports across a transect with model transports based on the empirical equation) and vice versa (via comparison of model transports based on the Viken-Skanör sea level difference to transports obtained via observed sea level differences). The agreement shows the models ability to correctly reproduce barotropic dynamics, but it might have problems in reproducing events on a shorter timescale as found in section 2.4.3, demonstrating that some inflow

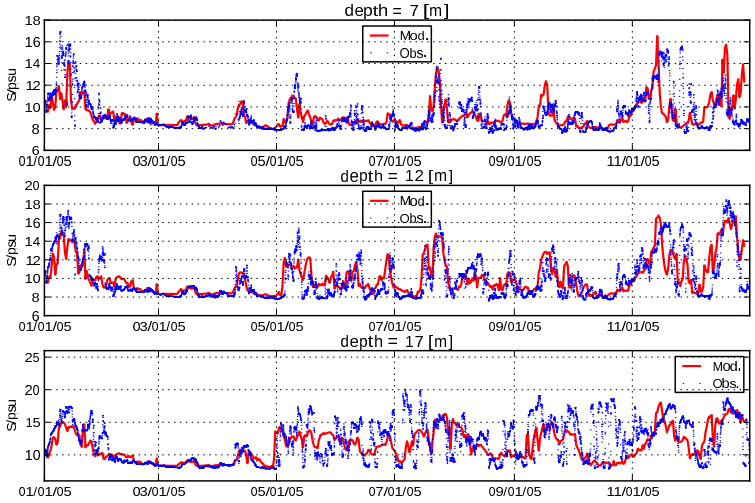

Figure 2.7: Time series of salinity at the Darss Sill mast for year 2005. Blue: observations, red: model results. Shown are data at 7 m, 12 m and 17 m below the mean sea level. The 19 m depth level as used for the 2003/2004 model simulation was not available in this year. The mean water depth at this station is 20 m.

events consist of several pulses of inflowing dense bottom water with different intensities and salinity.

2.4 Characteristics in vertical structure, pathways and spreading behavior

2.4.1 Salinity and passive tracer fields

Recent observations of vertical transects of salinity and temperature have illustrated that dense bottom plumes, due to the complex overflow situation in the Western Baltic Sea with two geographically separated sills being responsible for two more or less independent inflows, are potentially influenced by the process of interleaving due to different densities (see e.g. Sellschopp et al. (2006), their figure 2). By marking the two inflows at Drogden and Darss Sill with two passive tracers, an analysis might demonstrate the comparably significant process of interleaving of water masses from different origins in the Western Baltic Sea. This is presented and discussed in the next sections. Furthermore the passive tracer analysis gives additional knowledge about regions with significant three layer stratification in the Central Arkona Sea: (i) dense Drogden Sill water masses at the bottom, (ii) slightly lighter Darss Sill water masses above and (iii) fresh water at the surface. However, as the density difference between both water masses is rather small with values of a few psu, these differences are strong enough to maintain the separation between the water masses and avoid vertical mixing between them (see chapter 2.4.5). The investigation of the two passive tracer is additionally useful for giving estimates concerning the spreading times and behavior of the bottom plumes. The investigations of the inflow in early 2004 with directly comparing modelled salinities and velocities on vertical transects have been conducted with the help of the model simulation between September 2003 and May 2004 as published by Burchard et al. (2009). As observations at Drogden Sill are not fully available over the whole model period from September 2003 to May 2004 (see figure 2.5), the experiments with marking the Darss Sill and

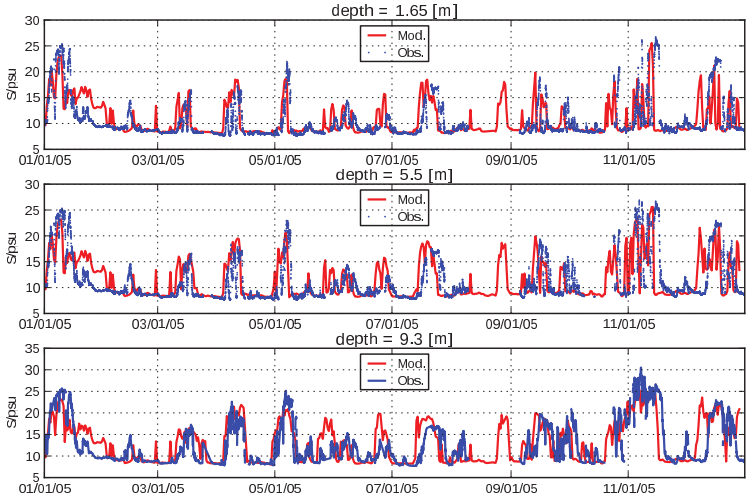

Figure 2.8: Time series of salinity at the Drogden Sill buoy for year 2005. Blue: observations, red: model results. Shown are data at 1.65 m, 5.45 m and 9.25 m below the mean sea level. The mean water depth at this station is 9.5 m. The levels 3.55 m and 7.35 m have been neglected in the 2005 model validation because of neglectable low vertical variation. However 5.45 m represents intermediate level at Drogden Sill.

Drogden Sill water masses by passive tracers, have been conducted via extending the model setup by Burchard et al. (2009) until Jan, 1 2006 where for the whole year 2005 observations for all three stations Darss Sill, Drogden Sill and Arkona Basin are available. The model reasonably well agrees with the observations in 2005 (section 2.3.1). Hence the passive tracer studies have been made with the help of the 2005 model simulation as investigations of Darss Sill and Drogden Sill plume branches separately requires that the model derived plume timing and salinities at Darss Sill and Drogden Sill agree well with the observations.

The two passive tracers were released continuously at a north-south transect east of Darss Sill (11.95°E) and a west-east transect at Drogden Sill (55.6°N) in such a way that they were set to a value equal to the salinity at these positions when the current was directed into the Arkona Sea and when salinities reached values greater than 10 psu. In all other cases the tracer was set to zero. This means that surface tracer concentrations remain close to values of zero as they are not being marked. However, after some months the surface tracer concentrations have reached background values of about $1-2$ due to vertical mixing and entrainment of marked water masses. This means that the tracer concentrations of the bottom current show values less than the plume salinity despite of being set equal to salinity at the tracer release transect because surface tracer concentrations are about close to zero (background concentrations $c = 1...2$) whereas surface salinities are between 7 and 8 psu resulting in different entrainment rates for salinity and tracer concentrations.

2.4.2 Annual mean velocities

As naturally induced mixing and spreading behavior of the dense bottom currents are both closely related to the current speed, figure 2.12b shows the calculation of annual mean current speed and annual mean current direction fields in the model domain. Although velocities are between 3 and 4.5 cm/s in the Central Arkona Sea, several areas with rather high mean velocities ($0.075 - 0.15$ m/s)

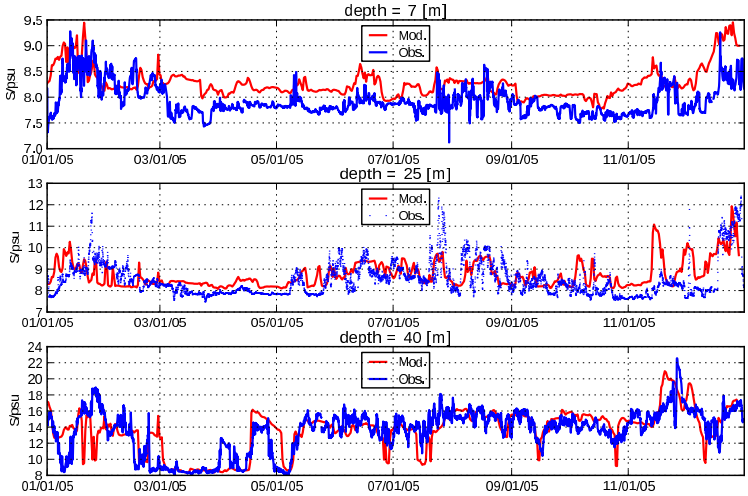

Figure 2.9: Time series of salinity at the Arkona buoy for year 2005. Blue: observations, red: model results. Shown are data at 7 m, 25 m and 40 m below the mean sea level. The mean water depth at this station is 43 m.

are found. The mean current velocities at the bottom in the Central Arkona Basin nicely agree with the estimations by Hagen and Feistel (2001) who derive permanent mean bottom current velocities of 3 cm/s for the Baltic deep water. The classical picture of the flow of a dense bottom current is the balance between Coriolis force and pressure gradient. Lass and Mohrholz (2003) mentioned that this geostrophic balance together with the minor impact of bottom friction (leading to a flow in direction of the core of the Arkona Basin), leads to a spiralling cyclonic current along the rim of the Arkona Basin. This is not supported by figure 2.12b where the mean current in the Arkona Basin is preferably directed in north-east direction.

Furthermore there are a few local areas in the domain, where the mean flow is in counter-clockwise direction which are (i) between Zingst and Gedser, (ii) about 20 km north of Zingst and most significantly (iii) directly on the shallower part of Adler Ground (north-east of the isle of Rügen). Additionally exchange flows at Darss Sill, south of Drogden Sill and in the Bornholm Channel are located west of the main dense bottom flow direction. A weak east-west directed residual flow of about $0.01 - 0.03$ m/s is found on the southern channel of Kriegers Flak with a general clockwise mean flow system surrounding Kriegers Flak. High velocities (yellow and red areas: $0.3 - 0.5$ m/s) indicate main pathways of dense bottom currents or accelerated flow conditions due to steep slopes (e.g. south of Drogden Sill, Bornholm Channel) or narrow underwater channels (see e.g. north of Kriegers Flak) which agrees well with the estimates of hot spots of turbulent mixing in this area as discussed in section 2.4.7 and shown in figure 2.30. The maximum velocities obtained with the help of the nine month model run in 2003/2004 is shown in figure 2.12b and reveals a qualitative similar picture than the annual mean velocities. Highest values of up to 0.5 m/s current speeds especially at Darss Sill, Drogden Sill and the Bornholm Channel are found.

Furthermore figure 2.12 indicates that the dense bottom water prefers the southern trench, which may be due to the geostrophic balance, of the Bornholm Channel consisting of two narrow underwater channels. Surprisingly, mean bottom velocities in the southern trench are about 14 cm/s and even 9 cm/s in the northern trench. This supports the conclusions drawn with the help of figure 2.30 that

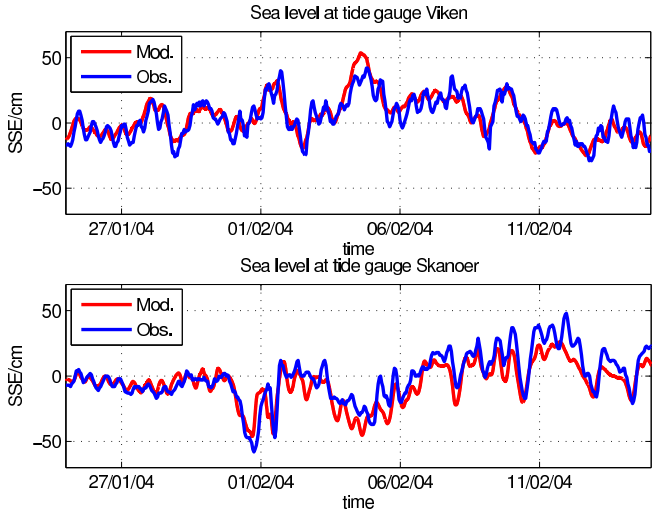

Figure 2.10: Simulated versus observed sea level variations in Viken and Skanör, located north and south of the Øresund, respectively, see figure 2.1 for the positions. The time series are shown for a period of three weeks focussed on the inflow event starting on February 1, 2004.

unexpected strong turbulent mixing in the Bornholm Channel is due to the permanent outflow of dense water from the Arkona Basin which is emptied on a time-scale between 1 and 3 months (Lass et al. (2005)). This rather high mixing is in contrast to the work of Kõuts and Omstedt (1993) who suggested only neglectable vertical mixing in the Bornholm Channel. High mean bottom current velocities in the Bornholm Channel are also due to the increasing bottom slope of the Bornholm Channel connecting the Arkona Sea with a depth of 50 m with the Bornholm Basin with a depth of 90 m.

2.4.3 Observed and modelled vertical plume properties

Comparisons between observed and modelled vertical structure of dense bottom currents south of Drogden Sill and at Kriegers Flak during the inflow in early February 2004 are conducted in this section. As already mentioned the inflow in early February is driven by a strong sea level difference between north and south of the Øresund as shown with the help of modelled and observed Viken and Skanör sea levels in figure 2.10. This inflow has recently additionally been analyzed (Burchard et al. (2005), Sellschopp et al. (2006), Arneborg et al. (2007)) with the help of ship cruise measurements and numerical models. Some of the transects obtained during these ship cruises are used for model validation in this section.

Inflow conditions start on January 31 with reduced sea levels south of Drogden Sill at Skanör which results in a sea level difference of 0.5 m between Viken and Skanör. This pressure difference is underestimated by about 10 cm by the model (figure 2.10). This will potentially lead to an underestimated strength of the inflow event and delayed timing. The effect of this barotropic gradient is represented by the first salinity peak in the observations in early February (see figure 2.5). One day later the pressure difference between Viken and Skanör has finally reached a value of more than 0.8 m which is correctly being reproduced by the model (see figure 2.10) and can be seen by an almost stronger salinity value at Drogden Sill (figure 2.5). Furthermore an overestimation of transports through the Øresund is found

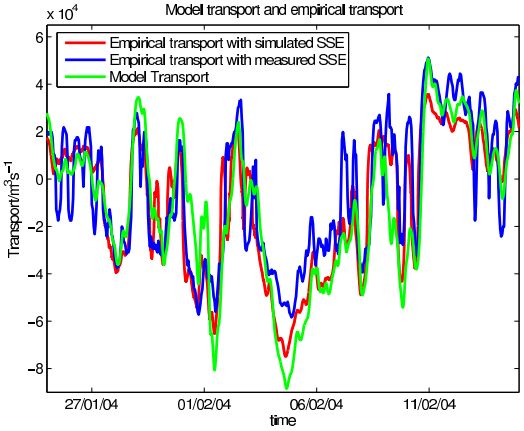

Figure 2.11: Time series of the volume transport across the Drogden Sill during three weeks in January/February 2004, with negative values representing inflow (southward transport). Shown are the simulated transports (green), and the transports estimated from the relation (equ. 2.1), calculated on the basis of simulated (red) and observed sea levels at the Viken and Skanör gauges.

as shown in figure 2.11. However it must be pointed out that the empirical transport equation with the resistance value by Jakobsen et al. (1997) is an empirical finding which is only based on long-term sea level observations at two local positions which might not fully capture the whole transport process correctly.

Basically the observations show that the inflow event in early 2004 consists of three pulses of different strength (figure 2.5) transporting dense bottom water in southward direction from Drogden Sill (see e.g. figure 2.20). The strength of each of these three pulses is not fully captured by the model leading to a different plume timing at Kriegers Flak which is shown later in this section.

A model-derived qualitative impression of horizontal bottom salinity distribution in the observed area before and after the inflow event in early 2004 is demonstrated by figure 2.13 representing bottom salinity snapshots on February 1 and February 10. On February 1 high salinities of more than 23 psu have already reached the Drogden Sill. The salinities in large areas are less than 11 psu, about 18 psu at Darss Sill and 16 psu in the central Arkona Basin. For most of the inflow events water from both the Darss and the Drogden Sill simultaneously enter the Arkona Basin (see e.g. figure 2.19). The Arkona Basin acts as a pool for the dense water entering the Arkona Sea via the sills. The water partly remains in the Arkona Basin until it is transported through the Bornholm Channel into the Bornholm Sea whereas only small amounts of dense bottom water takes the way east of the isle of Rügen. On February 10 almost the whole area surrounding Kriegers Flak consists of dense bottom water of about 18 psu. Even higher values of more than 19 psu are found at the northern trench of Kriegers Flak. The impact of dense Darss Sill water masses can be seen in the plot which have already passed the area north of the isle of Rügen (further discussion of the spreading behavior of the Darss Sill water masses can be found in section 2.4.5). Furthermore the amount of dense bottom water in the Arkona Basin as seen on February 1 (left panel in figure 2.13) has been reduced 10 days later (right panel in figure 2.13) which indicates that a significant amount of dense bottom water has already passed the Bornholm Channel.

As discussed in section 2.3.2 the early February inflow consists of several pulses of dense bottom water

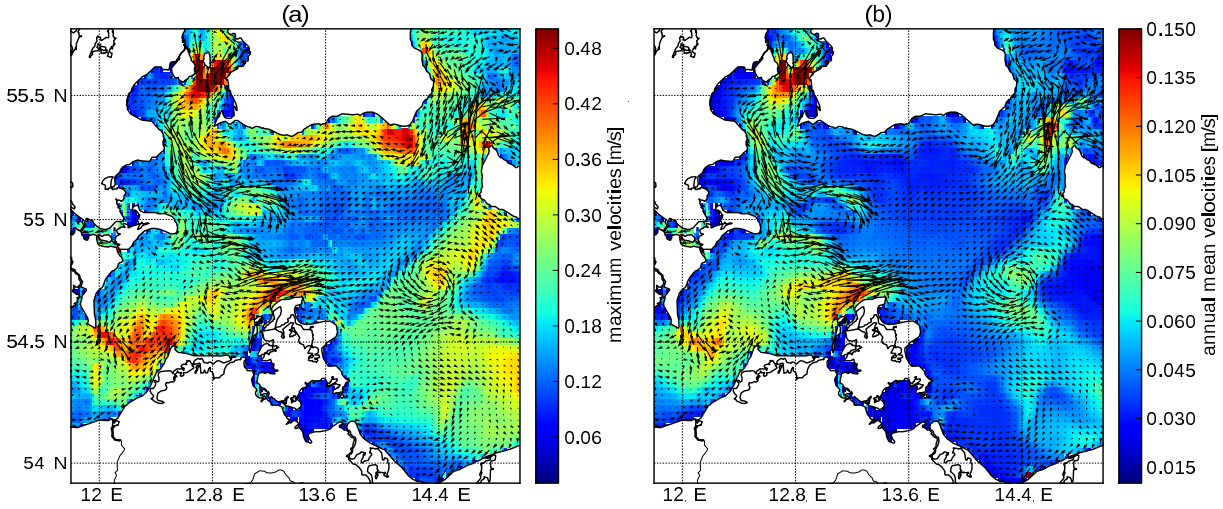

Figure 2.12: Left panel: model derived maxima in current velocities together with vectors of mean current velocity calculated on the basis of the nine month model run between 2003 and 2004. Right panel: Model derived mean current velocities calculated with the nine month model run. Both plots additionally shows current directions.

depending on the strength of the barotropic forcing along the Øresund. Figure 2.14 shows a time series of the vertical salinity distribution along a transect south of Drogden Sill (see figure 2.1 for transect location). A weak inflow (February 2) with a plume thickness of less than 5 m is followed by a strong inflow with a significantly higher salinity and with about twice the thickness at February 5. The separation of both pulses of dense water is clearly seen at February 4 at 55.5°N with salinities significantly below the values of the first and second pulse salinities. The vertical structure of the plume on February 6 is consistent with observations obtained from FWG Kiel (Forschungsanstalt für Wasserschall und Geophysik) as found in figure 2.15 (see also Burchard et al. (2005) and Sellschopp et al. (2006)). However, as already pointed out, the model underestimates the first pulse of dense bottom water. Hence February 6 has been used to prove the capability of the numerical model in correctly reproducing transport and turbulent mixing of dense bottom currents as shown by figure 2.15. Both salinities of 22 psu and the plume thickness of 10 m is reproduced. The eastward velocities at 55.3°N indicate an eastward propagation in model and observations of about 0.3 ms^{-1}. Furthermore southward directed currents of about 0.5 ms^{-1} are reproduced in both model and observations with a similar along-transect and vertical distribution.

The channel north of Kriegers Flak (see transect line in figure 2.1) is investigated in figure 2.14 showing the temporal development of the vertical salinity structure. It takes about 5.46 days for the plume to travel the way from south of Drogden Sill to north of Kriegers Flak which is shown in section 2.4.6. The plume is not yet visible on February 5, but high salinities of more than 18 psu have reached the channel on February 8. Observations of velocity and salinity obtained from the FWG Kiel on this section on February 5 have been compared with the modelled plume structure on February 7 which has been found to be comparable with the observations (2.17). The geostrophic alignment (balance between cross-channel pressure gradient and Coriolis forces) of the current is clearly visible with an alignment of the current to the northern part of Kriegers Flak. As in the observations the isolines of salinity are pinged in the northern part of the plume and widened in the south, a feature also been found

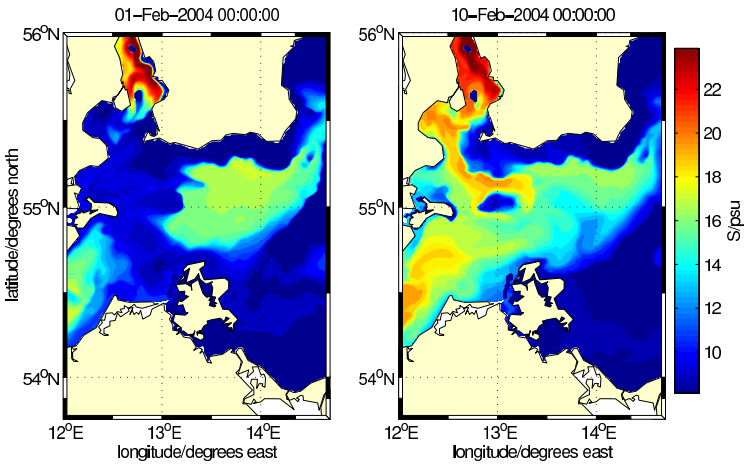

Figure 2.13: Simulated bottom salinity in the Arkona Basin before (February 1, left panel) and after (February 10, right panel) the medium intensity inflow over Drogden Sill (see also figure 2.19 for an investigation of Darss Sill and Drogden Sill plumes separately during four different inflows in 2005).

and described in more detail by Burchard et al. (2005), Sellschopp et al. (2006), Umlauf et al. (2007), Umlauf and Arneborg (2009a), Umlauf and Arneborg (2009b). The eastward velocity component has a maximum value of about 0.4 m/s in the plume interface which is a common feature which is in first order due to the lowest impact of bottom- and interfacial friction in this part of the plume. Furthermore in the interface region a southward current of about 0.1 m/s is found which is due to forces driven by the additional along-flow alignment of the current in the channel (Umlauf et al. (2007)). However, due to insufficient vertical and horizontal model resolution this physical feature cannot be fully resolved and is not further investigated in this study. As a successful additional numerical feature within the numerical ocean circulation model is the incorporation and use of adaptive vertical coordinates which has recently applied for this charaterictical physical feature of density driven dense bottom current in channels (Umlauf et al. (2010)) and in the Baltic Sea (Hofmeister et al. (2010a)). Anyhow, the model is able to capture the basic structure and spreading of dense bottom currents in the Western Baltic Sea as proved with the help of a number of observations in this work.

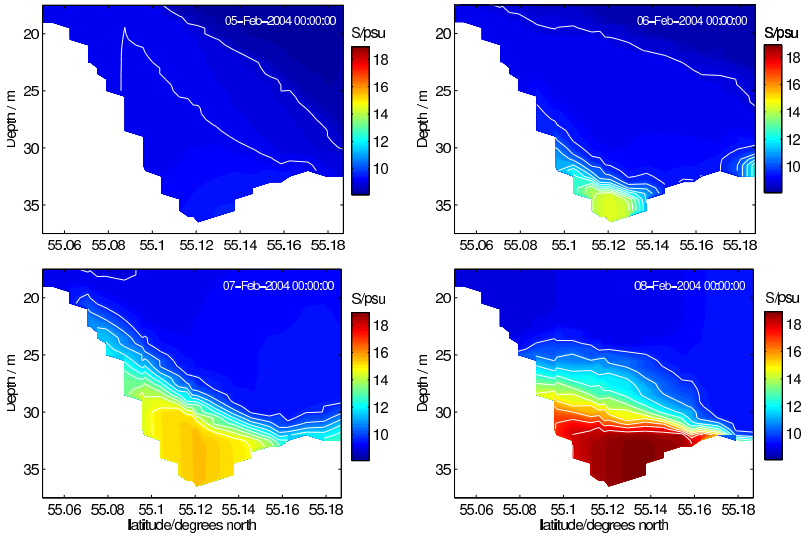

Figure 2.14: Simulated salinity along the cross section across the channel north of Kriegers Flak see the map in figure 2.1 for the location) during four consecutive days in early February 2004.

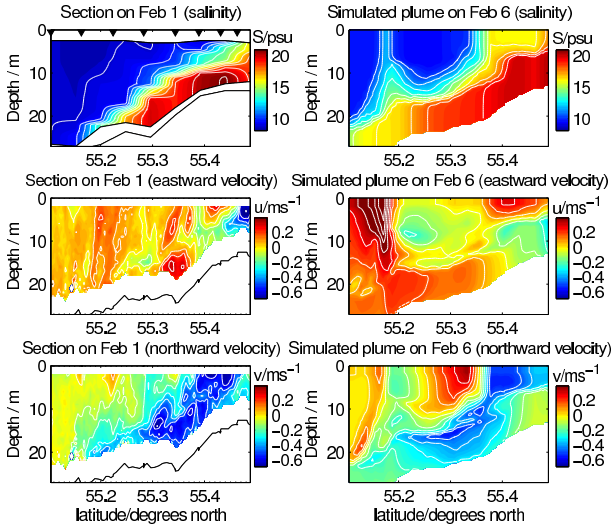

Figure 2.15: Observed (left) and simulated (right) salinity and current velocity on a north-south transect south from Drogden Sill, deduced from CTD profiles and Acoustic Doppler Current Profiler. The observations were taken on February 1 from 16:20 h - 20:41 h (UTC). The black triangles in the upper left panel show the positions of the single CTD profiles. These salinity and current velocity data have been obtained by FWG Kiel, Germany (see Burchard et al. (2005) and Sellschopp et al. (2006)).

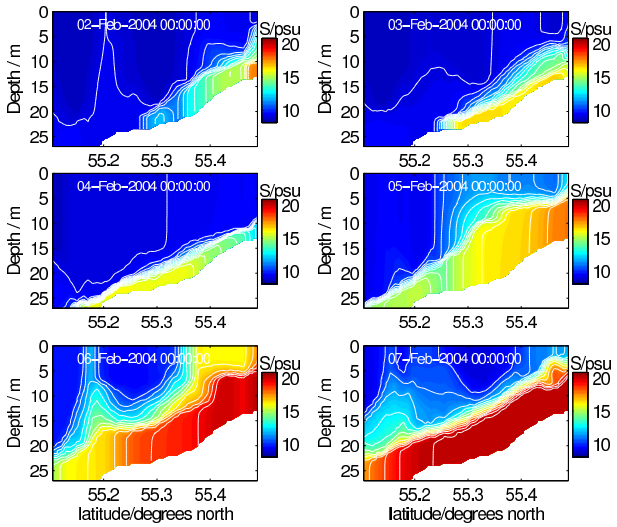

Figure 2.16: Simulated salinity along the cross section south of Drogden Sill (see the map in figure 2.1 for the location) during six consecutive days in early February 2004.

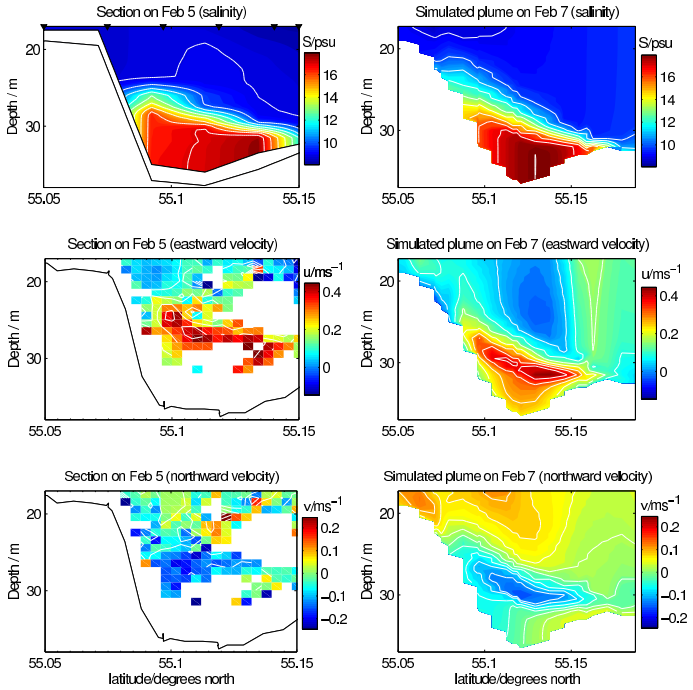

Figure 2.17: Observed (left) and simulated (right) salinity and current velocity on a north-south transect across the channel north of Kriegers Flak, deduced from CTD profiles and Acoustic Doppler Current Profiler. The observations were taken on February 5 from 10:45 h - 12:30 h (UTC). The black triangles in the upper left panel show the positions of the single CTD profiles. These salinity and current velocity data have been obtained by FWG Kiel, Germany (see Burchard et al. (2005) and Sellschopp et al. (2006)).

2.4.4 Interaction of Darss and Drogden Sill dense bottom currents at Kriegers Flak

Burchard et al. (2005) and Lass et al. (2005) argue that the dense bottom water originating from the Darss Sill divides into two branches north and south of Kriegers Flak whereas the trench west of Kriegers Flak limits the transport capacity along the southern trench. This finding is supported by figure 2.18b where the mean of the bottom tracer field for the Drogden Sill passive tracer has been calculated on the basis of the realistic model simulation and compared to mean bottom salinity (figure 2.18c). Interestingly the mean bottom salinity (2.18c) has similar values north and south of Kriegers Flak, indicating the strong influence of Darss Sill water masses (figure 2.18c) on the southern trench. The horizontal distribution of mean bottom salinity (figure 2.18c) is very much aligned to the topographic conditions (figure 2.1), whereas both plumes from Darss Sill (figure 2.18a) and Drogden Sill (figure 2.18b) show a significantly different spreading behavior into the central Arkona Basin. It seems that for a number of times the inflow events are such that the plumes from Darss Sill and Drogden Sill drain nearly at the same time into the central Arkona Basin, whereas the stronger Darss Sill plume pushes the Drogden Sill plume to the northern part of the Arkona Basin from where it propagates through the Bornholm Channel into the Bornholm Basin. Hence it is notable that the plume propagation in the central Arkona Basin and the development of mesoscale eddies as mentioned by Lass et al. (2005) is very much depending on local conditions of Darss Sill and Drogden Sill plume

timing.

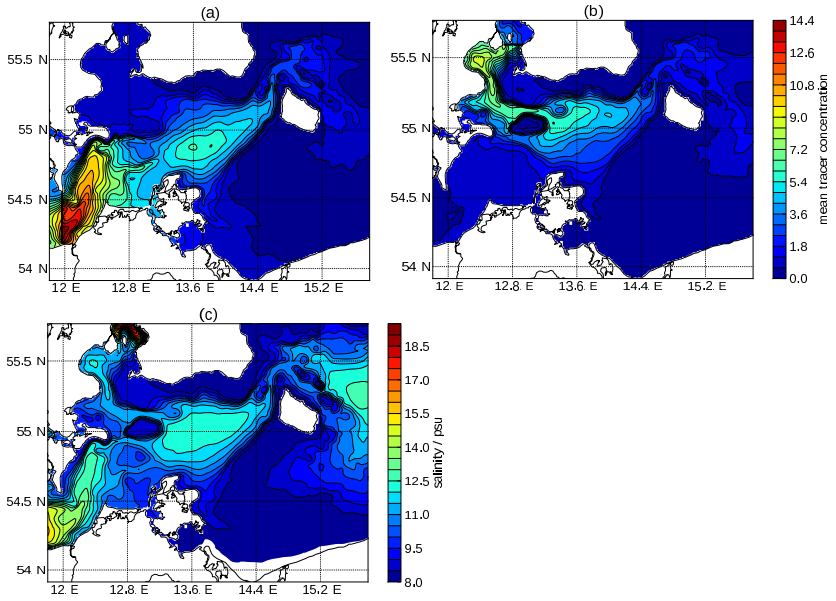

Figure 2.18: Annual mean bottom tracer concentrations for (a) the Darss Sill passive tracer, (b) the Drogden Sill passive tracer and (c) the bottom salinity.

Figure 2.19 shows snapshots of bottom tracer concentrations for a number of medium intensity inflow events. Considering these four inflows with different strengths of Darss Sill and Drogden Sill dense bottom currents, the timing between the start of the plume south of Drogden Sill and the time the plume has passed both northern and southern trench of Kriegers Flak is about less than 10 days. Notable is the strong separation between Darss Sill and Drogden Sill water masses due to their different salinities (and hence also tracer concentrations). In figure 2.19b,c the shift of denser Drogden Sill water below Darss Sill water is visible. These relations are leading to the abstract picture drawn in by figure 2.20. The image states that there is a short delay between Darss Sill water entering the western Arkona Basin first, followed by Drogden Sill water a few days later (see figure 2.29 for details of spreading times). The Drogden Sill water shifts below the Darss Sill water mainly propagating through the central and northern Arkona Basin. The Darss Sill water masses show a significantly higher transport capacity and mainly propagate on the southern rim of the Arkona Basin but also through the Central Arkona Basin (see also figure 2.18). When both water masses have entered the Arkona Basin they contribute to older Arkona Sea dense bottom water (indicated by the yellow circle) which is consequently being pushed away in direction of the Bornholm Channel and lifted at the same time. The right panel in figure 2.20 shows main pathways of Darss Sill water masses (black lines) and main pathways of Drogden Sill water masses (red lines). The blue circles indicate areas where both plumes have similar salinities and as such no general conclusions can be drawn about whether the Drogden Sill water shifts below Darss Sill water or vice-versa. Still it is notable that Darss Sill plumes prefer the southern trench in the Bornholm Channel (see figure 2.18a).

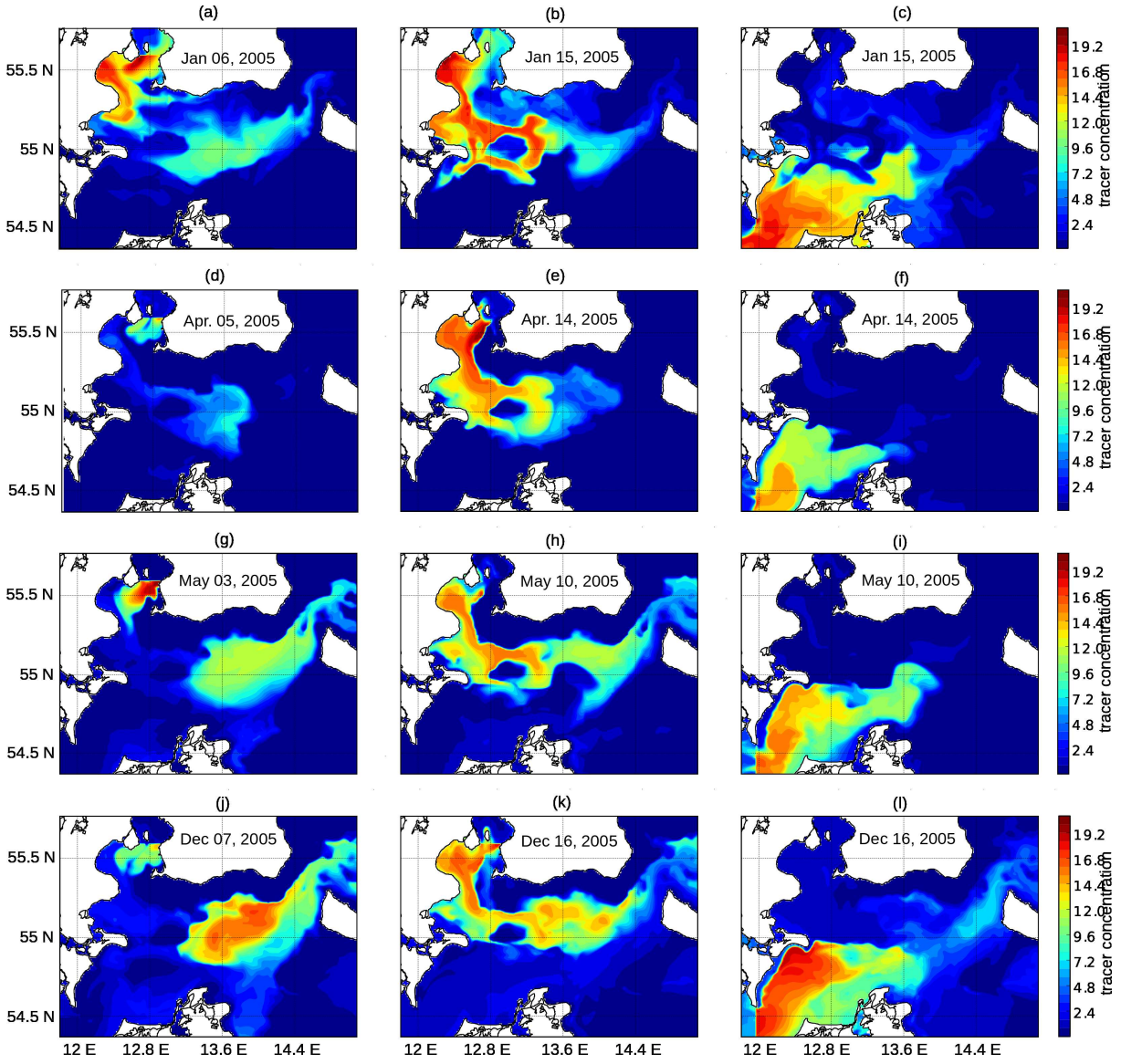

Figure 2.19: Each row of plots represents certain states of January, April, May and December 2005 inflow events. The first picture in a row shows the Drogden Sill bottom tracer concentration at the start of the inflow of dense water crossing Drogden Sill. The second picture shows the Drogden Sill bottom passive tracer concentration after the dense water has fully surrounded Kriegers Flak and the last panel in each of the rows represents the Darss Sill passive tracer concentration at the bottom at the same time when Drogden Sill water masses have surrounded Kriegers Flak.

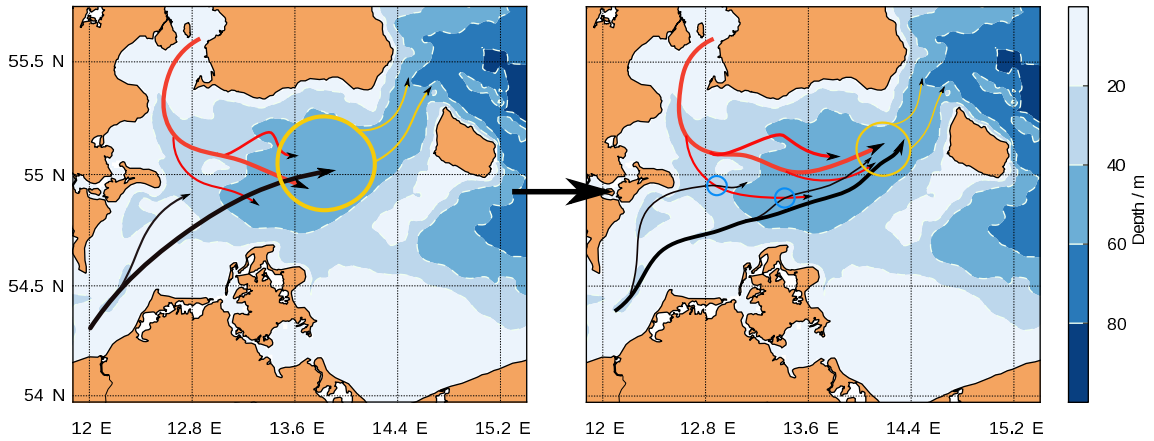

Figure 2.20: Estimated main pathways of dense bottom currents in the Western Baltic Sea based on model simulation results for dense bottom currents from Darss (black lines) and Drogden Sill (red lines). The Darss Sill water masses are found to enter the Western Arkona Basin earlier than water from Drogden Sill (see e.g. figure 2.19b,c), indicated by the thick black arrow already pointing further east than the thick red one (left panel). When dense Drogden Sill water enters the Western Arkona Basin, it is shifted below Darss Sill water because of higher salinities (left panel: red line is below black line). The yellow big circle in the left panel indicates old Arkona Basin water masses are being pushed in eastern direction by the inflowing dense bottom water from the different origins which shifts below the older Arkona Basin water. There are several thin black and red lines indicating further pathways of the dense bottom currents with lower transport capacity, lower salinities and hence lower propagation velocity than the main propagation pathways (thick red and black line). The right panel shows the situation some days later when the old dense bottom water in the Central Arkona Basin has already partly left the Arkona Basin through the Bornholm Channel (indicated by the comparably smaller yellow circle than in left panel). Furthermore it is shown that the dense bottom water discharges mainly through two narrow channels in the Bornholm Channel, where Darss Sill water masses prefer the southern Channel (see figure 2.18a), but Drogden Sill water masses are similarly distributed in both channels (see figure 2.18b). Small blue circles denote that salinities of Darss Sill and Drogden Sill water masses show similar values in this regions and hence none of them is found to be preferably shifted below the other. However, Drogden Sill water masses are mainly found in lowermost parts of the water column with Darss Sill water masses above, especially in the centre of the Arkona Basin (see e.g. figure 2.24). Even though the horizontal salinity distribution of Darss Sill and Drogden Sill water masses in the Arkona Sea can not explicitly predicted for each individual inflow event, mean fields reveal that Darss Sill water are preferably found in the southern Arkona Basin and Drogden Sill water on the northern rim (see 2.18a, b).

However, Lass et al. (2005) presume that the water masses south of Kriegers Flak mainly consists of inflow events from Drogden Sill, which is disproved with the simulations conducted. Figure 2.18a demonstrates the significant impact of Darss Sill water masses on the distribution of water masses south of Kriegers Flak. Flow pathways and quantitative comparisons of tracer concentrations and salinities north and south of Kriegers Flak are further analyzed with the help of figure 2.21. Here bottom time series of passive tracer marked Darss Sill and Drogden Sill water masses are compared together with bottom time series of salinity in the northern and southern trench of Kriegers Flak. Figure 2.21a reveals that Darss Sill water masses do not reach the northern part of Kriegers Flak. It is still notable that there are two events in February and August 2005, where plume fronts partly reached the northern trench with low tracer concentrations. This is because in the current simulations the water in the Darss Sill is marked whenever salinities are above 10 psu which can be the case for water masses moving into the domain but also out of the domain. Hence marked Darss Sill water is partly being advected via surface currents back through the Danish Belts to be partly added to water in the Sound as seen by tracer concentrations of $c = 1 - 2$ in figure 2.21a for the Darss Sill tracer. Figure 2.18a, b shows that both tracer concentrations have similar values. A time series of both tracer concentrations south

of Kriegers Flak (figure 2.21b) additionally reveals that both situations with higher Darss Sill or with higher Drogden Sill concentrations occur depending on the different strengths of inflowing Drogden and Darss Sill water with resulting interleaving (to be discussed in the next chapters, see e.g. figure 2.24 of the different water masses).
Figure 2.21c,d shows a comparison of time series north and south of Kriegers Flak for both tracer concentrations and salinities. Basically a time shift between the bottom time-series north and south of Kriegers Flak in salinity should be found which is not the case. The more clear is the time shift when regarding bottom time-series of the Drogden Sill passive tracer only (2.21c). The percentual difference between northern trench peak value and southern trench peak value was calculated for each inflow (2.21c,d) in salinities and passive tracers. It is found that the peak salinity in the south is about 89% of the peak value found in the northern trench. For the passive tracer concentrations it is in average 66% of the northern peak value which demonstrates how strong the southern current is modified compared to the northern branch. As the salinity signal is influenced by plume fronts originating from the Darss Sill (2.21b, d) it cannot be alone used to calculate the time shift for plume fronts passing the northern and southern part of Kriegers Flak originating from the Øresund. A much better data basis for the time shift calculation is to use the Drogden Sill passive tracer (see figure 2.21c) which reveals a time shift between the two points considered, of 2.5 days (see also figure 2.29) whereas it is clear that such an analysis of time shifts in the Western Baltic Sea is only possible marking the water masses, since salinity correlations are heavily influenced by water masses from the different origins. Additionally the time series reveal that there are certain stronger events from Drogden Sill where there has been no inflow from Darss Sill. An example of such a situation are the small inflows at Drogden Sill in March/April 2005 (figure 2.8) which can not be seen at Darss Sill (2.7). The passive tracer method is used in section 2.4.6 (see figure 2.29) as an analysis method to calculate the individual mean spreading times of dense bottom currents based on cross-correlation calculations of bottom passive tracer time-series at several different positions.

2.4.5 Interaction of plume branches in the Arkona Sea

As the properties of the mean flow (e.g. entrainment rate, eddies) are potentially influenced by the complex vertical stratification due to the two inflows from Darss and Drogden Sill and corresponding interleaving in the Central Arkona Basin, the correlation coefficient (R) of the vertical profiles of the two tracers has been calculated investigating all water columns over a one year period covering several medium intensity inflow events. Figure 2.22 shows a snapshot of vertical passive tracer profiles and salinity in November 2005 in the Central Arkona Basin at 13.8°E, 54.9°N. A strong separation between Darss Sill and Drogden Sill water masses is found, leading to a high anti-correlation coefficient when correlating both passive tracer profiles which indicates interleaving of the two water masses. Calculating the correlation/anti-correlation coefficient of every water column in the domain over the whole year 2005 gives a quantitative picture of the strength of interleaving between gravity current from Darss Sill and Drogden Sill. Moreover this allows to quantify the strength and location of vertical mixing between both water masses, indicated by high positive correlation coefficients. Thus, the correlation coefficient between the vertical profiles of the passive tracers has been calculated using the following

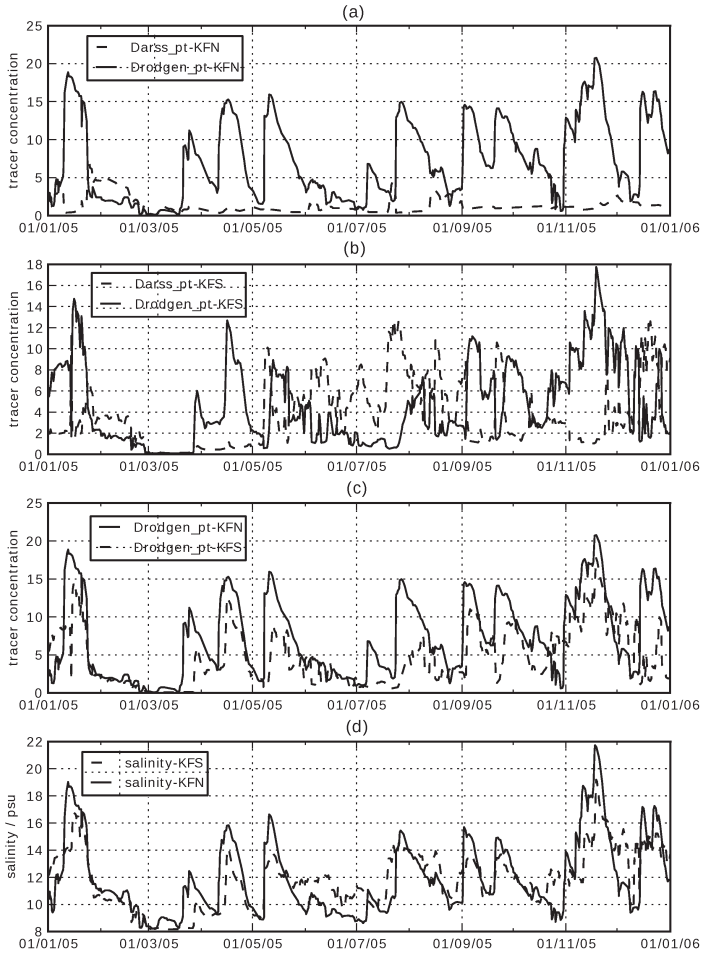

Figure 2.21: Time series of bottom passive tracer concentrations and bottom salinity in the trenches north and south of Kriegers Flak: (a) Concentration signal of marked Darss Sill and Drogden Sill water north of Kriegers Flak, (b) bottom concentrations of passive tracers south of Kriegers Flak, (c) comparison of bottom concentrations of Darss Sill marked water masses north and south of Kriegers Flak (KFN, KFS), (d) time series of bottom salinities north and south of Kriegers Flak. The observations at KFN and KFS are shown in figure 2.27 and do cover only most of the year 2006.

restrictions and conditions:

- The maximum value in tracer concentration of each individual water column must exceed $c = 4.0$ at the same time for both tracers. This guarantees strong inflow conditions from Darss Sill and Drogden Sill at the same time and the concentrations are well above the background level of tracer concentrations of $c = 1...2$;

- As the vertical profiles of the passive tracers are very similar at the surface above the upper interface of the plume (figure 2.22), the comparisons of the vertical profiles of the passive tracers neglect this surface part of the vertical profiles. The depth of the plume interface is obtained via calculation of the depth of the maximum vertical gradient of salinity. The correlation coefficient of the vertical profiles of the two passive tracers will then only be compared from the bottom to the depth of the plume interface. This is necessary as the correlation coefficient will otherwise be influence by surface tracer concentrations which are similar for both tracers and independent

from the vertical tracer distribution below the plume interface.

- The correlation coefficient has to be higher than $R = 0.4$ and the anti-correlation coefficient has to be less than $R = -0.4$ to be included in the calculations presented in this section.

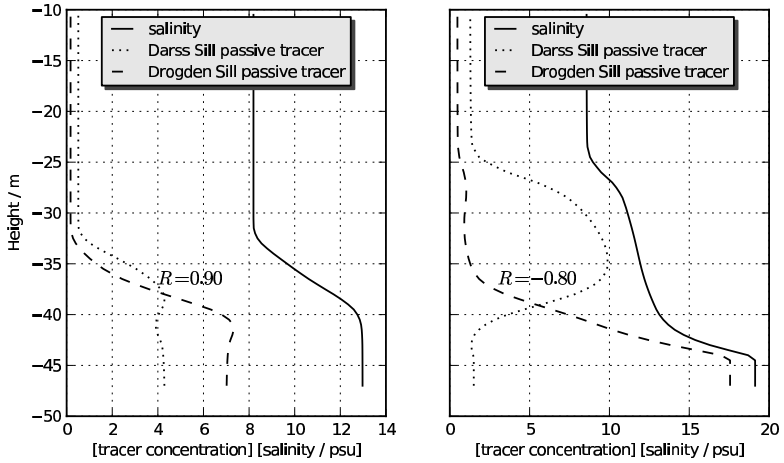

Figure 2.22: Snapshots of passive tracer concentrations of marked Darss Sill and Drogden Sill water masses and corresponding salinities for a case with vertically well-mixed tracer masses (left panel) and a case with strong separation of the two water masses (right panel). The correlation coefficient considering the vertically well-mixed case gives $R = 0.90$ and $R = -0.80$ for the case with a three layer stratification: (i) bottom layer containing Drogden Sill water masses, (ii) intermediate layer containing Darss Sill water masses and (iii) less saline surface water on top. Obvious is the stronger deviation of passive tracer concentrations compared to salinity for the vertically well-mixed case. This is, as already discussed, because the water masses shown in the left panel already joined the dense bottom water pool in the Arkona Basin during an earlier inflow event. Hence the passive tracers show stronger dilution (than salinity) due to higher bottom-surface tracer concentration differences. This is because the surface tracer concentrations were not set equal to salinity as it has been done at the bottom during inflow conditions and hence show values of $c < 2$ (see surface passive tracer concentrations in the two panels). The snapshots of vertical profiles are from early November 2005 (left panel) and mid of November 2005 (right panel) at 13.94°E, 55.0°N which is in the Central Arkona Basin.

This investigation reveals that as expected the mean (positive) correlation coefficient increases to the east (figure 2.23a) with highest values ($R > 0.75$) found on the southern edge of the Central Arkona Basin and in the area of the Bornholm Channel and its entrance where the plumes are traveling down the incline from 50 m to 90 m, indicating increased mixing between the two water masses from Darss and Drogden Sill. As figure 2.23a only gives a conclusion of mean conditions, the occurrence of strong positive correlation coefficients over the whole year is given in percent in figure 2.23c. This even more indicates the strong mixing further east between both water masses which shows a significant peak value upstream of the Bornholm Channel where during 5% of the year R has been in the order of 0.75. Increased correlation coefficients are additionally found on a south-west north-east directed area in the Central Arkona Basin where interaction between both water masses is strongest as the two plume fronts interact east of Kriegers Falk (see e.g. figure 2.19h, i). High positive correlation coefficients are also found east of the isle of Rügen (during less than 2% of the year, figure 2.23c), which may be due to a single event where thin layers of dense Drogden Sill and Darss Sill water where pushed into this area.

The anti-correlation on the other hand even shows significantly higher values with $R > 0.8$ over large

areas of the western Baltic Sea (figure 2.23b). Combined with the result shown in figure 2.23d (showing how often high anti-correlation coefficients occur over the year given in percent), it is demonstrated that negative correlations, indicating strong separation (interleaving) of water masses, are substantially stronger distributed over the year with about $18 - 27\%$ within the investigated period than positive correlation coefficients occurring during less than 5% of the year. Notable is the significant peak in the central Arkona Basin where anti-correlation of $R > 0.8$ has been found during 27% of the year. The reason for this strong interleaving is very likely due to the fact that whenever both inflows are comparably strong, both plume fronts at the very first time meet in this area, see for example snapshots of Darss Sill and Drogden Sill bottom tracer concentrations in May 2005 (figure 2.19h,i), with corresponding shift of more saline Drogden Sill water below slightly lighter Darss Sill water masses (see figure 2.24b, d), resulting in the mentioned three layer stratification with corresponding high anti-correlation coefficients of Drogden Sill and Darss Sill passive tracer profiles.

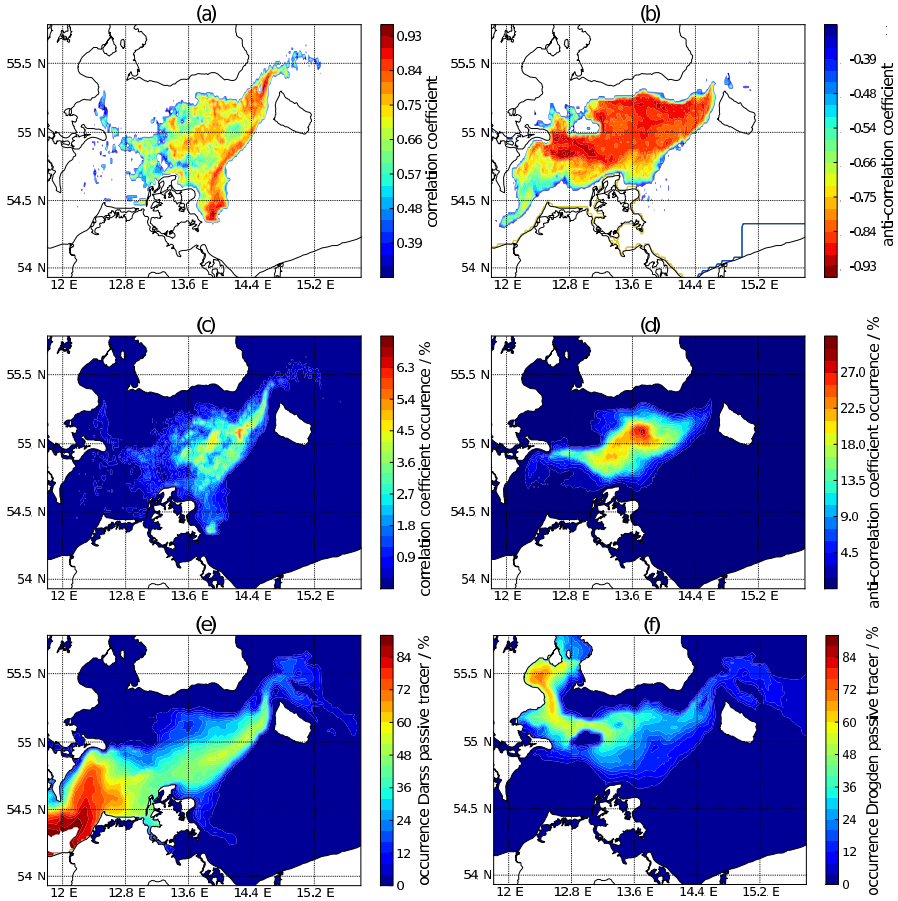

Figure 2.23: The above statistical results were obtained by calculating the correlation coefficient between the vertical profiles of Darss Sill and Drogden Sill passive tracer concentrations over the whole domain. The conditions behind this calculation are that the maximum tracer concentration found in each water column should be $c_{max} > 4.0$ for both tracers at the same time and the correlation coefficient must be higher than 0.5 or accordingly less than -0.5 for anti-correlation. (a) Mean (positive) correlation found and (b) mean anti-correlation coefficient over the 12 month period in 2005. Lower panels showing how often the condition ($c_{max} > 4.0$, correlation coefficient higher than 0.5 or anti-correlation less than -0.5) occurred over the 12 month period for (c) positive correlation (potentially well mixed tracers) and (d) negative correlation (comparably strong interleaving of Darss and Drogden Sill plumes).

A calculation of annual mean passive tracer concentrations and salinities during inflow conditions reveals that higher concentrations of Darss Sill water are found on the southern rim of the Arkona Basin (figure 2.24a, b) and higher concentrations of Drogden Sill water in the central and northern part of the Arkona Basin. However, both water masses from Drogden Sill and Darss Sill show a geostrophic alignment as also found by observations and model simulations in the 10 km wide channel north of Kriegers Flak (Burchard et al. (2005), figure 2.24). Even in annual mean Darss Sill passive tracer concentrations it is found that the denser water originating from Drogden Sill is uplifting Darss Sill water masses. This feature is exceptionally strong when calculating the mean of Darss Sill and Drogden Sill passive tracer concentrations over the period of the inflow in November and December 2005 only (figure 2.24b, d). As figure 2.24b has even been calculated on a full two month basis (November+December 2005), which might include several peak values in salinity, the following main features are still persistent: (i) water from the Darss Sill has lower density than the water from Drogden Sill and is hence found with highest bottom concentrations 10 m above the sea bed whereas the Drogden Sill water is shifted below Darss Sill water, (ii) highest concentrations of Drogden Sill water is found in the central and the northern part of the Arkona Basin and (iii) highest bottom concentrations of Darss Sill water is found on the southern rim of the Arkona Basin whereas all panels in figure 2.24 show the geostrophic alignment with the pinching of isolines of density in the northern part and spreading in the southern part. This has been investigated in detail for an observed dense bottom current north of Kriegers Flak by Umlauf et al. (2007) and has its origin in transversal dynamics driven by the alignment of isopycnals in current flow direction inducing a secondary transversal circulation.
In order to quantify the amount of physical mixing for each of the flows from Darss Sill and Drogden Sill separately, figure 2.25 shows model-derived values of volume-integrated physical tracer mixing in early 2005 compared to absolute wind speed at Arkona buoy. As both water masses are suspect to different amounts of physical mixing due to their different pathways, it is found that both water masses obviously show different values (lower mixing for Drogden Sill water masses due to lower transport capacity) but a similar frequency with a high correlation coefficient between both time series ($R = 0.95$). This indicates that mixing is heavily wind influenced inducing several direct and indirect mixing processes as there are e.g. (i) increased vertical shear acting against stratification, (ii) boundary mixing (Ocean: Ledwell et al. (2000); Lake: Wüest and Lorke (2003)), (iii) differential advection, (iv) coastal upwelling (Fennel and Seifert (1995)), (v) internal wave generation (see Garrett and Munk (1975), Polzin et al. (1995) for models of internal wave field; see Lass and Mohrholz (2003) for a discussion of observed internal waves and mixing in the Baltic Sea) and their dissipation into turbulent mixing, (vi) vertical mixing due to mesoscale Baltic eddies ('Beddies', see Reissmann et al. (2009)) and (vii) convective entrainment. The strength and contribution of the above mentioned mixing processes to the total mixing on the stratified flow in the Baltic Sea is not yet fully understood and quantified. Internal waves for instance could potentially lead to boundary mixing, differential advection and wave breaking and corresponding knowledge on the individual contribution of each of the processes to the total turbulent mixing is rather poor. However, two ongoing PhD projects at the IOW (Leibniz Institute for Baltic Sea Research Warnemünde) investigate internal wave mixing (ILWAO project, `www.io-warnemuende.de/copps-projects/articles/ILWAO.html`) and boundary mixing (BatRE project, `www.io-warnemuende.de/batre.html`) in the Baltic Sea. An overview of the

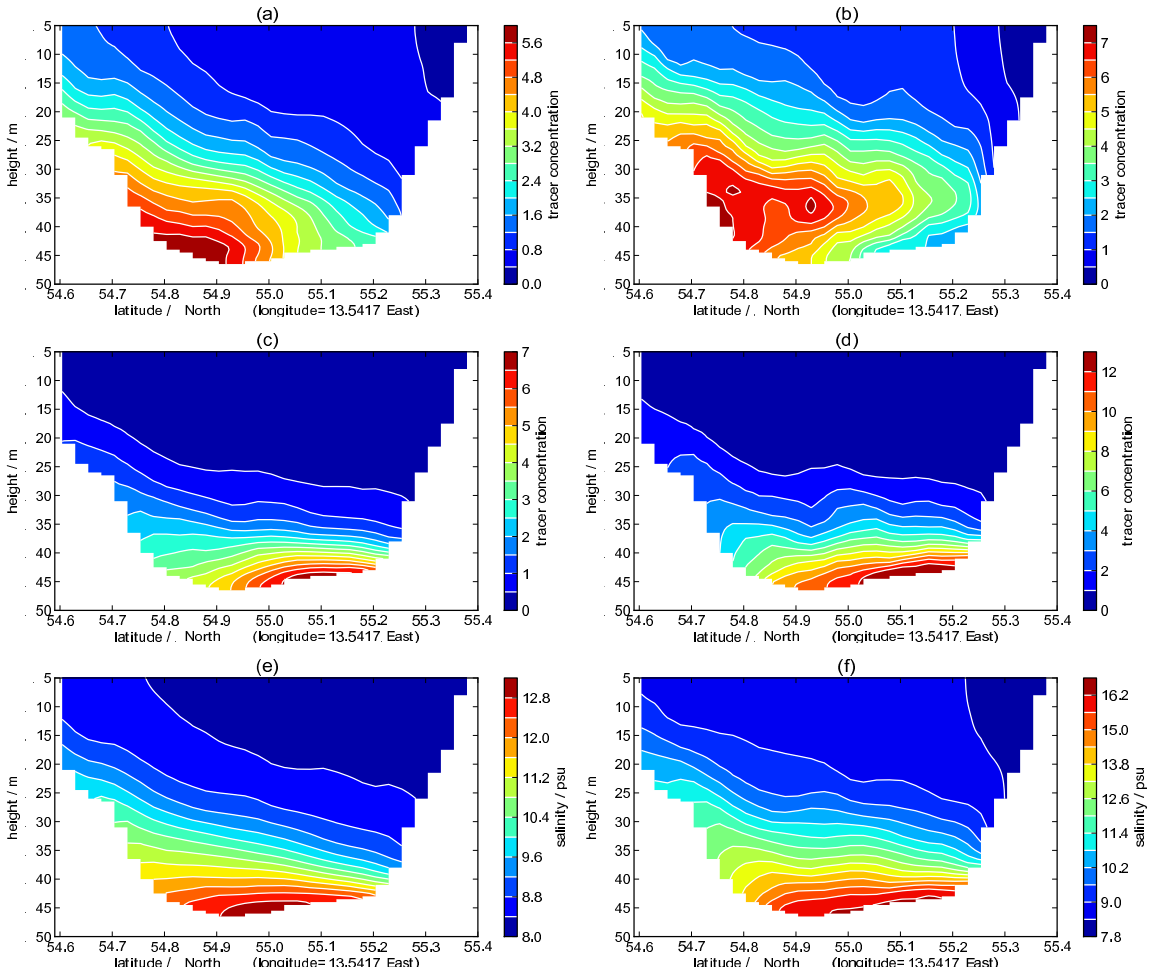

Figure 2.24: (a) Annual mean Darss passive tracer concentration and (b) mean Darss passive tracer during observed inflow in November/December 2005. (c) and (d) showing the corresponding mean Drogden Sill tracer concentrations. (e) and (f) the corresponding mean salinities. Note the different range in the colormaps.

vertical mixing processes and their individual contribution in the Baltic Sea is given in the work of Reissmann et al. (2009). As the three main mixing processes in the Western Baltic Sea, Lass and Mohrholz (2003) identified the wind-induced mixing at the shallow sills, differential advection at the plume front and shear-induced entrainment. As barotropic gradients due to wind forces are the main driver of barotropic Baltic Sea inflow events (see section 1.1.4), also the observed absolute value of the wind speed at the Arkona buoy (10m height) is plotted in figure 2.25 which highly correlates with the volume integrated measures of physical mixing of the passive tracers. The correlation coefficient between observed absolute wind speed and each of the two volume-integrated mixing values of Darss Sill and Drogden Sill water masses has a same value of $R = 0.65$, which demonstrates that wind-induced mixing induces a similar impact of the different mixing processes on both Darss Sill and Drogden Sill plumes.

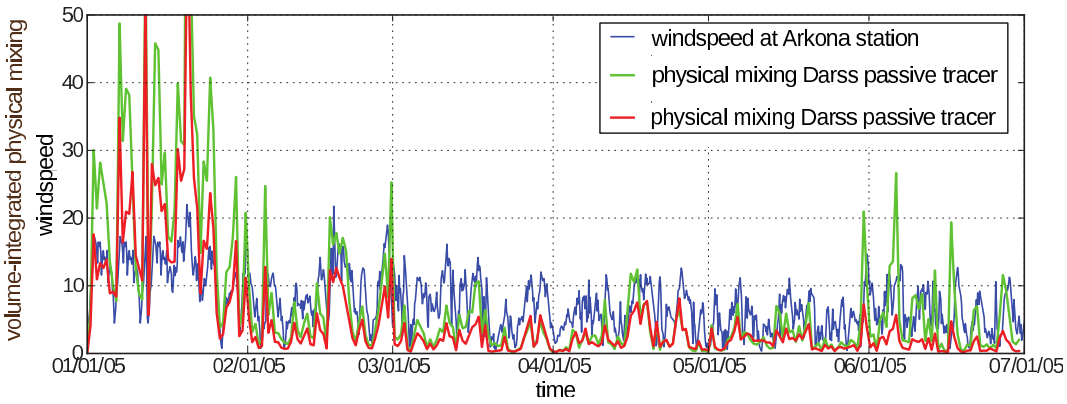

Figure 2.25: Observed absolute wind speed at Arkona buoy (10 m height) in early 2005 versus volume-integrated mixing ($2\nu_t^S(\partial S/\partial z)^2$) for Darss Sill and Drogden Sill plume separately. High values in volume integrated tracer variance decay in January 2005 are due to strong wind fields together with strong fluctuations in the wind directions (not shown here) inducing a number of different physical mixing processes (e.g. boundary mixing, differential advection, coastal upwelling) with significantly increasing the vertical turbulent mixing and entrainment. That the physical mixing in this area has been very effective can be seen for example in figure 2.26 for the January 2005 inflow event. Surprisingly this inflow event seems to have been mixed so strong that dense bottom water did not even enter the Bornholm Channel.

2.4.6 Spreading times of Drogden Sill and Darss Sill plume into the Western Baltic Sea

In order to obtain spreading times of dense bottom currents into the Arkona Sea, it is helpful to use the two passive tracers included in the realistic model setup. A correlation of salinity time series in the Arkona Sea with time series from Darss sill contains inconsistencies as it is hard to separate the signal from the Drogden Sill water masses which will very likely be included in the salinity signal (see discussion in section 2.4.4 based on correlations north and south of Kriegers Flak). Hence the correlation of passive tracer time series gives a better representation of individual spreading times and behavior from Drogden Sill and Darss Sill water masses separately.

None the less it needs to be considered that the dynamics of mixing and the corresponding spreading behavior of the dense bottom currents are potentially highly variable. For the plume propagation between Drogden Sill and Kriegers Flak Sellschopp et al. (2006) estimated an entrainment velocity (see equation 1.1) of $3\text{x}10^{-6}$ m/s based on assuming simple mass conservation. Arneborg et al. (2007) obtained an entrainment velocity of $3.75\text{x}10^{-5}$ when observed plume properties north of Kriegers Flak are inserted into their entrainment equation which is almost an order of magnitude higher than the estimates by Sellschopp et al. (2006). This indicates a high variability in turbulent mixing and supports the picture of the western Baltic Sea as physically very active area and as such a hot spot of water mass transformation with almost unpredictable values of turbulent mixing and spreading behavior due to different intensities of the individual inflows and the ignorance of the exact plume frequency crossing the sills. This section tries to give answers about spreading times in the Western Baltic Sea which could even be validated with the help of long-term observations.

Within the previous sections it was demonstrated that the strength of the inflows crossing Darss and Drogden Sill and the position of corresponding plume fronts varies significantly. This will very likely produce a huge amount of different flow characteristics in the central Arkona Sea. However, the

propagation time of the high saline Drogden Sill plume which shifts below slightly lighter Darss Sill water (see figure 2.24b, d) may be less influenced than Darss Sill water masses and hence probably show a characteristic propagation velocity from Drogden Sill at least until they reach Kriegers Flak. A method on how to obtain whether a characteristic propagation velocity for Drogden Sill can be derived is a Hovmöller diagram as shown by figure 2.26 of Darss Sill and Drogden Sill bottom tracer concentrations along tracks from each of the sills until the entrance of the Bornholm Channel (see tracks in figure 2.1). It seems that Drogden Sill plumes underly a well defined propagation velocity. A closer investigation revealed that the propagation times from the start until the end of the track differ from 13 days until up to 27 days. The spreading time of dense currents during the major Baltic inflow event in January 2003 has been found to be about 12 days from the Sills to the Bornholm Deep (Feistel et al. (2003a), Piechura and Beszczyińska-Möller (2003)) which is faster than model derived spreading times of medium intensity inflow events in this thesis due to higher salinities and higher transport capacity of major Baltic inflows. However Lass and Mohrholz (2003) obtained with the help of observations during small and medium-strength inflows in November and December 1998 and in August/September 2002 (Mohrholz et al. (2006)) a spreading time of about 12 days between Drogden Sill and and the Bornholm Channel which agrees with the model derived propagation time of 13 days of the Drogden Sill plume in November 2005 as shown in figure 2.26. For this comparably strong inflow event in November 2005 the plume reached significantly higher mean propagation velocities of more than 0.55 m/s on the section due to comparably high saline water as well as due to obviously persistent wind fields (forcing of this individual inflow event not further investigated). The inflow in September 2005 (see lower panel in figure 2.26) reveals that the Drogden Sill plume has been added to the bottom pool of dense water in the central Arkona Basin to be partly pushed back and finally slowly being advected through the Bornholm Channel. The horizontal lines at about 30, 40 and 80 km of the Drogden Sill track are due to decreased water depth on the track extracted which is not exactly on the main pathway of those dense bottom currents and hence represented by lower concentrations.
The Hovmöller diagram of the Darss Sill passive tracer on the other hand reveals a similar picture of almost unpredictable spreading behavior and propagation velocity. At 80 km of the section, the passive tracer even suddenly disappears which is due to the shift of Drogden Sill water below Darss Sill water as shown in figure 2.24. However, there are at least three inflows for which their signals are significant all over the section. Even here, the propagation on the whole section underlies a high variability with sudden jumps in the time-series. Still, propagation times between 13 days and 27 days are found with propagation velocities of $0.22 - 0.29$ m/s which are significantly lower as found for Drogden Sill water masses. This is basically due to higher salinities of Drogden Sill water masses and because Darss Sill water is primarily lifted and interleaved in the Arkona Basin above denser Drogden Sill water.
Figure 2.28 shows some examples of cross-correlations obtained via bottom passive tracer and bottom salinity time series at Drogden Sill, Kriegers Flak Nord (KFN) and Kriegers Flak South (KFS) using model results in 2005 and observations between Jan, 1 2005 and Jan,1 2007 (Drogden Sill) and for the KFN and KFS moorings observations in 2006 are used to be compared with model results. Figure 2.27 shows these observations, where it is demonstrated that both KFN and KFS observations are only available in 2006 at the same time. However, with the help of figure 2.27c it must be pointed out that the observations also show partly higher salinities south of Drogden Sill indicating the potential

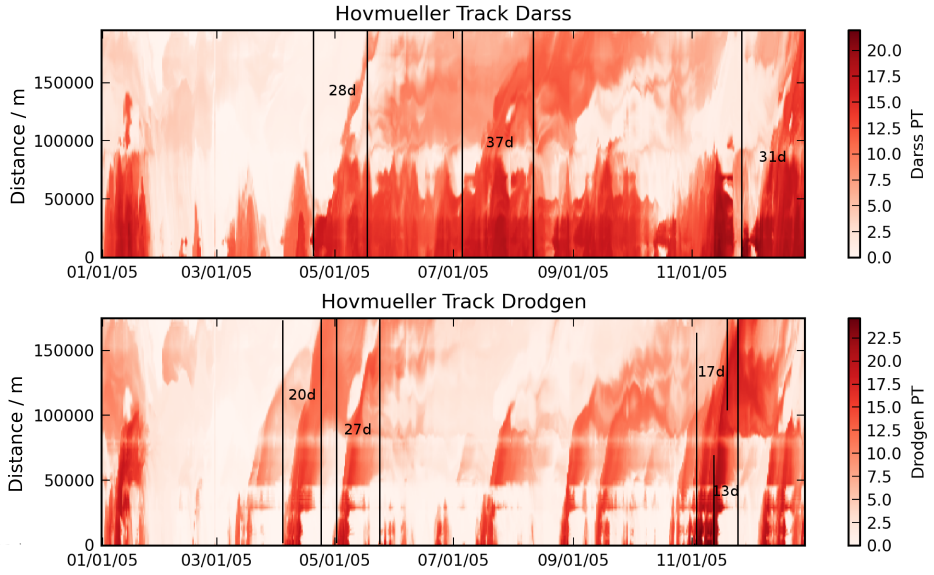

Figure 2.26: Panels showing Hovmöller diagrams of bottom tracer concentrations versus track length from Darss Sill and Drogden Sill to the entrance of the Bornholm Channel. With the help of the above figures spreading times for Darss Sill and Drogden Sill water masses can be estimated by the numerical model. For Darss Sill water masses spreading times between 28 and 37 days are found and 13-27 days for Drogden Sill water masses respectively.

influence of Darss Sill water masses which has also been found by the model simulations and shown in section 2.4.4 via comparing modelled salinities and modelled passive tracers south of Kriegers Flak. Figure 2.28a proves the good agreement between modelled and observed spreading time between Drogden Sill (4.29 days) and KFN (5.4 days) with a correlation coefficient of $R = 0.55$ for the observations and $R = 0.72$ for the model derived spreading time. The difference between modelled and observed spreading time can have a number of different reasons as there are e.g. (i) model period covers the year 2005 and observations mainly 2006 (Nov 16, 2005 until August 15, 2006 where both KFN and KFN were available) including a number of comparably different strength of inflows, (ii) several pulses of inflowing dense water across Darss Sill are notable at Drogden Sill but have merged and influenced each other south of Drogden Sill resulting in a different signal at KFN, (iii) peak values of plume salinities are underestimated by the model resulting in lower propagation velocities (see e.g. bottom salinity in figure 2.8).

Figure 2.28b compares the cross correlation north and south of Kriegers Flak (KFN, KFS) using observations and the numerical model. The model overestimates the time shift between water masses passing the northern and southern trench of Kriegers Flak by about 0.9 days. Reasons for the overestimation might be (i) an incorrect reproduction of the plume thickness leading to lower dense bottom water transport along the western and southern trench of Kriegers Flak which again leads to lower propagation velocities at KFS, (ii) a partly incorrect bathymetry not correctly resolving the channels around Kriegers Flak due to the horizontally restricted resolution of about 1 km or (iii) the different period where both KFN and KFS observations were fully available for (Feb 05, 2006 until June 09, 2007) leading to different statistical results because of inflows with different intensities in the investigated periods.

Cross correlating the signals of the Darss passive tracer at Arkona station and the Drogden passive tracer at KFN is shown in figure 2.28c compared to the result based on observations of bottom salinity. Based on this it is found that Darss Sill water masses arrive about 7.0 days (model derived) or 5.57 days (obtained by observations) later at Arkona station than Drogden Sill plumes arrive at KFN. It may be that the observed salinity signal at Arkona station is modified by Drogden Sill water. However, the reasonably well agreement between model and observations indicate that, as already shown in previous sections, Darss Sill water masses contribute mainly to the stratification at Arkona buoy. Furthermore it must be pointed out that the correlation coefficients are comparably low (figure 2.28c) and correlation coefficients with values higher than R = 0.45 are found for time shifts in the range of about 5-10 days.

Figure 2.28d compares the different results in cross-correlations obtained using bottom time-series of passive tracers and modelled salinities between KFN and KFS. Obvious is the delay of the salinity signal by about half a day and the higher correlation coefficient using the passive tracers. This is mainly because bottom salinities from both origins (Drogden Sill and Darss Sill) are found south of Kriegers Flak (see section 2.4.4) influencing the cross correlation between KFN and KFS.

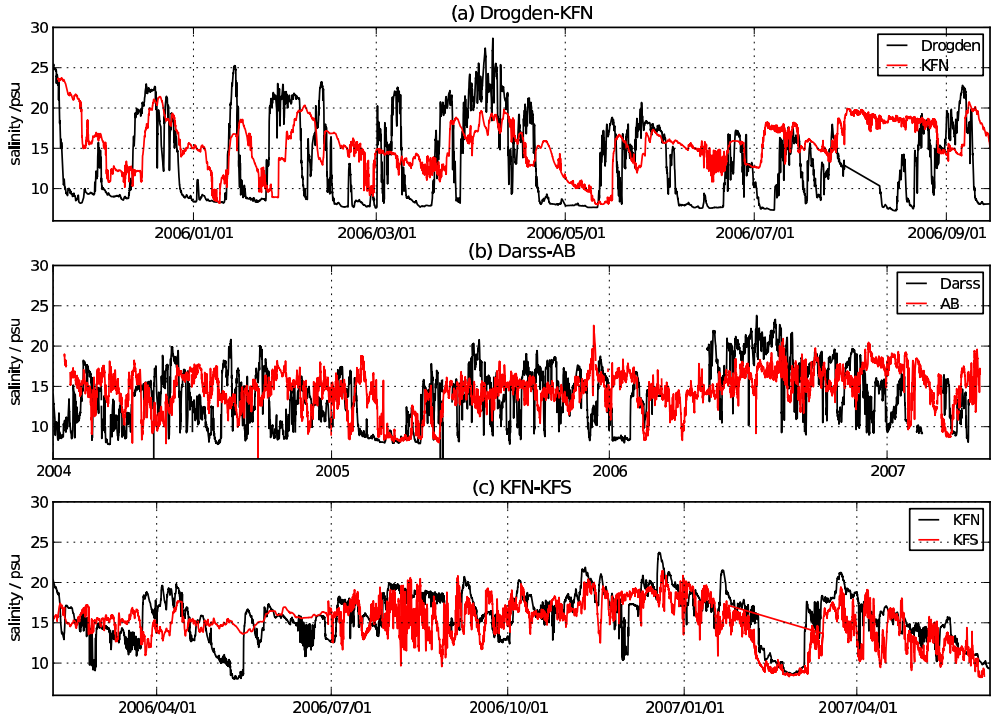

Figure 2.27: Panels showing moorings north and south of Kriegers Flak and Drogden Sill which cover most of the year 2006 and have been used to validate the numerical model concerning spreading behavior of dense bottom currents. Each panel shows the period where data for both stations/mooring is available. Unfortunately the observations north and south of Kriegers Flak do not cover the model period of the year 2005. However the observed time series of bottom salinity reveal that the impact of Darss Sill water masses south of Kriegers Flak is grooved also by observations as salinities south of Kriegers Flak are partly higher than north of Kriegers Flak.

Figure 2.29 shows spreading times in the Western Baltic Sea obtained via cross-correlations (see examples in figure 2.28) of several different positions investigating the Drogden Sill and the Darss Sill water masses separately (green: Drogden Sill water masses; blue: Darss Sill water masses). Most time

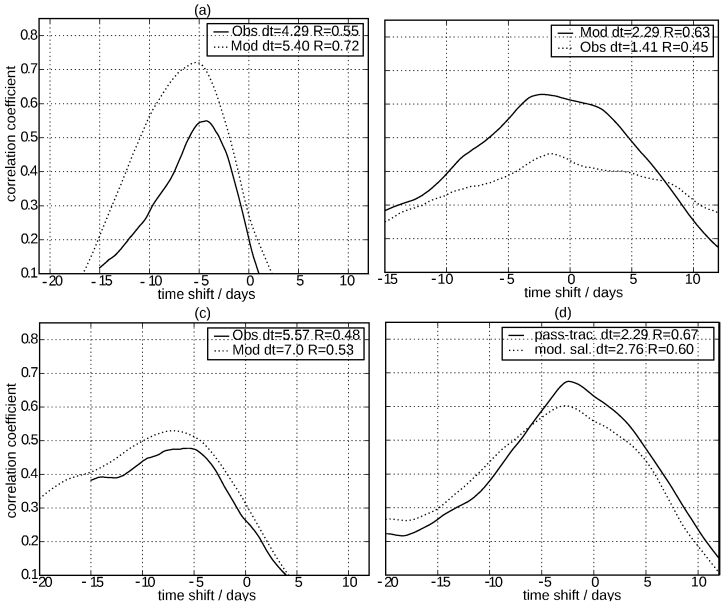

Figure 2.28: Examples showing the cross-correlation derived via comparing bottom passive tracer and bottom salinity time-series at Drogden Sill, KFN and KFS using model results and observations. (a) Cross correlation of Drogden Sill and KFN time-series using the Drogden Sill passive tracer in the model and bottom salinities in the observations, (b) Cross correlation of KFN and KFS time-series using the Drogden Sill passive tracer in the model and bottom salinities in the observations, (c) purely model derived cross correlations based on the Drogden Sill passive tracer and model salinity and (d) compares the different results in cross-correlations obtained using bottom time-series of passive tracers and modelled salinities between KFN and KFS.

shifts derived with the cross-correlations show relatively high correlation coefficients of $R > 0.7$. Maximum correlation coefficients between Darss Sill and Drogden Sill water masses in the central Arkona Basin have been found by time shifts of more than 70 days - which are certainly unrealistic statistical estimates, especially regarding the relatively low number of inflow events included in one year - with corresponding low correlation coefficients (indicated by (*) in figure 2.29). Furthermore (*) indicates that several peak values in the cross-correlations have been found with similar correlation coefficients where no significant spreading time could be derived. The spreading times obtained west of the Arkona Basin are reliable realistic estimations with comparably high correlation coefficients especially for the Drogden Sill plume (e.g. figure 2.28a) which is very much restricted to the shape of the bathymetry with underwater channels, which is in contrast to the broad transition area of the Darss Sill area where the horizontal distribution of salinity gradients may strongly vary between each individual inflow event. Time shifts derived via cross correlation in the central Arkona Basin must be taken with care due to the broader transition area, slower velocities, small bottom slopes, the significant impact of the wind fields indicating strong fluctuations in the tracer fields in the Arkona Basin as seen in the Hovmöller plot (figure 2.26) and strong interleaving of Darss Sill and Drogden Sill water masses in the Central Arkona Basin as shown in figure 2.23. Also the flow of dense bottom water out of the Arkona Sea is, at first order, restricted to the transport capacity through the Bornholm Channel. However, the result as shown earlier in figure 2.26 is potentially being influenced by older water masses in the Arkona Basin, which are pushed eastward by new inflow events and hence may influence the signal in bottom time series and the dynamics in the Arkona Basin. A not expected feature is the unrealistic high

propagation speed from south-east of the Darss Sill station to the Darss Sill station which is less than two days from DS1 to DS. This can be explained with the help of figure 2.18a showing the annual mean Darss Sill passive tracer concentrations at the bottom in 2005. In the area of the Darss Sill comparably high passive tracer concentrations can be found which is not visible south of Drogden Sill. The reason is that the fronts of dense bottom water is continuously pushed back and forward due to the influence of wind fields but it not always successfully entering the Central Arkona Sea. Hence the different positions of the plume fronts significantly influence the results of the cross correlations in this area leading to unrealistically high propagation velocities (e.g. DS1→DS3; DS1→DS2; DS2→DS in figure 2.29). Again this issue reveals how difficult it is to draw very general conclusions about spreading behavior in this area. The extracted positions in figure 2.29 are partly positions from permanent stations (Drogden Sill, Darss Sill, Arkona Station) and moorings in the year 2006 (KFN, KFS) but also several others obtained with the help of figure 2.18 revealing main pathways of the dense bottom plumes.

More detailed investigation of figure 2.29 (and figure 2.28a) reveals that, based on observations in 2006, the plume from Drogden Sill travels in about 4.29 days to the northern trench of Kriegers Flak. This is in contrast to the numerical model result, predicting a propagation time of about 5.46 days with a corresponding correlation coefficient of $R = 0.72$ (observations: $R = 0.55$). As expected the cross-correlation between time-series of positions with shorter distance is significantly higher (e.g. DR→DRS: $R = 0.83$; DRS→KFNE: $R = 0.85$, see white panel in figure 2.29) because the salinity signal is less distorted due to turbulent mixing and entrainment. A further example of this result is comparing the stepwise correlations DS→RG1, RG1→AB, AB→A3, A3→B1, B1→B2 which result in correlation coefficients between $R = 0.71$ and $R = 0.91$ compared to directly correlating DS→B2 which results in a significantly lower value of $R = 0.46$ because the signal of the bottom tracer concentrations (or salinities) between two positions which are far away from each other has already been smoothed and modified due to a number of different mixing processes. A comparison between time shifts using salinity (observations) bottom time-series at Arkona Station with either Darss Sill or Drogden Sill station salinities gives low correlation coefficients (KFN→AB: $R = 0.48$; DS→KFS: $R < 0.5$) and more than one maxima in the cross correlation (see e.g. DS→KFS). Even the use of the passive tracers in the numerical model results in rather low correlation coefficients (KFN→AB: $R = 0.34$; DS→AB: $R = 0.57$; KFS→AB: $R = 0.41$). The cross-correlation between KFS and AB even revealed positive and negative time shifts as presented in the white box in figure 2.29. A reason may be that old Arkona Sea bottom water potentially influenced the signal at Arkona Station. Additionally no significant individual time shift between DR→AB and DS→KFS could be obtained by the model as the cross correlation results in several maxima with low values in correlation coefficients (marked by a (*)). However, with the help of figure 2.29 the model predicts propagation times of about 20 days from both tracer release positions to the Bornholm Channel (DR→B2, DS1→B2). The spreading time from west to east across the Central Arkona Basin is in the order of about 10 days.

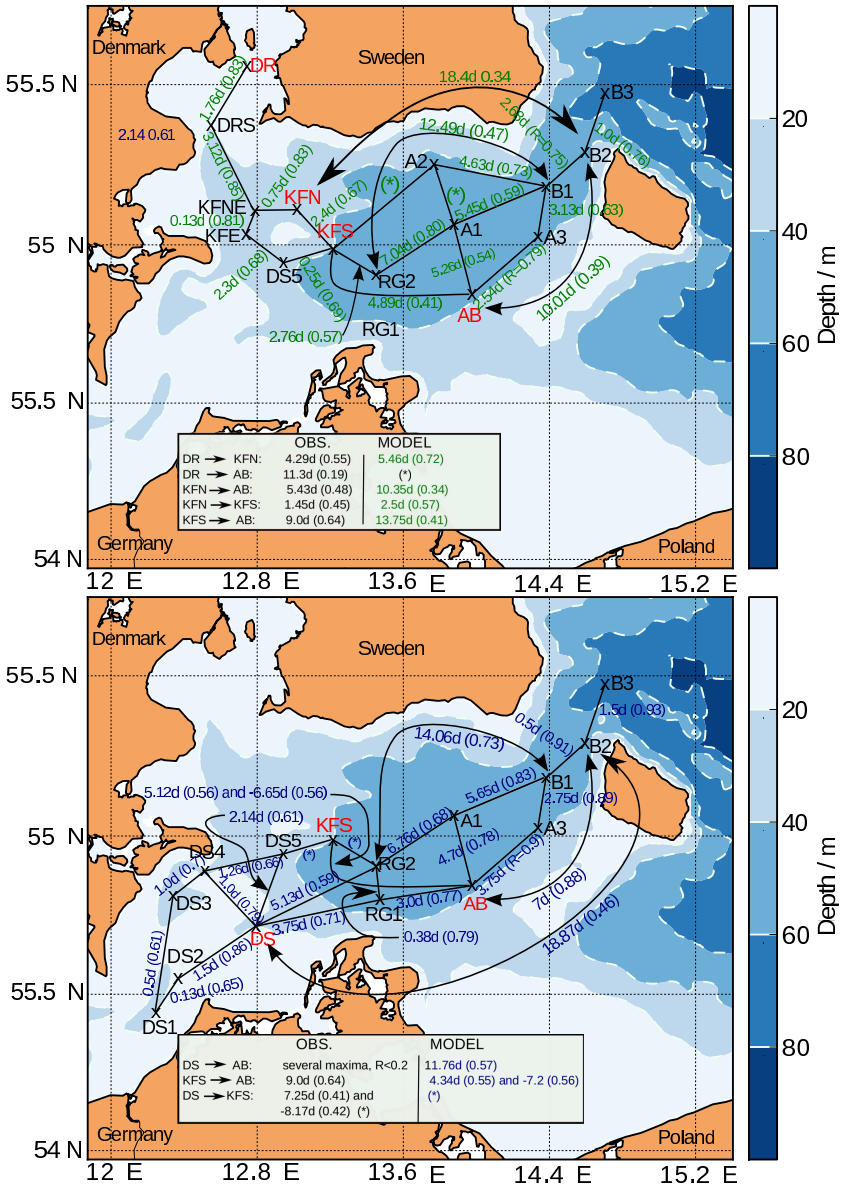

Figure 2.29: Estimated spreading times (in days) of Drogden Sill (upper panel) and Darss Sill (lower panel) dense bottom currents into the central Arkona Basin. The time shift in days is given as the first value together with the correlation coefficient in brackets. The '(*)' means that the cross-correlation has revealed unrealistically high time shift values of more than 70 days in combination with low correlation coefficients ($R < 0.3$). The same holds for Darss Sill water masses in the northern Arkona Basin, especially when trying to obtain significant correlations in the northern Arkona Basin (e.g. A1→A2) which is almost impossible at least for the investigated period in 2005. The geographical positions are as follows: DS-12.7°E-54.709°N (Darss Sill station), DS1-12.21°E-54.45°N, DS2-12.39°E-54.53°N, DS3-12.39°E-54.78°N, DS4-12.52°E-54.89°N, DS5-12.525°E-55.33°N, DR-12.711°E-55.535°N (Drogden Sill station), DRS-12.99°E-54.93°N, KFN-13.006°E-55.119°N (Kriegers Flak North mooring in 2006), KFS-54.98°E-13.2°N (Kriegers Flak South mooring in 2006), KFE-12.74°E-55.01°N, KFNE-12.825°E-55.088°N, RG1-13.46°E-54.79°N, RG2-13.41°E-54.89°N, AB-13.867°E-54.832°N (Arkona Station), A1-13.78°E-55.06°N, A2-13.74°E-55.214°N, A3-14.258°E-55.029°N, B1-14.3°E-55.18°N, B2-14.55°E-55.275°N, B3-14.692°E-55.43°N

2.4.7 Regional estimates of turbulent mixing

In the following a bulk measure of physically induced mixing in the numerical model is derived and discussed as presented in the work of Burchard et al. (2009). This measure based is based on the tracer variance decay (e.g. of temperature and salinity) and is later in this work directly being compared to numerically induced mixing (3).
Since salt mixing occurs on the micro-scale, we have to consider the molecular salinity equation which is valid down to these small scales:

$$\partial_t S + v_j \partial_j S - \nu^S \partial_{jj} S = 0, \tag{2.2}$$

with the salinity S, the velocity vector $v_1 = u$, $v_2 = v$ and $v_3 = w$, the coordinates $x_1 = x$, $x_2 = y$, and $x_3 = z$ (upward looking) and the molecular diffusivity $\nu^S \approx 10^{-9}$ m^{2}s^{-1}. In (2.2), we use $j = 1, \ldots, 3$, $\partial_j = \partial/\partial_{x_j}$ and the summation convention due to which terms with double occurrence of indices are summed over these indices. The three terms in (2.2) are the time derivative, the advection and the molecular diffusion of salt, respectively.
When applying the Reynolds decomposition of all state variables into an ensemble averaged (denoted by an overbar) and a fluctuating part (denoted by a prime), i.e. $u = \bar{u} + u'$, the following equation is obtained for the ensemble averaged salinity $\bar{S}$:

$$\partial_t \bar{S} + \bar{v}_j \partial_j \bar{S} + \partial_j \overline{v'_j S'} - \nu^S \partial_{jj} \bar{S} = 0, \tag{2.3}$$

with the turbulent salt flux $\overline{v'_j S'}$.
When applying the shallow water approximation and the eddy viscosity assumption and neglecting the molecular diffusivity which is typically some orders of magnitude smaller than the eddy diffusivity ν_t^S, the following dynamic equation for the ensemble averaged salinity is obtained:

$$\partial_t \bar{S} + \bar{v}_j \partial_j \bar{S} - \partial_z \left(\nu_t^S \partial_z \bar{S} \right) = 0. \tag{2.4}$$

In (2.4), the vertical turbulent salt flux has been parameterised by means of the down-gradient approximation, which is the basis of the eddy viscosity assumption:

$$\overline{w' S'} = -\nu_t^S \partial_z \bar{S}. \tag{2.5}$$

Horizontal mixing is not considered here, since in the present high-resolution application mesoscale dynamics which dissipate geostrophic turbulence are resolved by the model. Horizontal dispersion is represented in a realistic way by the interaction of vertical shear and vertical mixing.
With the same assumptions, a dynamic equation for the variance of the salinity fluctuations can be derived (see Burchard (2002) for details):

$$\partial_t \overline{S'^2} + \bar{v}_j \partial_j \overline{S'^2} + \partial_z F_z(\overline{S'^2}) = 2\nu_t^S (\partial_z \bar{S})^2 - 2\nu^S \overline{(\partial_j S')^2}, \tag{2.6}$$

with the vertical flux of salinity variance, $F_z(\overline{S'^2})$, the salinity variance production, $P_S = 2\nu_t^S (\partial_z \bar{S})^2$ and

the salinity variance dissipation, $\varepsilon_S = 2\nu^S\overline{(\partial_j S')^2}$ the latter of which show a remarkable similarity with P_S being based on eddy diffusivity and ensemble averaged gradients and ε_S being based on molecular diffusivity and micro-structure gradients.

In this context, it is instructive to study the resulting dynamic equation for the variance of the ensemble averaged salinity. Assuming for a moment a closed model domain without lateral open boundaries, and considering zero salt and freshwater flux through the sea surface and bed, the volume averaged salinity S_m is a constant in time and space. With this, (2.4) may be transformed to a transport equation for vertically integrated salinity variance

$$\bar{\sigma}^2 = \int_{-H}^{\eta} (\bar{S} - S_m)^2 \mathrm{d}z \tag{2.7}$$

with the bottom coordinate H and the surface elevation η. With this definition, a transport equation for the vertically integrated salinity variance can be derived:

$$\partial_t \bar{\sigma}^2 + \partial_x F_x\left(\bar{\sigma}^2\right) + \partial_y F_y\left(\bar{\sigma}^2\right) = -2\int_{-H}^{\eta} \nu_t^S (\partial_z \bar{S})^2 \mathrm{d}z \tag{2.8}$$

with the horizontal advective fluxes

$$F_x\left(\bar{\sigma}^2\right) = \int_{-H}^{\eta} u(\bar{S} - S_m)^2 \mathrm{d}z, \quad F_y\left(\bar{\sigma}^2\right) = \int_{-H}^{\eta} v(\bar{S} - S_m)^2 \mathrm{d}z. \tag{2.9}$$

Equation (2.8) has been obtained from (2.4) by first replacing S by $(S - \bar{S})$ (which is possible since $\bar{S}$ is a constant), then multiplying the resulting equation by $2(S - \bar{S})$ and finally integrating the whole equation vertically. With the standard kinematic boundary conditions, the Leibniz rule for integration over variable integration bounds and the no-flux conditions for salt and freshwater at bottom and surface, (2.8) is finally derived.

A comparison between equations (2.6) and (2.8) shows that the vertically integrated production term of salt fluctuation variance is identical to the decay term of the variance of ensemble averaged salinity. Since for stable stratification, the small-scale salinity variance equation is close to equilibrium (see e.g. the discussion by Umlauf and Burchard (2005)), i.e. the left hand side of (2.6) is negligible, production and dissipation of $\overline{S'^2}$ are close to each other. Therefore, the decay of $\bar{\sigma}^2$,

$$P_T^{int} = 2\int_{-H}^{\eta} \nu_t^S (\partial_z \bar{S})^2 \mathrm{d}z \tag{2.10}$$

which is a non-negative term, typically equals the salt variance dissipation and is a suitable measure for vertical mixing. Full vertical mixing is reached for zero salinity variance, with the consequence of zero vertical salinity gradients and thus zero salinity variance decay. For unstable stratification however, the right hand side of (2.6) is not in balance and the transport terms on the left hand side play a major role. For model simulations with explicit horizontal diffusion of salt, also horizontal salinity gradients would contribute to the decay of salinity variance.

In contrast to the decay of salinity variance, the vertically integrated turbulent salt flux $-\int \nu_t^S \partial_z \bar{S} \mathrm{d}z$ is a measure for the potential energy gain due to turbulent mixing. This can be clearly seen for a linear

equation of state, where $\bar{S}$ is proportional to density $\bar{\rho}$ for which we obtain:

$$\begin{aligned}\partial_t \int_{-H}^{\eta} (gz\bar{\rho})\,\mathrm{d}z \propto \partial_t \int_{-H}^{\eta} \left(z\bar{S}\right)\mathrm{d}z = \partial_t \left(\frac{\eta^2}{2}\right)\bar{S}\,(\eta) \\ -\partial_x \int_{-H}^{\eta} \left(\bar{u}z\bar{S}\right)\mathrm{d}z - \partial_y \int_{-H}^{\eta} \left(\bar{v}z\bar{S}\right)\mathrm{d}z + \int_{-H}^{\eta} \bar{w}\bar{S}\mathrm{d}z - \int_{-H}^{\eta} \nu_t^S \partial_z \bar{S}\mathrm{d}z,\end{aligned} \tag{2.11}$$

where the last two terms on the right hand side are proportional to sources of potential energy due to vertical salt advection and vertical turbulent salt flux. The latter is however not a fully consistent estimate for turbulent mixing, since it may consist of positive or negative contributions, depending on the sign of the vertical salt gradient, such that convective mixing would counteract to mixing of stably stratified water.

For the present model study with open lateral boundaries and surface freshwater fluxes the spatially averaged salinity S_m would be time dependent and fluxes of variance through the surface would be present, such that in (2.8) additional terms would be required. It can however be seen that the decay of salt variance is exactly the decay of $\int(\bar{S}-S_0)^2\mathrm{d}z$ with any constant reference salinity S_0. Therefore, it is a suitable measure for turbulent salt mixing also for studies with lateral and vertical salt and freshwater fluxes.

In figure 2.30, the decadal logarithm of the vertically integrated decay of salinity variance and the vertically integrated upward turbulent salt flux are shown as averages over the whole nine-month model simulation period. With this, areas of generally strong mixing in the Western Baltic Sea can be identified. It can be seen from both measures that highest values occur on Drogden Sill, Darss Sill and in the Bornholm Channel as well as north-west of the island of Rügen. Furthermore, the complete dense water pathways from the sills at Drogden and Darss into the Arkona Basin are characterised by strong mixing. Levels of elevated mixing are also observed north-east of Kriegers Flak, the area covered by the dense bottom current observations shown in figure 2.17. For that cross-section, figure 2.31 shows the two mixing parameters as snapshots at the same time as salinity and current velocity are shown in figure 2.17. For both measures, enhanced vertical mixing due to entrainment is visible in the region of the halocline on top of the plume and in the marginally stratified region above the plume. Interestingly, the upward salt flux is slightly negative near the bottom of the plume, where probably differential advection due to straining of vertically aligned isohalines leads to convective overturning.

The general agreement between the two methods can be explained by the fact that convective mixing plays a minor role in the Western Baltic Sea. Furthermore, the vertical turbulent salt flux and the decay of ensemble averaged salinity variance are proportional to each other, with a factor of proportionality of $\partial_z\bar{S}$. This means that for stable stratification ($\partial_z\bar{S} < 0$) the more consistent decay of ensemble averaged salinity variance would reproduce the same structure and simply better pronounce regional differences, as can be seen from figure 2.30.

It should be noted that numerically induced mixing due to the discretisation of salt advection may increase the effective mixing shown in these model results, see Burchard and Rennau (2008) for idealised investigation and Rennau and Burchard (2009) for the realistic model setup applied in this thesis (chapter 4). Such discretisation errors do not directly appear in the calculated decay of salinity

variance or the vertical turbulent salt flux, but they do indirectly influence these estimates by generating decreased vertical density differences. A detailed model study of the amount of numerically induced mixing to be directly compared to physically induced mixing is shown in chapter 3. It is found that the model derived physical mixing and the numerical mixing due to discretisation errors in the tracer advection schemes do show different vertical and horizontal distributions (Rennau and Burchard (2009)). With a calculation of volume-integrated amount of physical and numerical mixing it is found that both surprisingly show similar values (chapter 3).

The result on vertical turbulent salinity mixing can be extended by calculating the vertical integral of turbulent tracer fluxes on an annual basis for the two passive tracers marking Drogden Sill and Darss Sill separately. Figure 2.32 shows the model derived upward (figure 2.32a,c) and downward turbulent fluxes (figure 2.32b, d) for the two passive tracers. Figures 2.32a,c reveal a similar result as shown by 2.30 with increased mixing at the Sill areas and pronounced mixing at Bornholm Channel. However, the vertical mixing of the two passive tracers is less than found in figure 2.30. This is because of low surface passive tracer concentrations (background value of $c = 1...2$) as they are not set equal to salinity. The consequence is that the passive tracers are stronger being diluted during propagation than salinities (figure 2.18). This leads to comparably lower values in annual mean vertically integrated upward turbulent salt flux in the Bornholm Channel as seen in figure 2.32 and explains the different horizontal distribution of hot spots of vertical turbulent mixing as found in figure 2.30. The downward turbulent salt flux as shown in figure 2.32b indicates strong values east of the Darss Sill tracer release section as well as in the central Arkona Basin, which may be due to convection, differential advection or - especially for the high values in the central Arkona Basin - due to interleaving with where higher tracer concentrations may occur above lower tracer concentrations. Since the peak value in downward turbulent fluxes in the central Arkona Basin is mainly due to interleaving of Drogden Sill and Darss Sill water masses is proved by figure 2.23 where it is shown that this is exactly the area of highest probabilities ($> 25\%$) of anti-correlation values with $R > 0.8$ for correlating the vertical profiles of both passive tracers.

2.5 Discussion and conclusions

The overflow of fresh and dense Kattegat water into the estuarine system of the Western Baltic Sea was studied in a realistic 3D model setup using the hydrostatic ocean circulation model GETM. After improving the barotropic transport and calibration of the model bathymetry, a successful model validation concerning salinity, temperature, velocity and sea surface level has proved the ability of the model to quantitatively reproduce dense overflows. It is found that the applied turbulence model together with higher order advection schemes used in the model is suitable for reproducing the observed characteristics. Although the model did not fully reproduce the correct timing of the inflow event observed in early 2004, the model was still able to reproduce the observed vertical structure of salinity and current velocity on two different transects south of Drogden Sill and north of Kriegers Flak. Furthermore an empirical barotropic transport equation based on sea surface elevation differences north and south of the Øresund has been successfully applied. With this it was found that the model partly underestimates the barotropic gradient across the Øresund resulting in a weaker first pulse of inflowing

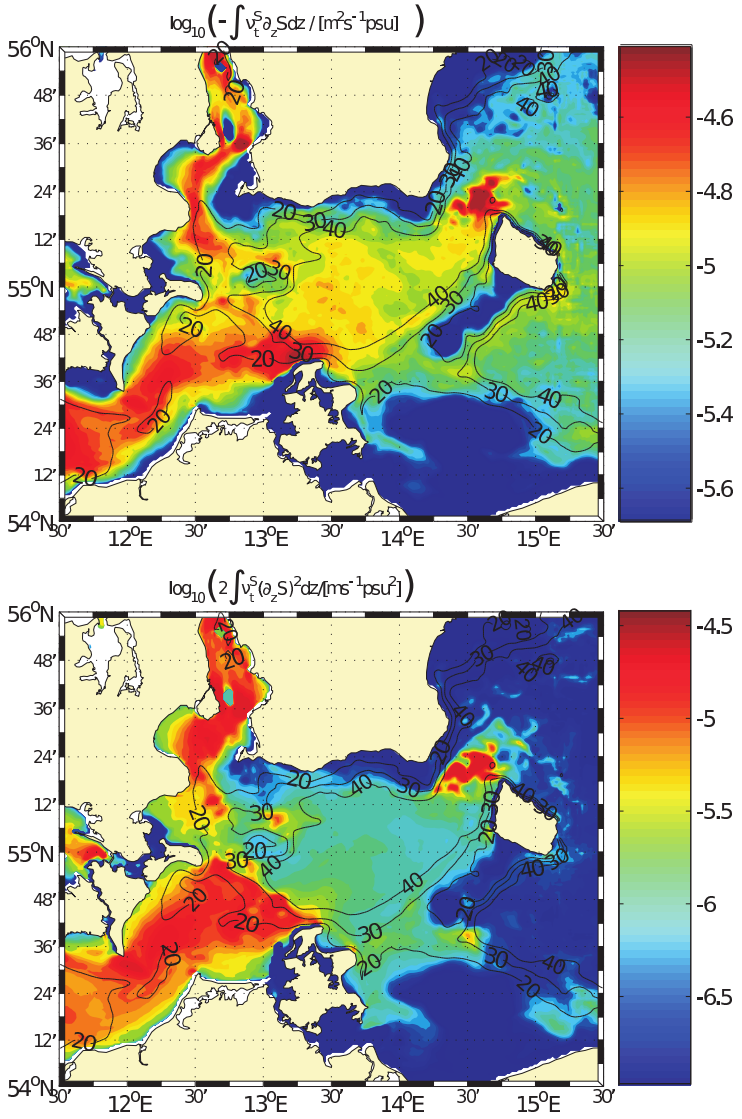

Figure 2.30: Simulated decadal logarithm of vertically integrated upward turbulent salt flux $\log_{10}\left(-\int \nu_t' \partial_z S \mathrm{d}z\right)$ in $[\mathrm{m^2 s^{-1} psu}]$ (upper panel) and decadal logarithm of vertically integrated salinity variance dissipation, $\log_{10}\left(2\int \nu_t' (\partial_z S)^2 \mathrm{d}z\right)$ in $[\mathrm{m\,s^{-1} psu^2}]$ (lower panel), both temporally averaged over the nine-month simulation period.

dense water of the January/February 2004 medium-intensity inflow event.

The calibrated model did nicely reproduce dense bottom current spreading and mixing as demonstrated with a number of observations. Hence the numerical model was used as a tool to investigate the dense bottom current flow across Darss Sill and Drogden Sill separately and further to give answers on the spreading times and spreading behavior into the Central Arkona Basin. As such two passive tracers have been added to the numerical model, marking dense bottom water during inflow conditions at the Darss Sill and Drogden Sill such that spreading times in this area can more precisely being calculated. As model derived spreading time of about 5.46 days from Drogden Sill to the northern trench of Kriegers Flak were related to rather high correlation coefficients, the flow of Darss Sill and Drogden Sill water masses through the Central Arkona Basin is significantly stronger which makes it harder to obtain characteristic individual pathways and spreading times. This is mainly due to (i) the

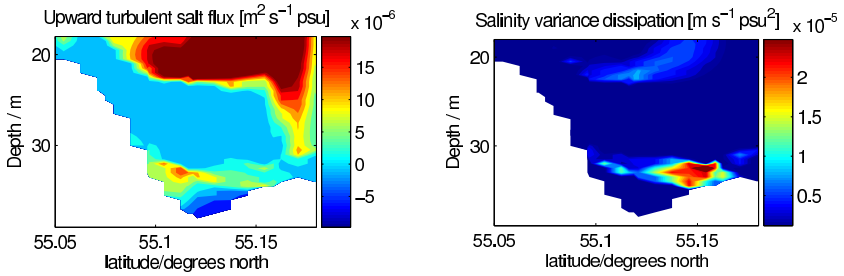

Figure 2.31: Simulated upward turbulent salt flux (left panel) and salinity variance dissipation (right panel) along the cross section north of Kriegers Flak.

strong influence of the wind fields inducing barotropic gradients across this area forcing dense bottom currents to propagate either faster, slower or even on different pathways though the Arkona Basin and (ii) because of the different intensities of Darss Sill and Drogden Sill water for each individual inflow event with the difficulty in giving fully reliable answers on main pathways and on propagation times. Anyhow, the spreading times of Darss Sill and Drogden Sill dense bottom currents could be obtained to be in the order of roughly between 15 to 30 days for Darss Sill and Drogden Sill dense bottom currents. The propagation speed of the fastest Drogden Sill plume in 2005 (during the November/December inflow event) has been found to be 13-17 days with a mean current speed of almost more than $0.5 ms^{-1}$. This is in agreement with the value of 12 days derived by previous publications on the basis of major Baltic inflow events which are faster due to higher bottom-surface density differences and persisting wind-fields in advantageous directions.

However, main pathways based on the calculation of annual mean passive tracer fields revealed that both water masses from Darss Sill and Drogden Sill propagate through the Central Arkona Basin, whereas Drogden Sill plumes are primarily found on the northern rim and Darss Sill plumes on the southern rim of the Central Arkona Basin. A general sketch of how inflows propagate into the Arkona Sea was drawn, indicating that the Darss Sill plume enters the Western Arkona Sea earlier than the Drogden Sill plume. When the Drogden Sill plume enters the Western Baltic Sea a few days later it shifts below the Darss Sill plume due to higher salinities of Drogden Sill water masses which is mainly due to the shorter distance to the Kattegat, the source of dense and vertically well-mixed water masses. Both plumes then continue their pathways through the Arkona Basin and the Bornholm Channel where both are found to be strongly separated from each other. Via correlating vertical profiles of Darss Sill and Drogden Sill passive tracers all over the domain and the year 2005, some mixing between both water masses is found, indicated by increased correlation coefficients. Anyhow, the strong separation (interleaving) of the two water masses is the prior feature in the Arkona Basin and anti-correlation coefficients are almost as high as 0.7 in large areas of the Arkona Basin and the Bornholm Channel occurring more often than well-mixed conditions between the two water masses.

As found in earlier publications, the flow north and south of Kriegers Flak is also found to be different with higher salinities and higher transports in the northern trench. Furthermore the studies conducted in this work reveal a delay of 2.5 days (derived by the model simulations in 2005) and 1.45 days (derived with the help of observations in 2006) when the plume front from Drogden Sill passes each of the trenches. An additional finding is that the Darss Sill plume significantly contributes to the dense

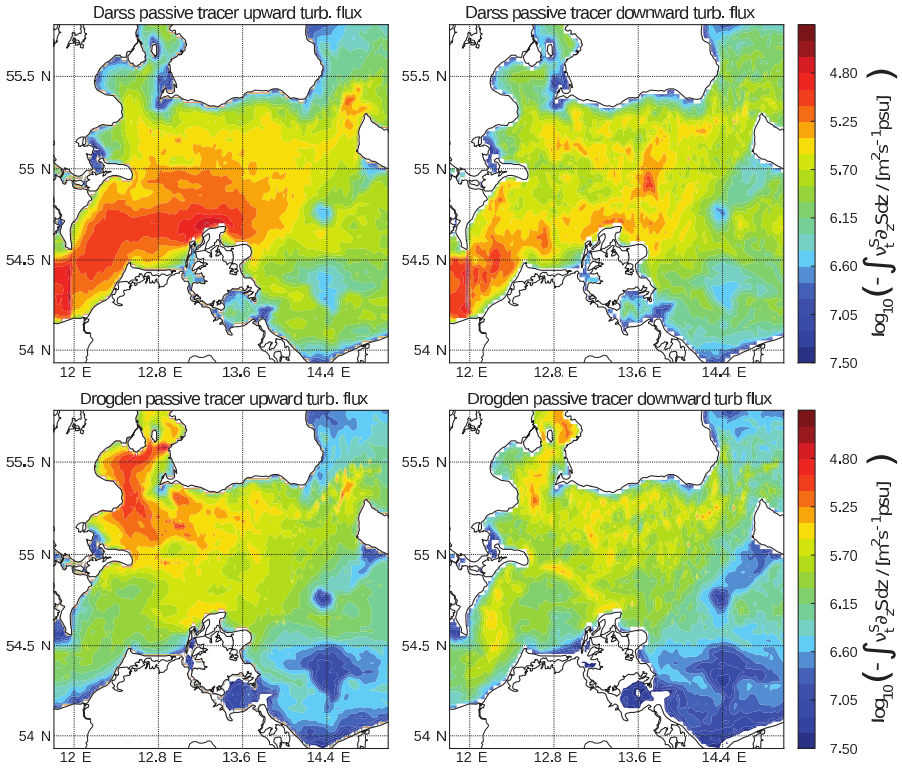

Figure 2.32: Simulated decadal logarithm of vertically integrated turbulent salt flux $\log_{10}\left(-\int \nu_t' \partial_z S \mathrm{d}z\right)$ in $[\mathrm{m}^2\mathrm{s}^{-1}\mathrm{psu}]$ for each of the two passive tracers and upward and downward direction separately. Upper left panel: upward contributions of the turbulent salt flux ($\nu_t' \partial_z S \mathrm{d}z > 0$) for Darss Sill passive tracer, upper right panel: downward contributions of the turbulent salt flux ($\nu_t' \partial_z S \mathrm{d}z < 0$) for Darss Sill passive tracer, and same for Drogden Sill passive tracer in the two lower panels. All measures were temporally averaged over the year 2005.

bottom water flow south of Kriegers Flak, with comparable salinity values.

Furthermore the model was able to reproduce spreading times comparable to previous work and to observations as conducted and extensively discussed in this chapter. A potential improvement of the research using passive tracers is to extend the current model simulation until mid of 2007 in order to include not only the main stations (Drogden Sill, Darss Sill, Arkona Station) but also the two moorings at Kriegers Flak (KFN, KFS) which are available in 2006 only. A further potential improvement while using the two passive tracers as marker to quantify spreading behavior of Darss Sill and Drogden Sill plumes is to use the vertical maximum of the passive tracers instead of bottom time series because interleaving (which has been quantified in previous sections and found to be a significant feature) may influence the success in applying cross-correlations of time-series. Also the surface tracer concentrations should be set equal to salinity to obtain passive tracer concentrations in the Central Baltic Sea and Bornholm Channel which are comparable to salinity values.

A regional plot showing the calculation of the annual mean vertically integrated upward turbulent salt flux and the salinity tracer variance decay demonstrates how the naturally induced vertical turbulent mixing is distributed horizontally in the Western Baltic Sea. Three main hot spots of water mass transformation can be identified which are the Darss Sill, the Drogden Sill and the Bornholm Channel, a finding additionally supported by annual mean current speeds and current directions in 2005. It

reveals the major role of the Western Baltic Sea as an important region with enhanced entrainment of dense bottom plumes. Strong mixing is further found in the channel north of Kriegers Flak where the bottom currents are accelerated due to continuously reduced channel width. Further east of Kriegers Flak the mixing is even more pronounced which may be due to the widening of the accelerated plume together with coincidentally being flattened. Rather unexpected are the high values of integrated vertical mixing as found in the Bornholm Channel. Kõuts and Omstedt (1993) suspected the Bornholm Channel to show only negligible physical mixing but turbulence observations as presented by Reissmann et al. (2009) proved that there may be events with strong mixing. The main reason for increased physical mixing in the Bornholm Channel are (i) the continuous flow of dense water from the Arkona Basin acting as a pool for dense bottom water and (ii) the flow acceleration due to increasing depth.
As potential human impact on dense bottom current spreading in the Western Baltic Sea requires the knowledge of pure naturally induced mixing in the Western Baltic Sea, the first chapter can also be regarded as a precondition to finally conduct the implementation of additional mixing due to offshore wind farms into the numerical model as presented in chapter 4. Furthermore the research on numerically induced mixing in the presented numerical model setup of the western Baltic Sea, which is presented in chapter 3, requires a realistic reproduction of naturally induced mixing as both numerically and physically induced mixing are highly influenced by each other as discussed in detail in chapter 3.

Chapter 3

Quantitative comparison of numerically and physically induced mixing: idealised and realistic numerical model studies

3.1 Introduction

A realistic reproduction of dense bottom plumes requires reliable numerical schemes as there are, for example for certain parts in the ocean, sharp gradients to be advected over long distances without much physical mixing activity (Rooth and Östlund (1972); Veronis (1977); Ledwell et al. (1993); Toole et al. (1994); Kunze and Sandford (1996), Munk (1966), Broecker (1991), Toggweiler and Samuels (1998)). This additionally holds on regional scale (see e.g. Bethoux et al. (1999) for the Mediterranean Sea and Meier et al. (2006) for the Baltic Sea but also on smaller scales such as in lakes (Wüest and Lorke (2003)) and fjords (Austin and Inall (2002)) which exactly makes it a modelling challenge in maintaining the adiabatic property of advection without spurious - numerically induced - mixing. Same holds for reproduction of vertical oscillations (internal waves) without significant mixing (see e.g. van Haren et al. (1999) for the North Sea).

Ocean models with calculation of transport of biogeochemical tracers have to rely on non-dispersive advection schemes on all scales, since strong gradients of these tracers would thus lead to negative tracer concentrations. Therefore, also large scale models are equipped with high-order advection schemes, see e.g. Gerdes et al. (1991) and Eden and Oschlies (2006) for MOM (Modular Ocean Model, `www.gfdl.noaa.gov/~fms/pubrel/l/mom4/doc/mom4_manual.html`, Griffies et al. (2007)) type models.

There have been various methods in estimating the amount of numerical mixing in different ocean models and idealised or realistic applications (Smolarkiewicz (1983); James (1996); Sanderson (1998); Morales Maqueda and Holloway (2006); Riemenscheider and Legg (2007); Winther et al. (2007)). By carrying out the same model simulation with different advection schemes and comparing the model

results, general numerical properties of the advection schemes can be studied, see e.g. Gerdes et al. (1991) and Matear (2001). Griffies et al. (2000) use a method for diagnosing the effective diapycnal mixing (sum of physical and numerical mixing) in ocean models. This is done by adiabatically resorting all density values in the model grid for calculating the available potential energy. The result of this diagnosis is a vertical profile of the horizontally averaged diapycnal diffusivity for each model time step. Marshall et al. (2006) derive near-surface horizontal effective diffusivities due to meso-scale activity by numerically analysing the lengthening of idealised tracer contours strained by the geostrophic flow.
Since spatial resolution in large-scale and regional-scale model simulations is always limited, numerical models can only reproduce natural processes up to a certain accuracy. However, the increasing improvement of computational power is continuously extending the scope of detachable problems. Additionally there are notable improvements in numerical schemes as there are for example recently developed pressure gradient schemes for models using nonaligned vertical coordinates (Shchepetkin and McWilliams (2003)) or various higher-order advection schemes (Pietrzak (1998); Smolarkiewicz and Margolin (1998); Morales Maqueda and Holloway (2006)) reproducing a greater accuracy of advection of sharp tracer gradients and co-instantaneous reducing numerical artefact's as numerical mixing (Riemenscheider and Legg (2007),Burchard and Rennau (2008)), numerical dispersion (Fernández et al. (2005); Shchepetkin and McWilliams (1998)) and spurious instabilities. The well known numerical diffusivity of the first order upwind scheme for example is defined by $(u\Delta x - \Delta t u^2)/2$ (Smolarkiewicz (1983)). This will consequently erode any sharp pycnocline in tidal shelf seas after only a few tidal cycles.
It is notable that Sanderson (1998) and Winther et al. (2007) have shown that for a model setup already resolving the dominant dynamic scales, it may be more efficient to improve the order of the numerical schemes than doing grid refinement. The analysis of Sanderson (1998), based on the evaluation of truncation errors of the numerical schemes, has shown that the tracer advection terms would benefit substantially from the use of higher order advection schemes. It has been found that the optimum choice of the numerical scheme is either order D or D+1, where D denotes the total dimension (spatial and temporal) of the model. Additionally Winther et al. (2007) found that a fourth order scheme at 4 km resolution gives results close to a second order scheme at 2 km resolution as far as the model already resolves the dominant scales of motion. Their model evaluation was based on comparison with an analytical solution and observations. In the application of Webb et al. (1998) it was found that the use of higher-order advection schemes is indeed useful for tracers but on the contrary not to the same extent for the advection terms of momentum. They pointed out that a fourth-order scheme for the advection of tracers seems to be the optimum choice. To finally obtain any kind of information about whether it is even useful to apply numerical schemes higher than fourth-order, Winther et al. (2007) showed that moving from fourth-order schemes to higher-order schemes will most likely not improve the efficiency. They summarized that the minimum wavelength that can be properly represented is only reduced from 4.4 to 3.6 going from fourth order to six order scheme. Besides the theoretical knowledge of the behavior of different numerical advection schemes where higher order together with 'sufficient' resolution means automatically increasing 'model truth', it additionally must be pointed out that two different numerical models can show similar model results using different orders for the numerical advection schemes. Ezer et al. (2002) directly compared results of a second, third and fourth

order scheme where third order in ROMS (Regional Ocean Model System) gave better results than fourth or second order. Even an applied second order scheme in POM (Princeton Ocean Model) showed results similar to those made with third order in ROMS. Their work nicely demonstrates how strong the individual numerical model architecture, concerning numerical schemes, options and parameterisations, contributes to the general performance of the model.

Gerdes et al. (1991) again mentioned the importance of resolving the necessary scales in a numerical simulation in which models with a horizontal resolution smaller than the internal Rossby Radius are required. For the case of coarse resolution models there is a close connection between the numerical schemes and the mixing formulations. For the coastal model application presented here a horizontal resolution of $\sim$ 1 km is used which is below the known values for the baroclinic Rossby Radius of O($\sim$ 3 km) in the Western Baltic Sea (Fennel et al. (1991)), but may not fully resolve it.

An existing high-resolution coastal model study of the Western Baltic Sea (Burchard et al. (2009)) has then been used to quantify and qualify the amount of natural mixing of these dense gravity currents on their way through the Western Baltic Sea. This model setup is applied for sensitivity studies giving answers about the strength and location of numerical mixing to be compared to the physically induced mixing. For the realistic coastal model simulation used in this chapter, the advection of sharp tracer gradients is of high interest, as advection and mixing of dense bottom currents play a major role for the Baltic Sea ecosystem (Lass and Mohrholz (2003); Burchard et al. (2005); Reissmann et al. (2009)). Hence numerical mixing might introduce wrong estimates of physical mixing in the Western Baltic Sea. Lass and Mohrholz (2003) identified three major mixing processes for the Arkona Sea which are (i) wind mixing at relatively shallow depths, (ii) differential advection at the front of dense bottom currents and (iii) entrainment of ambient water into the dense bottom current.

As density driven plumes have dynamics which are far too complex to be described completely with an analytical solution (Winther et al. (2007); Winton et al. (1998b); Mesinger and Arakawa (1976); Rood (1987)), model simulations have to be compared with observations (Winther et al. (2007); Riemenscheider and Legg (2007)). Riemenscheider and Legg (2007) found that in a z-level model without any mixing parameterisation, the spurious mixing due to discretisation errors of the numerical advection schemes is in the order of the measured mixing rates for the Faroe Bank Overflow even with grid refinement. However, they also showed the improvements that can be reached by grid refinement which has also been shown by Ezer (2006) with idealised simulations of the Faroe Bank Overflow. For z-level models, Winton et al. (1998b) showed with process experiments that the model solutions converge when the model has sufficient vertical resolution to resolve the bottom viscous layer. They concluded that the horizontal grid spacing must have the value of the vertical grid spacing divided by the maximum slope.

Several model studies conclude for example the importance of the correct reproduction of the bottom boundary layer (BBL) and developed several schemes (Beckmann and Döscher (1997); Campin and Goosse (1999); Killworth and Edwards (1999); Song and Chao (2000)) with reasonable improvements. However, Hodges and Delavan (2004) illustrate convergence problems at which the numerical mixing is not convergent for grid refinement in horizontal direction with a coincidentally increasing diffusive error. By wavelength analysis they found that this is due to the development of shorter wavelength horizontal waves being generated during the steepening of an internal wave modelled with a hydrostatic

model. As the small aspect ratio between the vertical and horizontal scales of motion is the necessary constraint for a hydrostatic model, this justification is violated for waves becoming very steep. As for the shallow water limit the dispersion of horizontally propagating waves disappears. The phase speed c varies with the wavenumber k for steep waves when the aspect ratio is of the order of one and hence non-hydrostatic effects and non-hydrostatic dispersion becomes important. This is not resolved with the hydrostatic model. If in case of a hydrostatic model waves become too high and too steep, this will lead to unwanted numerical effects as there are for example numerical dispersion or waves trapped on the finest grid scales. The importance of modelling non-hydrostatic effects for example to correctly represent the tidally induced mixing in a sill region was shown by Xing and Davies (2007) who found significant artificial convective mixing using the hydrostatic assumption leading to excessively high vertical mixing compared to the non-hydrostatic case. However, Ezer (2005) found that a hydrostatic model with terrain-following grid and 10 km horizontal resolution matches extremely well with a non-hydrostatic model of 0.5 km resolution concerning the transport and dilution of a dense bottom plume.

A generally very different kind of numerical model with a striking advantage and disadvantage compared to z-level and sigma-coordinate models is the so called isopycnal layer model where isopycnals are discretised explicitly. This has the advantage that for any density field the adiabatic property of advection is maintained. On the other hand the most serious problem of these models is their degeneration in unstratified and statically unstable water columns because these models preserve a predefined number of potential density classes.

Finally there exist various publications on the influence of advection schemes on flow dynamics and mixing of which most point out, that the model resolution has to respect the admitted scales of motion (importance of eddies on transport and mixing, Robinson (1983)) in order to reduce the spurious mixing and maintain a small amount of mixing consistent with that measured within the oceans pycnocline (Rooth and Östlund (1972); Veronis (1977); Ledwell et al. (1993); Toole et al. (1994); Kunze and Sandford (1996)).

To some extent, numerical mixing during momentum and tracer advection can be minimised by careful choice of the advection scheme and grid resolution. However, it must be pointed out that numerical mixing will remain one of the most important issues in running prognostic and diagnostic models of the ocean and estuarine systems.

In absence of physical mixing, a measure of numerical mixing is the integrated second moment:

$$I(t) = \int s(t)^2 dV / \int s(t=0)^2 dV \tag{3.1}$$

with the integration of the salinity s over the whole model domain (see for example James (1996)). For closed lateral boundaries and zero surface freshwater fluxes and no mixing, the value of $I(t)$ stays analytically constant when no sources or sinks are present. For a perfect numerical scheme this consequently means that the amount of s^2 is constant over the entire simulation time. A decreasing value of I hence provides an integral measure of numerical mixing. For the present coastal model simulation this measure is difficult to implement as the presence of open boundaries consequently act as sources and sinks for the active tracer salinity.

In the present study, the additional numerical mixing is qualified and quantified using the recently developed diagnostic method suggested by Burchard and Rennau (2008). With this generic algorithm we obtained for the first time direct quantities, reasons and the information about the localisation of high numerical mixing which are directly being compared to physical mixing.
In this chapter a generalised vertical coordinate (*gvc*) model is used in which the bottom and sea surface are the lowermost and uppermost coordinate levels, respectively (Burchard and Bolding (2002)). Such bottom-fitted coordinate models allow for along-bed advection without steps (z-level models introduce new additional truncation errors here). However, bottom-fitted models suffer from the problem of the inclination of the vertical layers especially at regions of steep slopes. When advection is predominantly in geopotential direction it has to be advected through the inclined coordinates of the *gvc* system. Hence it is easy to understand how this causes unwanted numerical mixing in the vicinity of a halocline. A z-level model would have less numerical problems for advection in geopotential direction but has on the other hand more problems simulating overflows and advection of dense bottom currents, as they are mainly advected along the sea bed and consequently through the vertical coordinates of the z-level model on the stepped topography (Gerdes (1993); Beckmann and Döscher (1997); Winton et al. (1998b); Pacanowski and Gnanadesikan (1998); Ezer and Mellor (2004); Riemenscheider and Legg (2007)). Concerning terrain-following ocean models additional problems might occur for the representation of horizontal tracer gradients in areas of steep slopes which has been demonstrated in this work in section 3.1. A different numerical problem in terrain-following ocean models is the difficulty in representing the horizontal pressure gradients with the consequence of so called pressure gradient error (Mellor et al. (1994); Mellor et al. (1998)) and its improvements (Shchepetkin and McWilliams (2003)). In the Baltic Sea the typical bottom slopes are of the order of 10^{-3} to 10^{-4} (Fennel et al. (1991)) which is also a typical value for large-scale ocean circulation modelling.
The work of Burchard and Rennau (2008) provides a new and easy to implement non-invasive method for quantifying the amount of numerical mixing as defined by the numerical tracer variance decay (section 3.2.2). This new measure has been applied to different idealised scenarios ranging from a one-dimensional advection test case to the fully baroclinic three-dimensional simulation of a large-scale overflow (DOME test case, Ezer (2005); Legg et al. (2006)). For the latter scenario, the results have shown that numerical mixing in the applied ocean model GETM (Burchard and Bolding (2002)) is about one order of magnitude larger than the physical mixing. These results for high numerical mixing due to discretisation errors of the horizontal and vertical advection schemes require further systematic studies in realistic 3D model applications. Therefore the present study uses an existing validated high-resolution model (Burchard et al. (2009)) of gravity current dynamics and resulting vertical mixing processes in the Western Baltic Sea for investigating reasons, amount and localisation of numerically induced mixing.
This chapter is organised as follows: first, Sect. 3.2.1 gives a short explanation of the physical mixing measure used (Burchard et al. (2009)) directly followed by a brief motivation of the numerical mixing in Sect. 3.2.2 defined as the numerical variance decay rate (Burchard and Rennau (2008)). The first numerical experiment is a study of the one-dimensional advection equation (section 3.3.1), followed by two idealised 2D experiments (lock-exchange and overflow scenario) and then generalising to three dimensions (section 3.3.4) with the DOME (e.g. Ezer and Mellor (2004), Legg et al. (2006)) scenario

simulating a dense bottom current descending down a linear slope. In Sect. 3.4.1 some model results of a physically challenging area in the Western Baltic Sea are shown to obtain additional knowledge about location and amount of numerical mixing compared to physically induced mixing in a realistic model application. After analysis of different advection schemes in Sect. 3.4.2, more global calculations defining and analysing the numerically and physically induced mixing in the whole model domain, are done in Sect. 3.4.3. The results applying this new diagnostic tool are summarised and discussed in section 3.5.

3.2 Methods

3.2.1 Physically induced variance decay as measure for mixing

The physically induced mixing measure used is explained in detail in section 2.4.7, hence only a small introduction into this measure is given here. To derive the bulk measure for vertical mixing suggested by Burchard and Rennau (2008), the conservative Reynolds averaged salinity budget equation is used to derive a conservation equation of the tracer concentration:

$$\partial_t s + \partial_x(us) + \partial_y(vs) + \partial_z(ws) - \partial_z(K_v \partial_z s) = 0. \tag{3.2}$$

Here s is the tracer salinity, u and v the horizontal velocity components, w the vertical velocity component, K_v the vertical eddy diffusivity, t the time and ∂_t the derivative in time and $\partial_x, \partial_y, \partial_z$ the derivatives in space. Here the horizontal diffusivity is generally neglected. In the numerical model GETM, horizontal diffusion is calculated along the sigma layers but is set to zero for all simulations in this work.
After some mathematical transformations, a conservation equation for the square of the mean tracer concentration can be directly derived from (3.2):

$$\begin{aligned} \partial_t s^2 + \partial_x(us^2) + \partial_y(vs^2) + \partial_z(ws^2) - \partial_z(K_v \partial_z s^2) \\ = -2K_v(\partial_z s)^2. \end{aligned} \tag{3.3}$$

The last term on the right hand side of (3.3) is the turbulent mean tracer variance decay quantifying the physical mixing measure in this study such that we define:

$$D^{phy}(s^2) = 2K_v(\partial_z s)^2. \tag{3.4}$$

This is a more appropriate measure for physical mixing than the eddy diffusivity which may result in high values under well-mixed conditions with no tracer mixing. As a second step we add the contributions of vertical molecular diffusion to the physical mixing such that the physical mixing is composed of the turbulent and viscous contributions. For additional theoretical background on the above physical mixing measure the reader is referred to the work of Burchard and Rennau (2008).

3.2.2 Diagnosing numerically induced variance decay

A diagnostic tool is suggested (Burchard and Rennau (2008)), similar to the method by Morales Maqueda and Holloway (2006), based on the variance decay of individual tracers. For any linear or non-linear advection scheme and for all z-level or layer models (such as σ-layer or general vertical coordinate models) with equidistant or non-equidistant grid spacing the numerical tracer variance decay is simply calculated as the rate of change between the advected square of the tracer and the square of the advected tracer.
In order to obtain a measure for numerical mixing (Burchard and Rennau (2008)) it is suggestive to start with the first order upstream (FOU) discretised 1D advection equation for any tracer s:

$$\frac{s_i^{n+1} - s_i^n}{\Delta t} + \frac{u}{\Delta x}\left(s_i^n - s_{i-1}^n\right) = 0 \tag{3.5}$$

with s_i^{n+1} representing a value of the new time level, and s_i^n representing a value of the old (known) time level, the constant positive advection velocity u, the time step Δt and the spatial increment Δx. Let us now introduce the advection operator A as:

$$s_i^{n+1} = (1-c)s_i^n + cs_{i-1}^n = A\{s_j^n\}_i, \tag{3.6}$$

with $c = u\Delta t/\Delta x$ being the Courant number for which the stability criterion $0 < c < 1$ must be fulfilled. Multiplication of (3.5) by $(s_i^{n+1} + s_i^n)$ leads, after some additional mathematical transformations, to the discretised equation calculating the amount of numerical variance decay induced by the first order upstream scheme:

$$\frac{(A\{(s_j^n)\}_i)^2 - A\{(s_j^n)^2\}_i}{\Delta t} = \quad -2\frac{u\Delta x}{2}(1-c)\frac{s_i^n - (s_{i-1}^n)^2}{(\Delta x)^2}. \tag{3.7}$$

The term $1/2u\Delta x(1-c)$ is the well known numerical diffusivity of the FOU scheme (Smolarkiewicz (1983)) that can be easily obtained via the truncation error in a Taylor series extension. Hence the right hand term in equation (3.7) resembles a discretisation of the right hand side of equation (3.3) for the square of the mean tracer (see also Morales Maqueda and Holloway (2006)) with the numerical instead of the physical diffusivity. Furthermore, the sink term on the right hand side of eq. (3.7) exactly quantifies the local numerical tracer variance decay for the FOU scheme. Consequently, Burchard and Rennau (2008) defined for any advection scheme A:

$$D^{\mathrm{num}}\left\{\left(s_j^n\right)^2\right\}_i = \frac{A\left\{\left(s_j^n\right)^2\right\}_i - \left(A\left\{s_j^n\right\}_i\right)^2}{\Delta t}, \tag{3.8}$$

which clearly is the local rate at which tracer variance is decaying, as the measure for numerically induced mixing. The diagnostics of (3.8) can be easily calculated as the difference between the advected square of the tracer and the square of the advected tracer, divided by the time step. Since the discrete advection of the square of the tracer is conserving the total tracer variance when finite volume schemes are used, this method does indeed calculate the total numerical tracer variance decay in an exact way. Locally, this numerical mixing calculation is subject to discretisation errors, just as the calculation of

any tracer such as temperature and salinity. The implementation of this diagnostic method is simple: before the advection step for a tracer, the tracer square is calculated and the advection scheme is applied to the tracer and its square independently. After the tracer advection step, the square of the advected tracer is calculated such that (3.8) can be computed. Afterwards, the squares of the old and the new tracer fields are discarded, and only the advected tracer concentration is used for the further simulation.
In numerical ocean models this generic and non-invasive method in obtaining the numerical mixing should generally be implemented very easily as advection and diffusion are mostly implemented as two different operational steps (Burchard and Bolding (2002); Shchepetkin and McWilliams (2005)). In a model with closed boundaries and without any fluxes through the bottom and surface, the following relation must hold:

$$\int S^2(t=t_2)dV - \int S^2(t=t_1)dV \quad = \int_{t_1}^{t_2} \int D^{num} dV dt \tag{3.9}$$

where the loss of the salinity squared must be equal to the volume integrated numerical mixing as calculated by 3.8. Here $S^2(t=t_1)$ denotes the salinity at a certain time t_1 and $S^2(t=t_1)$ at time t_2 and D^{num} the numerical mixing due to the applied advection steps. Up to an uncertainty this can also be applied to a model with open boundaries and fluxes through the surface or bottom. For a domain with open boundaries, the net flux of S^2 through the lateral boundaries would need to be added to the left hand side.
Additionally it should be pointed out that for the model used in this study (GETM; Burchard and Bolding (2002)) the spatial discretisation is staggered with the tracer points being located at the center of each grid cell and the eddy diffusivity being located at the interfaces.
For further theoretical background on the numerical variance decay, the reader is referred to Burchard and Rennau (2008).

3.3 Idealised model scenarios

3.3.1 One-dimensional numerical experiments

In order to prove the diagnostic concept for quantification of numerically induced mixing suggested here, numerical simulations of the linear advection equation:

$$\partial_t s + \partial_x (us) = 0, \tag{3.10}$$

are carried out for $L = 100$, $u = 1$, $\Delta x = 1$, and $\Delta t = 0.5$ and results are analysed for $t = 100$. Two different initial profiles are used, the box profile and a Gaussian bell-shaped profile, see figure 3.1.
The numerical schemes applied are the forward in time and upstream in space scheme as formulated in eq. (3.5) and the third-order TVD-limited P2-PDM scheme, see Pietrzak (1998). The simulation results are shown in figure 3.1. It can be clearly seen that the upstream scheme with the numerical diffusivity $(u\Delta x - \Delta t u^2)/2$ (Smolarkiewicz (1983)) has a positive tracer variance decay (see also Burchard and Rennau (2008)). In contrast to that, the TVD scheme partially shows antidiffusive, negative tracer

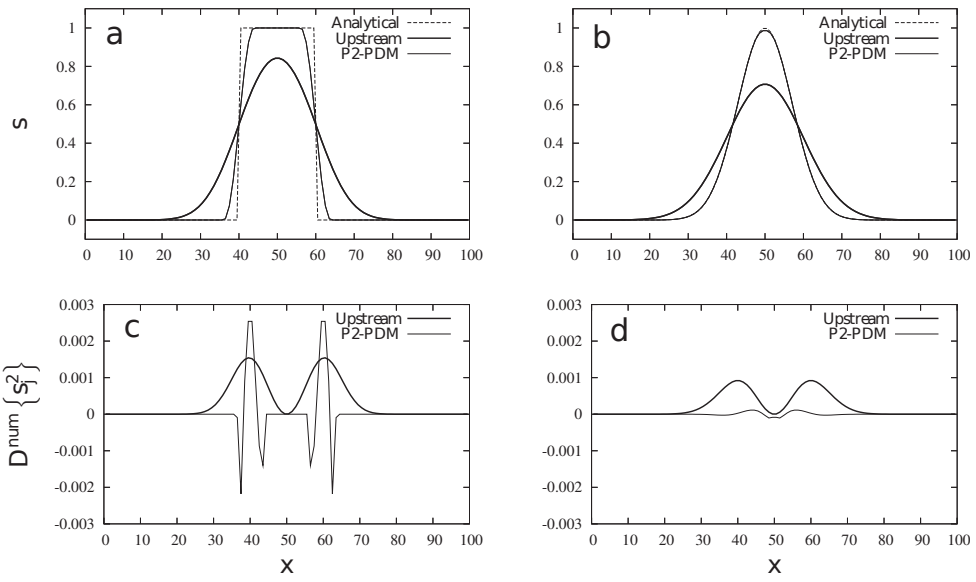

Figure 3.1: One-dimensional advection. Panels a and b: Numerical solutions of e.g.. (3.10) for $L = 100$, $u = 1$, $\Delta x = 1$, and $\Delta t = 0.5$ at $t = 100$. The analytical solution which is here identical to the initial solution is shown as dashed line, the first-order upstream scheme (see eq. (3.5)) as bold line and the P2-PDM scheme as thin line. Panels c and d show the numerical variance decay $D^{\text{num}}\left\{s_j^2\right\}$ for the two schemes. Panels a and c show simulation results initialised with a box profile, panels b and d show simulations initialised with a Gaussian profile.

variance decay and partially strong positive tracer variance decay, where the former is an effect of the underlying non-monotone higher-order scheme and the latter an effect of the TVD limiter ensuring monotonicity. With defining the spatially integrated variance decay rates as

$$D_{tot}^{\text{num}} = \Delta x \sum_i D^{\text{num}} \left\{s_j^2\right\}_i , \tag{3.11}$$

for the forward in time and upstream in space scheme $D_{tot}^{\text{num}} = 3.5 \cdot 10^{-2}$ (box profile) and $D_{tot}^{\text{num}} = 2.2 \cdot 10^{-2}$ (Gauss profile) and for the P2-PDM scheme $D_{tot}^{\text{num}} = 4.7 \cdot 10^{-3}$ (box profile) and $D_{tot}^{\text{num}} = 3.6 \cdot 10^{-4}$ (Gauss profile) are obtained. Interestingly, for the Superbee scheme (see Roe (1985), results are not shown here) which is known for its antidiffusive properties an increasing spatially integrated variance with the negative variance decay of $D_{tot}^{\text{num}} = -1.6 \cdot 10^{-3}$ for the Gauss profile is obtained.

3.3.2 Lock exchange

For the lock exchange test case, a closed two-dimensional vertical domain with a constant depth of $H = 20$ m and a length of $L = 64$ km is considered. Initially, the left half of the domain ($x < 32$ km) has a density of $\sigma_t = 5$ kg m^{-3} and the right half of the domain ($x \geq 32$ km) has a density of $\sigma_t = 0$ kg m^{-3}, separated by a vertical line. Initial surface elevation and velocity are zero. At $t = 0$, the separation is removed such that the dense water is forced under the fresh water. Earth rotation, bed friction and mixing are neglected, such that the effective density mixing is only due to advection of density. This scenario been suggested by Haidvogel and Beckmann (1999) as a test case for advection schemes in ocean models, and has been intensively used by Burchard and Bolding (2002) for testing the advection schemes in GETM. Here, the numerical mixing of the first-order upstream and the P2-PDM

schemes will be assessed for five different resolutions:

A: $\Delta x = 2000$ m, $N = 10$, $\Delta t = 600$ s;

B: $\Delta x = 1000$ m, $N = 20$, $\Delta t = 300$ s;

C: $\Delta x = 500$ m, $N = 40$, $\Delta t = 150$ s;

D: $\Delta x = 250$ m, $N = 80$, $\Delta t = 75$ s;

E: $\Delta x = 125$ m, $N = 160$, $\Delta t = 37.5$ s;

where N is the number of vertical σ-layers.

For the resolution C, figure 3.2 (upper panels) shows the density distribution at $t = 5$ h for the central part of the domain for both advection schemes.

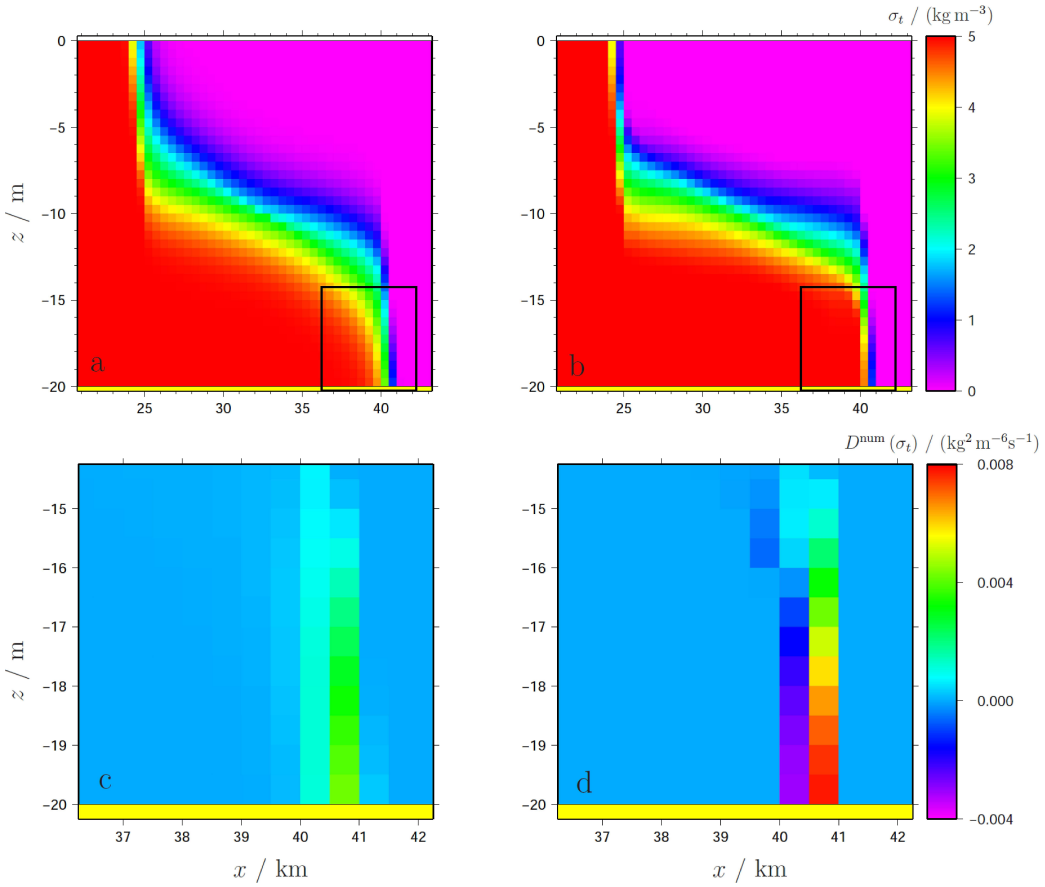

Figure 3.2: Lock exchange scenario for resolution C ($\Delta x = 500$ m, $N = 40$, $\Delta t = 150$ s). Panels a and b show the density distribution at $t = 5$ h, panels c and d show the numerical tracer variance decay, $D^{\mathrm{num}}(\sigma_t)$, in the frontal area. Results for panels a and c have been obtained with the first-order upstream advection scheme, for panels b and d with the P2-PDM scheme. The black square in panels a and b indicate the frame for panels c and d.

For the upstream schemes the density front at the bed stretches over more than 3 grid boxes, while for the P2-PDM scheme it stretches over only two grid boxes. The lower panels show the numerical tracer variance decay in the frontal area for both schemes. For the upstream scheme, D^{num} is, as expected, entirely positive, while the P2-PDM scheme shows a strong positive mixing directly at the front and a compensating negative mixing (anti-diffusion) after the front, similar to the one-dimensional case documented in section 3.3.1. At $t = 5$ h, the upstream scheme generated a higher volume integrated numerical mixing of $\int_V D^{\mathrm{num}} \mathrm{d}V = 31.0$ kg^{2}m^{-3}s^{-1} as opposed to a value of $\int_V D^{\mathrm{num}} \mathrm{d}V =$

24.7 $kg^2m^{-3}s^{-1}$ for the P2-PDM scheme.

In figure 3.3, time series of the volume integrals of σ_t^2 are shown for both advection schemes at all resolutions (upper panels), as well as the volume integrated numerical tracer variance decay (lower panels).

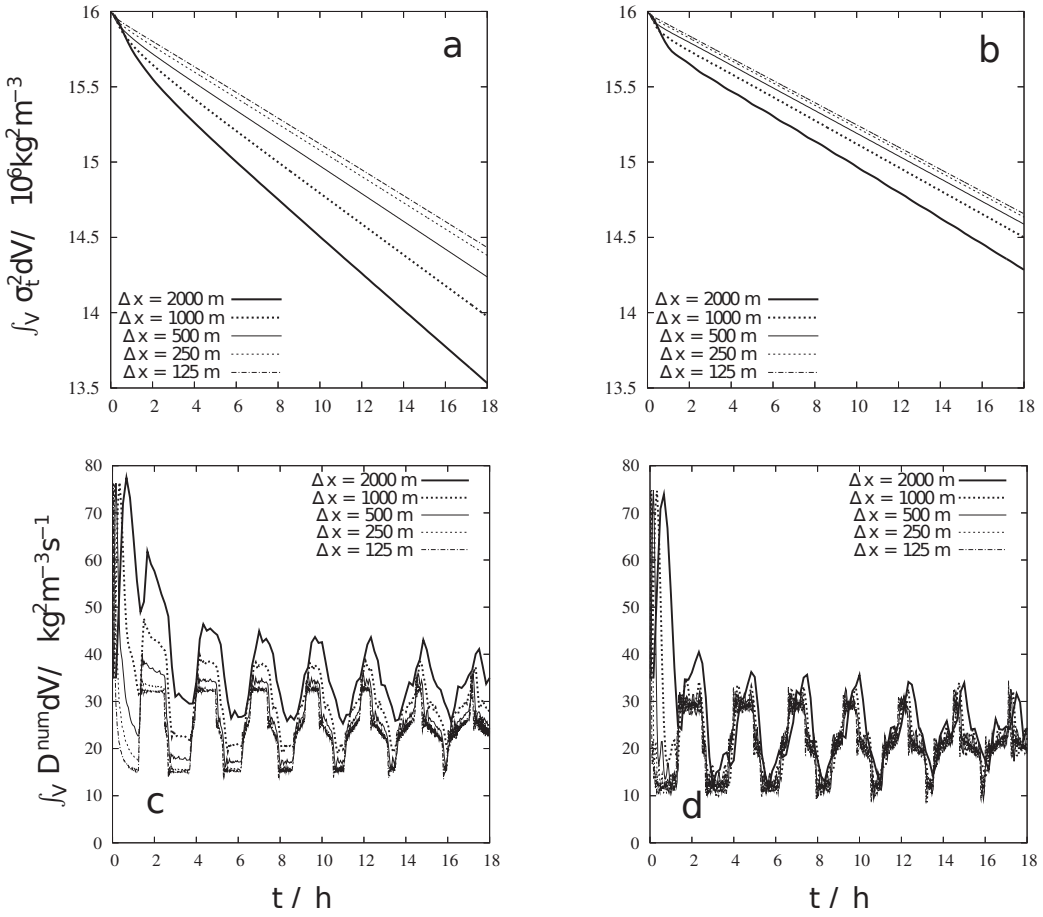

Figure 3.3: Time series of volume integrated density variance (panels a and b) and volume integrated numerical variance decay (panels c and d) for the lock exchange scenario calculated with four different resolutions. For panels a and c, the first-order upstream scheme has been used, and for panels b and d, the P2-PDM scheme has been used.

Clearly, the upstream scheme is generally generating more mixing than the P2-PDM scheme, and the higher the resolution is, the lower is the mixing for both schemes. The volume integrated variance decay shows for all schemes and resolutions strong oscillations due to the external seiche period of about 2 1/2 hours. For the upstream scheme, also the volume integrated variance decay after the initial seiche period is significantly decreasing with higher resolution. This effect is much weaker for the P2-PDM scheme. This small gain in model accuracy for the P2-PDM scheme with increasing resolution may be due to the fact, that the horizontal motion of a vertical front will result in infinite vertical velocity directly at the front for the frictionless case, with the consequence that the discretised vertical velocity cannot converge for refined resolution.

3.3.3 Marginal sea overflow study

In order to compare numerical and physical tracer variance decay for a more realistic overflow situation, a two-dimensional (horizontal-vertical) marginal sea scenario has been generated, with a bathymetry similar to the major pathway of Baltic Sea inflow events (for the oceanography of these events, see e.g. Feistel et al. (2006) and references therein). For the present study, the domain has been closed, physical mixing is included (see section 1.2.1), but meteorological forcing and earth rotation are neglected. The four basins shown in figure 3.4 are, from left to right, the Arkona Sea ($D = 48$ m), the Bornholm Sea ($D = 99$ m), the Stolpe Furrow ($D = 98$ m) and the Gotland Deep ($D = 250$ m).

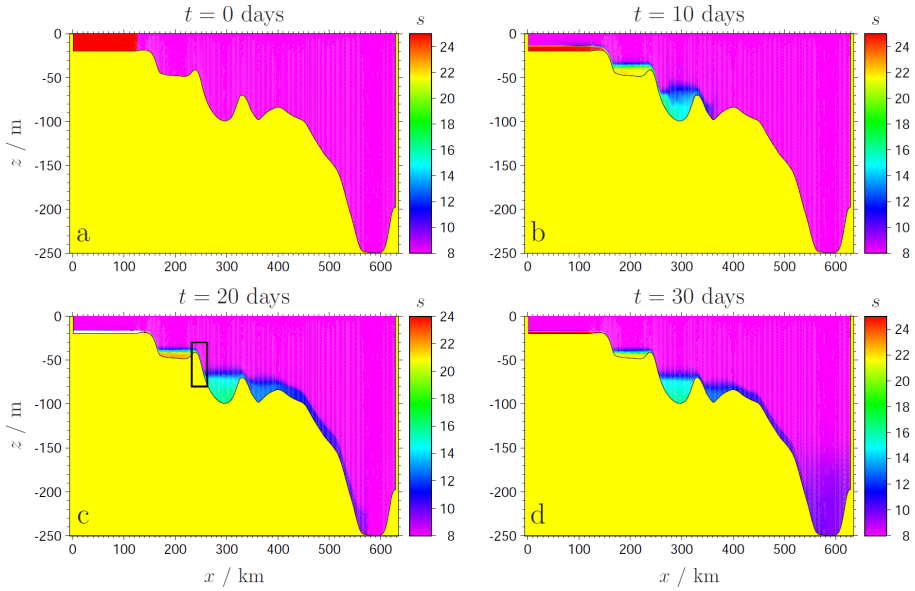

Figure 3.4: Salinity distribution for the two-dimensional marginal sea overflow study at the beginning of the simulation (panel a) and after 10 days (panel b), 20 days (panel c) and 30 days (panel d) of simulation. The small rectangle inserted in panel c shows the domain for the numerical mixing analysis shown in figure 3.5. The results have been calculated with the medium resolution of $\Delta x = 2100$ m.

A major inflow event into a brackish domain simulated here by initialising the salinity to $s = 25$ for $x \leq 125$ km and to $s = 8$ elsewhere, see panel a of figure 3.4. Similar to the lock exchange study discussed in section 3.3.2, an exchange flow is forced by horizontal pressure gradients. This develops then into to a cascading dense bottom current flowing over sills into subsequent basins, subject to significant entrainment of overlaying brackish water. Figure 3.4 shows, how the dense bottom current has filled the Bornholm basin after 10 days, has reached the bottom of the Gotland Deep after 20 days, and has partially filled the Gotland Deep after 30 days. It should be noted that in reality, with Earth rotation, background stratification and three-dimensional basin structure such an inflow event may need a couple of months to reach the Gotland Deep.

For this inflow scenario, three different resolutions are used:

A: $\Delta x = 6300$ m, $N = 20$, $\Delta t = 1600$ s;

B: $\Delta x = 2100$ m, $N = 40$, $\Delta t = 80$ s;

C: $\Delta x = 700$ m, $N = 80$, $\Delta t = 40$ s;

Figure 3.6 shows the horizontal distribution of temporally averaged numerical and physical variance

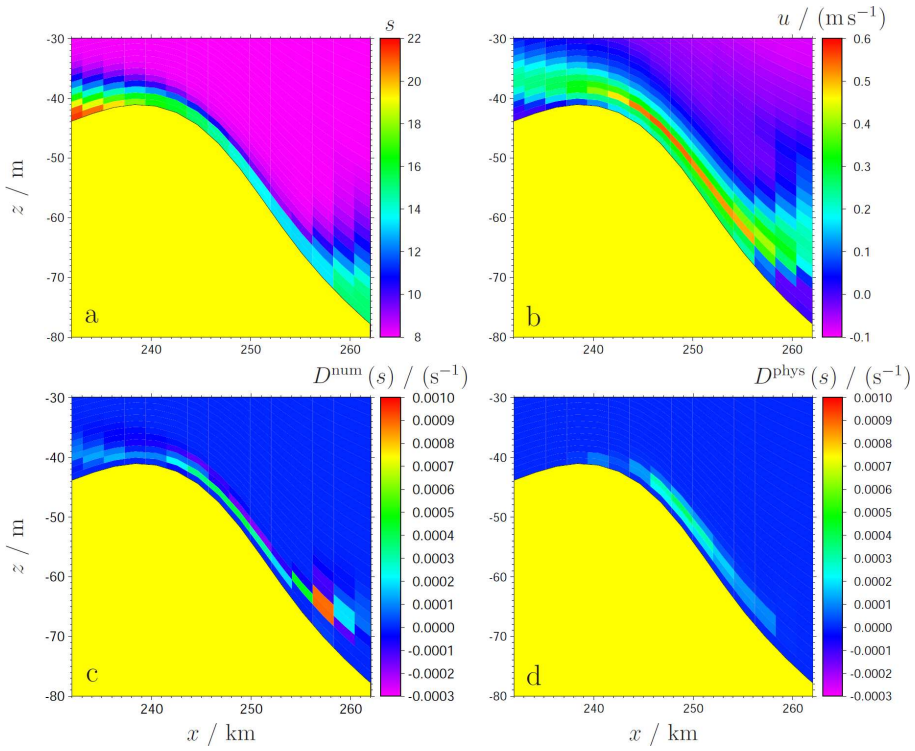

Figure 3.5: Analysis of effective mixing processes inside the small subdomain indicated in figure 3.4. Panel a: Salinity; panel b: horizontal velocity; panel c: numerical salinity variance decay; panel d: physical variance decay. All values are shown as coloured polygons as they are located in the numerical grid. The physical variance decay (panel d) has been interpolated onto the tracer grid.

decay for all three resolutions. Significant peaks in numerical mixing occur in the overflow regions, where dense water is cascading down the slope, and these locations do approximately coincide with the peaks in physical mixing.

Numerical mixing is decreasing with increasing resolution, as seen in the volume integrated time averaged salinity variance which decreases from a value of 143 m^2s^{-1} (resolution A) to 105 m^2s^{-1} (resolution B) and to 82 m^2s^{-1} (resolution C), see figure 3.6. With increasing resolution, also the amount of negative mixing decreases, indicating that a better resolution of fronts leads to less violations of monotonicity for unlimited, linear schemes. In the same time, physical mixing is slightly increasing with increasing resolution, i.e. the total effective mixing decreases. However, even for a resolution as high as $\Delta x = 700$ m, which is substantially higher than the resolution of currently used Baltic Sea models (see, e.g. Meier et al. (2003)), numerical mixing is still larger than physically induced mixing. It is therefore useful to study where exactly the numerical and the physical mixing occurs.

In figure 3.5, a snapshot of the overflow into the Bornholm Sea is shown at day 20 after the initialisation. Before and after the separating sill the inflow is detached from the bed, since the overflow water is riding on denser, stagnant water, see the velocity distribution in panel b of figure 3.5. Over and slightly behind the sill, the flow velocity peaks to more than 0.5 $m\,s^{-1}$ at the density interface separating the dense bottom current from the ambient flow. In this region, where the vertical velocity shear is largest, also the physical mixing has a maximum, expressing strong entrainment of ambient water into the dense plume. There, also the numerical mixing is elevated, resulting in the local maximum of time

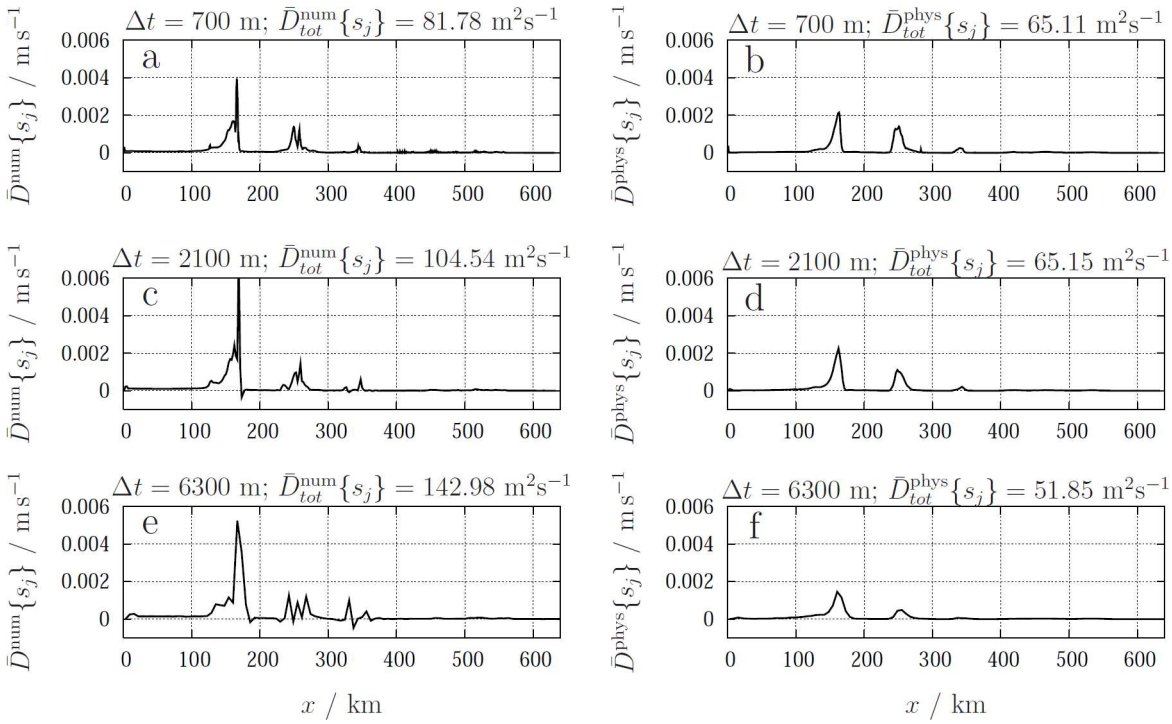

Figure 3.6: Horizontal distribution of vertically integrated and temporally averaged numerical salinity variance decay, $\bar{D}^{\mathrm{num}}\{s_j\} = \frac{1}{T}\int_0^T \int_{-H}^{\eta} D^{\mathrm{num}}\{s_j\}\mathrm{d}z\mathrm{d}t$, (panel a, c and e) and physical salinity variance decay, $\bar{D}^{\mathrm{phys}}\{s_j\} = \frac{1}{T}\int_0^T \int_{-H}^{\eta} D^{\mathrm{phys}}\{s_j\}\mathrm{d}z\mathrm{d}t$, (panels b, d and e). Three different resolutions have been used, a fine resolution of $\Delta x = 700$ m (panels a and b), a medium resolution of $\Delta x = 2100$ m (panels c and d), and a coarse resolution of $\Delta x = 6300$ m (panels e and f), for details, see section 3.3.3. For quantitative comparison, the spatially integrated and time averaged variance decay, $\bar{D}^{\mathrm{num}}_{tot}\{s_j\} = \int_0^L \bar{D}^{\mathrm{num}}\{s_j\}\mathrm{d}x$ or $\bar{D}^{\mathrm{phys}}_{tot}\{s_j\} = \int_0^L \bar{D}^{\mathrm{phys}}\{s_j\}\mathrm{d}x$, is given for each panel.

averaged numerical salinity variance decay at approximately $x = 260$ km as shown in panel c of figure 3.6. However, the maximum value of numerical mixing is reached further downstream, where the plume water plunges into the pool of dense water in the Bornholm Sea. The explanation for this is that here the along-coordinate density gradient is large as well as the horizontal flow velocity. In contrast to that, further upstream the isopycnals and the flow are parallel to the coordinates, such that numerical mixing remains relatively small.

3.3.4 DOME test case

As a three-dimensional example for the mixing diagnostics introduced here, the DOME (Dynamics of Overflow Mixing and Entrainment) test case, which has been used for several model studies of mixing in overflows (see e.g. Ezer and Mellor (2004), Legg et al. (2006)) is used. The bathymetry for the DOME setup consists of a linearly sloping plain, descending from 600 m depth at $y = 200$ km to a depth of 3600 m at $y = 500$ km. For $y > 500$ km the bathymetry has a constant depth of 3600 m. There is no depth variation in x-direction, except for a channel of 600 m depth, 100 km width and 200 km length appended to the upper part of the slope. The domain is closed at the lateral boundaries. Horizontal viscosity and diffusivity are set to zero. A linear equation of state is used, with a constant salinity and a linear stable background stratification with a surface to bottom density gradient of $\Delta\rho = 2\ \mathrm{kg\,m^{-3}}$.

In the channel, a geostrophically balanced inflow of $5 \cdot 10^6$ $m^3 s^{-1}$ with an excess density of $\Delta\rho = 2$ $kg\,m^{-3}$ is imposed. This inflowing water is marked by a passive tracer concentration of $c = 1$, whereas the rest of the domain is initialised to $c = 0$. For details of the DOME setup, see Ezer and Mellor (2004).

Here, the horizontal resolution is $\Delta x = \Delta y = 10$ km, and 21 equidistant σ-layers have been used for this simulation.

Figure 3.7 shows the temporal evolution of the dense bottom current (expressed as bottom concentration of tracer c) as snapshots 10, 20, 30 and 40 days after the initialisation.

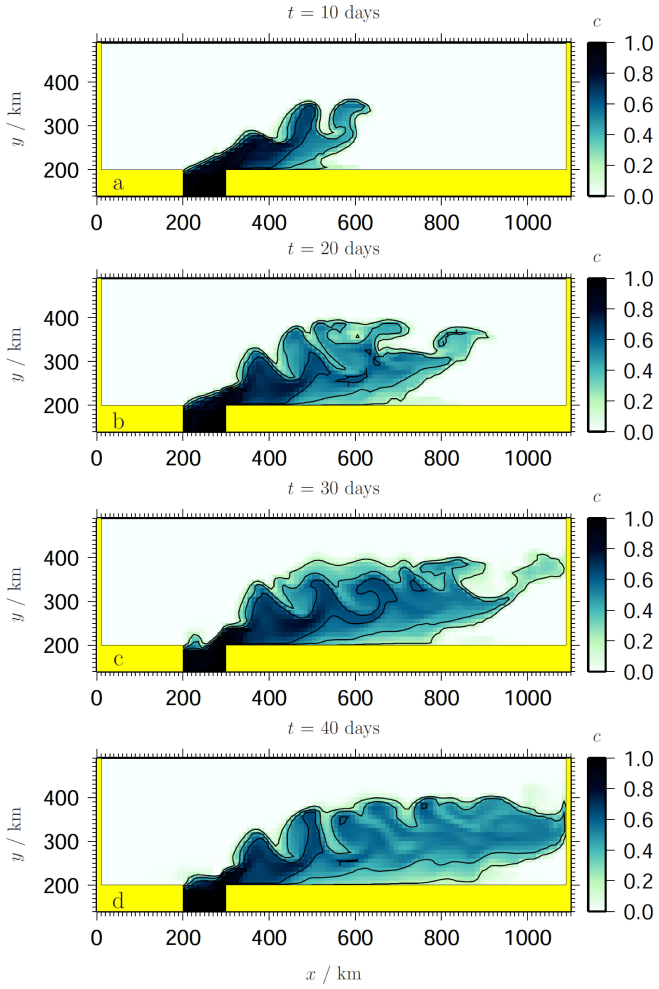

Figure 3.7: Bottom concentration of tracer c for the DOME simulation after 10 days (panel a), 20 days (panel b), 30 days (panel c) and 40 days (panel d) of simulation. Parts of the domain ($0 \leq y \leq 150$ km and $450 \leq y \leq 780$ km) have been cut out for clarity.

These results agree well with the σ-coordinate results of Ezer and Mellor (2004), when a low horizontal diffusivity is used (see their figure 5). As shown in figure 3.8, numerical mixing is clearly dominating over the physical mixing.

The numerical mixing (here shown as vertically integrated numerical variance decay of tracer c) is strongest in regions of moving fronts, where it shows the same characteristic picture as for the lock exchange experiment: along the front, strong positive and negative mixing filaments are adjacent to

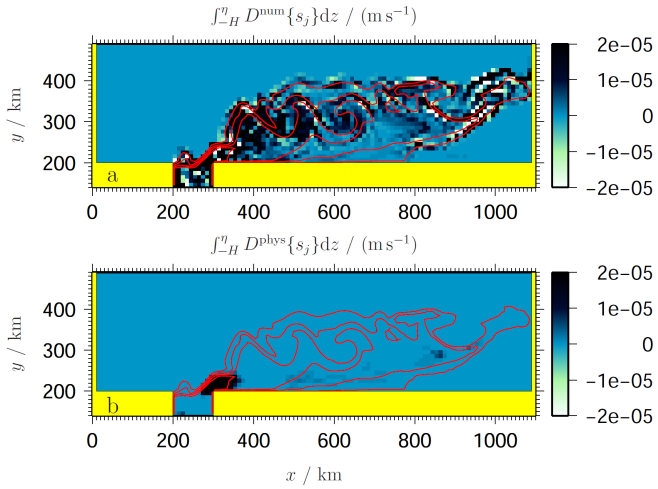

Figure 3.8: Horizontal distribution of vertically integrated numerical (panel a) and physical (panel b) variance decay of tracer c for $t = 30$ days. All values larger than $2 \cdot 10^{-5}$ m s^{-1} are shown in black, all values smaller than $-2 \cdot 10^{-5}$ m s^{-1} are shown in white. The red isolines are lines of constant concentration of tracer c, the contour interval is 0.2, and the contour lines are identical to those shown in panel c of figure 3.7.

each other. Significant physical mixing only occurs near the entrance of the dense water into the domain.

The time series of total numerical and physical mixing (see figure 3.9) clearly shows that the numerical mixing for this model experiment is about one order of magnitude larger than the physical mixing.

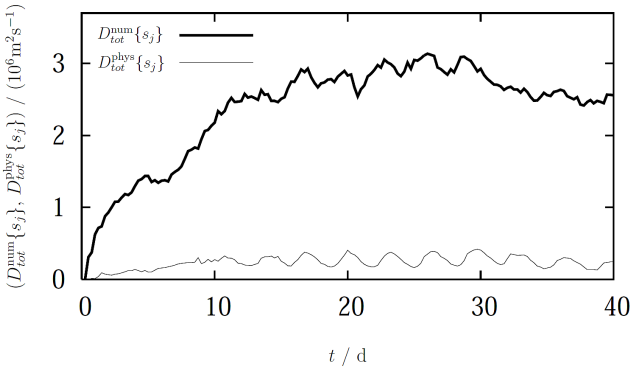

Figure 3.9: Time series of total (volume integrated) numerical (bold line) and physical (thin line) variance decay of tracer c for the DOME simulation. The mixing within the entrance area ($y \leq 200$ km) has not been considered for this calculation.

3.4 Realistic model scenarios

The coastal model application analysed here covers the area of the Western Baltic Sea. Here, frequent and high-saline inflow events from the North Sea are driven by sea level differences between the Kattegat and the Arkona Basin (Figure 3.10). This model application with general vertical coordinates (gvc) was used by Burchard et al. (2009) to investigate the natural mixing on the pathway of these dense bottom currents in the dynamic Arkona Sea. These moving tracer gradients in a complex bathymetry might

introduce significant numerical dispersion and dissipation to the advection of salinity. It is therefore of great interest to compare the magnitude and distribution of numerical mixing compared to physically induced mixing. The diagnostic method explained in section 3.2.2 is then applied to obtain the amount of numerical mixing within this model simulation. Further experiments are carried out to identify the reasons and locations of high numerical mixing. As the advection scheme for momentum and tracer a TVD (Total Variation Diminishing) scheme with the ULTIMATE QUICKTEST limiter is used, for details, see Pietrzak (1998).

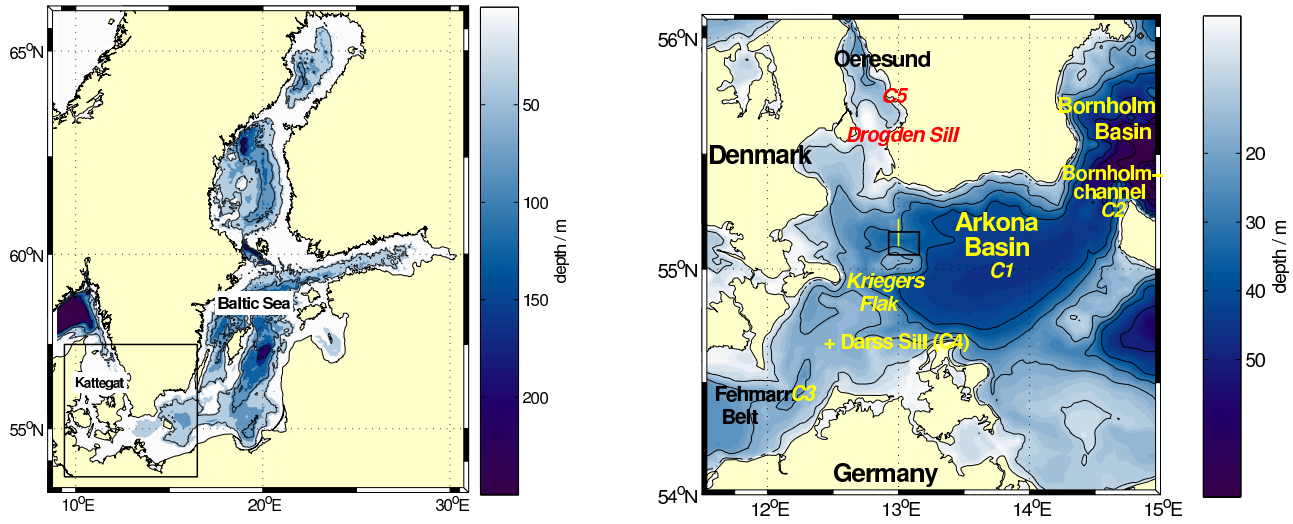

Figure 3.10: The left panel shows the Baltic Sea with the marked region denoting the model domain. The right panel shows a part of the model domain which is the region of the Arkona Sea where the physical and numerical mixing investigations of this work is based on.

3.4.1 Quantification and qualification of numerical mixing

The medium-intensity inflow event of early February 2004 (Burchard et al. (2009); Sellschopp et al. (2006)) is used to investigate the sources of high numerical mixing. Here the 10 km wide channel north of Kriegers Flak (see yellow section in Figure 3.10) was chosen due to the very localised occurrences of strong salinity gradients and high velocities. Two factors demonstrate the advantages in taking this region for numerical mixing investigations: there are strong gravity currents and these currents propagate in the west-east direction (Umlauf et al. (2007)) which substantially simplifies the analysis. As seen in Figure 3.11d the gravity current is in geostrophic balance with high velocities of up to 0.3 ms^{-1} in the centre of the plume.

This model derived velocity is underestimated compared to the observational data of the the medium-intensity inflow event in February 2004 (Sellschopp et al. (2006); Burchard et al. (2009)) because the tilting of the geostrophic interface is underestimated. This is probably due to the low horizontal resolution with less than 10 grid boxes across the dense bottom current inducing stronger numerical damping.

The critical point for high numerical mixing within the plume is the exchange flow in the cross-direction as seen in Figure 3.11c as well as the sawtooth-type vertical distribution of salinity and thus density

(Figure 3.11a) due to the discretisation of the gvc. The transverse dynamics consist of a northward current at the bottom and a southward current above the plume interface. It can be seen that there is an advection of high density gradients in the northward direction at the bottom which causes a spreading of the isolines in the southern part of the channel (see isolines of salinity in Figure 3.11g). Due to the sawtooth-type character of the horizontal distribution of salinity (a consequence of gvc in areas with steep slopes), strong spurious horizontal gradients, together with high velocities, are advected through the interfaces of the vertical coordinates. It is shown in Figure 3.11i,j that the advection of the tracer through the vertical coordinates (also due to the upward and downward motion of the isopycnals during inflow events) plays the dominant role regarding the increased numerical mixing shown in Figure 3.11i,j. Here the numerical mixing is calculated with respect to the directional split in the x-direction and y-direction only. Since the eastward propagation of the plume occurs mainly in the direction of the coordinate levels, exchange between the vertical layers occurs mainly due to vertical mixing processes and less due to vertical advection. This is not the case for the transverse dynamics which drives a flow regime through the vertical interfaces inducing much higher numerical mixing (Figure 3.11j). This is generally a problem that might be solved using adaptive vertical coordinates (Burchard and Beckers (2004)) or hybrid isopycnic-Cartesian coordinates (Bleck (2002)) where coordinate levels are more parallel to the isopycnals and the described problems of gvc might occur to a lower degree.
Figure 3.11h shows the vertical numerical diffusivity,

$$\nu_t^{num} = \frac{D^{num}}{2(\partial_z S)^2}, \tag{3.12}$$

as a snapshot during the inflow event in early February 2004, as well as the physical model derived diffusivity ν_t^{phy} in vertical slices at the same time. Figure 3.11g shows eddy diffusivities having the expected range between $10^{-4}\mathrm{m}^2\mathrm{s}^{-1}$ in the centre of the plume and much higher values of $10^{-3}\mathrm{m}^2\mathrm{s}^{-1}$ at the bottom. This is consistent with the work of Sellschopp et al. (2006) who analysed observational data from the same inflow event at a slightly different position north of Kriegers Flak. The numerical diffusivity has values which are of the same orders of magnitude, even showing values of $10^{-1}\mathrm{m}^2\mathrm{s}^{-1}$. The high numerical diffusivities at the bottom ($\sim$ 35 m depth) and above the plume ($\sim$ 20 m depth) are due to low vertical salinity gradients $\partial_z S$ in this areas.
To improve the understanding of the underlying reasons for high numerical mixing, time-series of salinity, velocity, physical and numerical mixing are presented in Figure 3.12 and Figure 3.13.
A good example to illustrate the differences in numerical and physical mixing is a comparison between Figure 3.12 for a water column northeast of the Drodgen Sill with high numerical mixing and Figure 3.13 for the centre of the Arkona Basin showing much less numerical mixing. Both example figures show very different conditions around the Drodgen Sill (high velocities and high fluctuations in salinity) and the Arkona Basin (comparably strong pycnocline, weaker fluctuations in the vertical density distribution and much lower velocities). Hence this confirms that high tracer gradients together with high velocities induce a numerical mixing that is orders of magnitude higher than the physical mixing. Quantitatively this is visible in Figure 3.14 where the vertically integrated values of physical and numerical mixing are plotted against each other for the stations shown in Figure 3.12 and Figure 3.13.
In Figure 3.14a it is demonstrated that for regions of steep topography and high fluctuations in the

tracer field, the quotient between numerically and physically induced mixing shows remarkable values of up to 1500 and even more. Even in areas of low variations in depth (less horizontal tracer gradients in the sigma space) and less transport of tracer fronts like in the Arkona Basin (Figure 3.13), the numerical mixing has the same orders of magnitude for physical and numerical mixing (Figure 3.14b). It is also notable that high physical mixing may occur coincidently with low numerical mixing and vice versa.

As numerical diffusion in a certain grid box is significantly correlated to the variations in the horizontal tracer gradient and the strength of the velocity field, a decadal logarithmic scatter plot for this relationship is given in Figure 3.15a, showing the following relationship:

$$CN = |u| \left(\frac{\partial_x S + \partial_y S}{2} \right)^2 h_\sigma, \tag{3.13}$$

with the horizontal salinity gradient $((\partial_x S + \partial_y S)/2)^2$, the absolute value of the current velocity in the grid cell $|u|$ and the height of the sigma level h_σ.

We see a strong correlation between both measures which gives the already well known picture of numerical mixing being strongly dependent on the strength of the tracer gradients and the velocity field.

High numerical mixing is also in balance with the physically induced mixing as shown with Figure 3.15b, which is generally clear because transport of strong tracer gradients and high velocities induces both high numerical and physical mixing. The correlation is not dependent on the vertical level or time frame being used to produce the scatter plot. Differences in the scatter plot distribution are only found for plotting different areas of the model domain which is demonstrated in Figure 3.16.

The scatter plot was created using snapshot grid cell values in the area $12° - 15°E$, $54° - 56°N$ from February, $01 - 15$ 2004.

Figure 3.16 shows scatter plots of physical versus numerical salinity mixing for different water columns in the model domain. It is shown that for all six water columns (named C1-C6 in Figure 3.10) the numerical mixing is on average higher than the physically induced mixing.

3.4.2 Investigation of different advection schemes

Several studies investigated the impact of numerical mixing using different kinds of advection schemes. Gerdes et al. (1991) have discussed the marked differences between model simulations using different advection schemes in a long-term GCM (General Circulation Model) simulation which have been found out to be markedly different. Griffies et al. (2000) used the analysis method provided by Winters et al. (1995) and Winters and D'Asaro (1996) to quantify the rate of spurious diapycnal mixing associated with numerical advection.

In this section investigations on three different advection schemes are carried out. These are the monotone first order upstream (FOU) scheme and two high-order advection schemes with a monotone TVD one-step scheme applied in a directional split mode. The first high-order advection scheme is the monotone third-order ULTIMATE QUICKTEST method (Leonard (1991) and Pietrzak (1998)) and the second is the monotone second-order Superbee (Pietrzak (1998); Hirsch (1988) and LeVeque (1992)) limiter. Together with the FOU scheme these advection schemes cover the range from a very

simple and diffusive advection scheme up to two different less diffusive higher-order advection schemes. Both high-order advection schemes resolve sharp tracer gradients much better. The higher-order TVD schemes have been successfully used for large-scale ocean modelling (Gerdes et al. (1991)) as well as for coastal model simulations (Burchard et al. (2009)).

In Figure 3.17 the time series of the volume integrated physical and numerical mixing (time average every 12 hours) in the region north of Kriegers Flak, see the black rectangle in the right panel of Figure 3.10, are shown.

Due to a local inflow of dense bottom water in February (Burchard et al. (2009)), both physical and numerical mixing reach a maximum in the middle of February. It can be seen that the FOU scheme shows much less numerical mixing than the other two schemes because FOU has already destroyed sharp tracer gradients which allows less numerical and consequently less physical mixing. Here it must be pointed out that this comparatively unexpected low numerical mixing for the FOU scheme compared to the higher order schemes applies only for this individual gravity current scenario, with already strongly reduced density gradients due to high numerical diffusion of FOU. The quotient

$$R = \left(\int D^{\mathrm{num}} dV \right) / \left(\int D^{\mathrm{phy}} dV \right), \tag{3.14}$$

for the integration over February 2004, becomes $R = 9.4$ for FOU, $R = 5.3$ for Superbee and $R = 4.5$ for ULTIMATE QUICKTEST. The relationship supports using ULTIMATE QUICKTEST as the favourite scheme, even though, compared to Superbee, the difference is not big. Generally the response of both Superbee and ULTIMATE QUICKTEST to the dense bottom current (red and black line in Figure 3.17) is qualitatively and quantitatively very similar.

Figure 3.18a,b,c shows the relationship between D^{num} and CN.

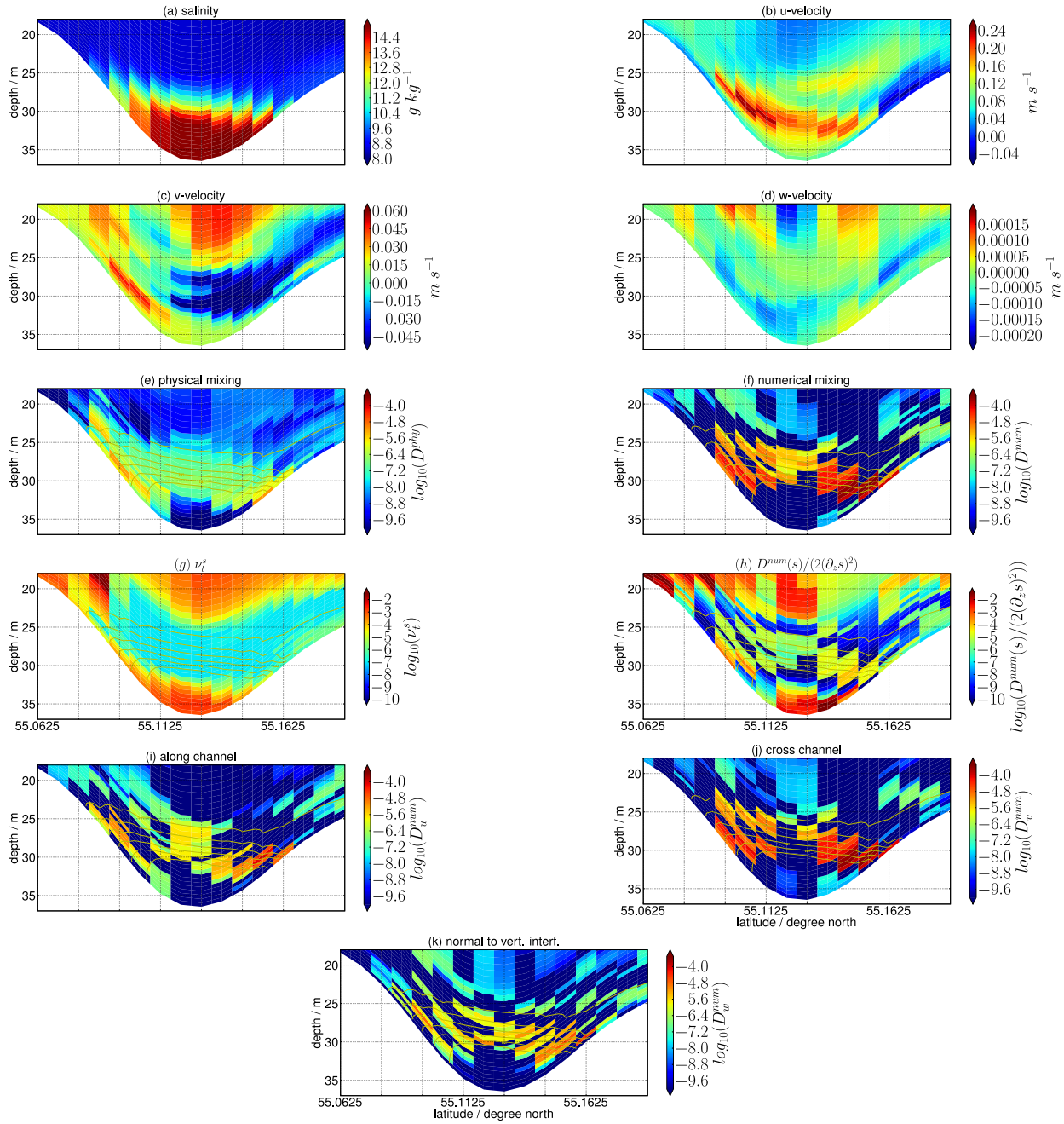

Figure 3.11: Panels showing snapshots of different physical and numerical quantities during an inflow event in early February 2004, which are (a) the salinity, (b) the horizontal along channel u-velocity, (c) the horizontal cross channel v-velocity, (d) the vertical velocity w normal to the vertical interfaces, (e) the numerical mixing compared to (f) the physical diffusion. Panel (g) shows the snapshot of the model derived eddy diffusivity and (h) a snapshot of the vertical numerical diffusivity. Plots (i), (j) and (k) are showing the numerical mixing in each spatial dimension.

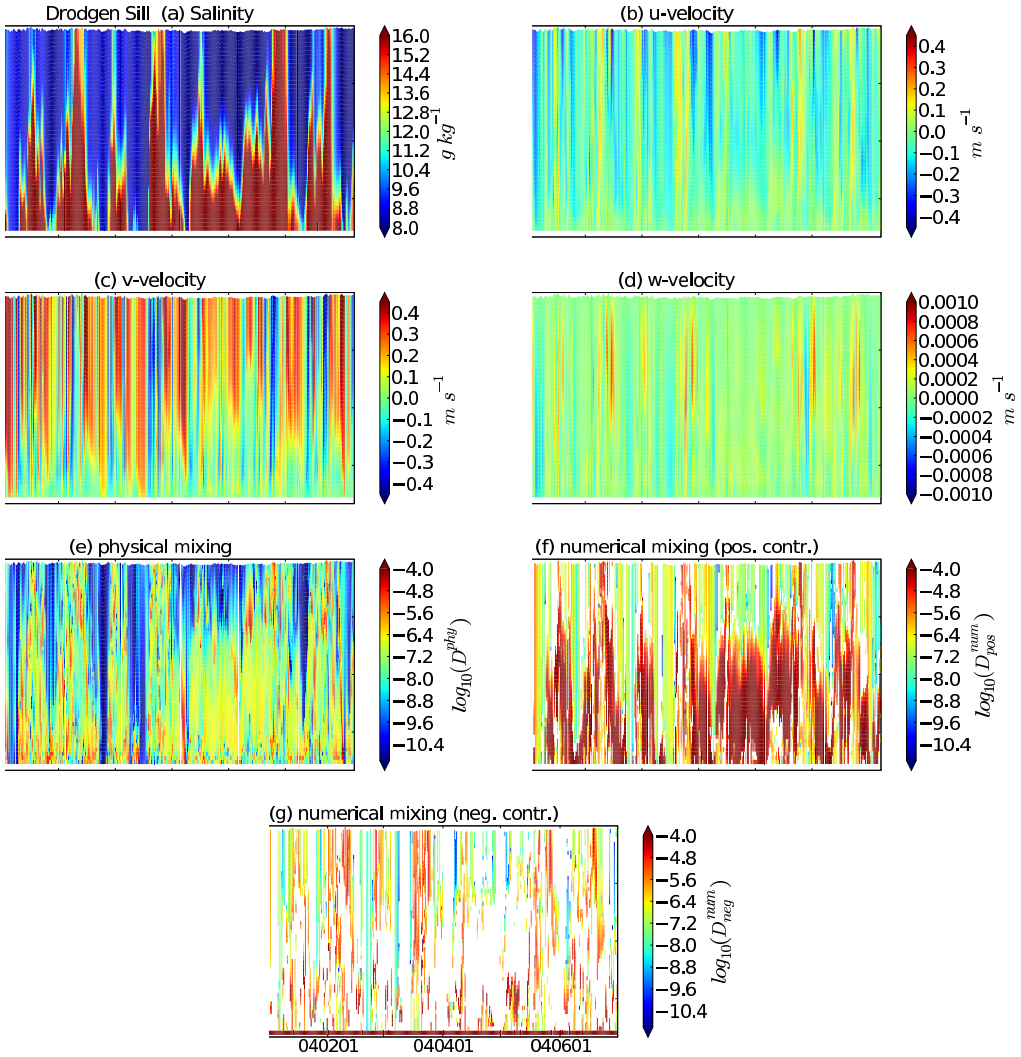

Figure 3.12: Panels showing a time-series of (a) salinity, (b) u-velocity, (c) v-velocity, (d) w-velocity, (e) physical mixing and (f) the positive and (g) the negative contributions of the numerical mixing. The column was taken at $12.875°E$ and $55.7542°N$ north of the Drodgen Sill. The position is named C3 in Figure 3.10.

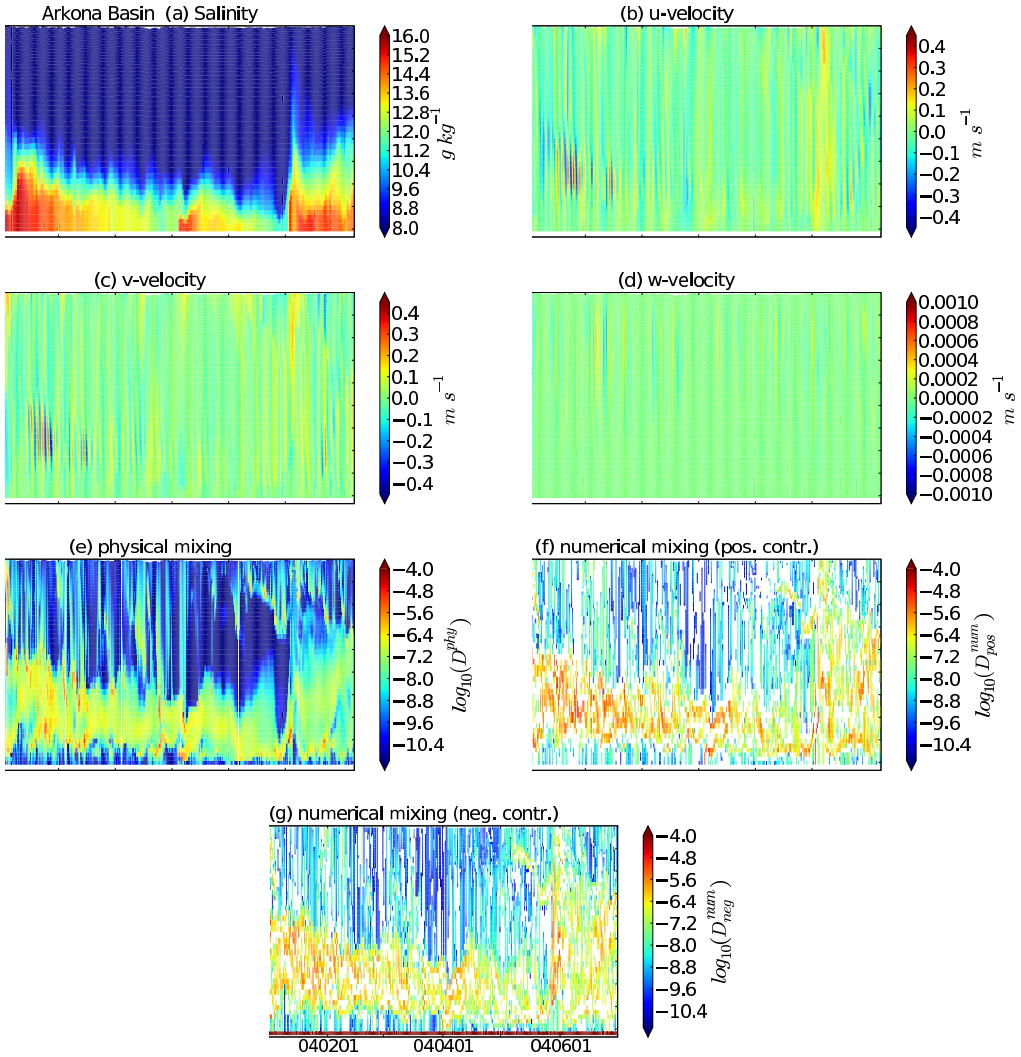

Figure 3.13: Panels showing a time-series of (a) salinity, (b) u-velocity, (c) v-velocity, (d) w-velocity, (e) physical mixing and (f) the positive and (g) the negative contributions of the numerical mixing. The column was taken at $13.6917°E$ and $54.9958°N$ in the central Arkona Basin. The position is named C5 in Figure 3.10.

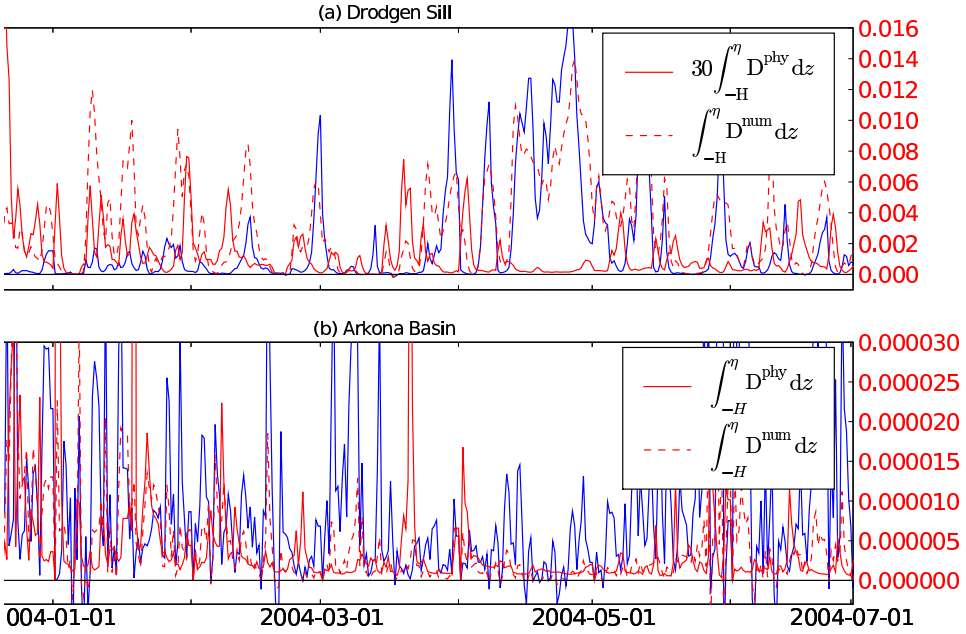

Figure 3.14: Panels showing quotient and difference between numerical and physical mixing over seven months simulation time for different water columns in the model domain. The positions are marked by C3 (Drodgen Sill) and C5 (Arkona Basin) in Figure 3.10.

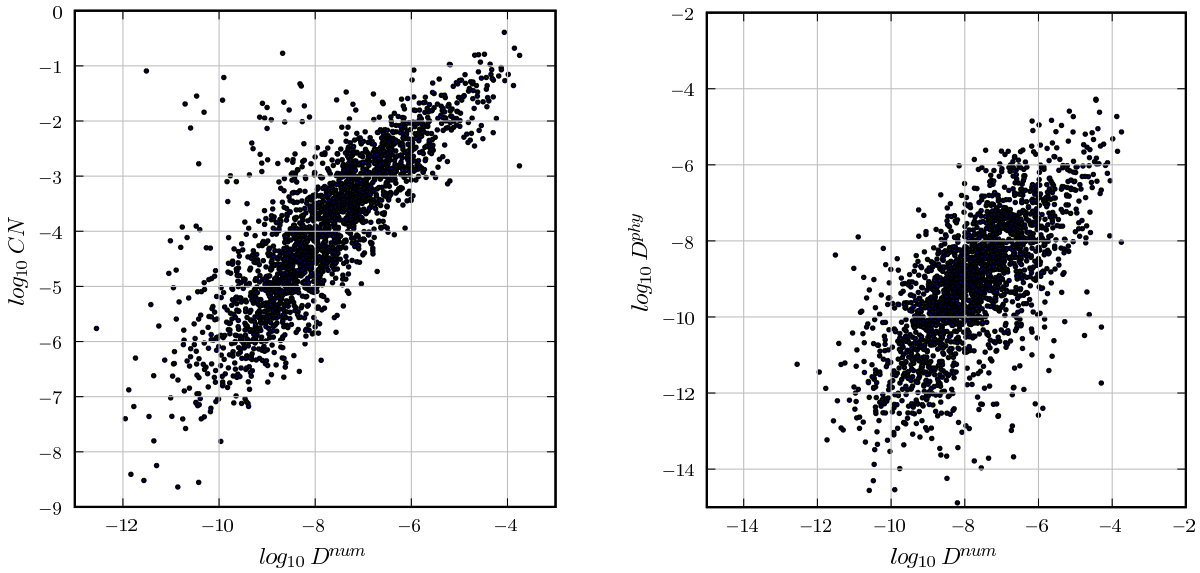

Figure 3.15: Upper panel showing scatter plots of numerical mixing against velocity multiplied by square of the horizontal salinity gradient. The lower panel shows the numerical mixing against the physically induced mixing in the model. Each point denotes the snapshot values in a certain grid box, nearly 10000 randomly chosen grid boxes in the model domain are used to reproduce these two relations.

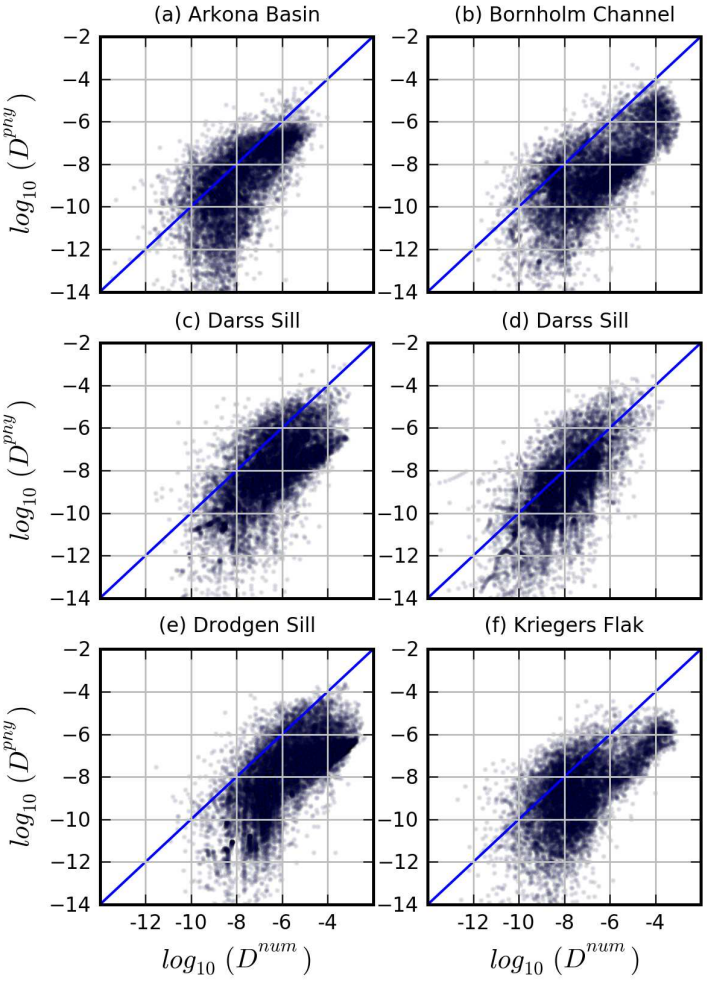

Figure 3.16: Here each point in the plot denotes the snapshot values of a certain grid box for both values, physical and numerical mixing (several 10000 points were taken for each plot). The green line shows where numerical and physical mixing have same values and with the contribution around is demonstrated how strong numerical mixing is. The blue line tries to give an estimate of maximum numerical mixing of certain physical mixing values. (a) taken at $13.6917°E$ and $54.9958°N$; (b) taken at $14.5417°E$ and $55.2875°N$; (c) taken at $12.175°E$ and $54.4542°N$; (d) taken at $12.4083°E$ and $54.6875°N$ (e) taken at $12.875°E$ and $55.7542°N$; (f) taken at $13.0083°E$ and $55.1375°N$. Each of the water columns are marked by C1-C6 in Figure 3.10.

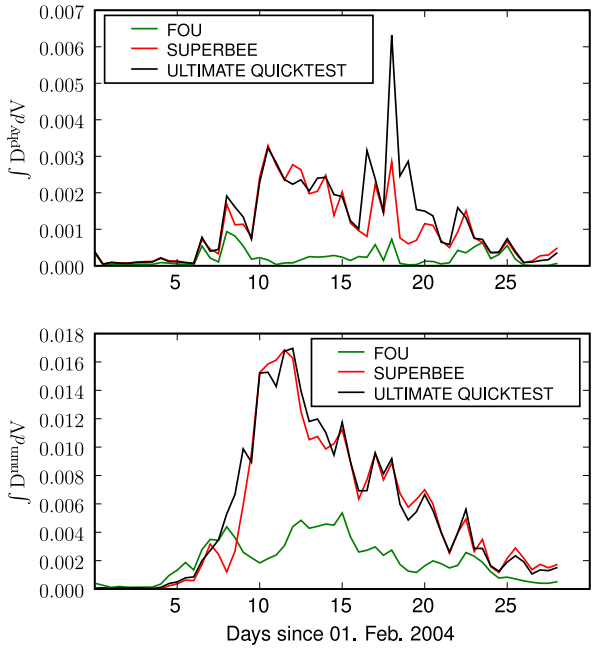

Figure 3.17: Time series of volume integrated and time averaged (every 12 hours) physical (upper panel) and numerical (lower panel) mixing for different advection schemes.

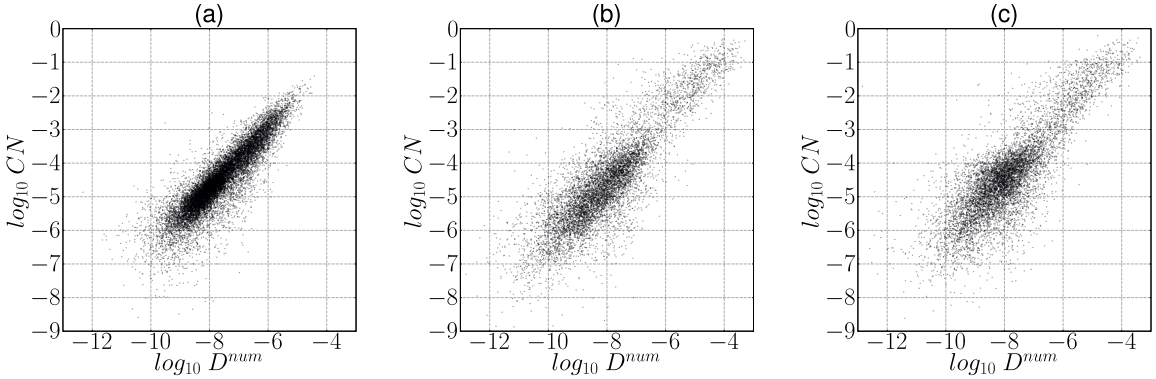

Figure 3.18: Panels showing scatter plots of numerical mixing and CN for different advection schemes. FOU: (a); Superbee: (b); ULTIMATE QUICKTEST: (c).

It is clear that CN for both higher order advection schemes shows a statistically significant lower degree of numerical mixing than the FOU scheme. This points out, as expected, that FOU shows much stronger numerical mixing for the same physical conditions. Additionally it is notable, that CN and D^{num} of Superbee and ULTIMATE QUICKTEST are one order of magnitude stronger for the peak values. As already shown (Figure 3.17), the response of both higher order advection schemes is very similar, hence the scatter plots for the correlation of numerical diffusion to physical quantities such as velocity and tracer gradient (Figure 3.18b,c) and relationship between numerical and physical mixing (Figure 3.19b,c) shows a similar distribution.

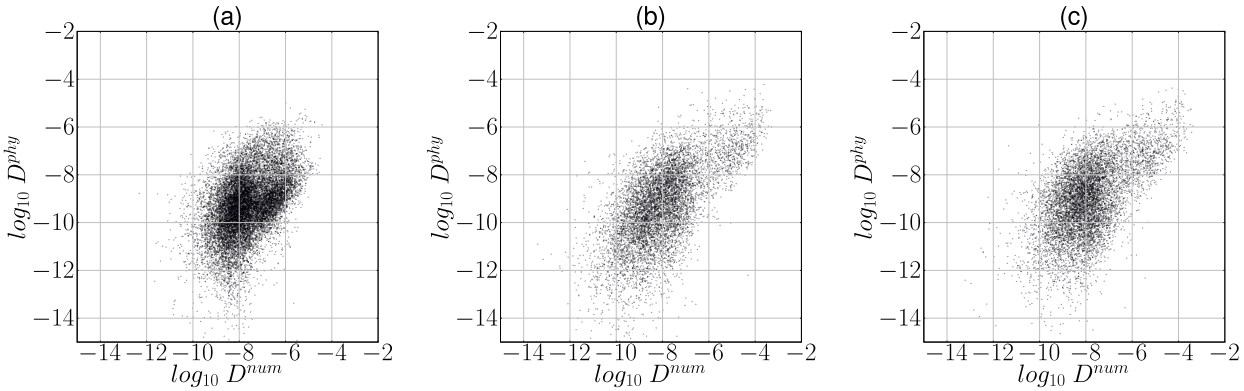

Figure 3.19: Panels showing scatter plots of numerical mixing and physical mixing for different advection schemes. FOU: (a); Superbee: (b); ULTIMATE QUICKTEST: (c).

The ULTIMATE QUICKTEST advection scheme, which has been used in this work for most of the simulations, shows the lowest values in R. Nevertheless it must be pointed out, that for all advection schemes the numerical mixing is higher than the physically induced mixing. Even with the non-invasive variance decay method used in this work, it is not trivial to evaluate different advection schemes, since less numerical mixing in some regions allows for higher gradients and thus higher numerical mixing in other regions and vice versa.

3.4.3 Vertically integrated and time-averaged estimate of numerical mixing

Due to the anti-diffusive contributions of the TVD advection schemes (Burchard and Rennau (2008)), the instantaneous spatial distribution of numerical tracer variance decay is quite noisy. Therefore spatial and temporal averaging is applied to obtain an easy to interpret comparison of physical and numerical mixing. Figure 3.20 demonstrate what has already been discussed in section 3.4.1.
The highest numerical mixing occurs generally at moving fronts and is hence located exactly in physically energetic areas where dense bottom plumes are crossing sills and passing channels. A general property of the numerical mixing can also be seen in Figure 3.20 with areas of high numerical variance decay along lateral plume boundaries. In these areas where density gradients are advected vertically through the layers and coincidentally over steep bathymetry, numerical mixing is of the order of physical mixing and even stronger (Figure 3.21b,c). As one might consider the alignment of terrain-following coordinates on sloping bathymetry as the main problem for the occurrence of high numerical mixing

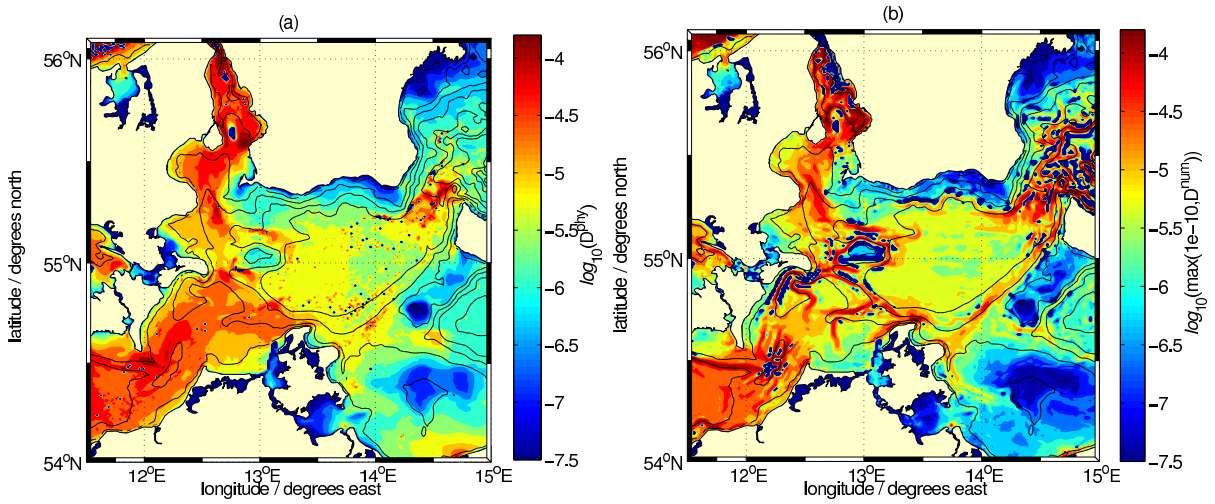

Figure 3.20: Picture showing the vertically integrated and over nine months time averaged values of (a) physically and (b) numerically induced mixing. Here ULTIMATE QUICKTEST has been used.

in this setup, such high numerical mixing will also been found in z-level models. This for example can be proved with this model setup for the region of the central Arkona Basin which shows low depth variations. Even here, where the alignment of the vertical coordinates can be nearly neglected and the model behaves nearly like a z-level model, the physical mixing (3.20a) still shows same orders of magnitude than the numerical mixing (3.20b). In this context, Burchard and Rennau (2008) additionally found high numerical mixing for a lock exchange experiment on a flat bottom.

The results demonstrate that numerical mixing has a significant impact on the overall mixing over large areas of the model domain. Figure 3.20b and 3.21c demonstrate that the numerical mixing plays a major role when salinity is advected through the coordinates vertically in regions where the moving plume front passes areas with steep bottom.

Another point that must be considered is that, additionally, high fluctuations of wind fields push the numerical mixing to high levels as can be seen for the region of the Arkona Basin (Figure 3.20). To what amount local physical mixing processes or, on the other hand, fluctuating wind fields or differential advection (Lass and Mohrholz (2003)) contribute to the overall amount of numerical mixing is not investigated in this study.

Further relationships can be obtained with the help of Figure 3.21. Here also the amount of anti-diffusive contributions of the ULTIMATE QUICKTEST scheme are directly plotted. The outcome is that the absolute value of the anti-diffusive contributions makes 6.7% of the positive contributions of D^{num} in the right panel of Figure 3.20.

Additional information about the strength of numerical mixing is shown in Figure 3.21b,c.

Here only the model domain regions where the physical mixing is greater than the numerical mixing (obtained by $\log_{10}(\max(10^{-10}, D^{\mathrm{phy}} - D^{\mathrm{num}}))$ and vice versa (obtained by $\log_{10}(\max(10^{-10}, D^{\mathrm{num}} - D^{\mathrm{phy}}))$ are shown. If we integrate over both fields, the quotient is even $R = 1.7$. With Figure 3.21b,c it is demonstrated, that there are large areas around the Darss Sill where physically induced mixing is much higher than numerical diffusion due to discretisation errors of the numerical advection schemes.

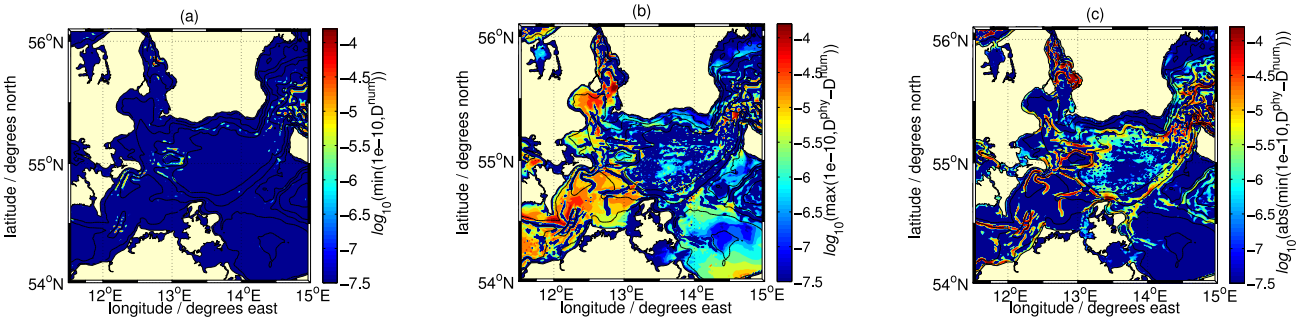

Figure 3.21: All panels show vertically integrated and time averaged (nine months) values of: (a) the anti-diffusive contributions of the numerical mixing, (b) regions where the physical diffusion is higher than the numerical mixing and (c) regions where the numerical mixing is higher than the physical mixing. Here ULTIMATE QUICKTEST has been used.

As a variation of the horizontal resolution for a realistic model setup would dramatically increase the computational costs, only a variation of the vertical resolution is investigated here. Figure 3.22 demonstrates that the relationship $R = (\int D^{\mathrm{num}} dV)/(\int D^{\mathrm{phy}} dV)$ is being reduced from $R = 2.43$ to $R = 1.24$.

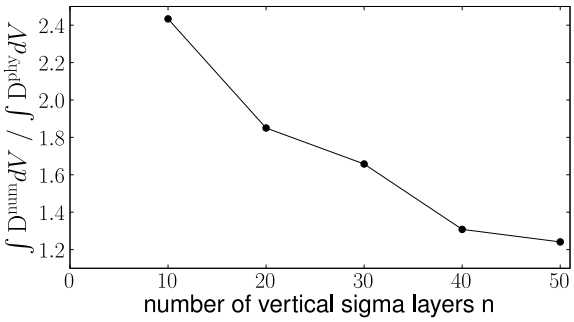

Figure 3.22: Panel showing the quotient between numerical and physical mixing for different amount of vertical layers. Here ULTIMATE QUICKTEST has been used.

3.5 Conclusions

With the help of model simulations using the hydrostatic coastal ocean model GETM it was found, that physically and numerically induced mixing have same orders of magnitude for both idealised and realistic model scenarios modelling the propagation of dense bottom currents.

The generic calculation of numerical tracer variance decay, which is explicitly calculating via the rate of decay between the advected square of the tracer and the square of the advected tracer, is a method which can easily being implemented to different kinds of ocean models with uniform, non-uniform, curvilinear or geopotential grids to be directly compared quantitatively to the physical mixing (micro-structure variance decay) without high computational overhead. Burchard and Rennau (2008) and Rennau and Burchard (2009) stated that z-level model and non-uniform models (curvilinear of unstructured grids) very likely suffer from the same problems of high numerical mixing than the sigma-coordinate model applied in this work, because high gradients being advected between cells

with different horizontal resolution is supposed to increase numerical mixing.
The proposed generic method can be additionally applied to improve model bathymetries by correlating local bathymetry smoothing procedures by the corresponding model derived numerically induced mixing of the individual model application conducted. Another potential use may be to use the numerical variance decay to optimise grid layouts. It can also be used to calculate the numerical variance decay of momentum advection to be compared to the physically induced shear production of turbulent kinetic energy.
Even the analysis of numerically induced mixing of more than one tracer (e.g. temperature and salinity) at a time can independently being investigated by this non-invasive method. Whereas earlier methods depend on zero boundary fluxes to estimate numerical mixing, this method correctly solves the total numerical variance decay (volume integral of numerical tracer variance decay) for non-zero boundary fluxes as in the realistic simulation conducted in this work. As demonstrated for the realistic model scenario of the Western Baltic Sea, this method can even be used to obtain the numerical diffusivities in each spatial dimension due to the use of directional-split advection schemes in the GETM.
In the second part of this chapter, the diagnostic method in obtaining the numerical mixing (Burchard and Rennau (2008)) has been successfully applied to an existing realistic 3D coastal ocean model. Besides the knowledge obtained with idealised simulations by Burchard and Rennau (2008), this study demonstrates that even for the energetic system of the Western Baltic Sea, the numerical mixing has comparable magnitude than the physical mixing. Vertical slices in the numerically very challenging model area north of Kriegers Shoal have shown the connection between horizontal density gradients due to general vertical coordinates and numerical mixing. Together with vertically integrated and time-averaged measures of numerical and physical mixing, a significant different horizontal and vertical distribution of numerical and physical mixing was found.
A correlation between strong horizontal tracer gradients and high velocities on one hand and high numerical mixing on the other hand could be shown as well as a correlation between physical mixing and numerical mixing. It would also be interesting to investigate how physical processes such as internal waves, differential advection or mixing at shallow areas contribute to the overall physical and numerical mixing.
An improvement to the numerical mixing issues discussed in this study might be to incorporate adaptive vertical coordinates (Bleck (2002); Burchard and Beckers (2004) and Adcroft and Hallberg (2006)) which would consequently decrease the strength of the saw tooth type horizontal density profile, decrease the vertical advection through the vertical coordinate levels and would act vertically refining. Only recently Hofmeister et al. (2010a) reduced the numerically induced mixing in dense gravity currents significantly applying non-uniform adaptive vertical grids in a terrain-following coordinate model.

Chapter 4

The impact of offshore wind farms on transport and dilution in density-driven bottom currents: a numerical model study

4.1 Introduction

To reduce greenhouse gas emissions substantially, it is the goal of the German Federal government to increase the portion of power generated from renewable energies to at least 20% until 2020 (BMU (2007)). Since the use of water and sun for power generation is limited, as well as space for land-based wind turbines, the establishment of offshore wind farms in the German EEZ areas of the North Sea and the Baltic Sea is planned (figure 4.1).
Neighbouring countries such as Denmark have comparable goals (TRM (2005)). While additional vertical mixing due to offshore wind farms in the well-mixed coastal waters of the German Bight (South-Eastern North Sea) have a negligible impact on the marine ecosystem, there may be significant effects for the stratified, almost tide-less Western Baltic Sea.
The Baltic Sea is a semi-enclosed almost non-tidal estuarine system on the North West European Continental Shelf with only shallow and narrow connections to the North Sea (figure 4.2).
Due to dominant river runoff and precipitation the water exchange between the North Sea and the Baltic Sea is composed of a net outflow of brackish surface water and frequently occurring so-called medium-intensity inflow events (Burchard et al. (2005)) as well as major Baltic barotropic and baroclinic inflows, occurring at the inter-annual time scale (Matthäus and Frank (1992); Kõuts and Omstedt (1993); Feistel et al. (2003a)). As this salty bottom water is generally carrying sufficient amounts of oxygen, this process is the only way to ventilate the deeper parts of the Baltic Sea (Reissmann et al. (2009)). Hence, dense bottom currents are a very important process for the whole Baltic Sea ecosystem.
It was first discussed by Lass (2003), that structures such as foundations of wind turbines assembled in offshore wind farms could induce additional vertical mixing in stratified shear flow. Such a wind farm

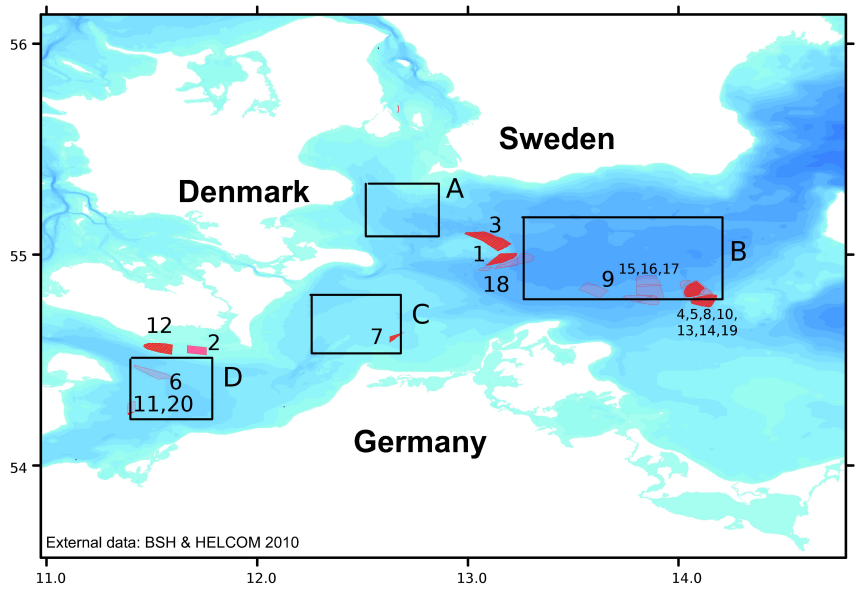

Figure 4.1: Distribution of offshore wind farms (OWFs) in the Western Baltic Sea (external data from Bundesamt für Seeschifffahrt und Hydrographie, see Marnet website at `www.bsh.de`, situation in April 2009) as used for model scenarios R1.4 and R0.6. The status of each of the OWF's is as follows: red: approved, dark magenta: operational and light magenta: projected. Please note that some of the projected OWF sites overlap each other. The black rectangles indicated by A,B,C,D are the OWF's for the unrealistically extensive distribution applied in model runs U1.4 and U0.6. The black line north-west and the black cross west of the Isle of Bornholm indicate locations for model output (see figure 4.2 for geographical locations). The numbers in this map refer to the wind farms detailed in table 4.1.

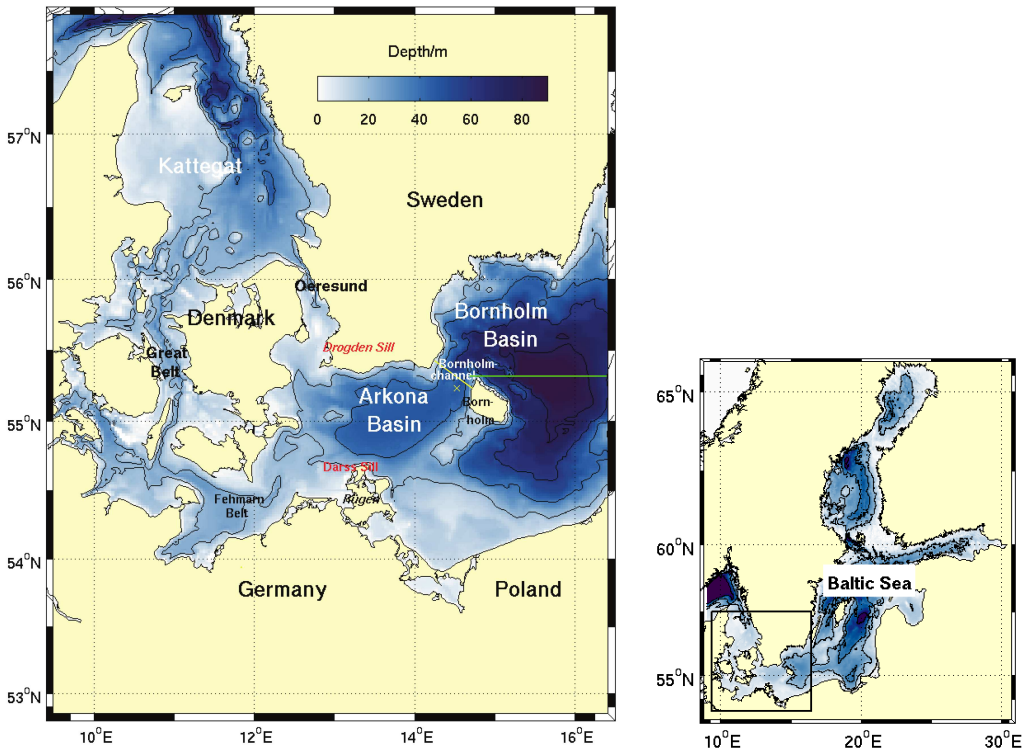

Figure 4.2: Map of the model domain in the Western Baltic Sea including bathymetry (upper panel); map of the Baltic Sea including bathymetry with the boundaries of the model domain indicated (lower panel).

Name	Position	Area [km^2]	# of turbines	Area density a
1. Kriegers Flak	55.00°/13.16°	41.61	80	$1.92 \cdot 10^{-5}$
2. Nystedt	54.53°/11.67°	33.69	72	$2.14 \cdot 10^{-5}$
3. Kriegers Flak 2	55.10°/13.00°	68.37	128	$1.87 \cdot 10^{-5}$
4. Arkona-Becken Südost	54.77°/14.30°	44.59	80	$1.79 \cdot 10^{-5}$
5. Adlergrund GAP	54.83°/14.12°	5.94	31	$5.21 \cdot 10^{-5}$
6. Beltsee	54.41°/11.55°	38.64	25	$6.47 \cdot 10^{-6}$
7. Baltic 1	54.58°/12.61°	15.85	21	$1.32 \cdot 10^{-5}$
8. Ventotec Ost 2	54.86°/14.06°	46.57	50	$1.07 \cdot 10^{-5}$
9. ARCADIS Ost 1	54.83°/13.52°	30.72	70	$2.28 \cdot 10^{-5}$
10. ARCADIS Ost 2	54.82°/14.10°	14.86	25	$1.68 \cdot 10^{-5}$
11. GEOFReE	54.25°/11.38°	5.94	5	$8.41 \cdot 10^{-6}$
12. Rødsand 2	54.55°/11.47°	49.54	≈50	$1.01 \cdot 10^{-5}$
13. Adlergrund 500	54.82°/14.10°	13.87	20	$1.44 \cdot 10^{-5}$
14. ArkonaSee Ost	54.85°/14.00°	9.91	≈40	$4.04 \cdot 10^{-5}$
15. ArkonaSee Süd	54.80°/13.85°	20.81	80	$3.84 \cdot 10^{-5}$
16. ArkonaSee West	54.80°/13.82°	25.76	≈80	$3.11 \cdot 10^{-5}$
17. BalticEagle	54.80°/13.85°	62.42	80	$1.28 \cdot 10^{-5}$
18. BalticPower	54.93°/13.12°	71.34	≈80	$1.12 \cdot 10^{-5}$
19. Adlergrund Nordkap	54.83°/14.03°	39.63	31	$7.82 \cdot 10^{-6}$
20. Sky2000	54.30°/11.38°	21.80	≈50	$2.29 \cdot 10^{-5}$

Table 4.1: Names, geographical position, area, number of turbines and area density of OWFs for the scenarios R1.4 and R0.6. Values with ≈ have been estimated by the authors because no data was available for these OWFs. Area densities have been calculated on the basis of an assumed diameter of $d = 10$ m for each wind turbine.

Name	Area [km^2]	# of turbines	Area density a
A. WP-Fehmarn	645.6	1379	$1.0 \cdot 10^{-5}$
B. WP-Darss	298.8	638	$1.0 \cdot 10^{-5}$
C. WP-KFNE	199.2	425	$1.0 \cdot 10^{-5}$
D. WP-Arkona	6972.6	14886	$1.0 \cdot 10^{-5}$

Table 4.2: Names, area, number of wind turbines and area density of unrealistically extensive OWFs at Fehmarn (WP-Fehmarn), Darss (WP-Darss), Kriegers Flak North-East (WP-KFNE) and at the Arkona Sea (WP-Arkona). A,B,C,D refers to figure 4.1.

induced dilution of the inflowing water could result in a decreased ventilation of the halocline in the Baltic Sea. As a result of this, the region of oxygen depletion in the Baltic Sea could be extended to higher levels in the water column, with significant environmental consequences for pelagic and benthic organisms. It is the goal of the present study to quantify this impact.

An existing high-resolution coastal model of the Western Baltic Sea (Burchard et al. (2009)) has been used to identify the pathways of dense bottom currents and to quantify the associated amount of natural mixing on their way through the Western Baltic Sea. These results are in good agreement with field observations of medium intensity inflows in the Western Baltic Sea (Sellschopp et al. (2006), Umlauf et al. (2007)).

Since many years the flow around vertically and horizontally aligned cylinders have been investigated, mainly with the aim to study structural design and flow-induced acoustic emissions and vibrations. Other studies concentrated on the transition area in the wake of the cylinder (see e.g. Henderson (1997), Xu et al. (1995)). Behind a vertically aligned cylinder a van Karman vortex street may evolve inducing turbulence and mixing far away from the structure. Internal waves may be generated in stratified flow around structures, which propagate away and cause mixing remotely due to dissipation. The main problem concerning previous work is the lack of research on mixing induced by vertical structures in a stratified flow. Most of the past studies were conducted on homogeneous water flow without Earth rotation or at horizontally aligned cylinders (Arntsen (1998)). Recent field studies conducted by Lass et al. (2008) on enhanced tracer (here: salinity) mixing in the Baltic Sea at the Western Great Belt Bridge revealed significantly increased mixing downstream of the bridge. Therefore, it is necessary to develop numerical methods for quantifying structure-induced mixing in stratified shear flows and its impact on larger scales.

To get an impression of the regional dynamics of dense gravity currents in the Western Baltic Sea, two passive tracers were released continuously at transects across the Darss Sill and the Drodgen Sill in such a way that they were set to a value equal to the salinity at these positions when the current was directed into the Arkona Sea and to zero for outgoing currents. The mean passive tracer concentrations are shown in Figure 2.18 together with the mean salinity. It is demonstrated that plumes from Darss Sill show lower salinities but transport higher amounts of salt due to the broader transitions area at the Darss Sill than at the Drodgen Sill. It is also shown that both plumes take different pathways through the Arkona Basin and through the Bornholm Channel. It is hypothesised that structure-induced physical mixing may significantly dilute dense bottom currents generated by inflow events such that their ability to reach deeper parts of the Baltic Sea is reduced as well as the ventilation of these basins.

The existing and validated realistic coastal model setup for the Western Baltic Sea (Burchard et al. (2009)) is extended to quantify potential additional dilution of medium intensity inflow events due to vertical structures. Since monopile foundations of offshore wind farms (OWFs) typically have diameters in the order of 5-10 m, mixing induced by the structures is a sub-grid scale process which cannot be resolved by the coastal ocean models with typical horizontal resolutions of $\mathcal{O}$(1km). The parameterisation is obtained by calibrating an extended k-ε turbulence closure model by means of results from a set of local high-resolution RANS model experiments as described by Schimmels (2008) and Schimmels and Markofsky (2010).

This manuscript is structured as follows: section 4.2 describes how the parameterisation for the process of sub-grid scale cylinder-induced mixing was obtained by means of high resolution non-hydrostatic RANS modelling; section 4.3 introduces the applied hydrostatic coastal model and the mixing measures used for the investigations; section 4.4 investigates the behaviour and impact of the parameterisation in the hydrostatic model for idealised overflow scenarios and section 4.5 shows the results of realistic simulations on the intensity of diapycnal mixing, dilution and changes on annual mean gradients due to the OWFs for two realistic cases and two cases with over-exaggerated wind farm coverage in the Western Baltic Sea. Finally, some conclusions are drawn in section 4.6.

4.2 Parameterisation of structure friction in density-driven bottom currents

4.2.1 Model equations

The frictional force per unit height on a cylinder in an unstratified flow perpendicular to the cylinder can be calculated as

$$\vec{F} = \frac{1}{2} C_D \rho_0 d \vec{u} |\vec{u}|, \tag{4.1}$$

with the drag coefficient $C_D = 0.63$ (for a smooth cylinder), the diameter of the cylinder, d, and the undisturbed velocity vector $\vec{u}$ (see e.g., Sumer and Fredsøe (1997)). After division by the mass of the reference volume (which in finite volume methods is the mass of the finite volume in which the structure is contained) the frictional deceleration of the vertically resolved horizontal velocity components u and v, respectively, is calculated as:

$$G_d^u = \frac{1}{2} C_D a u \sqrt{u^2 + v^2}, \quad G_d^v = \frac{1}{2} C_D a v \sqrt{u^2 + v^2}, \tag{4.2}$$

with the area density of the structures, $a = X \cdot d/A$, where X is the number of cylinders in the flow and $A = \Delta x \Delta y$ (with the local horizontal grid dimensions, Δx and Δy) is the horizontal area of the finite volume for which the dynamic equations are representative.
Taking the classical u- and v-momentum equations in three-dimensional hydrostatic ocean models (see, e.g., Burchard and Bolding (2002), Shchepetkin and McWilliams (2005)), and adding the friction terms due to structures in the water column from eq. (4.2), the following dynamic equations result:

$$\begin{aligned} &\partial_t u + \partial_x(u^2) + \partial_y(uv) + \partial_z(uw) - \partial_z\left(A_v \partial_z u\right) \\ &\quad -\partial_x\left(2A_h \partial_x u\right) - \partial_y\left(A_h(\partial_y u + \partial_x v)\right) - fv + G_d^u \\ &\quad = -g\partial_x \zeta - \frac{g}{\rho_0}\int_z^\zeta \partial_x \rho \, dz', \end{aligned} \tag{4.3}$$

$$\begin{aligned}
&\partial_t v + \partial_x(vu) + \partial_y(v^2) + \partial_z(vw) - \partial_z\left(A_v \partial_z v\right) \\
&-\partial_y\left(2A_h \partial_y v\right) - \partial_x\left(A_h(\partial_y u + \partial_x v)\right) + fu + G_d^v \\
&= -g\partial_y \zeta - \frac{g}{\rho_0}\int_z^\zeta \partial_y \rho \, dz'.
\end{aligned} \tag{4.4}$$

In eqs. (4.3) and (4.4), w is the vertical velocity component. The vertical coordinate z ranges from the bottom $z = -H(x, y)$ to the surface $z = \zeta(t, x, y)$ with t denoting time. A_v is the vertical eddy viscosity, $f = 2\omega \sin\phi$ is the Coriolis parameter, with the angular velocity of the Earth, ω, and the latitude, ϕ, ρ is the potential density, ρ_0 is the reference density, and g is the gravitational acceleration. The horizontal mixing is parameterised by terms containing the horizontal eddy viscosity A_h, see Blumberg and Mellor (1987). In realistic hydrodynamic simulations, prognostic equations for temperature and salinity are calculated as well (see Burchard and Bolding (2002) for details), using the eddy diffusivity K_v for vertical mixing.

Both eddy viscosity and eddy diffusivity are calculated as functions of the turbulent kinetic energy per unit mass (TKE), k, and the dissipation rate of the TKE, ε:

$$A_v = c_\mu \frac{k^2}{\varepsilon}, \quad K_v = c'_\mu \frac{k^2}{\varepsilon}, \tag{4.5}$$

with the non-dimensional stability functions c_μ and c'_μ containing the algebraic second-moment turbulence closure (see Umlauf and Burchard (2005) for details). The TKE and its dissipation rate are calculated here by means of the k-ε two-equation model:

$$\begin{aligned}
&\partial_t k + \partial_x(uk) + \partial_y(vk) + \partial_z(wk) - \partial_z\left(\frac{A_v}{\sigma_k}\partial_z k\right) \\
&= P + P_d + B - \varepsilon,
\end{aligned} \tag{4.6}$$

$$\begin{aligned}
&\partial_t \varepsilon + \partial_x(u\varepsilon) + \partial_y(v\varepsilon) + \partial_z(w\varepsilon) - \partial_z\left(\frac{A_v}{\sigma_\varepsilon}\partial_z \varepsilon\right) \\
&= \frac{\varepsilon}{k}\left(c_1 P + c_4 P_d + c_3 B - c_2 \varepsilon\right),
\end{aligned} \tag{4.7}$$

with the shear production

$$P = A_v S^2 \tag{4.8}$$

and the buoyancy production

$$B = -K_v N^2, \tag{4.9}$$

with the vertical shear squared, $S^2 = (\partial_z u)^2 + (\partial_z v)^2$ and the buoyancy frequency squared, $N^2 = -(g/\rho_0)\partial_z \rho$.

In the TKE equation (4.6) the loss of mean kinetic energy from (4.3) and (4.4) due to structure-induced friction,

$$P_d = \frac{1}{2} C_D a \left(u^2 + v^2\right)^{3/2}, \tag{4.10}$$

has been included as further production term. Following Svensson and Häggkvist (1990), P_d has been included as source term into the dissipation rate equation as well, scaled by the empirical parameter c_4, see eq. (4.7). Other constant empirical parameters are the Schmidt numbers, σ_k and σ_ε and the weighting parameters c_1, c_2 and c_3 for the source and sink terms in the ε equation.

4.2.2 Structure mixing parameterisation

In the turbulence closure model, the parameters c_1 - c_3 all have a clear physical meaning, see, e.g., Umlauf and Burchard (2005). For their interpretation as well as the interpretation of the additional parameter c_4, it is instructive to investigate the k-ε model for homogeneous shear layers, e.g., in the absence of gradients except for spatially and temporally constant shear S and buoyancy frequency N (see Burchard and Baumert (1995)). Under these conditions, the model reduces to the following system of ordinary differential equations:

$$\dot{k} = P + P_d + B - \varepsilon, \quad \dot{\varepsilon} = \frac{\varepsilon}{k}\left(c_1 P + c_4 P_d + c_3 B - c_2 \varepsilon\right). \tag{4.11}$$

For stationary solutions of (4.11) with $\dot{k} = 0$ and $\dot{\varepsilon} = 0$, the following necessary condition can be derived:

$$\Gamma = -\frac{B}{\varepsilon} = \frac{c_1 - c_2}{c_3 - c_1} + \frac{c_4 - c_1}{c_3 - c_1}\,\frac{P_d}{\varepsilon}, \tag{4.12}$$

with the local mixing coefficient Γ (see Umlauf (2009), Burchard and Hetland (2010)). Following Rodi (1980), $c_1 = 1.44$ and $c_2 = 1.92$ and following Umlauf and Burchard (2005) $c_3 = -0.74$ (when applying the second moment closure by Cheng et al. (2002)), such that for $P_d = 0$ a mixing coefficient of $\Gamma = 0.22$ is obtained, a value close to the generic value of $\Gamma = 0.2$ suggested by Osborn (1980). It should be noted that the flux Richardson number, $R_f = P/\varepsilon$ (for which $R_f = \Gamma/(\Gamma + 1)$ is obtained for local turbulence equilibrium with $P + B = \varepsilon$), is a measure for mixing efficiency. For non-zero structure-induced turbulence production, the gross mixing efficiency is reduced for $c_4 > c_1$ and enhanced by $c_4 < c_1$ (because $c_3 - c_1 < 0$).

An interesting idealisation is also given by considering homogeneously stratified flow without shear ($P = 0$) for which (4.11) with $\dot{k} = \dot{\varepsilon} = 0$ yields

$$\Gamma = \frac{c_2 - c_4}{c_4 - c_3} \quad \Rightarrow \quad c_4 = \frac{c_2 + c_3\Gamma}{1 + \Gamma}. \tag{4.13}$$

For a mixing coefficient not modified by structure friction, this gives $c_4 = c_1$ (which is consistent with (4.12)), and, again, the gross mixing efficiency is reduced for $c_4 > c_1$ and enhanced by $c_4 < c_1$. The advantage of the formulation (4.13) is that it does not explicitly contain the turbulence production due to structure friction. However, this formulation can only be used for calibrating c_4 on the basis of shear-free experiments.

Svensson and Häggkvist (1990) estimated for an unstratified atmospheric boundary layer $c_4 = 1.95$, i.e., $c_4 > c_1$ which would induce reduced mixing efficiency for stratified flows.

4.2.3 RANS model simulations

To analyse the process of structure-induced mixing and entrainment more thoroughly, to assess the impact of a cylindrical structure on the dilution of a dense bottom current and finally to provide calibration data for the parameterisation of the regional model described in section 4.2.4, a fully three-dimensional high resolution numerical model based on the Reynolds Averaged Navier-Stokes (RANS) equations has been set up. Besides the balance equations for mass and momentum an additional transport equation for salinity is solved and turbulence is simulated with the SST k-ω model (Wilcox (1988)). A detailed description of the numerical model, the model setup, the validation procedure and a thorough discussion of mixing and entrainment induced by a circular cylinder in density currents not influenced by earth rotation, i.e. without the effect of Coriolis acceleration, can be found in Schimmels (2008). Simulations of cylinder induced dilution of dense bottom currents with the effect of Coriolis acceleration, which have been used as a reference for the present study are described in Schimmels and Markofsky (2010), where the results of a parameter study with varying Froude and Ekman numbers are presented and the impact of offshore wind farms is assessed.
All simulations were made on the same computational domain which is sketched in figure 4.3a, with the cylinder in the centre.

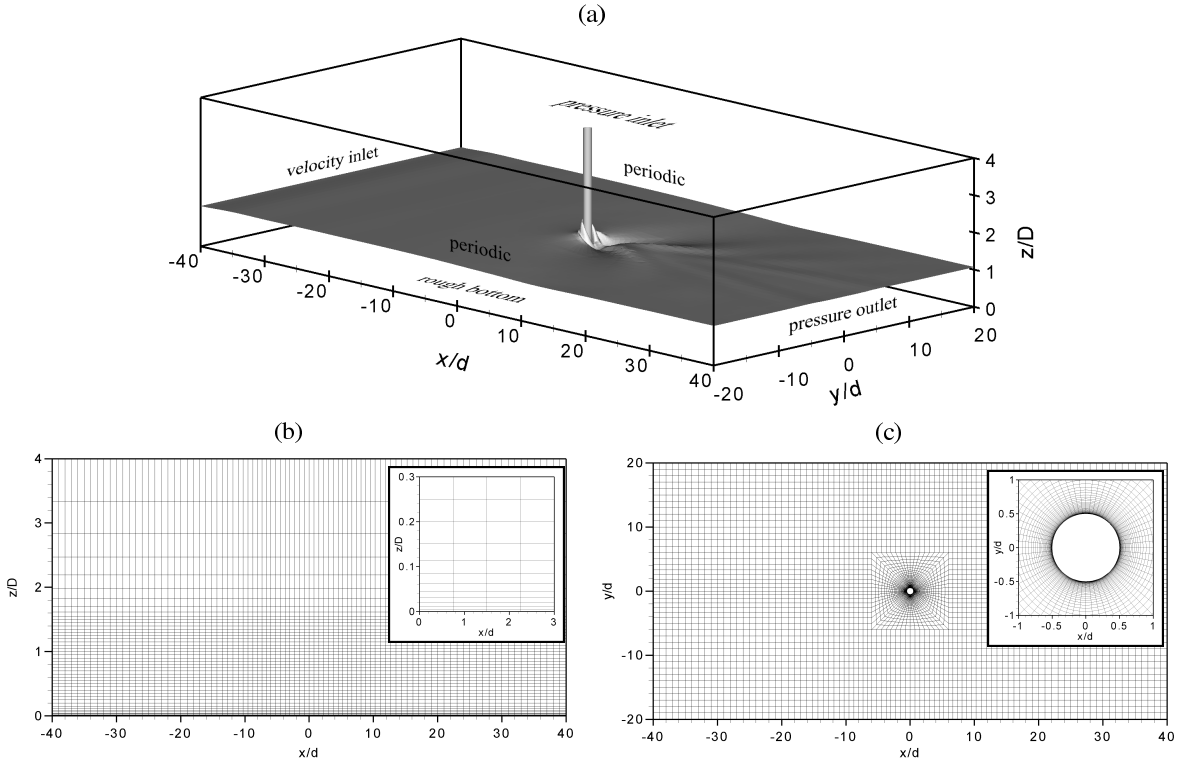

Figure 4.3: Computational domain for three dimensional high resolution RANS simulations. (a) Definition sketch of complete computational domain with the cylinder in the centre, boundary conditions assigned by the text and current depth indicated by the shaded plane. (b) Side view and (c) top view of the numerical grid. Small panels showing the refined resolution at the bottom and cylinder, respectively.

The shaded plane is the result of one simulation and denotes the current depth which has been added to better visualise the model setup. Horizontal length scales are normalised by the cylinder diameter

d and the vertical scale is normalised by the thickness of the density current, D.
The boundary conditions are a pressure boundary condition at the free surface, periodic conditions at the lateral boundaries, a closed rough bottom boundary condition with an equivalent sand roughness of $k_s = 0.025$ m, corresponding to a drag coefficient of about $C_d \approx 0.0022$ for $D \geq 10$ m, and open boundaries at the inflow and outflow. The profiles for velocity, salinity, turbulent quantities and pressure needed for the inflow and outflow boundary conditions as well as initial conditions were gained from preliminary simulations of undisturbed currents with a one-dimensional model.
The numerical grid is block-structured and the grid topology is the same for all simulations, as shown in figure 4.3b and figure 4.3c. In the vertical the grid is refined at the bottom and within the interface between $0.5 < z/D < 1.5$ in order to adequately resolve the steep gradients of velocity, density and turbulence quantities in these regions. In the horizontal the grid is circular up to 3 diameters around the cylinder and then converted over the next 3 diameters to the rectangular shape of the channel. The finest resolution at the cylinder accounts for the requirements of the wall function approach with y^+ being in the order of 10^2 or slightly below and in the far field the resolution is $\Delta x/d = \Delta y/d = 1$ which is slightly condensed in the wake region.
All simulations were run for 8000 time steps which were adjusted to let the current pass the domain within about 1500 time steps. In order to remove initial disturbances the simulations were first run for 4000 time steps and subsequently the mean values for the parameters in question were calculated from the following 4000 time steps, corresponding to about 30 shedding cycles.
With the model described so far Schimmels and Markofsky (2010) conducted a comprehensive parameter study to quantify the effect of the Froude number, aspect ratio d/D and Coriolis forces on the mixing process. They focused their analysis on the local patterns of the cylinder induced entrainment rates and gave an estimation of the total impact of offshore wind farms on density currents in the Baltic Sea based on the total entrainment induced by one cylindrical structure.
A direct result of the three dimensional RANS simulations is the total buoyancy flux B_{tot} including the buoyancy flux of an undisturbed current B_{base} and that induced by the structure B_{cyl}. It can either be used to calculate the entrainment rates as done by Schimmels and Markofsky (2010) or as a direct reference for the calibration of the parameterisation described in section 4.2.4. Integrating the three dimensional quantity over depth allows for an estimation of the local intensities of mixing induced by the cylinder as well as the area of influence of the cylinder. Before, however, the naturally occurring buoyancy flux B_{base} must be subtracted from the total buoyancy flux B_{tot} in order to analyse the effect of the cylinder alone.
Figure 4.4 shows the patterns of the depth integrated cylinder induced buoyancy flux for an aspect ratio $d/D = 1$, a constant Ekman number $K = 0.8$ and different Froude numbers ranging from $\mathrm{Fr} = 0.4$ to $\mathrm{Fr} = 0.7$, see equation (4.17) for definitions of these numbers.
These can be compared to the patterns for the cylinder induced entrainment rates shown by Schimmels and Markofsky (2010), where also a more comprehensive analysis is presented. It is nicely seen from figure 4.4 how the buoyancy flux is deflected to the right as a consequence of the lateral currents induced by Coriolis forces. Moreover it is obvious that the influence of the cylinder is generally rather limited and measures only a few diameters. There is also only a relatively small dependence on the Froude number but it can already be guessed that mixing slightly increases with increasing Froude

number.
Integrating further over the horizontal plane eventually leads to the total structure-induced volume-integrated buoyancy flux

$$\mathcal{B}_s = \int_V B_{cyl}\,\mathrm{d}V = \int_V B_{tot}\,\mathrm{d}V - \int_V B_{base}\,\mathrm{d}V, \tag{4.14}$$

which is a measure for the impact of the cylinder on the additional dilution of the density current and confirms the latter assumption. It is beyond the scope of the present paper to go into further details, which can be found in Schimmels and Markofsky (2010), but the results of the RANS simulations for the structure-induced volume-integrated buoyancy flux $\mathcal{B}_s$ are excellently suited as a reference for the calibration of the parameterisation described in the following section 4.2.4.

4.2.4 Calibration

The parameterisation of structure-induced mixing will be calibrated and validated as a function of instantaneous current speed and parameters of a dense bottom current. To determine these numbers, the following bulk parameters have been defined by Arneborg et al. (2007):

$$G'D = \int_{-H}^{\eta'} \frac{\rho-\rho_0}{\rho_0} g\,\mathrm{d}z, \quad \frac{1}{2}G'D^2 = \int_{-H}^{\eta'} \frac{\rho-\rho_0}{\rho_0} gz\,\mathrm{d}z, \tag{4.15}$$

$$UD = \int_{-H}^{\eta'} u\,\mathrm{d}z, \quad VD = \int_{-H}^{\eta'} v\,\mathrm{d}z, \tag{4.16}$$

where D is the thickness of the density current, G' its reduced gravity, U and V its velocity components and η' the vertical position of a reference density. With the bottom slope with respect to the direction of the density current, the Froude number Fr and the Ekman number K can be defined:

$$\mathrm{Fr} = \frac{U_s}{(G'D\cos\alpha_s)^{1/2}}, \quad K = \frac{C_d U_s}{fD} \tag{4.17}$$

where

$$U_s = (U^2+V^2)^{1/2} \tag{4.18}$$

is the depth-averaged speed of the density current.
The calibration is based on the RANS simulations described in section 4.2.3, where the Ekman number is kept at a constant value of $K = 0.8$, and the Froude number was varied as Fr = 0.4, 0.5, 0.6, and 0.7 covering the Fr range of dense bottom currents in the Arkona Sea (Arneborg et al. (2007)). Figure 4.5 shows structure-induced volume-integrated buoyancy fluxes $\mathcal{B}_s$ (see eq. 4.14) between 0.3 $\mathrm{m^5 s^{-3}}$ and 0.6 $\mathrm{m^5 s^{-3}}$, which corresponds to energy fluxes between 300 W and 600 W.
As expected already from figure 4.4, $\mathcal{B}_s$ increases with Fr in this Froude number range.
The strategy for calibrating the parameterisation of structure-induced mixing is to first reproduce with a one-dimensional model the dynamics of pressure-gradient driven dense bottom currents for the same configurations as in the RANS experiments without structure-induced mixing. Afterwards, the effect of one cylinder is parameterised into the model by setting the area density to a $a = d/A$ where A is the

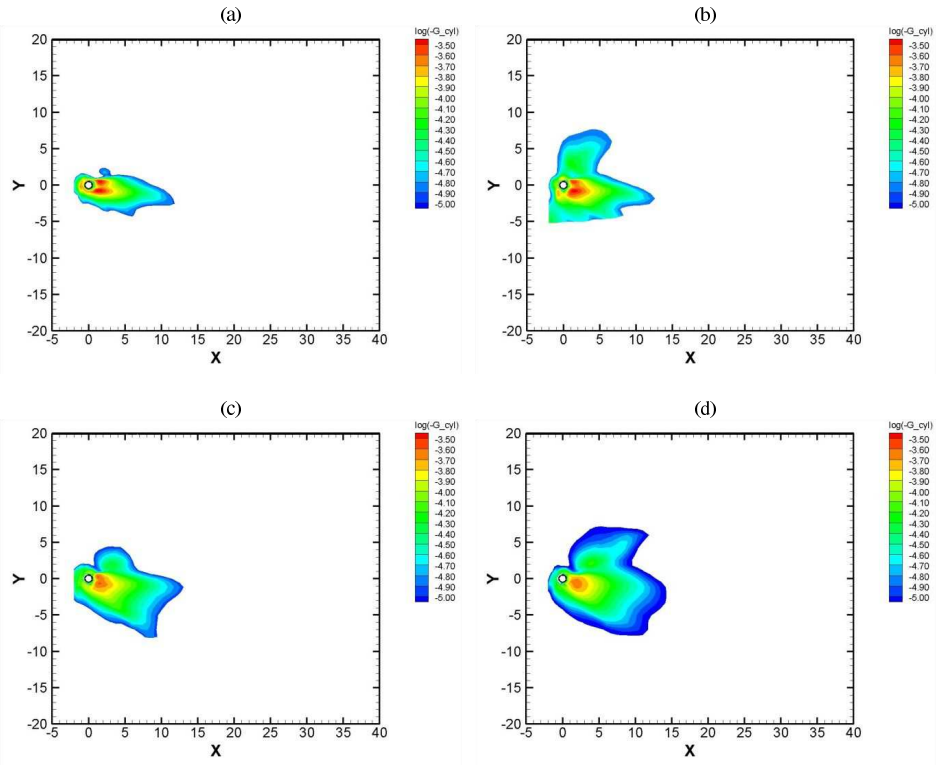

Figure 4.4: Spatial distribution of cylinder induced buoyancy production B_{cyl} for different Froude numbers with the cylinder diameter $D = 10$ m and a constant Ekman number $K = 0.8$. (a) Fr $= 0.4$, (b) Fr $= 0.5$, (c) Fr $= 0.6$ and (d) Fr $= 0.7$.

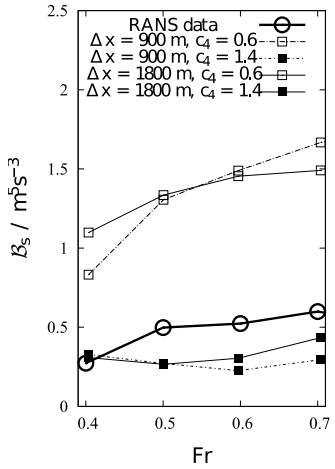

Figure 4.5: Comparison of structure-induced volume-integrated buoyancy flux, $\mathcal{B}_s$, as function of the Froude number, Fr, calculated from RANS simulations (large open circles) and from GOTM using two values of c_4 and references areas with two different sizes, $\Delta x = 900$ m and $\Delta x = 1800$ m.

reference area (corresponding to the area of a grid box in a three-dimensional hydrodynamic model). For each value of c_4 one simulation is then carried out. The vertically integrated buoyancy flux for both experiments (with and without cylinder) is then multiplied with the reference area A, such that the difference between them gives the additional integrated buoyancy flux due to the cylinder. This value can finally be quantitatively compared to the structure-induced buoyancy flux $\mathcal{B}_s$ calculated from the RANS experiments.

For this calibration procedure the one-dimensional water column model GOTM (General Ocean Turbulence Model, see `www.gotm.net` and Umlauf et al. (2005)) is applied.

In both, the RANS and the GOTM simulations, the Coriolis parameter was set to $f = 1.195 \cdot 10^{-4}\mathrm{s}^{-1}$ (according to a latitude of 55°N, characteristic for the Western Baltic Sea). The initial plume thickness was set to $D = 9.5$ m, with a linear interface of 1 m thickness. Each simulation was run for one inertial period of $2\pi/f = 14.6$ h. With this configuration a pressure gradient driven plume was reproduced, with balanced dynamics and a plume thickness of approximately $D = 10$ m. To reproduce the values of Fr and K under consideration for the end of the simulation period, the interfacial slope, α, and the bottom to surface density difference, $\Delta\rho$ have been varied independently. This was obtained by executing 48 $\times$ 48 GOTM simulations with variations in α and $\Delta\rho$, resulting in variations of Fr and K at the end of one inertial period for each simulation. For the calibration simulations, the optimal combination of α and $\Delta\rho$ was then evaluated in terms of the structure-induced integrated buoyancy flux for values of Fr and K close to the prescribed RANS values.

To demonstrate the impact of varying c_4 on the structure-induced integrated buoyancy flux, $\mathcal{B}_s$, c_4 was varied over a wide range for the scenario with Fr = 0.4 and $K = 0.8$. Results for $A = \Delta x \Delta y = 900^2$ m^2 (with $D = 10$ m yielding an area density of $a = D/(\Delta x \Delta y) = 1.2 \cdot 10^{-5}$ m^{-1}) are shown in figure 4.6.

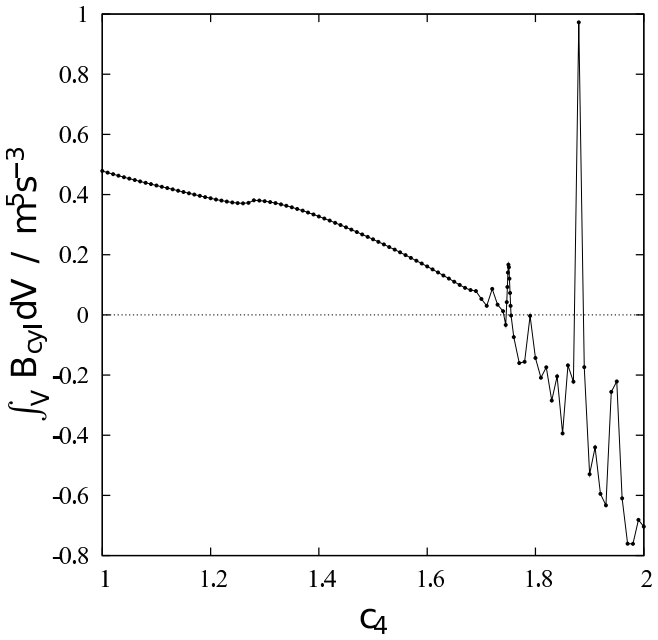

Figure 4.6: Structure-induced integrated buoyancy flux cylinder friction at Fr = 0.4 and $K = 0.8$, as function of c_4, with $\Delta x = 900$ m.

The structure-induced integrated buoyancy flux is generally increasing with decreasing c_4 which is consistent with (4.12) and (4.13). For $c_4 > 1.75$, $\mathcal{B}_s$ is reduced with respect to the simulations without cylinder friction parameterisation. Even if in the chosen parameter range for c_4 numerical instabilities occur, results are numerically stable for $c_4 \leq 1.75$, with almost monotonically increasing $\mathcal{B}_s$ for decreasing c_4, except for low values of c_4 (strong mixing), where some irregularities occur. The critical value of 1.75 for this two-layer flow is larger than the critical value of $c_1 = 1.44$ which has been theoretically derived for homogeneous shear layers.

The RANS results for $K = 0.8$ and Fr = 0.4, 0.5, 0.6, and 0.7 along with $\mathcal{B}_s$ calculated by means of the one-dimensional model including the structure friction parameterisation for values of $c_4 = 0.6$ and $c_4 = 1.4$ and horizontal resolutions of $\Delta x = \Delta y = 900$ m and $\Delta x = \Delta y = 1800$ m are shown in figure 4.5. As expected, the level of structure-induced integrated buoyancy flux $\mathcal{B}_s$ increases with decreasing c_4. Except for the weak mixing case with $c_4 = 1.4$, $\mathcal{B}_s$ is generally increasing with increasing Froude number, a feature which is in agreement with the results of the RANS simulations. Furthermore, the resulting $\mathcal{B}_s$ is only weakly dependent on the size of the reference value $A = \Delta x \Delta y$. The latter is a precondition for using the structure mixing parameterisation in three-dimensional models without re-calibrating for each horizontal grid layout.

Concerning the implementation of this parameterisation into the hydrostatic coastal ocean model, the value of $c_4 = 1.4$ is applied into the model as the *weak mixing* case, whereas $c_4 = 0.6$ represents the *strong mixing* scenario. Based on (4.13) which calculates the structure-induced mixing efficiency for flow without shear, the *weak mixing* scenario employs a mixing coefficient of $\Gamma = 0.24$ (mixing efficiency $R_f = 0.19$) and the *strong mixing* case a mixing coefficient of $\Gamma = 0.98$ (mixing efficiency $R_f = 0.49$). Thus, for *weak mixing* about 20% of the structure- induced buoyancy production of turbulence is used for mixing (the rest being dissipated into heat) and for *strong mixing* about 50% of the buoyancy production is used for mixing. It should be noted that compared to the complex processes of internal waves and mixing in stratified flow occurring in the vicinity of the structure the parameterisation suggested here is still quite simple, such that quite some inaccuracy is included in the present approach. Therefore, instead of only using a *best guess* calibration of the structure-induced mixing, two calibrations are used, a reasonably realistic *weak mixing* case, and a *strong mixing* case, for which it can be assumed that the real impact of offshore wind farms in the Baltic Sea is always smaller.

4.3 Methods

4.3.1 Numerical model

The numerical model GETM (General Estuarine Transport Model, see Burchard and Bolding (2002) and `www.getm.eu`), which is applied for the present study, is a fully baroclinic and hydrostatic coastal ocean model using terrain-following vertical coordinates. Various turbulence closure schemes are implemented in to GETM via the well-tested state-of-the-art turbulence model GOTM (General Ocean Turbulence Model, see Umlauf and Burchard (2005) and `http://www.gotm.net`.

The turbulence closure model used for the coastal model setup in this study is the k-ε model with

transport equations for the turbulent kinetic energy (TKE), k, and the turbulence dissipation rate, ε, extended by production terms due to structure-induced friction, see section 4.2.1. It should be noted that for simplicity the advection of turbulent quantities is neglected in the simulations presented here. For more details of the model setup, see Burchard et al. (2009).

4.3.2 Physical and numerical mixing analysis

Since numerical mixing is a serious issue for all coastal ocean models, it needs to be taken into account when mixing and its changes due to structures in the water has to be quantified. Burchard et al. (2009) argued, that for each tracer s the variance decay idue to physical mixing, defined as

$$D^{phy}(s^2) = 2K_v(\partial_z s)^2, \tag{4.19}$$

is the appropriate measure for turbulent mixing as, e.g., the eddy diffusivity alone may take high values although under well mixed conditions there is almost no tracer mixing, see also the detailed discussion by Burchard et al. (2009).

Advection of tracers does not change the volume integrated variance of a tracer in a closed domain. However, monotone tracer advection schemes as they are generally required in coastal ocean models do reduce the volume integrated tracer variance in closed domains. Burchard and Rennau (2008) suggested an analysis method to quantify the numerically induced mixing: The tracer under consideration is as usual advected with the advection scheme of choice, but additionally, also the square of the tracer is advected with the same scheme. After the advection step, the square of the advected tracer is subtracted from the advected tracer square. This difference is the local reduction of the tracer square due to the advection scheme, and divided by the time step (to get a rate), this is defined as the numerically-induced tracer variance (or short: numerical mixing), $D^{num}(s^2)$.

Rennau and Burchard (2009) showed that numerical mixing for the realistic regional Western Baltic Sea model simulation presented by Burchard et al. (2009) amounts to about 50% of the total mixing composed of physical and numerical mixing. They also showed that reductions in numerical mixing due to improved advection schemes lead to increases in physical mixing in such a way that the total mixing is only slightly reduced by improved advection schemes. Therefore, it is the total mixing which needs to be quantified in ocean models and not only physical mixing.

4.4 Impact of parameterisation in idealised hydrostatic model setups

In this section idealised model simulations are carried out with GETM to study the impact of the parameterisation (section 4.2.4) implemented into the hydrostatic model. The differences in the simulations are changes in mixing efficiency (set by the parameter c_4) due to cylindric structures as well as different horizontal model resolutions ($\Delta x = \Delta y = 500$ m, $\Delta x = \Delta y = 1000$ m and $\Delta x = \Delta y = 1500$ m). For all simulations a constant diameter of $d = 10$ m was used for the structures. These simulations also had the purpose to demonstrate that the parameterisation is independent on the model resolution and grid layout.

The domain for the test scenario has a dimension of 80 km × 22 km, with a linear slope in the x-direction descending from a depth of 20 m for $x = 0$ to a depth of 60 m at $x = 80$ km. The model is initially at rest, with a salinity of 30 psu for $x < 2$ km and a background salinity of 8 psu elsewhere. The domain is discretised with $\Delta x = \Delta y = 1000$ m, and 20 vertical layers. The region with structure-induced friction is centred at $x = 18$ km and $y = 39$ km and has an extension of 3 km × 3 km, with an area density of $a = 3 \cdot 10^{-5}$.

Figure 4.7a shows a time series of vertically integrated physical mixing in the centre (1×1 km) of the structure-affected area.

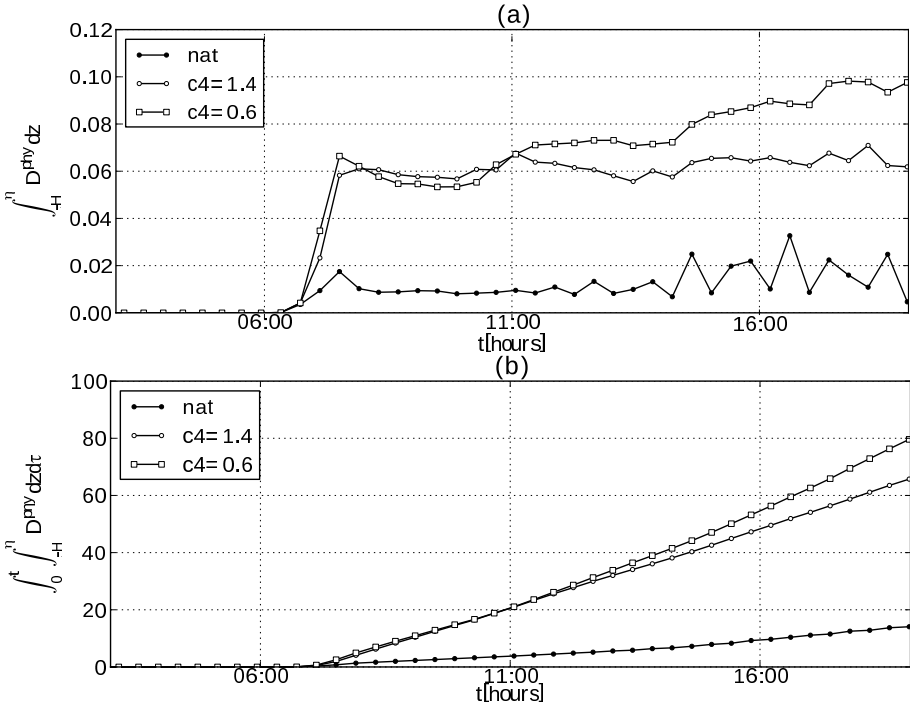

Figure 4.7: Time series of vertically integrated mixing within the centre water column with the structure implementation for 3D downslope plume experiment and $\Delta x = 1000$ m: (a) snapshots of vertically integrated physical mixing and (b) physical mixing integrated in time.

The scenario with $c_4 = 0.6$ clearly shows more mixing than the scenario with $c_4 = 1.4$. Figure 4.7b shows the accumulated physical mixing within the same area (1×1 km in centre of structure) with orders of magnitude higher mixing than for the natural case.

Figure 4.8 shows for the same physical scenario the dependence of total salinity mixing (physical & numerical) on the horizontal model resolution ($\Delta x = 250$ m, $\Delta x = 500$ m and $\Delta x = 1000$ m) introduced by structure-induced mixing.

For each of the three model resolutions almost 100 model simulations with the idealised 3D plume setup were carried out using different area densities a as well as different values for c_4. To quantify the structure-induced mixing, mixing was integrated over a 2 km wide volume around the location of the parameterised structure. The values of up to 25% increased mixing (figure 4.8) are lower than the increase found in figure 4.7 because only the high mixing area in the vicinity of the structure was considered here. However, it is found that the total salinity mixing induced by the structure-induced mixing is slightly depending on grid resolution and some convergence of the total mixing for decreased

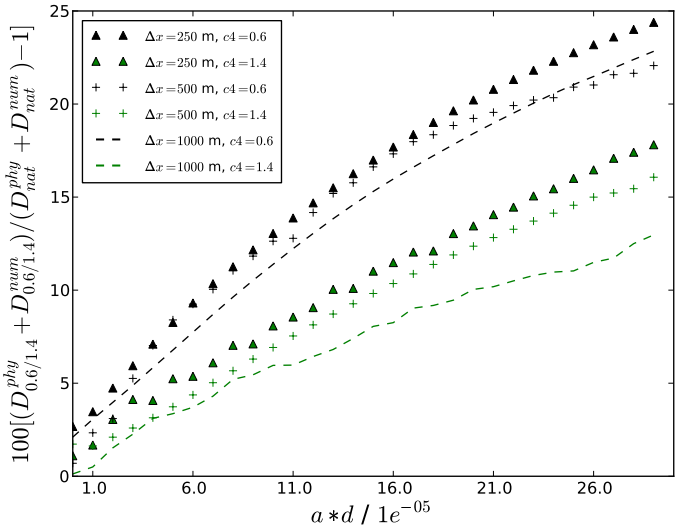

Figure 4.8: 3D downslope plume experiment: Impact of different horizontal model resolutions on the total (numerical + physical) salinity mixing. For this image more than hundred scenarios with different values for the area density a and values of c_4 were calculated.

resolution can be noted, except for $c_4 = 0.6$ at high area densities. To summarise, it is found that the impact of the structure-induced mixing parameterisation is sufficiently independent on the model resolution.

4.5 Application to the Western Baltic Sea

To quantify the potential impact of offshore wind farms in the Western Baltic Sea, the validated realistic model setup using GETM as presented by Burchard et al. (2009) has been used as a reference case. This model setup which has an open northern boundary in the Kattegat and an open eastern boundary in the Stolpe sill area (see figure 4.2), is forced by open boundary values from a multi-annual Baltic Sea model with a resolution of 3 nm (nautical miles) described by Neumann et al. (2002) and meteorological forcing from the German Weather Service Local Model with a resolution of 7 km and 3 hours. The Western Baltic Sea model has a horizontal resolution of 0.5 nm and is vertically resolved by 50 general vertical coordinate layers, with a non-linear zooming towards the bed. The simulation is initialised on Sep 1, 2003 and the 16 month evaluation periods start on Jan 1, 2004. For further details, see Burchard et al. (2009).

In addition to this natural mixing study, four scenarios with different horizontal distributions of offshore wind farms (OWFs) and different values for c_4 are calculated over a period of 16 months. This period covers a sufficient amount of medium-intensity inflow events to provide enough statistical certainty concerning the impact of structure-induced mixing. For the four different scenarios two distributions of OWFs (a realistic distribution with all existing and planned wind farms, see table 4.1 and a very extensive distribution, see table 4.2) and two degrees of structure-induced mixing efficiencies with *weak mixing* ($c_4 = 1.4$) and *strong mixing* ($c_4 = 0.6$) are investigated. Both wind farm distributions are shown in figure 4.1. The specifications of these five scenarios are summed up in table 4.3.

The impact of OWFs is quantified by means of calculating net transports of different density and salinity classes through the Bornholm Channel and mean vertical density profiles in this area. The Bornholm Channel is well suited for such a quantification because of the topographic conditions in the Western Baltic Sea which ensure that almost all dense, oxygen carrying bottom water from the North Sea has to pass through this narrow channel on its way towards the eastern basins of the Baltic Sea (see also figure 2.18).

4.5.1 Diapycnal mixing

Figure 4.9a shows a time series (Jan 2004 - Sep 2004) of the bottom salinity at the Bornholm Channel (see figure 4.1 for the exact position) for the reference case and figure 4.9b shows the differences between the time series of the natural case (REF) and the four OWF cases (R1.4, R0.6, U1.4 and U0.6).

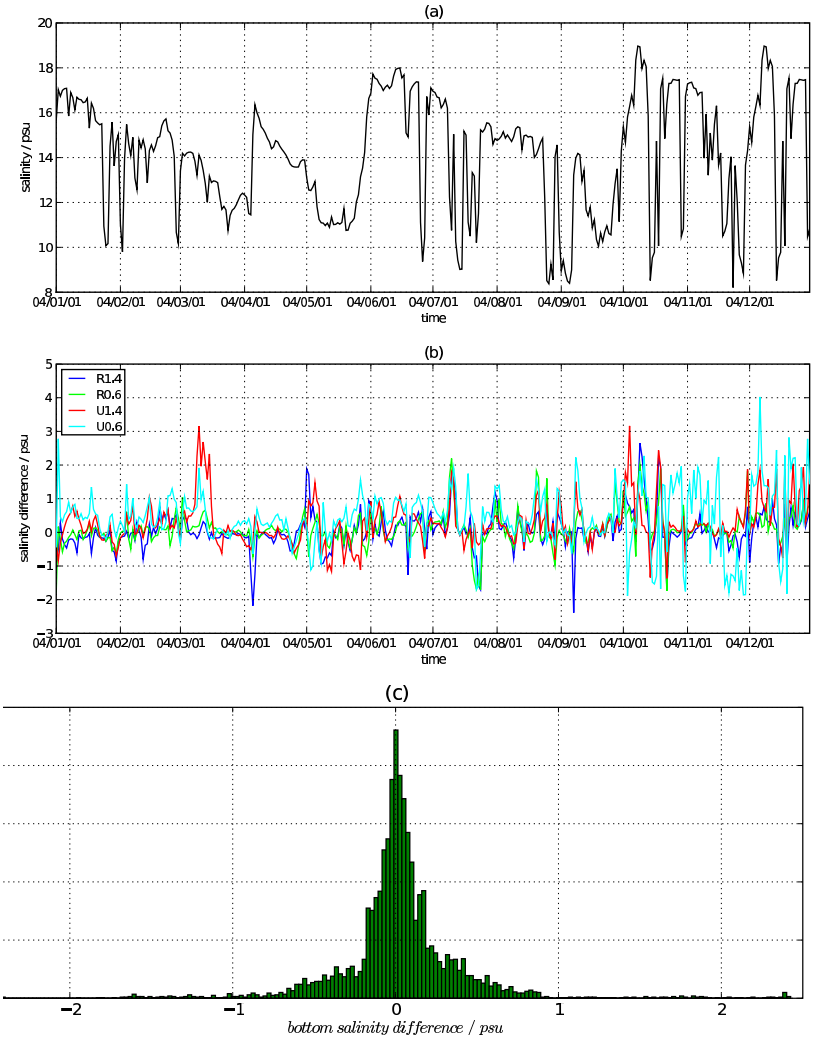

Figure 4.9: Western Baltic Sea simulation: a) Time series of bottom salinity in the Bornholm Channel (see figure 4.1 for the location); b) time series of difference in Bornholm Channel bottom salinity between the reference case (REF) and the scenarios with OWFs ($\Delta s_b > 0$ means reduction of salinity due OWF impact); c) probability distribution for this time series for scenario R1.4.

As an expected result it is found, that both U1.4 and U0.6 cases show higher difference values than

the realistic scenarios R1.4 and R0.6. With a few exceptions, maximum differences are below 1 psu for all cases.
Plotting these data as a probability distribution reveals that both positive and negative differences show a similar distribution around zero (figure 4.9c, only shown for R1.4). The mean values for the bottom salinity differences over these 12 months are $\Delta s_b = 0.0059 \pm 0.491$ for R1.4, $\Delta s_b = 0.0222 \pm 0.469$ for R0.6, $\Delta s_b = 0.1728 \pm 0.595$ for U1.4, and $\Delta s_b = 0.4222 \pm 0.560$ for U0.6. This indicates a small net decrease of bottom salinity due to a realistic distribution of OWFs in the Western Baltic Sea which is even for the *strong mixing* case more than one order of magnitude smaller than the standard deviation of the impact. As expected, the signal is much clearer for the scenarios with unrealistically extensive OWF distributions, but even for the most extreme case the standard deviation is larger than the signal. Since the statistics for one position shown in figure 4.9 do not conclusively show the net effect of OWFs in the Western Baltic Sea on the ventilation of the Baltic Sea basins, changes in salinity distribution during one month (June 2004) with relatively strong saline inflows through the Bornholm Channel are shown in figure 4.10. Clearly, highest monthly mean salinities occur at the bottom of the eastern part of the Bornholm Channel. There, the decrease of salinity due to OWFs are between 0.05 psu (R1.4) and 0.1 psu (R0.6). Above the bottom mixed layer, a relative increase of salinity due to OWFs is detected, which indicates that additional entrainment diluted these dense bottom currents further upstream in the Arkona Sea and consequently elevated the density interface.

Figure 4.11a shows results of an investigation of water mass transport within certain density classes (with $\Delta\rho = 0.2\ \mathrm{kg\,m^{-3}}$) for the reference case (REF).
The expected behaviour of dense bottom water propagating into the Bornholm Basin (positive values) and lighter near-surface water flowing out of the Baltic Sea can be clearly seen. The model derived water mass transport averaged over 4 months with significant inflow events (Nov 2003, Mar 2004, Jun 2004 and Jul 2004) amounts to about $0.42 \cdot 10^6\ \mathrm{kg\,s^{-1}}$ which is consistent with the findings by Reissmann et al. (2009). The inflowing water mass transport is distributed over more density classes than the outflows, because inflow events show a strong variability in salinity. Figure 4.11b shows that water mass transport within the highest four density classes is strongly reduced (by up to 100%) and moved downwards the density class scale (with some increases and decreases of water mass transport in respective classes). As only higher densities have the ability to ventilate the deeper layers in the eastern parts of the Baltic Sea, this may have some theoretical ecological impact. However, figure 4.11b shows that the total salt flux reduction in the highest four density classes is small. In the following section 4.5.2 an inflow in Mar 2004 which causes a significant decrease in bottom salinity for the scenario with extensive wind farms but weak mixing (U1.4) is investigated in detail with regard to changes in depth of interleaving of dense bottom currents in the Bornholm Sea.

4.5.2 Impact of one single inflow

As seen in figure 4.9a and discussed in the previous chapter, there may be certain events with higher densities that are strongly diluted by the OWFs (density differences of up to 3 psu for the U1.4 scenario in Mar 2004). Although the strong mixing during this inflow event can be regarded as a single extreme

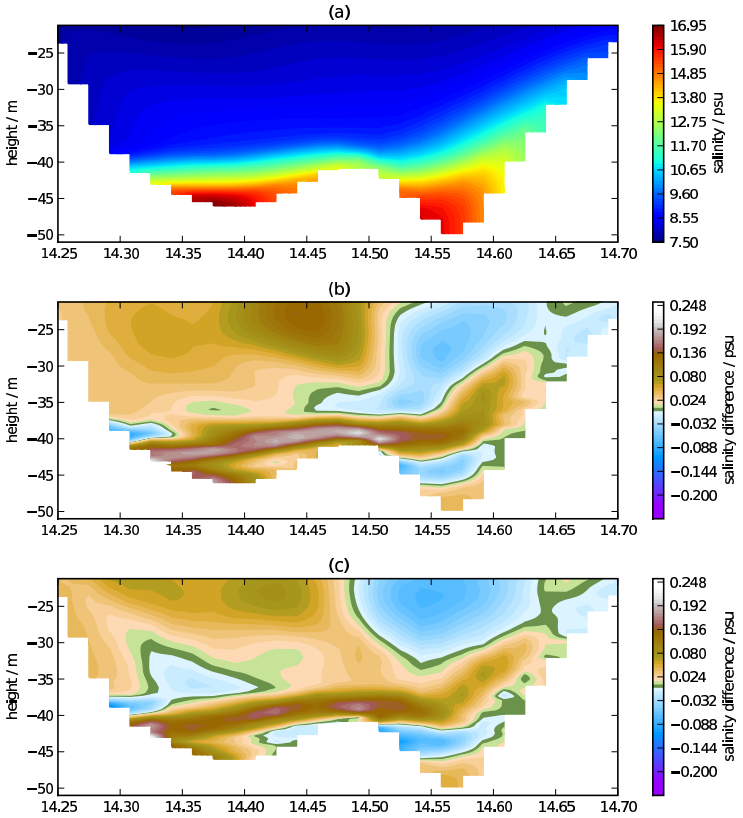

Figure 4.10: Western Baltic Sea simulation: a) monthly mean (June 2004) salinity for the reference scenario (REF) along a transect across the Bornholm Channel (see figure 4.1 for the location); b) monthly mean salinity change due to OWF along same transect for the scenario R1.4; c) monthly mean salinity change due to OWF along same transect for the scenario R0.6.

event, we analyse it to see how a strong mixing signal affects the ventilation in the Bornholm Sea. In average, as shown by figure 4.11c, the change in transport of highly saline water is negligibly small. It can be assumed that a complete dilution of the highest density classes has a negligible ecological effect since the total transport into the Bornholm Sea connected to these classes is small.

When considering a time-series of bottom salinity at the Bornholm Channel as demonstrated by figure 4.9a it is seen that the differences between the REF case and all four cases is positive in average, meaning a net decrease in salinity due to OWFs. In Mar 2004 bottom salinity is decreased by 3 psu for the U1.4 case. In order to study the impact of this decrease on the ventilation of intermediate layers in the Bornholm Sea, a passive tracer is released in the Bornholm Channel with a concentration of unity in the REF case and also in the U1.4 case. The resulting bottom tracer concentrations on Mar 31 are shown in figure 4.12a for the reference case and in figure 4.12b the difference in bottom tracer concentration for the U1.4 scenario is shown.

The decrease in bottom tracer concentration due to the extensively distributed OWFs is up to 30%, which indicates that the detachment of the tracer from the bottom is taking place higher in the water column. Figure 4.12c demonstrates for a cross-section through the Bornholm Sea how this interleaving process with a typical depth of 60 m happens. To quantify the changes in interleaving depth due to the extreme OWFs case (U1.4), the centre of gravity of the tracer cloud for each scenario has been

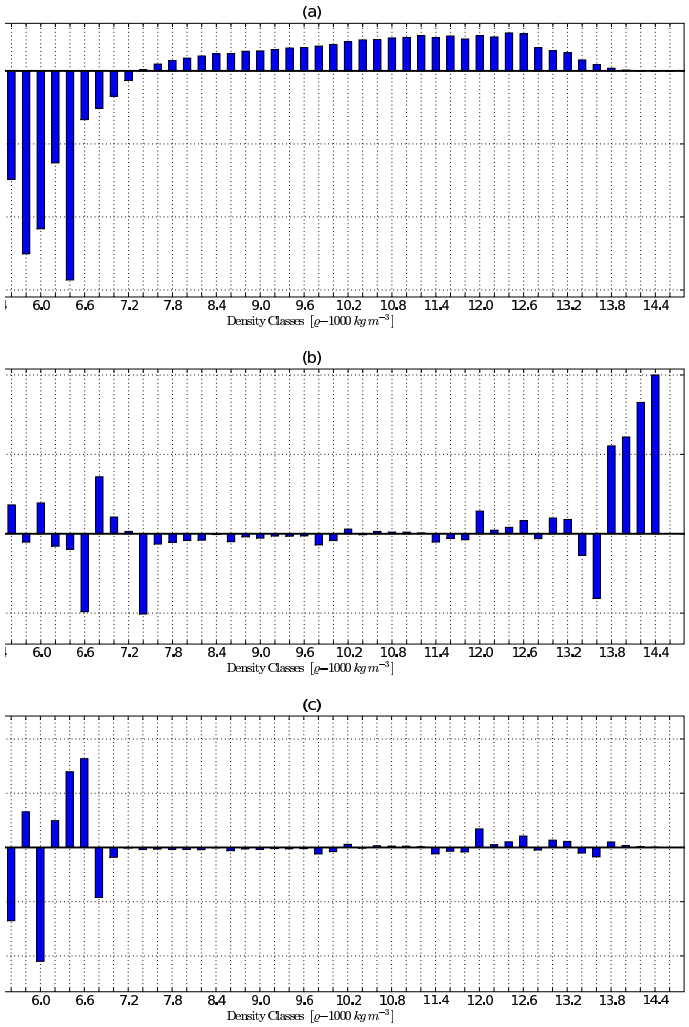

Figure 4.11: Western Baltic Sea simulation: monthly mean (averaged over Nov 2003, Mar 2004, Jun 2004 and Jul 2004 during which relative strong inflow activity was detected) water mass transport M across a transect at Bornholm Channel (see figure 4.1 for the location), shown as contributions from density classes. a) water mass transport M for reference scenario (REF); b) difference in % between reference (REF) and R0.6; c) difference in water mass transport ΔM between reference (REF) and R0.6;

calculated as function of the tracer concentration on Mar 31. Clearly, for a wide range of tracer concentrations the interleaving depth is decreased by up to 3 m due to OWF mixing in the Western Baltic Sea. One should however keep in mind that this is an extreme case (compare to figure 4.9a) and that for scenarios with realistic OWF distributions (scenarios R1.5 & R0.6) changes in interleaving depth are substantially below 1 m.

4.5.3 Impact on annual time scale

To investigate on how mean salinities are affected for the four OWF scenarios, the bottom salinity of the reference case (REF) is compared to the four OWF scenarios by taking the 16 month mean bottom salinity of the natural case and subtracting the mean bottom salinity of each of the four cases (see figure 4.13). The bottom salinity differences found for the cases with realistic OWF distribution, R1.4 and R0.6, are in the order of up to 0.2 psu.

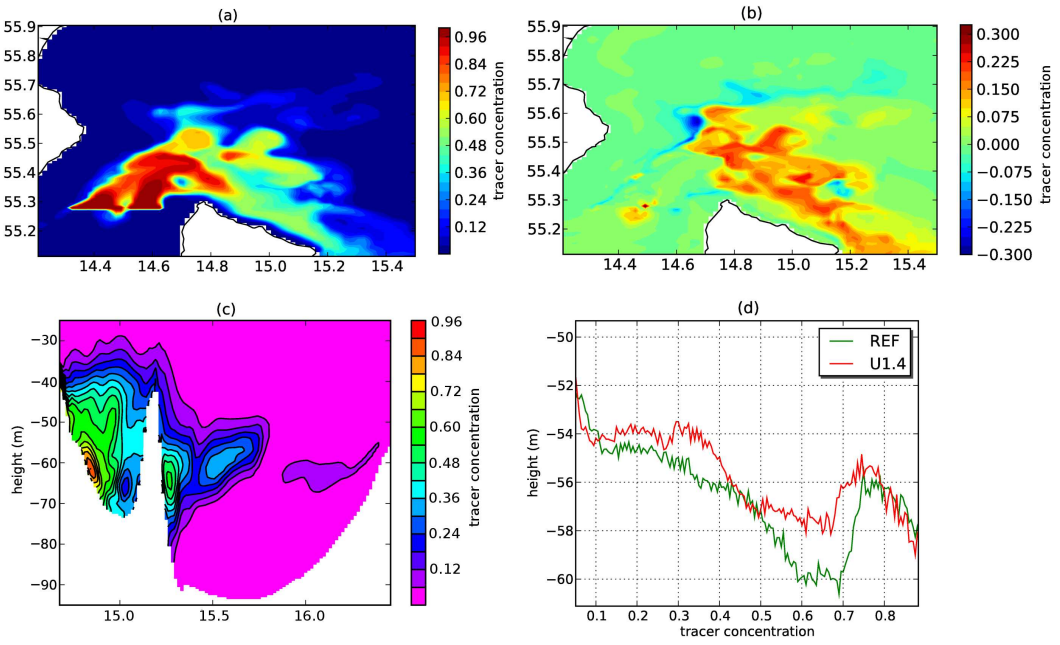

Figure 4.12: Western Baltic Sea simulation, monthly mean (Mar 2004) results from numerical tracer release experiment as example for strong impact of OWF (scenario U1.4): a) bottom tracer distribution for reference case (REF); b) difference in bottom tracer distribution between REF and U1.4 (positive means reduction of tracer concentration due to OWFs); c) tracer distribution along a transect through the Bornholm Sea (see figure 4.1 for the location); d) height of centre of gravity of tracer cloud as function of tracer concentration.

Interestingly, in the Arkona Sea the saline bottom waters seem to be less diluted by OWFs when strong mixing is assumed (R0.6). This may be explained by the fact that dense bottom currents are decelerated by OWFs such that entrainment of less saline ambient waters may be locally reduced. However, for the R0.6 scenario, bottom salinities are reduced more significantly than for the weak mixing R1.4 scenario, which is consistent with a net increase in mixing and which is more relevant for the ventilation of intermediate layers in the Bornholm Sea.

A different picture is found for the two cases with extensive OWF distributions, U1.4 and U0.6, where the mean bottom salinity is decreased by up to 0.3 psu for U1.4 and by up to 0.6 psu for U0.6. A similar picture between the four different scenarios arises along a transect through the Bornholm Channel. Figure 4.14 shows the differences in annual mean salinity between the reference scenario (REF) and the four OWF scenarios.

The bottom salinity differences for the two cases with realistic distribution of OWFs are in the order of up to 0.03-0.05 psu and for the extensive OWF cases between 0.15 psu (U1.4) and 0.45 psu (U0.6). All difference plots show a similar behaviour with decreased bottom salinities and stronger impact at the western channel. The feature of decreased mean bottom salinities, increased mean salinities due to the OWFs in the area of the pycnocline and decreased transport above the pycnocline, which has been found investigating monthly differences at this transect (see figure 4.10), was not found in the annual mean differences. This is because of the different plume strengths passing the Bornholm Channel which averages away the area of increased mean salinities in the area of the pycnocline.

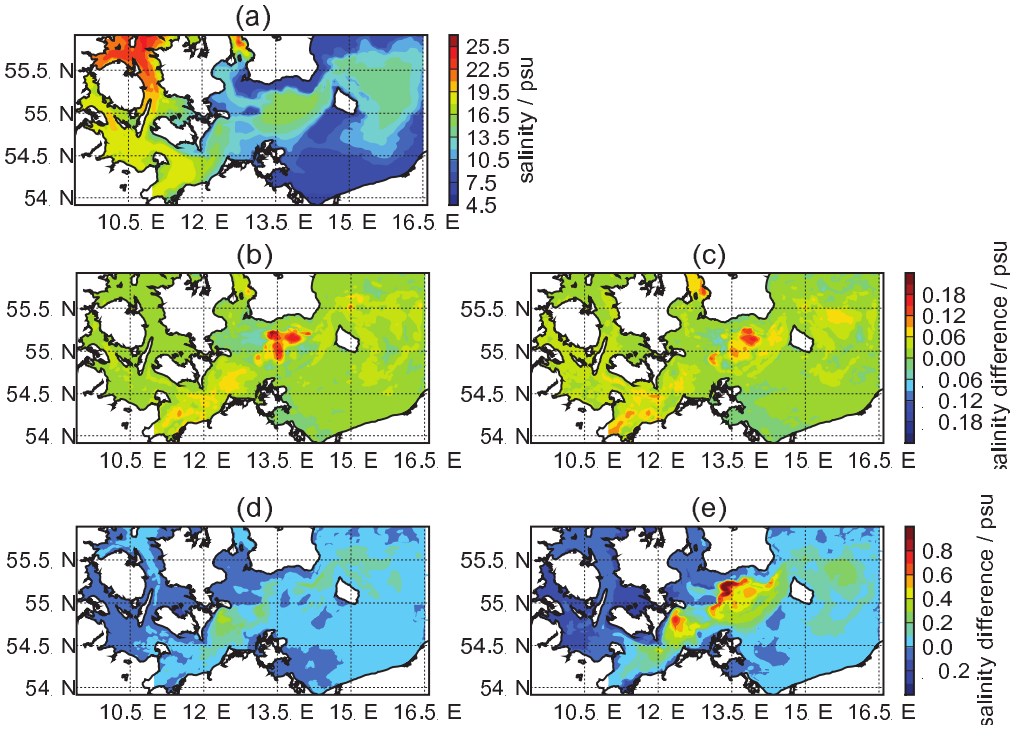

Figure 4.13: Western Baltic Sea simulation; annual mean (year 2004) of bottom salinity and bottom salinity difference due to OWFs: a) reference scenario REF; b) scenario REF - R1.4; c) scenario REF - R0.6; d) scenario REF - U1.4; e) scenario REF - U0.6.

4.6 Discussion and conclusions

Based on a carefully validated three-dimensional model for the Western Baltic Sea (Burchard et al. (2009)), the impact of offshore wind farms on dense water inflows into the Baltic Sea has been studied. To include the effects of these structures which are of a fairly small scale into a regional and hydrostatic ocean model, a parameterisation for structure-induced friction in unstratified flow (Svensson and Häggkvist (1990)) had to be recalibrated to properly represent vertical mixing in strongly stratified flow. This parameterisation is based on additional quadratic friction terms in the momentum equations as well as additional production terms in the dynamic equations for turbulent kinetic energy and its dissipation rate, the latter of which includes a calibration parameter (c_4). The physical meaning of this parameter could be identified to be connected to the structure-induced mixing efficiency. The calibration strategy applied here was to compute structure-induced mixing by means of a numerical model resolving the structure as well as the small-scale hydrodynamic processes in the vicinity of the structure. For simplicity and to be fairly general, cylindric structures had been chosen for this purpose. A numerical model based on the Reynolds-Averaged Navier-Stokes (RANS) equations and using an SST k-ω turbulence closure model to compute eddy viscosity and diffusivity had been found appropriate to resolve the relevant dynamics (Schimmels (2008)). An idealised dense bottom current as it is typically seen in the Western Baltic Sea during inflow situations (Burchard et al. (2005); Arneborg et al. (2007)) had been forced in this model, such that various mixing parameters could be calculated under a variety of Froude numbers and Ekman numbers with and without influence of a cylinder. The volume integrated additional buoyancy flux (difference in buoyancy flux between cases with and

without cylinder-induced friction) had been identified as the critical parameter to quantify the mixing impact of a cylinder. For an Ekman number ($K = 0.8$) typical for inflows in the Western Baltic Sea, and a dense bottom current of 10 m thickness with a cylinder of 10 m diameter, structure-induced buoyancy production from the RANS model was compared to equivalent buoyancy production from a high-resolution water column model for a variety of Froude numbers and values for c_4. It was found that a value of $c_4 = 1.4$ resulted in mixing slightly smaller than predicted (20% mixing efficiency) and that a value of $c_4 = 0.6$ (mixing efficiency of about 50%) resulted in an overestimation of mixing by about a factor of two. Due to the uncertainty of the RANS model and the fact that the design of wind turbine foundations often strongly deviates from cylindric structures, it was decided to use both values, i.e. $c_4 = 1.4$ as *weak mixing* case and $c_4 = 0.6$ as *strong mixing* case.

Several idealised numerical experiments showed that the parameterisation is consistent in the sense that mixing is indeed increased for increased structure-induced mixing efficiency. It was furthermore shown that the total mixing (physical & numerical) is fairly independent of the horizontal model resolution. It can therefore be concluded that the approach chosen here has the capability to give reliable quantitative estimates of additional mixing due to offshore wind farms and its ecological consequences for the Baltic Sea.

Besides the reference experiment without structure-induced mixing, four impact assessment simulations have been carried out, with two wind farm distributions, one including all existing, approved and planned wind farms, and a second one with unrealistically extensive wind farms, just to study the potential impact of such a worst case scenario.

First of all, it requires a careful analysis to see any significant changes in saline inflows due to the offshore wind farms. Since almost all inflows into the Baltic Sea proper have to pass the Bornholm Channel just east of the Western Baltic Sea region with potential wind farm impact, a study of the near-bottom salt and mass inflow in that region has been made. One result is that the impact of wind farm mixing leads to spatially and temporally varying changes in bottom salinity, with decreases for realistic wind farm distributions by 0.0059 ± 0.491 psu for weak mixing (R1.4) and by 0.0222 ± 0.469 psu for strong mixing (R0.6). Clearly, these changes are small compared to the natural variability and also small compared to the variability of the impact itself. In contrast to this negligible reduction scenarios with over-exaggerated wind farm distribution led to reduction in bottom salinity in the Bornholm Channel by 0.1728 ± 0.595 psu for weak mixing (U1.4) and 0.4222 ± 0.560 psu for strong mixing (U0.6).

A statistical analysis of the net salt transport into the Bornholm Sea quantified in terms of density classes reveals that the salt transport in the four highest density classes of 0.2 $\mathrm{kg\,m^{-3}}$ width each are partially or completely vanishing in the scenario with realistic wind farm distribution and strong mixing. However, the relative contribution of these high salinity classes to the net salt inflow is small, since only during short single events thee high densities are obtained.

To investigate in depth an event with a significantly strong impact of offshore wind farms, the scenario with the strongest impact on bottom salinity in the Bornholm Channel has been analysed for the month during which this impact happened. During this month, a passive bottom tracer has been released continuously in the Bornholm Channel and it was found that the tracer intruded in the stratified Bornholm Sea water column about 2 m (58 m instead of 60 m depth) higher when wind farm mixing

was considered. This means that in such an extreme month ventilation occurs a few percent of the water depth higher in the water column.
In general, bottom salinities in the Arkona Sea are decreased locally by about up to 0.2 psu for realistic scenarios and by about up to 0.3-0.6 psu, depending whether weak or strong mixing is assumed.
It can be concluded that the impact of realistic wind farm distributions on the Baltic Sea ecosystem, according to the present planning state is insignificant compared to the natural variability. Even if a structure-induced mixing efficiency of twice the best guess is assumed, bottom salinities in the Arkona Sea are decreased only locally by about 0.2 psu. In the most extreme month during the entire simulation period, ventilation of the Bornholm Sea occurred about 2 m higher in the water column. This is in accordance with the finding that only the highest density classes vanish due to wind farm mixing. Those contribute however only little to total ventilation. Although only the impact of cylindric wind farm foundations with diameters of 10 m was quantified, potential increase of structure-induced mixing due to more complex foundations (e.g., jacket constructions) or larger numbers of foundations with smaller diameters (leading to the same area density) was accounted for by the consideration of strong mixing (twice the mixing efficiency of the best guess).
It should however be noted that a coverage of large parts of the Western Baltic Sea with offshore wind farms could lead to more significant impacts, such as bottom salinity decreases in the Bornholm Channel by 0.4222 ± 0.560 psu and local bottom salinity decreases in the Arkona Sea of typically 0.6 psu. Therefore, in case of planned offshore wind farm coverages substantially exceeding the present planning state, the ecological impacts would need to be reassessed.

Code	OWF distribution	c_4	meaning
R1.4	as planned in 2010	1.4	realistic OWF distribution, *weak mixing*
R0.6		0.6	realistic OWF distribution, *strong mixing*
U1.4	unrealistically extensive	1.4	unrealistic OWF distribution, *weak mixing*
U0.6		0.6	unrealistic OWF distribution, *strong mixing*
REF	none (natural case)	-	reference case

Table 4.3: Specifications of different Western Baltic Sea simulations with and without OWFs.

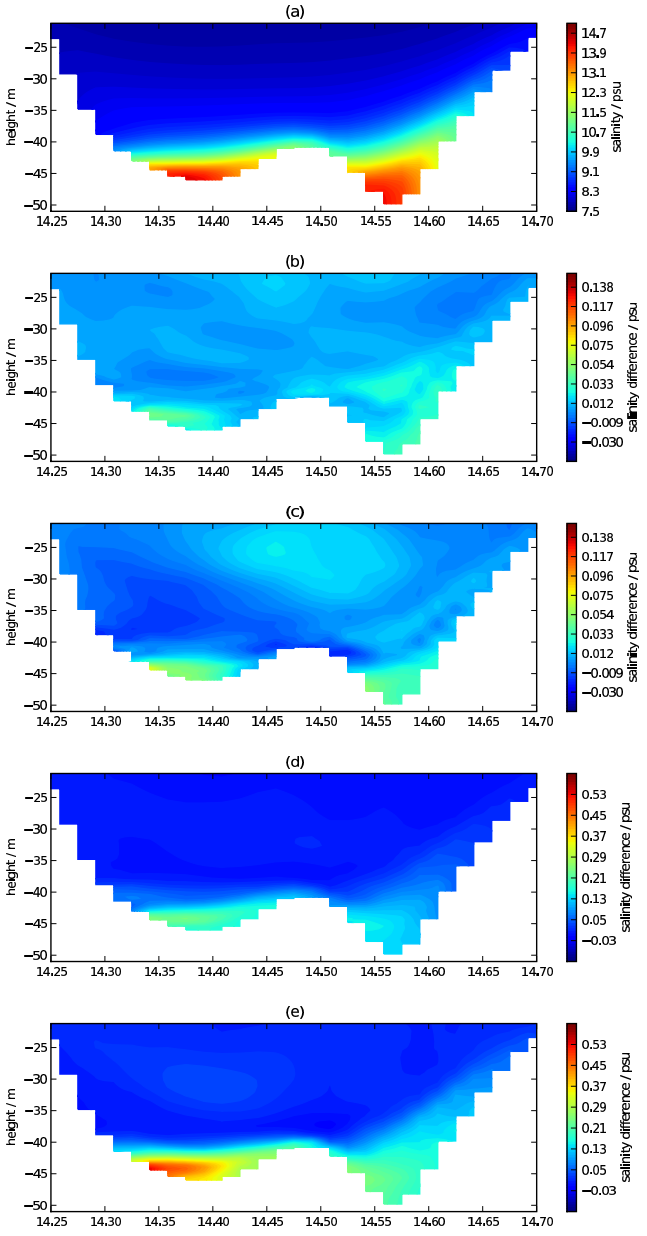

Figure 4.14: Western Baltic Sea simulation: annual mean (year 2004) of salinity difference along a transect through the Bornholm Channel (see figure 4.1 for the location); due to OWFs: a) reference scenario REF; b) scenario REF - R1.4; c) scenario REF - R0.6; d) scenario REF - U1.4; e) scenario REF - U0.6.

Summary and Conclusions

This work focused on mixing in dense bottom bottom currents in the coastal regime of the Western Baltic Sea has compiled several idealised and realistic numerical model studies in order to estimate numerically-, physically- and structure-induced mixing. As each of the chapters in this thesis are different journal publications, they already include a rather long and detailed discussion of each of the three main topics. Hence, this summary is a brief conclusion of the previous - and already discussed - chapters.

The numerical model was able to reproduce barotropically driven overflows of dense bottom water entering the western Baltic Sea whereas timing, dilution and vertical structure are found to be in good agreement with station- and ship cruise measurements. The flow propagation of dense bottom water surrounding Kriegers Shoal is in agreement with previous work, where higher salinities and stronger flows are found in the channel north of Kriegers Shoal than compared to the southern trench. Water mass investigations applying a passive tracer found that the flow north of Kriegers Shoal is not influenced by Darss Sill bottom water whereas the flow in the channel south of Kriegers Shoal is highly influenced by both Darss Sill and Drogden Sill water as both show similar salinity values in this area. Previous work has discussed that the flow south of Kriegers Flak consists only of Drogden Sill water masses (Lass et al. (2005)). As the water masses from Drogden Sill show higher salinities than originating from Darss Sill, a strong separation (interleaving) of water masses is found east of Kriegers Shoal in the central Arkona Basin where denser Drogden Sill water is shifted below Darss Sill water masses. A correlation of vertical profiles of passive tracers in the whole model domain over a one year period has revealed that the anti-correlation with mean values of $R = -0.8$ occurs during about 25 % of the year whereas for positive correlation (vertically mixed water masses) with mean values of $R = 0.6$ occurs during only 6 % of the year. In the results of the mean positive correlation coefficients, increased correlation coefficients are found the closer the flow reaches the Bornholm Channel indicating increased mixing between both water masses. However, when considering one or the other passive tracer only, it is found that Drogden Sill water masses are potentially found in the northern central Arkona Basin and Darss Sill water mainly on the southern part of the Arkona Basin. During inflow conditions in the central Arkona Basin a three layer stratification is found with Drogden Sill water at the bottom, Darss Sill water in the intermediate layers and fresh surface water. Based on the model simulations a regional estimate of turbulent mixing of dense bottom water based on the salinity variance decay could be calculated indicating strongest mixing at the shallow sills and deep underwater channels. Surprisingly strong mixing on the basis of calculating the annual mean could be

found in the Bornholm Channel which is due to an continuous flow of dense bottom water out of the central Arkona Basin.

As a second step the numerically induced mixing has been quantified with the help of idealised and realistic model studies. Idealised numerical model simulations have revealed that numerically induced mixing due to the truncation errors of the numerical advection schemes are in the same orders of magnitude than pure physically induced mixing. For an idealised large scale overflow experiment, the volume integrated numerically induced mixing has even been up to 10 times higher than the physically induced mixing. For a coastal ocean model setup of the physically active Western Baltic Sea it has been found that both measures have same orders of magnitude. Further it was found that decreasing the horizontal resolution of the numerical model, the overall contribution of numerically induced mixing is reduced compared to the pure physically induced mixing. But compared to the changes in the numerical and physical contributions the total mixing stays almost constant for the different horizontal resolutions - a finding also been supported via idealised 2D scenarios of an overflow experiment conducted within this work. An additional new finding is the different horizontal and vertical distribution of numerically and physically induced mixing which depends on the numerical grid used, the individual model bathymetry and the general tracer conditions (salinity and temperature) of the geographical area which is being simulated. Numerical diffusivities calculated with the help of derived numerical tracer variance decay are partly found to be orders of magnitude higher than the turbulent diffusivity derived via the turbulence model. Especially at the lateral boundaries of dense bottom currents where strong vertical shear or differential advection may induce strong physical mixing, high amounts of numerical mixing has been found that can even be several times as high as the pure physical mixing. Hence it is suggested that physical process studies should always discuss their results with care, as model derived entrainment rates may significantly being influenced by numerical diffusion due to errors in the tracer advection schemes.

Based on the validated three-dimensional model for the Western Baltic Sea (see chapter 2, Burchard et al. (2009)), the impact of offshore wind farms on dense water inflows into the Baltic Sea has been studied. As the effect of these structures with diameters of less than 10 m is a subgrid-scale process in the coastal ocean model applying a horizontal resolution of about 1 km, a parameterisation has been developed and calibrated to represent additional vertical mixing in stratified flow. Several idealised and realistic experiments revealed a relatively low overall impact of the vertical structures even for a 'worst-case' scenario with an unrealistically extensive distribution of offshore wind farms. A comparison of time series between the different windpark scenarios has revealed significant fluctuations in the order of up to $+/-2$ psu, but low impact of about $0.1-0.3$ psu has been found when calculating differences in mean bottom fields compared to the reference (pure natural) model simulation. Finally it was discussed that the impact of such structures is comparably weak as the horizontal distance of the vertical structures in a realistic offshore wind farm of about 800 m has a neglectable impact on the flow resistance and dilution of the investigated dense bottom currents. Another reason for the low impact of the structures is that the tidal influence in the Western Baltic Sea is neglectable and that Froude numbers are rather low.

Outlook

This work has proved the ability of numerical models to successfully reproduce the complex natural phenomenon of gravity currents such as dense bottom currents in the transition area between vertically well-mixed, high-saline Kattegat water masses and the stratified Baltic Sea. However, the numerical model result contains a surprisingly high amount of numerically induced (spurious) mixing which was explained due to discretisation errors in the numerical advection schemes. Burchard et al. (2009) and Rennau and Burchard (2009) showed that the contribution of this spurious mixing can be significantly reduced using increased spatial resolution which will significantly reduce the numerically induced mixing as demonstrated in chapter 3. Global climate models which does not allow for realistically resolve the source and product regions of dense overflows in the oceans due to the low horizontal and vertical resolution, will significantly improve when using higher horizontal model resolution which will significantly reduce spurious mixing. Only by the future development in parallel computers the horizontal model resolution can be more and more refined. However, the use of higher order advection schemes and the development of advanced numerical methods in both advection schemes and physical mixing schemes is still needed. Furthermore the research of spurious mixing due to discretisation errors in the numerical tracer advection schemes should be extended by analysing the discretisation errors in the momentum advection equations which commonly use similar advection schemes than used for tracer advection. Even the qualitative result obtained when making use of Lagrangian tracers can be indirectly influenced by the discretisation errors in the momentum advection when the Lagrangian tracers are coupled to the velocity fields of a hydrostatic ocean circulation model where the momentum advection may be significantly influenced by numerical diffusion. A promising new numerical feature in ocean modelling has recently been shown by Hofmeister et al. (2010b) via developing and testing adaptive vertical coordinates which are able to significantly reduce numerically induced mixing as they allow for a better representation of tracer gradients (e.g. the gravity current interface).

Numerical models alone cannot replace moorings, long-term observations and field experiments which are the essential source in successful calibration of numerical models and physical mixing schemes. Both the mismatch and agreement between model and observations have been documented and discussed in this work in chapter 2. Especially for model setups covering a larger domain and which are hence not governed primarily by the boundary conditions alone, the availability of long-term observations together with a realistic internal reproduction of at least most of the governing physical processes is highly necessary. Without the long-term observations at the three main stations in the

Western Baltic Sea, namely Arkona, Darss Sill and Drogden Sill station, the results of the model could have been easily called into question whether each of the separate inflow events crossing Darss and Drogden Sill are correctly reproduced which was a precondition of the research on spreading behaviour conducted in this work. As such long-term monitoring, moorings and ship cruises is an essential resource for both numerical and physical model development (e.g. turbulence parameterisation, bottom boundary layer in level coordinate models) and the calibration of coastal and large-scale ocean models.

Concerning the quantitative model study on enhanced mixing of Offshore Wind Farms on stratified flow, a number of things could be improved or further analysed. A first step would be to analyse the presented parameterisation in more detail with several idealised model setups to quantify the amount of additional structure induced mixing based on different gravity current and environment parameters as for example bottom friction, plume thickness, bottom surface density difference, current velocity (e.g. shear-induced entrainment with and without strong surface currents in different directions), Froude number and Coriolis force. Further studies may include the effect of tides which would significantly increase the internal Froude number with values above unity (Lass et al. (2008) - observations in the Great Belt). As the entrainment rate can be related to the Froude number, this may drastically increase turbulent mixing rather than compared to the almost tide-less Baltic Sea with Froude numbers in the order of about 0.6 (see e.g. Arneborg et al. (2007) or figure 1.2). Also research on internal waves and corresponding mixing as observed by Lass et al. (2008) at the Great Belt Bridge may be an interesting research subject, as they are able to export momentum and turbulent mixing far from the underwater structures which has not further been analysed in this thesis.

Bibliography

Adcroft, A., Hallberg, R., 2006. On methods for solving the oceanic equations of motion in generalized vertical coordinates. Ocean Modelling 11, 224–233.

Arakawa, A., Lamb, V. R., 1977. Computational design of the basic dynamical processes of the ucla general circulation model. Meth. Comput. Phys. 17, 173–263.

Arneborg, L., Fiekas, V., Umlauf, L., Burchard, H., 2007. Gravity current dynamics and entrainment - a process study based on observations in the Arkona Basin. J. Phys. Oceanogr.,In print.

Arntsen, O. A., 1998. Lee waves and hydrodynamical load due to the motion of a submerged horizontal circular cylinder in a three layer fluid. Journal of Hydraulic Research 35, 435453.

Austin, W. E. N., Inall, M. E., 2002. Deep-water renewal in a scottish fjord: temperature, salinity and oxygen isotopes. Polar Research 21, 251257.

Baines, P. G., 2001. Mixing in flows down gentle slopes into stratified environments. J. Fluid Mech. 443, 237–270.

Banas, N. S., Hickey, B. M., 2005. Mapping exchange and residence time in a model of Willapa Bay, Washington, a branching, microtidal estuary. J. Geophys. Res. 110, C11011, doi: 10.1029/2005JC002950.

Beckmann, A., Döscher, R., 1997. A method for improved representation of dense water spreading over topography in geopotential-coordinate models. J. Phys. Oceanogr. 27, 581–591.

Bethoux, J. P., Gentili, B., Morin, P., Nicolas, E., Pierre, C., Ruiz-Pino, D., 1999. The Mediterranean Sea: a miniature ocean for climatic and environmental studies and a key for teh climatic funtioning of the North Atlantic. Progr. Oceanogr. 44, 131–146.

Bleck, R., 2002. An oceanic general circulation model framed in hybrid isopycnic-cartesian coordinates. Ocean Modelling 4, 55–88.

Blumberg, A. F., Mellor, G. L., 1987. A description of a coastal ocean circulation model. In: Heaps, N. S. (Ed.), Three dimensional ocean models. American Geophysical Union, Washington, D.C., pp. 1–16.

BMU, 2007. Offshore wind power deployment in Germany.

Bo Pedersen, F., 1980a. Dense bottom currents in Rotating Ocean. Published as: Journal of the Hydraulic Division, Proceedings of the American Society of Civil Engineers,19.

Bo Pedersen, F., 1980b. A monograph on turbulent entrainment and friction in two-layer stratified flow. Ph.D. thesis, Danish Technical University, Lyngby, Denmark, published as: Series Paper 25, IHHE, DTU, Lyngby, Denmark, 397 pp.

Britter, R. E., Linden, P. F., 1980. The motion of the front of a gravity current travelling down an incline. J. Fluid Mech. 99, 531–543.

Broecker, W. S., 1991. The great ocean conveyor. Oceanography 4, 79–89.

Buch, E., 1982. On entrainment observed in laboratory and field experiments. Tellus 34, 307–311.

Burchard, H., 2002. Applied turbulence modelling in marine waters. Vol. 100 of Lecture Notes in Earth Sciences. Springer, Berlin, Heidelberg, New York.

Burchard, H., Baumert, H., 1995. On the performance of a mixed-layer model based on the k-ε turbulence closure. J. Geophys. Res. 100, 8523–8540.

Burchard, H., Beckers, J.-M., 2004. Non-uniform adaptive vertical grids in one-dimensional numerical ocean models. Ocean Modelling 6, 51–81.

Burchard, H., Bolding, K., 2002. GETM – a general estuarine transport model. Scientific documentation. Tech. Rep. EUR 20253 EN, European Commission.

Burchard, H., Bolding, K., Villarreal, M. R., 1999. GOTM – a general ocean turbulence model. Theory, applications and test cases. Tech. Rep. EUR 18745 EN, European Commission.

Burchard, H., Bolding, K., Villarreal, M. R., 2004. Three-dimensional modelling of estuarine turbidity maxima in a tidal estuary. Ocean Dynamics 54, 250–265.

Burchard, H., Hetland, R. D., 2010. Quantifying the contributions of tidal straining and gravitational circulation to residual circulation in periodically stratified tidal estuaries. J. Phys. Oceanogr.,Accepted for publication.

Burchard, H., Janssen, F., Bolding, K., Umlauf, L., Rennau, H., 2009. Model simulations of dense bottom currents in the Western Baltic Sea. Cont. Shelf Res. 29, 205–220.

Burchard, H., Lass, H., Mohrholz, V., Umlauf, L., Sellschopp, J., Fiekas, V., Bolding, K., Arneborg, L., 2005. Dynamics of medium-intensity dense water plumes in the Arkona Sea, Western Baltic Sea. Ocean Dynamics 55, 391–402.

Burchard, H., Rennau, H., 2008. Comparative quantification of physically and numerically induced mixing in ocean models. Ocean Modelling 20, 293–311.

Campin, J.-M., Goosse, H., 1999. Parameterization of density-driven downsloping flow for a coarse-resolution ocean model in z-coordinate. Tellus 51A, 412–430.

Cenedese, C., Whitehead, J. A., Ascarelli, J. A., Ohiwa, M., 2004. A dense current flowing down a sloping bottom in a rotating fluid. Journal of Physical Oceanography 34, 188–203.

Cheng, Y., Canuto, V. M., Howard, A. M., 2002. An improved model for the turbulent PBL. J. Atmos. Sci. 59, 1550–1565.

Eden, C., Oschlies, A., 2006. Adiabatic reduction of circulation-related CO_2 air-sea flux biases in a North Atlantic carbon-cycle model. Global Biogeochemical Cycles 20, doi:10.1029/2005GB002521.

Elken, J., Matthäus, W., 2008. The decay power law in grid-generated turbulence. [in:] Assessment of climate change for the Baltic Sea basin. Annex A.1.1, H. von Storch and A. Omstedt (eds.), BALTEX Publ., Springer, Berlin, 474pp.

Ellison, T. H., Turner, J. S., 1959. Turbulent entrainment in stratified flows. J. Fluid Mech. 6, 423–448.

Ezer, T., 2005. Entrainment, diapycnal mixing and transport in three-dimensional bottom gravity current simulations using the Mellor-Yamada turbulence scheme. Ocean Modelling 9, 151–168.

Ezer, T., 2006. Topographic influence on overflow dynamics: idealized numerical simulations and faroe bank overflow. J. Geophys. Res. 111, C02002, doi:10.1029/2005JC003195.

Ezer, T., Arango, H. G., Shchepetkin, A. F., 2002. Developments in terrain-following ocean models: intercomparisons of numerical aspects. Ocean Modelling 4, 249–267.

Ezer, T., Mellor, G. L., 2004. A generalised coordinate ocean model and a comparison of the bottom boundary layer dynamics in terrain-following and in z-level grids. Ocean Modelling 6, 379–403.

Feistel, R., Feistel, S., 2006. Die Ostsee als thermodynamisches System. in: Schimanski-Geier, L., Malchow, H., and Pöschel, T. (Eds.), Irreversible Prozesse und Selbstorganisation, Logos-Verlag Berlin, 247–264.

Feistel, R., Nausch, G., Hagen, E., 2006. Unusual Baltic inflow activity 2002/3 and varying deep-water properties. Oceanologia 48, 21–35.

Feistel, R., Nausch, G., Heene, T., Piechura, J., Hagen, E., 2004. Evidence for a warm water inflow into the Baltic Proper in summer 2003. Oceanologia 46, 581–598.

Feistel, R., Nausch, G., Matthäus, W., Hagen, E., 2003a. Temporal and spatial evolution of the Baltic deep water renewal in spring 2003. Oceanologia 45, 623–642.

Feistel, R., Nausch, G., Mohrholz, V., Lysiak-Pastuszak, E., Seifert, T., Matthäus, W., Krüger, S., Hansen, I. S., 2003b. Warm waters of summer 2002 in the deep Baltic Proper. Oceanologia 45, 571–592.

Fennel, W., Radtke, H., Schmidt, M., Neumann, T., 2010. Transient upwelling in the central Baltic Sea. Continental Shelf Research 30 (19), 2015–2026.

Fennel, W., Seifert, T., 1995. Kelvin wave controlled upwelling in the Baltic Sea. J. Mar. Sys. 6, 289–300.

Fennel, W., Seifert, T., Kayser, B., 1991. Rossby radii and phase spedds in the Baltic Sea. Cont. Shelf Res. 11, 23–36.

Fer, I., Voet, G., Seim, K. S., Rudels, B., , Latarius, K., 2010. Intense mixing of the faroe bank channel overflow. Geophys. Res. Lett. 37, L02604, doi:10.1029/2009GL041924.

Fernández, V., Dietrich, D. E., Haney, R. L., Tintoré, J., 2005. Mesoscale, seasonal and interannual variability in the Mediterranean Sea using a numerical ocean model. Progr. Oceanogr. 66, 321–340.

Fischer, H., Mattäus, W., 1996. The importance of the Drogden Sill in the Sound for major Baltic inflows. J. Mar. Sys. 9, 137–157.

Garrett, C. J., Munk, W., 1975. Space-time scales of internal waves: A progress report. J. Geophys. Res. 80, 291–297.

Gerdes, R., 1993. A primitive equation ocean circulation model using a general vertical coordinate transformation. 1. Description and testing of the model. J. Geophys. Res. 98, 14683–14701.

Gerdes, R., Köberle, C., Willebrand, J., 1991. The influence of numerical advection schemes on the results of ocean general circulation models. Clim. Dyn. 5, 211–226.

Gill, A. E., 1982. Atmosphere–ocean dynamics. Vol. 30 of International Geophysics Series. Academic Press.

Girton, J. B., Pratt, L. J., Sutherland, D., Price, J., 2006. Is the Faroe Bank Channel overflo hydraulically controlled? J. Phys. Oceanogr. 36, 2340–2349.

Girton, J. B., Sanford, T. B., 2003. Descent and modification of the overflow plume in the Denmark Strait. J. Phys. Oceanogr. 33, 13511364.

Griffies, S. M., Harrison, M. J., Pacanowski, R. C., Rosati, A., 2007. A technical guide to MOM4. Tech. Rep. 5, GFDL Ocean Group, NOAA/Geophysical Fluid Dynamics Laboratory, Princeton, NJ, available online at `http://www.gfdl.noaa.gov/~fms`.

Griffies, S. M., Pacanowski, R. C., Hallberg, R. W., 2000. Spurious diapycnal mixing associated with advection in a z-coordinate ocean model. Mon. Weather Rev. 128, 538–564.

Griffies, S. M., Pacanowski, R. C., Schmidt, M., Balaji, V., 2001. Tracer Conservation with an Explicit Free Surface Method for z-Coordinate Ocean Models. Mon. Weather Rev. 129, 1081–1098.

Hagen, E., Feistel, R., 2001. Spreading of Baltic deep water: A case study for the winter 19971998. Meereswiss. Ber. http://www.io-warnemuende.de/research/mebe.html 45, 99–133.

Hagen, E., Feistel, R., 2004. Observations of low-frequency current fluctuations in deep water of the Eastern Gotland Basin/Baltic Sea. J. Geophys. Res. 109, C03044, 15 PP.,doi:10.1029/2003JC002017.

Haidvogel, D. B., Beckmann, A., 1999. Numerical Ocean Circulation Modelling. Vol. 2 of Series on Environmental Science and Management. Imperial College Press, London.

Hallberg, R., 2000. Time integration of diapycnal diffusion and richardson number dependent mixing in isopycnal coordinate models. Mon. Weather Rev. 128, 1402–1419.

Haney, R. L., 1991. On the pressure gradient force over steep topography in sigma coordinate ocen models. J. Phys. Oceanogr. 21, 610–619.

Henderson, R. D., 1997. Nonlinear dynamics and pattern formation in turbulent wake transition. J. Fluid Mech. 352, 65–112.

Hirsch, C., 1988. Numerical computation of internal and external flows. Vol. 1: Fundamentals of numerical discretisation. Wiley Series in Numerical Methods in Engineering. Wiley, Chichester.

Hodges, B. R., Delavan, S. K., 2004. Numerical diffusion and dissipation in hydrostatic models of internal waves. ASCE Engineering Mechanics Conference Proceedings June 13-16.

Hofmeister, R., Beckers, J.-M., Burchard, H., 2010a. Realistic modelling of the exceptional inflows into the central Baltic Sea in 2003 using terrain-following coordinates. Ocean ModellingSubmitted.

Hofmeister, R., Burchard, H., Beckers, J.-M., 2010b. Non-uniform adaptive vertical grids for 3d numerical ocean models. Ocean Modelling 33, 70–86.

Hofmeister, R., Burchard, H., Bolding, K., 2007. Realistic modelling of stratification in the Limfjord. Cont. Shelf Res.,Submitted.

Hornung, H. G., Willert, C., Turner, S., 1995. The flow field downstream of a hydraulic jump. J. Fluid Mech. 287, 299–316.

Jakobsen, F., Lintrup, M. J., Møller, J. S., 1997. Observations of the specific resistance in Öresund. Nordic Hydrology 28, 217–232.

James, I. D., 1996. Advection schemes for shelf sea models. J. Mar. Sys. 8, 237–254.

Janssen, F., Neumann, T., Schmidt, M., 2004. Inter-annual variability in cyanobacteria blooms in the Baltic Sea controlled by wintertime hydrographic conditions. Mar. Ecol. Prog. Ser. 275, 59–68.

Janssen, F., Schrum, C., Backhaus, J. O., 1999. A climatological data set of temperature and salinity for the Baltic Sea and the North Sea. Dt. Hydrogr. Z. Suppl. 9, 1–245.

Jungclaus, J. H., Mellor, G. L., 2000. A three-dimensional model study of the Mediterranean outflow. J. Mar. Sys. 24, 41–66.

Kõuts, T., Omstedt, A., 1993. Deep water exchange in the Baltic Proper. Tellus 45 A, 311–324.

Kida, S., Price, J. F., Yang, J., 2008. The upper-oceanic response to overflows: A mechanism for the azores current. Journal of Physical Oceanography 38 (4), 880–895.

Killworth, P. D., Edwards, N. R., 1999. A turbulent bottom boundary layer code for use in numerical ocean models. J. Phys. Oceanogr. 29, 12211238.

Kliem, N., Pietrzak, J. D., 1999. On the pressure gradient error in sigma coordinate ocean models: A comparison with a laboratory experiment. J. Geophys. Res. 104, 29781–29800.

Knudsen, M., 1900. Ein hydrographischer lehrsatz. Ann. Hydrogr. Mar. Meteorol. 28(7), 316–320.

Kowalewski, M., Ostrowski, M., 2005. Coastal up- and downwelling in the southern Baltic. Oceanologia 4, 453–475.

Kunze, E., Sandford, T. B., 1996. Abyssal mixing: Where is it not. J. Phys. Oceanogr. 26, 2286–2296.

Large, W. G., Gent, P. R., 1999. Validation of vertical mixing in an equatorial ocean model using Large Eddy Simulations and observations. J. Phys. Oceanogr. 29, 449–464.

Large, W. G., McWilliams, J. C., Doney, S. C., 1994. Oceanic vertical mixing : a review and a model with nonlocal boundary layer parameterisation. Rev. Geophys. 32, 363–403.

Lass, H. U., 2003. Über mögliche Auswirkungen von Windparks auf den Wasseraustausch zwischen Nord- und Ostsee. In: 12. Meeresumwelt-Symposium 2002. Bundesamt für Seeschifffahrt und Hydrographie (BSH), Hamburg and Rostock, pp. 121–132.

Lass, H. U., Matthäus, W., 1996. On temporal wind variations forcing salt water inflows into the Baltic Sea. Tellus 48 A, doi:10.1034/j.1600–0870.1996.t01–4–00005.x.

Lass, H. U., Mohrholz, V., 2003. On the dynamics and mixing of inflowing salt-water in the Arkona Sea. J. Geophys. Res. 108, 3042, doi: 10.1029/2002JC001465.

Lass, H. U., Mohrholz, V., Knoll, M., Prandke, H., 2008. Enhanced mixing downstream of a pile in an estuarine flow. J. Mar. Sys. 74, 505–527.

Lass, H. U., Mohrholz, V., Seifert, T., 2005. On pathways and residence time of saltwater plumes in the Arkona Sea. J. Geophys. Res. 110, doi:10.1029/2004JC002848.

Lass, H. U., Prandke, H., Liljebladh, B., 2003. Dissipation in the Baltic Proper during winter stratification. J. Geophys. Res. 108, 3187, doi: 10.1029/2002JC001401.

Ledwell, J. R., Montgomery, E. T., Polzin, K. L., St-Laurent, L. C., Schmitt, R. W., Toole, J. M., 2000. Evidence for enhanced mixing over rough topography in the abyssal ocean. Nature 403, 179–182.

Ledwell, J. R., Watson, A. J., Law, C. S., 1993. Evidence of slow mixing across the pycnocline from an open-ocean tracer-release experiment. Nature 364, 701–703.

Lee, M.-M., Nurser, A. J. G., Coward, A., 2002. Spurious diapycnal mixing of the deep waters in an eddy-resolving global ocean model. J. Phys. Oceanogr. 32, 1522–1535.

Legg, S., Ezer, T., Jackson, L., Briegleb, B., Danabasoglu, G., Large, W., Wu, W., Chang, Y., zgkmen, T. M., Peters, H., Xu, X., Chassignet, E. P., Gordon, A. L., Griffies, S., Hallberg, R., Price, J., Riemenschneider, U., Yang, J., 2009. Improving oceanic overflow representation in climate models: The gravity current entrainment climate process team. Bulletin of the American Meteorological Society 90 (5), 657–670.

Legg, S., Hallberg, R. W., Girton, J. B., 2006. Comparison of entrainment in overflows simulated by z-coordinate, isopycnal and non-hydrostatic models. Ocean Modelling 11, 69–97.

Lehmann, A., 1995. A three-dimensional baroclinic eddy-resolving model of the Baltic Sea. Tellus 47A, 1013–1031.

Lehmann, A., Lorenz, P., Jacob, D., 2004. Modelling the exceptional Baltic Sea inflow events in 2002-2003. Geophys. Res. Lett. 31, doi:10.1029/2004GL020830.

Lehmann, A., Myrberg, K., 2008. Upwelling in the Baltic Sea – a review. Journal of Marine Systems 74 (Supplement 1), S3–S12, Baltic Sea Science Congress 2007.

Leonard, B. P., 1991. The ULTIMATE conservative difference scheme applied to unsteady one-dimensional advection. Comput. Meth. Appl. Mech. Eng. 88, 17–74.

LeVeque, R. J., 1992. Numerical methods for conservation laws. Birkhäuser, Basel, Boston, Berlin.

Marshall, J., Shuckburgh, E., Jones, H., Hill, C., 2006. Estimates and implications of surface eddy diffusivity in the Southern Ocean derived from tracer transport. J. Phys. Oceanogr. 36, 1806–1821.

Matear, R. J., 2001. Effects of numerical advection schemes and eddy parameterisations on ocean ventilation and oceanic anthropogenic CO_2 uptake. Ocean Modelling 3, 217–248.

Matthäus, W., 1984. Climatic and seasonal variability of oceanological parameters in the Baltic Sea. Beiträge zur Meereskunde 51, 29–49.

Matthäus, W., 2006. The history of investigation of salt water inflows into the Baltic Sea from the early beginning to recent results. Meereswissenschaftliche Berichte 65, 1–73.

Matthäus, W., Frank, H., 1992. Characteristics of major Baltic inflows – a statistical analysis. Cont. Shelf Res. 12, 1375–1400.

Meier, H. E. M., Döscher, R., Coward, A. C., Nycander, J., Döös, K., 1999. RCO - Rossby Centre regional Ocean climate model: model description (version 1.0) and first results from the hindcast period 1992/93. Tech. Rep. Reports Oceanography No. 26, Swedish Meteorological and Hydrological Institute, Norrköping, Sweden.

Meier, H. E. M., Döscher, R., Faxén, T., 2003. A multiprocessor coupled ice-ocean model for the Baltic Sea: Application to salt inflow. J. Geophys. Res. 108, 3273, doi:10.1029/2000JC000521.

Meier, H. E. M., Kauker, F., 2003. Modeling decadal variability of the Baltic Sea: 2. Role of freshwater inflow and large-scale atmospheric circulation for salinity. J. Geophys. Res. 108, 3368, doi:10.1029/2003JC001799.

Meier, M., Feistel, R., Piechura, J., Arneborg, L., Burchard, H., Fiekas, V., Golenko, N., Kuzmina, N., Mohrholz, V., Nohr, C., Paka, V. T., Sellschopp, J., Stips, A., Zhurbas, V., 2006. Ventilation of the Baltic Sea deep water: a brief review of present knowledge from observations and models. Oceanologia 48, 133–164.

Mellor, G. L., Ezer, T., Oey, L.-Y., 1994. The pressure gradient conundrum of sigma coordinate ocean models. Journal of Atmospheric and Oceanic Technology 11, 1126–1134.

Mellor, G. L., Oey, L.-Y., Ezer, T., 1998. Sigma coordinate pressure gradient errors and the seamount problem. Journal of Atmospheric and Ocean Technology 15, 1122–1131.

Mesinger, F., Arakawa, A., 1976. Numerical methods used in atmospheric models. GARP Publ. Series, No. 17, Vol. 1,WMO, Geneva, 64 pp. [Available from WMO/ICSU. Case Postale No. 2300, CH-1121 Geneva 20. Switzerland.].

Mohrholz, V., Dutz, J., Kraus, G., 2006. The impact of exceptionally warm summer inflow events on the environmental conditions in the Bornholm Sea. J. Mar. Sys. 60, 285–301.

Mohrholz, V., Rennau, H., 2010. Pathways and spreading behaviour of dense bottom currents in the western Baltic Sea.

Morales Maqueda, M. A., Holloway, G., 2006. Second-order moment advection scheme applied to Arctic Ocean simulation. Ocean Modelling 14, 197–221.

Munk, W. H., 1966. Abyssal recipes. Deep-Sea Research 13, 707–730.

Nakano, H., Suginohara, N., 2002. Effects of bottom boundary layer parameterization on reproducing deep and bottom waters in a world ocean model. JPO 32, 1209–1227.

Nausch, G., Matthus, W., Feistel, R., 2003. Hydrographic and hydrochemical conditions in the Gotland Deep area between 1992 and 2003. Oceanologia 45(4), 557–569.

Neumann, T., Fennel, W., Kremp, C., 2002. Experimental simulations with an ecosystem model of the Baltic Sea: A nutrient load reduction experiment. Global Biogeochemical Cycles 16, 10.1029/2001GB001450.

Oguz, T., Özsoy, E., Latif, M. A., Sur, H. I., Ünlüata, U., 1990. Modeling of hydraulically controlled exchange flow in the Bosphorus Strait. J. Phys. Oceanogr. 20, 945–965.

Osborn, T. R., 1980. Estimates of the local rate of vertical diffusion from dissipation measurements. J. Phys. Oceanogr. 10, 83–89.

Osiski, R., Rak, D., Walczowski, W., Piechura, J., 2010. Baroclinic Rossby radius of the deformation in the southern baltic sea. Oceanologica 52(3), 417–429.

Pacanowski, R. C., Gnanadesikan, A., 1998. Transient response in a z-level ocean model that resolves topography with partial cells. Mon. Weather Rev. 126, 3248–3270.

Pacanowsky, R., Philander, S. G. H., 1981. Parameterisation of vertical mixing in numerical models of tropical oceans. J. Phys. Oceanogr. 11, 1443–1451.

Papadakis, M. P., Chassignet, E. P., Hallberg, R. W., 2003. Numerical simulations of the mediterranean sea outflow: impact of the entrainment parameterization in an isopycnic coordinate ocean model. Ocean Modelling 5, 325356.

Peters, H., Johns, W. E., 2005a. Circulation and mixing in the Faroese Channels. Deep Sea Res. I 52, 883913.

Peters, H., Johns, W. E., 2005b. Mixing and Entrainment in the Red Sea Outflow Plume. Part ii: Turbulencei Characteristics. Journal of Physical Oceanography 35 (5), 584–600.

Piechura, J., Beszczyińska-Möller, A., 2003. Inflow waters in the deep regions of the southern Baltic Sea transport and transformations. Oceanologia 45(4), 593–621.

Pietrzak, J., 1998. The use of TVD limiters for forward-in-time upstream-biased advection schemes in ocean modeling. Mon. Weather Rev. 126, 812–830.

Polzin, K., Toole, J. M., Schmitt, R. W., 1995. Finescale parameterizations of turbulent dissipation. J. Phys. Oceanogr. 25(3), 306–328.

Reissmann, J. H., Burchard, H., Feistel, R., Hagen, E., Lass, H. U., Mohrholz, V., Nausch, G., Umlauf, L., Wieczorek, G., 2009. State-of-the-art review on Baltic mixing and consequences for eutrophication. Progr. Oceanogr.,In print.

Rennau, H., Burchard, H., 2009. Quantitative analysis of numerically induced mixing in a coastal ocean model. Ocean Dynamics 59, 671–687.

Rennau, H., Burchard, H., Schimmels, S., 2010. The impact of offshore wind farms on transport and dilution in density-driven bottom currents: a numerical model study. Coastal Engineering,Submitted.

Riemenscheider, U., Legg, S., 2007. Regional simulations of the Faroe Bank Channel overflow in a level model. Ocean Modelling 17, 93–122.

Robinson, A. R., 1983. Eddies in Marine Science. Springer, New York.

Rodi, W., 1980. Turbulence models and their application in hydraulics. Tech. rep., Int. Assoc. for Hydraul. Res., Delft, The Netherlands.

Roe, P. L., 1985. Some contributions to the modeling of discontinuous flows. Lect. Notes Appl. Math. 22, 163–193.

Rood, R. B., 1987. Numerical advection algorithms and their role in atmospheric transport and chemistry models. Rev. Geophys. 25, 71–100.

Rooth, C., Östlund, G., 1972. Penetration of tritium into the Atlantic thermocline. Deep-Sea Research 19, 481–492.

Sanderson, B., 1998. Order and resolution for computational ocean dynamics. J. Phys. Oceanogr. 28, 1271–1286.

Schimmels, S., 2008. Numerical simulation of the influence of circular cylinders on mixing and entrainment in natural density currents. Ph.D. thesis, Fluid Mechanics Institute, Leibniz University of Hannover, Germany.

Schimmels, S., Markofsky, M., 2010. Numerical near-field modelling of mixing induced by monopiles in a stratified flow. Coastal Engineering,In preparation.

Seifert, T., Kayser, B., 1995. A high resolution spherical grid topography of the Baltic Sea. Meereswiss. Ber., Warnemünde 9, 73–88.

Sellschopp, J., Arneborg, L., Knoll, M., Fiekas, V., Gerdes, F., Burchard, H., Lass, H. U., Mohrholz, V., Umlauf, L., 2006. Direct observations of a medium-intensity inflow into the Baltic Sea. Cont. Shelf Res. 26, 2393–2414.

Shchepetkin, A. F., McWilliams, J. C., 1998. Quasi-monotone advection schemes based on explicit locally adaptive dissipation. Mon. Weather Rev. 126, 1541–1580.

Shchepetkin, A. F., McWilliams, J. C., 2003. A method for computing horizontal pressure-gradient force in an oceanic model with a nonaligned vertical coordinate. J. Geophys. Res. 108, 10.1029/2001JC001047.

Shchepetkin, A. F., McWilliams, J. C., 2005. The regional oceanic modelling system (ROMS): a split-explicit, free-surface, topography-following-coordinate oceanic model. Ocean Modelling 9, 347–404.

Smolarkiewicz, P. K., 1983. A simple positive definite advection scheme wih small implicit diffusion. Mon. Weather Rev. 111, 479–486.

Smolarkiewicz, P. K., Margolin, L. G., 1998. Mpdata: A finite-difference solver for geophysical flows. J. Computat. Phys. 140, 459–480.

Song, Y. T., Chao, Y., 2000. An embedded bottom boundary layer formulation for z-coordinate ocean models. Journal of Atmospheric and Ocean Technology 17, 546560.

Stanev, E. V., Wolff, J.-O., Burchard, H., Bolding, K., Flöser, G., 2003. On the circulation in the East Frisian Wadden Sea: Numerical modelling and data analysis. Ocean Dynamics 53, 27–51.

Stigebrandt, A., 1992. Bridge-induced flow reduction in sea straits with reference to effects of a planned bridge across Öresund. Ambio 21, 130–134.

Stigebrandt, A., 2003. Regulation of vertical stratification, length of stagnation periods and oxygen conditions in the deeper deepwater of the Baltic proper. in: Fennel, W. and Hentzsch, B. (Eds.), Festschrift zum 65. Geburtstag von Wolfgang Matthus, Meereswissenschaftliche Berichte 54, 69–80.

Stigebrandt, A., Lass, H.-U., Liljebladh, B., Alenius, P., Piechura, J., Hietala, R., Beszczyińska, A., 2002. DIAMIX - an experimental study of diapycnal deepwater mixing in the virtually tideless Baltic Sea. Boreal Environment Research 7(4), 363–369.

Stips, A., Bolding, K., Burchard, H., Djavidinia, S., Peneva, E., 2005. Realistic multiannual simulations of the coupled North Sea and Baltic Sea system using te GETM model. Tech. Rep. EUR 21053 EN, European Commission.

Stips, A., Pohlmann, T., Bolding, K., Burchard, H., 2004. Simulating the temporal and spatial dynamics of the North Sea using the new model GETM (General Estuarine Transport Model). Ocean Dynamics 54, 266–283.

Sumer, B., Fredsøe, J., 1997. Hydrodynamics around cylindrical structures. World Scientific, Singapure.

Svensson, U., Häggkvist, K., 1990. A two-equation turbulence model for canopy flows. Journal of Wind Engineering and Industrial Aerodynamics 35, 201–211.

Sverdrup, H. U., 1937. On The Process Of Upwelling. J. Mar. Sys. 8, 155–164.

Toggweiler, J. R., Samuels, B., 1998. On the oceans large-scale circulation near the limit of no vertical mixing. J. Phys. Oceanogr. 28, 1832–1852.

Toole, J. M., Polzin, K. L., Schmidt, R. W., 1994. Estimates of diapycnal mixing in the abyssal ocean. Science 264, 1120–1123.

TRM, 2005. Energy strategy 2025. perspectives to 2025 and draft action plan for the future electricity infrastructure.

Turner, J. S., 1973. Buoyancy effects in fluids. Cambridge University Press.

Turner, J. S., 1986. Turbulent entrainment: the development of the entrainment assumption, and its application to geophysical flows. J. Fluid Mech. 173, 431–471.

Umlauf, L., 2009. A note on the description of mixing in stratified layers without shear in large-scale ocean models. J. Phys. Oceanogr. 39, 3032–3039.

Umlauf, L., Arneborg, L., 2009a. Dynamics of rotating shallow gravity currents passing through a channel. part i: Observation of transverse structure. J. Phys. Oceanogr. 39, 2385–2401.

Umlauf, L., Arneborg, L., 2009b. Dynamics of rotating shallow gravity currents passing through a channel. part ii: Analysis. J. Phys. Oceanogr. 39, 2402–2416.

Umlauf, L., Arneborg, L., Burchard, H., Fiekas, V., Lass, H. U., Mohrholz, V., Prandke, H., 2007. The transverse structure of turbulence in a rotating gravity current. Geophys. Res. Lett. 34, L08601, doi:10.1029/2007GL029521.

Umlauf, L., Arneborg, L., Hofmeister, R., Burchard, H., 2010. Entrainment in shallow rotating gravity currents: A modeling study. J. Phys. Oceanogr.,Accepted for publication.

Umlauf, L., Burchard, H., 2003. A generic length-scale equation for geophysical turbulence models. J. Mar. Res. 61, 235–265.

Umlauf, L., Burchard, H., 2005. Second-order turbulence models for geophysical boundary layers. A review of recent work. Cont. Shelf Res. 25, 795–827.

Umlauf, L., Burchard, H., Bolding, K., 2005. General Ocean Turbulence Model. Source code documentation. Tech. Rep. 63, Baltic Sea Research Institute Warnemünde, Warnemünde, Germany.

Umlauf, L., Lemmin, U., 2005. Inter-basin exchange and mixing in the hypolimnion of a large lake: the role of long internal waves. Limnol. Oceanogr. 50, 1601–1611.

van Aken, H. M., 1986. The onset of stratification in shelf seas due to differential advection in the presence of a salinity gradient. Cont. Shelf Res. 5, 475–485.

van Haren, H., Maas, L., Zimmerman, J. T. F., Malschaert, H. R. H., 1999. Strong inertial currents and marginal internal wave stability in the central North Sea. Geophys. Res. Lett. 26, 2993–2996.

Veronis, G., 1977. Use of tracers in circulation studies. The Sea , E.D. Goldberg et al.,Eds., Vol. 6, Wiley InterScience, 169–188.

Wahlin, A. K., Cenedese, C., 2006. How entraining density currents influence the ocean stratification. Deep Sea Research II 53, 172–193.

Walin, G., 1972. On the hydrographic response to transient meteorological disturbances. Tellus 24, 169–186.

Webb, D. J., Cuevas, B. D., Richmond, C., 1998. Improved advection schemes for ocean models. Journal of Atmospheric and Oceanic Technology 15, 1171–1187.

Wells, M., Cenedese, C., Caulfield, C. P., 2010. The entrainment ratio between flux coefficient and entrainment ratio in density currents. J. Phys. Oceanogr. DOI: 10.1175/2010JPO4225.1.

Wilcox, D. C., 1988. Reassessment of the scale-determining equation for advanced turbulence models. AIAA Journal 26, 1299–1310.

Willebrand, J., Bernier, B., Böning, C., Dieterich, C., Killworth, P. D., Le Provost, C., Lia, Y., Molines, J.-M., New, A. L., 2001. Circulation characteristics in three eddy-permitting models of the North Atlantic. Progr. Oceanogr. 48, 123–161.

Winters, K. B., D'Asaro, E. A., 1996. Diascalar flux and the rate of fluid mixing. J. Fluid Mech. 317, 179–193.

Winters, K. B., Lombard, P. N., Riley, J. J., D'Asaro, E. A., 1995. Available potential energy and mixing in density-stratified fluids. J. Fluid Mech. 289, 115–128.

Winther, N. G., Morel, Y. G., Evensen, G., 2007. Efficiency of high order numerical schemes for momentum advection. J. Mar. Sys. 67, 31–46.

Winton, M., Hallberg, R., Gnanadesikan, A., 1998a. Simulation of density-driven frictional downslope flow in z-coordinate ocean models. J. Phys. Oceanogr. 28, 2163–2174.

Winton, M., Hallberg, R., Gnanadesikan, A., 1998b. Simulation of density-driven frictional downslope flow in z-coordinate ocean models. J. Phys. Oceanogr. 28, 2163–2174.

Wüest, A., Lorke, A., 2003. Small-scale hydrodynamics in lakes. Annual Review of Fluid Mechanics 35, 373–412.

Wyrtki, K., 1954. Der große Salzeinbruch in die Ostsee im November und Dezember 1951. Kieler Meeresforsch. 10, 19–25.

Xing, J., Davies, A. M., 2007. On the importance of non-hydrostatic processes in determining tidally induced mixing in sill regions. Cont. Shelf Res. 27, 2162–2185.

Xu, X., Chang, Y. S., Peters, H., Özgökmen, T. M., Chassignet, E. P., 2006. Parameterization of gravity current entrainment for ocean circulation models using a high-order 3d nonhydrostatic spectral element model. Ocean Modelling 14, 19–44.

Xu, Y., Fernando, H. J. S., Boyer, D. L., 1995. Turbulent wakes of stratified flow past a cylinder. Phys. Fluids 7, 2243–2255.

Zhurbas, V. M., Paka, V. T., 1999. What drives thermohaline intrusions in the Baltic Sea? J. Mar. Sys. 21, 229–241.